

**STUDIES ON METAL OXIDES AND COBALT NITRIDE AS
PROSPECTIVE ANODES FOR LITHIUM ION BATTERIES**

BY

BIJOY KUMAR DAS

(M.Tech., Indian Institute of Technology (IIT-Kharagpur, India))

**A THESIS SUBMITTED
FOR THE DEGREE OF
DOCTOR OF PHILOSOPHY**

**DEPARTMENT OF PHYSICS
NATIONAL UNIVERSITY OF SINGAPORE
(2011)**

Acknowledgements

I would like to express my deep and sincere gratitude and heartfelt thanks to my supervisor Professor B. V. R. Chowdari, Department of Physics. His deep knowledge, unique way of thinking, constant guidance, help, timely advice and continuous encouragement have provided a good basis for the Thesis.

I owe my sincere thanks to Professor G. V. Subba Rao for his advice, constant words of encouragement, supports and academic interactions through out my research endeavour. Also, his linguistic and scientific feedback helped me to establish the overall direction of the research work.

I am thankful to Dr. M. V. Reddy for helping me with experimental techniques involved in the synthesis, characterization and electrochemical study of various materials. The financial support by the way of Research Scholarship and facilities from the National University of Singapore (NUS) are greatly acknowledged. I would like to thank Asst. Prof. R. Mahendiran for helping me with the magnetic data. Further, I would like to extend my thanks to Institute of Materials Research and Engineering (IMRE) and Dr. Sudhiranjan Tripathy for helping me with the Raman Spectroscopy data. Also, thanks are due to Center for Ion Beam Application (CIBA), Dept. of Physics for help with the RBS facility and data.

I thank the entire academic and administrative staff of the Department of Physics for their help and assistance. My sincere thanks are due to Prof. Wee Thye Shen Andrew, Dean of the Faculty of Science and Director, Surface Science Laboratory, Department of Physics, NUS for allowing me the use of SEM facilities. I am also thankful to Mr. Ho Kok Wen for assisting me in SEM analysis. I thank Mdm. Pang for helping me in using

XRD apparatus. I am also grateful to Mr. Mani Mohan and Mr. Suradi Bin Sukri for their help and assistance during my work. The help and assistance rendered by our Lab Officer, Mr. Abdul Karim is sincerely acknowledged. I am also thankful to Mdm. Leng Lee Eng of Chemistry Department for helping me with Elemental analysis.

Due acknowledgement has been made of research work done by others in the literature on Lithium Ion Batteries (LIBs) and electrode materials over the years, by referring them appropriately in the respective Chapters of the Thesis. Due to vast amount of literature on the topic of the Thesis, it has not been possible to quote all the available references and any omissions are due to over sight or to error in judgement, which may be condoned.

I would like to thank my colleagues Dr. Aravindan, Dr. Y. Sharma and Mr. Christie for their help and interaction. I am also thankful to Madhusmita Swain, Dr. N. Pramanik, Dr. Nidhi Sharma, Dr. Sunil Singh Kushvaha, Dr. Sanjiv Yadav and Dr. Pandey for their support and helping hand during my entire stay in Singapore.

I am indebted to my father (Mr. Mahendra Chandra Das) and Mother (Mrs. Ramamani Das) for their affection, encouragement and support. I also wish to acknowledge my brother (Mr. Mrutyunjoy Das), my sister-in-law (Mrs. Bhabalata Das), my sisters and brothers- in-law for their cooperation and understanding. I also wish to thank my loving nephews (Priyanka, Sanjoy, Sonu) for making my life pleasant during the hectic time. Above all, I would like to thank the Almighty, for His kindness, grace and blessings throughout my career.

Contents

Acknowledgements	i
Contents	iii
Summary	xi
List of Figures	xvii
List of Tables	xxv
List of publications/ Conference presentations	xxvi

Chapter I Introduction

Abstract	1
I.1. Definition of the Battery	1
I.1.1. Primary (Disposable) batteries	1
I.1.2. Secondary (Rechargeable) battery	2
I.2. Development of Li-ion batteries	2
I.3. Principle of operation of LIBs	3
I.4 Applications and World market	6
I.5. Need of R&D and selection criterion of electrode materials for LIBs	6
I.6. Prospective second generation cathode materials for LIBs	9
I.6.1. Modified LiCoO ₂	9
I.6.2. Layered LiNiO ₂	10
I.6.3. Layered LiMnO ₂ , Li(Ni _{1/2} Mn _{1/2})O ₂ and Li(Ni _{1/3} Mn _{1/3} Co _{1/3})O ₂	11
I.6.4. Spinel LiMn ₂ O ₄	12
I.6.5. Olivine- LiMPO ₄ (M = Fe, Co, Ni, Mn)	14
I.6.6. LiVPO ₄ F and Li ₃ V ₂ (PO ₄) ₃	15

I. 6.7. Heavily- doped LiMn_2O_4 as 5- V cathodes	17
I. 6.8. Theoretical studies on cathode materials	18
I.7. Prospective Anode materials for LIBs	19
I.7.1. Intercalation/ de-intercalation based anode materials	20
I.7.1.1. Graphitic carbon, carbon nanotubes, Fullerene and disordered carbon	20
I.7.1.2. Oxide Anodes based on intercalation/de-intercalation	23
I.7.1.2.1. $\text{Li}_4\text{Ti}_5\text{O}_{12}$	23
I.7.2. Anodes based on metals undergoing alloying/ de-alloying reaction	26
I.7.2.1. Electrochemistry of Si-Li system	27
I.7.2.2. Electrochemistry of Sn-Li system	29
I.7.2.3. Tin based inter-metallics and composites	31
I.7.2.4. Tin based oxides	32
I.7.2.4.1. Amorphous Tin composite oxides (ATCO)	32
I.7.2.4.2. Sn-based binary oxides	33
I.7.2.4.3. Sn-based ternary oxides	35
I.7.2.5. Antimony (Sb) based Anodes	37
I.7.3. Metal oxide anodes based on conversion reaction	38
I.7.3.1. Binary oxides	38
I.7.3.2. Ternary oxides with spinel structure	42
I.7.3.3. Ternary oxides with other structures	44
I.7.4. Metal nitrides as anodes	44
I.7.4.1. Binary metal nitrides	45

I.7.4.2. Ternary metal nitrides	47
I.7.5. Metal phosphides and sulfides	47
I.7.6. Metal fluorides and Oxyfluorides	49
I.7.7. Metal Hydrides, Carbonates and Oxalates	49
I.8. Electrolytes for LIBs	50
I.8.1. Liquid electrolytes	51
I.8.2. Solid Electrolytes	52
I.8.2.1. Ceramic Electrolytes	53
I.8.2.2. Glassy Electrolytes	54
I.8.3. Polymer Electrolytes	55
I.8.3.1. Solid polymer electrolytes	55
I.8.3.2. Gelled polymer electrolytes	56
I.9. Full cells (LIBs) with various cathodes and anodes	57
I.10. Motivation for Present Study	58
References	60

Chapter II Experimental Techniques

Abstract	76
II.1. Introduction	76
II.2. Synthesis of Materials	77
II.3. Characterization techniques	78
II.3.1. X-ray Diffraction	78
II.3.2. Fourier transform infrared spectroscopy	80
II.3.3. Raman spectroscopy	81

III.3.7.3. Zn ₂ Mo ₃ O ₈ -Li system	147
III.3.8. Electrochemical Impedance spectroscopy	148
III.4. Conclusions	153
References	156

Chapter IV Nanoflake CoN as a high capacity anode for Li- ion batteries

Abstract	160
IV.1. Introduction	161
IV.2. Experimental	163
IV.3. Results and Discussion	164
IV.3.1. Structural and morphological characterization	164
IV.3.2. Electrochemical properties	168
IV.3.2.1. Galvanostatic cycling	168
IV.3.2.2. Cyclic Voltammetry	172
IV.3.2.3. ex- situ XRD, TEM and SAED	175
IV.3.3. Reaction mechanism	177
IV.4. Conclusions	179
References	181

Chapter V

Part I. Li- cyclability and storage of tin hollandites, K₂(M₂Sn₆)O₁₆ (M = Co, In)

Abstract	184
V. 1. Introduction	185
V. 2. Experimental	188
V. 3. Results and Discussion	189

V. 3.1. Structure and Morphology	189
V. 3.2. Galvanostatic cycling	190
V. 3.3. Cyclic Voltammetry	195
V.3.4. Ex- situ XRD	196
V. 4. Conclusions	197
Part II. Nano-phase tin hollandites, $K_2(M_2 Sn_6)O_{16}$ (M = Co, In) as anodes for Li- ion batteries	
Abstract	199
V.5. Introduction	200
V.6. Experimental	201
V.6.1. Preparation of nano-phase $K_2(M_2Sn_6)O_{16}$	201
V.7. Results and Discussion	201
V.7.1. Structure and morphology	201
V.7.2. Electrochemical characterization	204
V.7.2.1. Galvanostatic cycling	204
V.7.2.2. Cyclic Voltammetry	210
V.7.3. Ex-situ XRD and TEM	212
V.7.4. Electrochemical Impedance Spectroscopy	215
V.7.4.1. Li-ion diffusion coefficient	220
V. 8. Summary and Conclusions	222
References	225
Chapter VI Nano- composites, $SnO(VO_x)$ as anodes for lithium ion batteries	
Abstract	228
VI.1. Introduction	229

VI.2. Experimental	232
VI.3. Results and discussion	233
VI.3.1. Structure and morphology	233
VI.3.2. Electrochemical Studies	237
VI.3.2.1. Galvanostatic cycling of nano- SnO	237
VI.3.2.2. Galvanostatic cycling of composites, nano-SnO(VO _x)	239
VI.3.2.3. Cyclic voltammetry	246
VI.3.3. Ex-situ XRD of nano-SnO(V ₂ O ₃) _{0.25}	250
VI.4. Conclusions	251
References	253
Conclusions and Suggestions for Future Work	256

Summary

Lithium ion batteries (LIBs) are the promising dc- energy source for portable electronic devices such as notebook computers, cell phones and camcorders due to their light weight, high energy density and durability. To satisfy the ever-increasing demand for high energy density LIBs for the applications in electric and hybrid electric vehicles (EV/HEVs), lot of research effort is expended to improve the performance of the LIBs in terms of higher energy density, lower cost and safety-in-operation. To achieve the improvements, there is a need to improve the performance of LIB components, i.e., cathode, anode and electrolyte. In this context, a number of materials are being investigated as alternatives to the graphite anode presently being used in LIBs. This Thesis presents studies on mixed metal oxides and cobalt nitride as prospective anode materials for LIBs based on the Li- recyclability by electrochemical processes such as ‘conversion’ reaction involving nano-size metals or formation/ decomposition of Li-metal alloy.

Chapter I describes the LIBs, principle of operation, development of LIBs, applications, world market and need for R&D and selection criterion of electrode materials for LIBs. This is followed by the literature survey on the major battery components, such as cathodes, anodes and electrolytes. The realization of LIBs using the various combinations of anodes and cathodes other than graphite and LiCoO_2 , and motivations of present study are also described. The methods for materials preparation, their physical and electrochemical characterizations have been described under the experimental techniques in Chapter II.

Chapters III to VI describe and discuss the results. Chapter III describes the studies on Mo- cluster compounds, LiYMo_3O_8 , $\text{LiHoMo}_3\text{O}_8$ and $\text{A}_2\text{Mo}_3\text{O}_8$ ($\text{A} = \text{Mn, Co, Zn}$). The compounds were synthesized by carbothermal reduction and characterized by XRD, SEM and HR-TEM. The lattice parameters were calculated by fitting the XRD patterns using Rietveld refinement (Topas R 2.1 software). Selected compounds were characterized by FT-IR, Raman and magnetic measurements. The electrochemical properties were evaluated by galvanostatic cycling, cyclic voltammetry (CV) and electrochemical impedance spectroscopy (EIS) techniques. The underlying reaction mechanism is the ‘conversion’ reaction of the Mo, Co and Zn particles with Li_2O to form MoO_2 , Co_3O_4 and ZnO reversibly except for Y, Ho, Mn. In addition, the reversible formation and decomposition of LiZn- alloy also contributes to the reversible capacity for the compound with, $\text{A} = \text{Zn}$. The reasons for an increasing trend of the reversible capacity with an increase in the cycle number for LiYMo_3O_8 and $\text{LiHoMo}_3\text{O}_8$ are explained. The heat- treated electrode (300°C ; 12 h; Ar) of $\text{A} = \text{Co, Zn}$ showed better Li-cycling performance compared to bare electrode and an explanation is given. The impedance data on LiYMo_3O_8 at different depths of discharge and charge during the 1st and 5th cycle have been analyzed and interpreted.

Chapter IV describes the studies on nanoflake CoN thin film. The compound was prepared by RF magnetron sputtering and characterized by XRD, SEM, HR-TEM and RBS technique. The composition and thickness of CoN was calculated from RBS measurements. Galvanostatic cycling and cycling voltammetry showed that the reaction appears to go through intermediate phases, $(\text{Li}_{3-x}\text{Co}_x)\text{N}$. The nanoflake CoN showed an initial reversible capacity of $760 (\pm 10) \text{ mAhg}^{-1}$ which increases consistently to 990

mAhg⁻¹ (2.7 moles of Li per mole of CoN) at the end of 80th cycle, when cycled at 0.33 C-rate in the voltage range, 0.005 – 3.0 V. The reasons for increasing trend in capacity are explained. Excellent rate capability is also shown by nanoflake CoN. At 0.59 C, a capacity of 950 (±10) mAhg⁻¹ (2.6 moles of Li) after 80 cycles, and at 6.6 C, a capacity of 690 mAhg⁻¹ (1.9 moles of Li) at the end of 50 cycles, are observed.

Chapter V consists of two parts. In Part I, results on micron- size tin hollandites, K₂(M₂Sn₆)O₁₆ (M = Co, In) are discussed. The compounds were synthesized by the high temperature solid- state reaction and characterized by XRD and SEM. Galvanostatic cycling and cyclic voltammetry showed that Co behaves as better matrix element compared to In in the voltage range, 0.005-0.8 V. The tin hollandite with M= Co showed a decreases in reversible capacity from 458(±10) mAhg⁻¹ at the 5th cycle to 415(±10) mAhg⁻¹ at the end of 40th cycle with a capacity retention of 91 %, whereas for M = In, the reversible capacity decreases from 584(±10) mAhg⁻¹ at the 5th cycle to 465(±10) mAhg⁻¹ at the end of the 40th cycle with a capacity retention of 80%. The higher capacity noticed for M = In is due to extra consumption of Li (formation of Li₃In alloy).

In Part II, results on nano-phase tin hollandites, K₂(M₂Sn₆)O₁₆ (M = Co, In) are discussed. The nano-phases were prepared from the pre-synthesized compounds (of Part I) by high energy ball-milling (HEB) and characterized by XRD, HR-TEM and SAED. The TEM data revealed that the particle size is < 10 nm. The crystallite size was calculated by using Scherrer equation. The nano-phase tin hollandites showed better Li-cycling performance compared to that of micron- size. When cycled at 60 mA g⁻¹ in the voltage range, 0.005-0.8 V, the nano-phase with M= Co showed a high and stable capacity of 500 mAhg⁻¹ up to 60 cycles after which a capacity- fade of 4 % occurs in the range of 60-80

cycles. Excellent rate capability was also shown: At 1 C-rate, it showed a capacity of 410 (± 5) mAhg⁻¹ stable up to at least 100 cycles. Under similar cycling conditions, nano-phase with M = In, showed an initial capacity of 570 (± 5) mAhg⁻¹, which dropped to 485 (± 5) mAhg⁻¹ (15 % loss). Significant improvement has been noted in the heat-treated (300 °C; 12 h; Ar) electrode of nano-phase with M = In, which showed a stable capacity of 570 (± 5) mAhg⁻¹ in the range of 5-50 cycles. Small capacity-fading (3%) is noted between 50 to 60 cycles. When cycled to the upper cut-off voltage of 1.0 V, the nano-phase with M = Co showed slightly higher capacity which is stable up to 30 cycles, after which capacity-fading of 6% occurs in the range of 30-60 cycles. Impedance spectra measurements on nano-phase with M = Co during the first-cycle and 11th discharge cycle have been carried out and the data was interpreted. The apparent Li-diffusion coefficients (D_{Li^+}) are also evaluated from EIS data and discussed.

Studies on nanocomposites, SnO(V₂O₃)_x (x = 0, 0.25, 0.5) and SnO(VO)_{0.5} are described in Chapter VI. The compounds were prepared by high energy ball-milling (HEB) and characterized by XRD, SEM and HR-TEM. The SnO and SnO(VO) are unstable to HEB and SnO disproportionate to Sn+SnO₂. The crystallite size of nanocomposite, SnO(V₂O₃)_{0.25} was calculated by using Scherrer equation. The SEM and TEM data revealed that the particle sizes of the nanocomposites are < 30 nm. Galvanostatic cycling and cyclic voltammetry showed that reduction of particle size to nano-size and introducing V₂O₃ and VO as inactive matrix improved the Li-cycling behavior of SnO. The reversible capacity of these nanocomposites arises due to the alloying and de-alloying of Sn. The nanocomposite, SnO(V₂O₃)_{0.5} showed a first-charge capacity of 435(± 5) mAhg⁻¹ which stabilized to 380(± 5) mAhg⁻¹ with no noticeable

fading in the range of 10- 60 cycles when cycled at 60 mA g^{-1} (0.12 C) in the voltage range, 0.005- 0.8 V. Under similar cycling conditions, nano-SnO, the nanocomposites, SnO(V₂O₃)_{0.25} and SnO(VO)_{0.5} showed initial reversible capacities between 630 and 390 (± 5) mA $h g^{-1}$. Between 10-50 cycles, nano-SnO showed a capacity- fade as high as 59% in good agreement with literature reports, whereas the above two VO_x- containing composites showed capacity- fade ranging from 10 to 28 %. Cycling to an upper cut- off voltage, 1.0 V gives rise to a slight increase in the reversible capacity in the case of nanocomposites, SnO(V₂O₃)_{0.25} and SnO(VO)_{0.5}. However, capacity- fading also increased in them in comparison to the performance with 0.8 V cut- off.

Significant findings from the present studies are:

1. For the first time, we have prepared the Mo- cluster oxide compounds Li(Y/Ho)Mo₃O₈ and A₂Mo₃O₈ (A = Mn, Co, Zn) at a lower temperature by the carbothermal reduction method. The FT-IR and Raman studies on the compounds, LiYMo₃O₈ and Mn₂Mo₃O₈ are reported for the first time. The Li- cycling performance is dependent on the counter ions like Li, Y, Ho, Mn, Co or Zn in these isostructural Mo- cluster compounds (Chapter III).
2. For the first- time, Li- cycling property of nano-flake CoN films are reported. The mechanism involves ‘conversion’ reaction. The observed high capacity at 0.33 C- rate (990 mA $h g^{-1}$ at the end of 80th cycle) and excellent rate capability (at 6.6 C- rate: 690 mA $h g^{-1}$ at the end of 50 cycles) show the potential use of nanoflake CoN as prospective anode material for LIBs (Chapter IV).

3. The nano-size particles (<10 nm) of the compounds perform much better than the micron size particles towards Li- cycling as is shown by the results on nano-phase tin hollandites, $K_2(M_2Sn_6)O_{16}$ (M = Co, In) (Chapter V).
4. The crystal structure and nano-phase along with suitable matrix elements play a crucial role in electrochemical performance of compounds undergoing alloying-de-alloying reaction mechanism as is shown by results on nano-SnO(VO_x) (Chapters V and VI).

List of Figures

Fig.I.1.	Schematic representation of the operation of LIB.	5
Fig.I.2.	Structure of a cylindrical LIB.	6
Fig.I.3.	The spinel structure of LiMn_2O_4 showing the MnO_6 octahedra and the Li 8a tetrahedral positions.	12
Fig.I.4.	Polyhedral representation of the structure of LiFePO_4 (space group, Pnma) viewed (a) along the b-axis and (b) along the c-axis. The FeO_6 octahedra are shown in blue, the PO_4 tetrahedra in yellow, and the Li-ions in green.	14
Fig.I.5.	Crystal structure of hexagonal graphite.	20
Fig.I.6.	Charge-discharge cycling of MCMB graphite.	23
Fig.I.7.	Voltage vs. capacity (x Li) of $\text{Li}_4\text{Ti}_5\text{O}_{12}$ at a current density 35 mA g^{-1} .	24
Fig.I.8.	Experimental (solid line) and calculated (dashed line) voltage profile for the lithiation of tin.	30
Fig.I.9.	Voltage- composition profile for various MO/Li cells. The cells were cycled at C/5 rate in the voltage range, 0.01-3.0 V.	39
Fig.I.10.	Crystal structure of Fe_3O_4 .	41
Fig.I.11.	Capacity vs. cycle number of ZnCo_2O_4 . Filled squares: Discharge; open squares: Charge.	43
Fig.I.12.	Voltage- capacity profiles of the Sn-C/GPE/ $\text{LiNi}_{0.5}\text{Mn}_{1.5}\text{O}_4$ Li- ion cell at various rates ($1\text{C} = 0.2 \text{ A cm}^{-2}$ with respect to the cathode mass) and at room temperature.	57
Fig.II.1.	Schematic diagram of X-ray diffraction by crystalline material.	79
Fig.II.2.	(a) Schematic diagram of cell assembly and (b) photograph of 2016 type fabricated coin cell.	89
Fig.II.3.	Vector diagram of the Cell impedance (Z).	92
Fig.II.4.	(a) Nyquist plot of an electrochemical cell with one semicircle and (b) Equivalent electrical circuit.	93

Fig.III.1.	The crystal structure of hexagonal (a) LiYMo_3O_8 and (b) $\text{Mn}_2\text{Mo}_3\text{O}_8$. Li: black sphere; Y: green sphere; Mn: Pink sphere; Mo: Light blue spheres; O: Red spheres. For clarity, all the ions are given the same size.	101
Fig.III.2.	Rietveld refined X-ray diffraction pattern of (a) LiYMo_3O_8 , (b) $\text{Mn}_2\text{Mo}_3\text{O}_8$, (c) $\text{Zn}_2\text{Mo}_3\text{O}_8$ and (d) $\text{Co}_2\text{Mo}_3\text{O}_8$. Miller indices (hkl) are shown. Symbols represent experimental data and continuous line represents the refined data. The difference pattern and positions of reflections (vertical lines) of LiYMo_3O_8 and $\text{A}_2\text{Mo}_3\text{O}_8$ and lines due to MoO_2 , Co (impurities) are also shown.	107
Fig.III.3.	SEM micrographs of (a) $\text{LiHoMo}_3\text{O}_8$, (b) LiYMo_3O_8 , (c) $\text{Mn}_2\text{Mo}_3\text{O}_8$, (d) $\text{Zn}_2\text{Mo}_3\text{O}_8$ and (e) $\text{Co}_2\text{Mo}_3\text{O}_8$. Scale bars are shown.	109
Fig.III.4.	HR- TEM lattice image of (a) $\text{LiHoMo}_3\text{O}_8$, (b) LiYMo_3O_8 , (c) $\text{Zn}_2\text{Mo}_3\text{O}_8$ and (d) $\text{Co}_2\text{Mo}_3\text{O}_8$. SAED patterns of (e) $\text{LiHoMo}_3\text{O}_8$ and (f) $\text{Zn}_2\text{Mo}_3\text{O}_8$. Miller indices (hkl) and scale bars are shown.	110
Fig.III.5.	The FT- IR spectra of LiYMo_3O_8 and $\text{Mn}_2\text{Mo}_3\text{O}_8$ recorded at room temperature. The numbers refer to band positions in cm^{-1} .	112
Fig.III.6.	Raman spectra at various temperatures (78 – 450 K): (a) LiYMo_3O_8 and (b) $\text{Mn}_2\text{Mo}_3\text{O}_8$. The numbers refer to band positions in cm^{-1} .	113
Fig.III.7.	(a) Temperature dependent magnetization of $\text{Mn}_2\text{Mo}_3\text{O}_8$ at 1kOe applied magnetic field. The inset shows inverse magnetic susceptibility as a function of temperature and Curie- Weiss law fit to data. (b) Magnetic field dependent magnetization hysteresis loop at T = 20 and 50 K. The arrow shows the loop at 50 K which has minimum coercive field.	117
Fig.III.8.	Magnetization data on $\text{Mn}_2\text{Mo}_3\text{O}_8$. (a) Temperature dependent coercive magnetic field (H_c) (left hand scale) and magnetization at 50 kOe (right hand scale). (b) Temperature dependent zero field cooled (ZFC) and field cooled (FC) magnetization under different magnetic fields. The inflexion point (arrow) refers to the T_c .	119
Fig.III.9.	Galvanostatic charge-discharge curves. LiYMo_3O_8 (at 24 $^\circ\text{C}$): (a) 1-20 cycles; (b) 30-120 cycles. At 50 $^\circ\text{C}$: (c) LiYMo_3O_8 ; 1-60 cycles. The numbers indicate cycle number. Voltage range, 0.005-3.0 V vs. Li, at a current rate of 30 mA g^{-1} (0.08C).	121
Fig.III.10.	Capacity vs. cycle number plots of $\text{Li(Y/Ho)Mo}_3\text{O}_8$ at 24 $^\circ\text{C}$ and 50 $^\circ\text{C}$ (0.005-3.0 V; 30 mA g^{-1}). Closed symbol: Discharge capacity; Open symbol: Charge capacity.	123

- Fig.III.11 Galvanostatic charge-discharge curves. $\text{LiHoMo}_3\text{O}_8$ (at 24°C): (a) 1-10 cycles; (b) 30-70 cycles. At 50°C : (c) $\text{LiHoMo}_3\text{O}_8$; 1-40 cycles. 124
The numbers indicate cycle number. Voltage range, 0.005-3.0 V vs. Li, at a current rate of 30 mA g^{-1} (0.1C).
- Fig.III.12. Cyclic voltammograms of LiYMo_3O_8 . (a) 1st and 2nd cycle, and (b) 5th 127
cycle. Scan rate, $58\ \mu\text{Vs}^{-1}$. Li- metal anode was the counter and reference electrode. Numbers represent the potentials in volts. (c) Differential capacity (dQ/dV) vs. Voltage plot extracted from the galvanostatic capacity- voltage profiles of Fig.III.9a for the 1st cycle. (d) Differential capacity vs. Voltage plot extracted from the galvanostatic capacity- voltage profiles of Fig.III.9b for the 30th cycle.
- Fig.III.13. Cyclic voltammograms of $\text{LiHoMo}_3\text{O}_8$. (a) 1st, 2nd and 10th cycle, and 128
(b) 20th and 30th cycle. Scan rate, $58\ \mu\text{Vs}^{-1}$. Li- metal anode was the counter and reference electrode. Numbers represent the potentials in volts. (c) Differential capacity (dQ/dV) vs. Voltage plot extracted from the galvanostatic capacity-voltage profiles of Fig.III.11a for the 1st, 2nd, 10th cycle. (d) Differential capacity vs. Voltage plot extracted from the galvanostatic capacity- voltage profiles of Fig.III.11b for the 20th and 30th cycle.
- Fig.III.14. Galvanostatic charge-discharge curves. (a) $\text{Mn}_2\text{Mo}_3\text{O}_8$; 1-50 cycles, 130
(b) $\text{Zn}_2\text{Mo}_3\text{O}_8$; 1-50 cycles and (c) $\text{Co}_2\text{Mo}_3\text{O}_8$; 1-40 cycles. The numbers indicate cycle number. Voltage range, 0.005-3.0 V vs. Li.
- Fig.III.15. Capacity vs. cycle number plots. (a) $\text{Mn}_2\text{Mo}_3\text{O}_8$, (b) $\text{Zn}_2\text{Mo}_3\text{O}_8$: (I) 131
Bare electrode; (II) Electrode heat- treated at 300°C for 12 h in Ar-atm. and (III) Bare electrode at 180 mA g^{-1} . (c) $\text{Co}_2\text{Mo}_3\text{O}_8$: (I) Bare electrode and (II) Electrode heat- treated at 300°C for 12 h in Ar-atm. Voltage range: 0.005- 3.0 V vs. Li. Closed symbol: Disch. capacity; Open symbol: Charge capacity.
- Fig.III.16. Cyclic voltammograms of $\text{Mn}_2\text{Mo}_3\text{O}_8$. (a) 1st and 2nd cycle, and (b) 135
10th, 20th, and 28th cycle. Scan rate, $58\ \mu\text{Vs}^{-1}$. Li- metal anode was the counter and reference electrode. Numbers represent the potentials in volts. (c) Differential capacity (dQ/dV) vs. Voltage plot extracted from the galvanostatic capacity-voltage profiles of Fig.III.14a for the 1st cycle. (d) Differential capacity vs. Voltage plot extracted from the galvanostatic capacity- voltage profiles of Fig. III.14a for the 28th cycle.
- Fig.III.17. Cyclic voltammograms. (a) $\text{Zn}_2\text{Mo}_3\text{O}_8$; 1-6 cycles. (b) $\text{Co}_2\text{Mo}_3\text{O}_8$; 1- 137
10 cycles. Scan rate is $58\ \mu\text{Vs}^{-1}$. Numbers represent the potentials in volts.

- Fig.III.18. XRD patterns of the cycled electrodes: (A) LiYMo_3O_8 and (B) $\text{LiHoMo}_3\text{O}_8$. Discharge/charge voltages and the cycle number are indicated. Miller indices assigned to the peaks are shown. The symbols (*,#) represent the lines due to Cu-metal (substrate of the electrode) and Al –metal (sample holder). MoO_2 impurity (+) is also shown. The y- axis values are normalized for better comparison at various voltages. 139
- Fig.III.19. XRD patterns of the cycled electrodes: (A) $\text{Mn}_2\text{Mo}_3\text{O}_8$ and (B) $\text{Co}_2\text{Mo}_3\text{O}_8$. Discharge/charge voltages and the cycle number are indicated. Miller indices assigned to the peaks are shown. The symbols (*,#) represent the lines due to Cu-metal (substrate of the electrode) and Al –metal (sample holder) and + represents lines due to MoO_2 . The y- axis values are normalized for better comparison at various voltages. 141
- Fig.III.20. (a, b) TEM photograph and HR-TEM lattice image of LiYMo_3O_8 cycled electrode in the charged state (3.0V; 1st cycle). (c, d) TEM photograph and HR-TEM lattice image of $\text{LiHoMo}_3\text{O}_8$ cycled electrode (charged to 3.0 V after 70 cycles). Scale bars are shown. 142
- Fig.III.21. Nyquist plots (Z' vs. $-Z''$) of LiYMo_3O_8 at different voltages. (a) During the 1st discharge reaction from 2.8 to 0.005 V, (b) 1st charge reaction from 0.8 to 3.0 V, (c) 5th discharge reaction from 3.0 to 0.005 V and (d) 5th charge reaction from 0.3 to 3.0 V vs. Li. Symbols represents experimental data and continuous lines represent the fitted curve using the equivalent circuit of Fig. III.22 c. Geometric area of the electrode is 2 cm^2 . 149
- Fig.III.22. (a) Nyquist plots (Z' vs. $-Z''$) of LiYMo_3O_8 in the discharged state (0.005 V vs.Li) at various discharge- charge cycles. The numbers represent the cycle number. (b) The Nyquist plot at the 20th cycle in an expanded scale. Selected frequencies are indicated. (c) The equivalent electrical circuit consisting of resistances (R_i), constant phase elements (CPEs), Warburg impedance (W_s) and intercalation capacitance (C_{int}). (d) Variation of $R_{(\text{sf+ct})}$ and R_b vs. cycle number of LiYMo_3O_8 , obtained by fitting the spectra of (a) with the circuit in (c). 150
- Fig.IV.1. X-ray diffraction pattern of nanoflake CoN grown on surface-oxidized Si substrate. The line due to Si substrate is shown. Miller indices (h k l) of CoN are shown. 164
- Fig.IV.2. XRD patterns of the bare CoN electrode grown on Cu- substrate and those of the electrodes of CoN discharged to 0.5 and 0.005 V, and charged to 3.0 V at the end of 1st cycle are shown. Miller indices assigned to the peaks of bare CoN are shown. The symbols (*,#) 165

represent the lines due to Cu-metal (electrode substrate) and Al –metal (sample holder). The y- axis values are normalized for better comparison of the XRD patterns.

- Fig.IV.3. Rutherford back scattering (RBS) spectrum of nanoflake CoN grown on surface- oxidized Si substrate. The simulated partial spectra due to the individual elements are indicated. 166
- Fig.IV.4. (a, b) FE- SEM photographs of nanoflake CoN grown on Cu- substrate at two different magnifications showing randomly oriented nanoflakes of size ≤ 100 nm. (c) HR- TEM lattice image of nanoflake CoN. The interplanar (d-) spacings are indicated by arrows. (d) The SAED pattern of nanoflake CoN. Miller indices are indicated. Scale bars are shown. 168
- Fig.IV.5. Galvanostatic discharge- charge curves of nanoflake CoN: (a) 1-10 cycles (b) 20- 80 cycles, at 250 mA g^{-1} (0.33 C) in the range $0.005\text{-} 3.0 \text{ V}$. Only selected cycles are shown for clarity. Numbers indicate cycle number. (c) Capacity vs. cycle number (up to 80 cycles) plots of nanoflake CoN, at C- rates of 0.33 , 0.59 and 6.6 C . (d) Discharge-charge profiles of nanoflake CoN up to 20 cycles at 450 mA g^{-1} (0.59 C) in the voltage range $0.005\text{-} 2.0 \text{ V}$. The numbers indicate cycle number. 170
- Fig.IV.6. Cyclic voltammograms of nanoflake CoN: (a) 1st cycle and (b) 2- 20 cycles. Only selected cycles are shown for clarity. Scan rate is $58 \mu\text{Vs}^{-1}$. Li- metal anode is the counter and reference electrode. Numbers represent the potentials in Volts. (c) Differential capacity (dQ/dV) vs. Voltage plot for the first- cycle extracted from the galvanostatic capacity- voltage profiles of Fig.IV.5a. (d) Differential capacity (dQ/dV) vs. Voltage plot for the 20th -cycle extracted from the galvanostatic capacity- voltage profiles of Fig.IV.5b. 174
- Fig.IV.7. (a) HR- TEM lattice image and (b) SAED pattern of cycled nanoflake CoN in the charged state (3.0 V) after 80 cycles in the range, $0.005\text{-} 3.0 \text{ V}$ vs. Li. Scale bars are shown. 176
- Fig.V.1. The structure of $\text{K}_2(\text{M},\text{Sn})_8\text{O}_{16}$ hollandite projected along the c - axis. 187
- Fig.V.2. Powder X-ray diffraction (XRD) patterns of (a) $\text{K}_2(\text{In}_2\text{Sn}_6)\text{O}_{16}$ (K-In) and $\text{K}_2(\text{Co}_2\text{Sn}_6)\text{O}_{16}$ (K-Co). Miller indices are indicated. (b) Ex-situ XRD patterns of (K-Co) at 1.0 , 0.5 and 0.005 V . Lines due to Cu-metal (substrate) and Al-metal (sample holder) are indicated. Cu $\text{K}\alpha$ -radiation. SEM micrograph of (c) $\text{K}_2(\text{Co}_2\text{Sn}_6)\text{O}_{16}$ (K-Co) and (d) $\text{K}_2(\text{In}_2\text{Sn}_6)\text{O}_{16}$ (K-In). Scale bar is shown. 190

Fig.V.3.	Galvanostatic capacity- voltage profiles of (a, b) $K_2(In_2Sn_6)O_{16}$ (K-In) and (c, d) $K_2(Co_2Sn_6)O_{16}$ (K-Co). Current density, 60 mA g^{-1} ; voltage range, 0.005-0.8V vs. Li at room temperature. The numbers refer to cycle numbers.	191
Fig.V.4.	Capacity vs. cycle number plot at a current density 60 mA g^{-1} in the voltage window 0.005- 0.8 V. Filled symbols: discharge capacity; open symbols: charge capacity.	194
Fig.V.5.	Cyclic voltammograms of (a) $K_2(In_2Sn_6)O_{16}$ (K-In) and (b) $K_2(Co_2Sn_6)O_{16}$ (K-Co) at the scan rate of $58 \mu\text{Vs}^{-1}$ and voltage range of 0.005-0.8V vs. Li at room temperature. The integer numbers indicate cycle numbers. The differential capacity vs. voltage plots of (c) (K-In) and (d) (K-Co) extracted from the galvanostatic data of the 1 st cycle from Fig. V.3 a, c.	196
Fig.V.6.	Powder X-ray diffraction patterns. (a) Nano- (K-Co); (b) nano- (K-In). Miller indices (hkl) are shown.	202
Fig.V.7.	Nano- (K-Co): (a) TEM photograph showing agglomerated nano-size particles. (b) HR-TEM lattice image. (c) HR-TEM lattice image at higher magnification. (d) Selected area electron diffraction (SAED) pattern. Scale bars are shown.	203
Fig.V.8.	Galvanostatic discharge-charge profiles. Nano- (K-Co): (a) 1 st cycle and (b) 2-80 cycles. Nano- (K-In): (c) 1 st cycle and (d) 2- 60 cycles. The numbers indicate cycle number. Voltage range, 0.005- 0.8 V vs. Li, at a current density of 60 mA g^{-1} (0.12 C).	206
Fig.V.9.	Capacity vs. cycle number plots. (a, b) Nano- (K-Co) in different voltage ranges. (c) At various current (C) rates of nano- (K-Co). (d) Nano- (K-In). Voltage range, 0.005-0.8 V vs. Li, at current density of 60 mA g^{-1} (0.12 C) assuming $1 \text{ C} = 500 \text{ mA g}^{-1}$. Filled symbols: Discharge capacity; Open symbols: Charge capacity.	208
Fig.V.10.	Cyclic voltammograms. (a) Nano- (K-Co) and (b) Nano- (K-In). Scan rate, $58 \mu\text{Vs}^{-1}$. Li- metal anode was the counter and reference electrode. Numbers represent the potentials in Volts. Integer numbers represent cycle numbers.	211
Fig.V.11.	Ex-situ XRD patterns of nano- (K-Co). (a) During first- discharge at 0.5 V; (b) during first- discharge at 0.005 V, and (c) during first-charge at 0.8 V vs. Li. Substrate (Cu) lines are indicated.	213
Fig.V.12.	Ex-situ TEM pattern of nano- (K-Co) at the 15 th charge cycle at 0.8 V: (a) HR-TEM lattice image and (b) SAED pattern. Scale bars are	214

shown.

- Fig.V.13. Impedance spectra (Nyquist plots: Z' vs. $-Z''$) for the cell with nano-(K-Co) as cathode vs. Li- metal at different voltages. (a) During the first-discharge. (b) During the first-charge. (c) During the 11th discharge. Stabilized cell voltages, after 3-h stand, are shown. Selected frequencies are shown. (d) Equivalent circuit used for fitting the impedance spectra. Different resistances, R_i and/or $R_i \parallel CPE_i$ components, Warburg element (W_s) and intercalation capacitance (C_i) are shown. 216
- Fig.V.14. Selected impedance spectra of nano- (K-Co) redrawn from Fig. V.13 a, b in an expanded scale, for the determination of the limiting frequency (f_L). First- discharge: (a) At 0.3 V and (b) at 0.005 V. First-charge: (c) At 0.03 V and (d) at 0.25 V. The f_L values and selected frequencies are shown. 221
- Fig.VI.1. Powder X-ray diffraction patterns. (a) SnO (commercial), and (b) nano-SnO (after high energy ball milling). Miller indices (h k l) are shown. 234
- Fig.VI.2. Powder X-ray diffraction patterns. (a) Nano-SnO(V₂O₃)_{0.25}, and (b) nano-SnO(VO)_{0.5}. Miller indices (h k l) are shown. 235
- Fig.VI.3. (a) SEM photograph of nano-SnO(VO)_{0.5}. (b) HR- TEM photograph of nano-SnO(V₂O₃)_{0.25}. Scale bars are shown. 237
- Fig.VI.4. Galvanostatic discharge-charge profiles of nano-SnO: (a) 1st cycle; (b) 2- 50 cycles. The numbers indicate cycle number. Voltage range, 0.005- 0.8 V vs. Li, at a current density of 60 mA g^{-1} (0.12 C). 238
- Fig.VI.5. Capacity vs. cycle number plots. (a) Nano-SnO; (b) Nano-SnO(V₂O₃)_{0.25} at 0.12 C and 0.5 C (1 C = 500 mA g^{-1}); (c) Nano-SnO(V₂O₃)_{0.5} and (d) Nano-SnO(VO)_{0.5}. Voltage range, 0.005-0.8 V vs. Li, at current density of 60 mA g^{-1} (0.12 C). Filled symbols: Discharge capacity; Open symbols: Charge capacity. 239
- Fig.VI.6. Galvanostatic discharge-charge profiles. Nano-SnO(V₂O₃)_{0.25}: (a) 1st cycle and (b) 2- 50 cycles. Nano-SnO(VO)_{0.5}: (c) 1st cycle and (d) 2- 50 cycles. Nano-SnO(V₂O₃)_{0.5}: (e) 1st cycle and (f) 2- 60 cycles. The numbers indicate cycle number. Voltage range, 0.005- 0.8 V vs. Li, at a current density of 60 mA g^{-1} (0.12 C). 242
- Fig.VI.7. Galvanostatic discharge-charge profiles. Nano-SnO(V₂O₃)_{0.25}: (a) 1st cycle and (b) 2- 40 cycles. Nano-SnO(VO)_{0.5}: (c) 1st cycle and (d) 2- 40 cycles. The numbers indicate cycle number. Voltage range, 0.005- 243

1.0 V vs. Li, at a current density of 60 mA g^{-1} (0.12 C).

Fig.VI.8. Cyclic voltammograms of (a) Nano-SnO(V₂O₃)_{0.5}, 1-40 cycles, (b) 248 Nano-SnO(VO)_{0.5}, 1- 6 cycles and (c) Nano-SnO, 1-6 cycles. Scan rate, $58 \mu\text{V s}^{-1}$. Li-metal anode was the counter and reference electrode. Numbers represent the potentials in volts. Integer numbers represent cycle numbers.

Fig.VI.9. Ex-situ XRD patterns of nano-SnO(V₂O₃)_{0.25}. (a) Bare electrode 250 (Miller indices are indicated); (b) During first- discharge at 0.5 V; (c) During first- discharge at 0.05 V, and (d) During first- charge at 0.8 V vs. Li.

List of Tables

Table. I.1	Li- alloying elements. Alloying composition, x in Li_xM , voltage range vs. Li- metal and theor. capacity based on the atomic weight of M are given.	27
Table. I.2	Selected LIB systems for PHEV. State of charge (SOC) and area specific impedance (ASI) are given.	58
Table. II.1	Physical properties of EC and DMC.	88
Table III. 1	Crystal lattice parameters, space groups and reported values with JCPDS card no. for LiYMo_3O_8 , $\text{LiHoMo}_3\text{O}_8$ and $\text{A}_2\text{Mo}_3\text{O}_8$.	108
Table III.2	Impedance parameters of the LiYMo_3O_8 during the 1 st and 5 th discharge-charge cycles at various voltages.	151
Table V.1.	Impedance parameters obtained by fitting the impedance spectra of the nano-(K-Co) (vs. Li) to the equivalent circuit elements during the first- cycle and 11 th discharge. The apparent diffusion coefficients (D_{Li^+}) are calculated using Eqn. V.4.	218
Table.VI.1	Theoretical and observed capacities (corresponding number of moles of Li per formula unit) of nano-SnO and nano-SnO(VO_x) composites. Voltage range, 0.005-0.8 V vs. Li at a current density 60 mA g^{-1} (0.12 C) (1 C = 500 mA g^{-1}).	240

List of Publications / Conference presentations

A. Results of the work presented in the Thesis have been published in the following International Journals and Conference Proceedings:

1. "Synthesis of Mo- cluster compound, $\text{LiHoMo}_3\text{O}_8$ by carbothermal reduction method and its reactivity towards Li" **B. Das**, M. V. Reddy, G.V. Subba Rao, B.V.R. Chowdari, J. Solid State Electrochem. 12 (2008) 953-959.
2. "Hollandite-type compounds, $\text{K}_2(\text{In}_2\text{Sn}_6)\text{O}_{16}$ and $\text{K}_2(\text{Co}_2\text{Sn}_6)\text{O}_{16}$ as anodes for lithium ion batteries" **B. Das**, M. V. Reddy, G.V. Subba Rao, B.V.R. Chowdari. Proceedings of the 11th Asian conference on Solid State Ionics, (2008) 69-77.
3. "Carbothermal synthesis, spectral and magnetic characterization and Li-cyclability of the Mo- cluster compounds, LiYMo_3O_8 and $\text{Mn}_2\text{Mo}_3\text{O}_8$ " **B. Das**, M.V. Reddy, C. Krishnamoorthy, S.Tripathy, R. Mahendiran, G.V. Subba Rao, B.V. R. Chowdari, Electrochim. Acta 54 (2009) 3360-3373.
4. "Nanoflake CoN as a high capacity anode for Li- ion batteries" **B. Das**, M. V. Reddy, P. Malar, Osipowicz Thomas, G.V. Subba Rao, B.V.R. Chowdari, Solid State Ionics 180 (2009) 1061-1068.
5. "Nano- composites, $\text{SnO}(\text{VO}_x)$ as anodes for lithium ion batteries" **B. Das**, M.V. Reddy, G.V. Subba Rao, B.V. R. Chowdari, J. Solid State Electrochem. 15 (2011) 259-268.
6. "Li-cycling behavior of Mo-cluster compounds, $\text{A}_2\text{Mo}_3\text{O}_8$ (A = Zn, Co)" **B. Das**, M. V. Reddy, G. V. Subba Rao, B. V. R. Chowdari, 12th Asian Conference on Solid State Ionics, China, 2010.
7. "Nano-phase tin hollandites, $\text{K}_2(\text{M}_2\text{Sn}_6)\text{O}_{16}$ (M = Co, In) as anodes for Li- ion batteries" **B.Das**, M. V. Reddy, G.V. Subba Rao, B.V.R. Chowdari, J. Mater. Chem. 21 (2011) 1171-1180.

B. Preliminary results of some of the work have been presented in the following International/ Local Conferences:

1. "Synthesis of Mo- Cluster compound, $\text{LiHoMo}_3\text{O}_8$ by carbothermal reduction method and its reactivity towards Li" **B. Das**, M. V. Reddy G. V. Subba Rao, B.V.R. Chowdari, presented at Intl. Conf. on Mater. for Adv. Technol. (ICMAT), July, 2007, Singapore.

2. “Metal cluster compounds, LiYMo_3O_8 and $\text{Mn}_2\text{Mo}_3\text{O}_8$ as anodes for lithium ion Batteries” **B.Das**, M. V. Reddy, G. V. Subba Rao, B.V.R. Chowdari, Paper presented at 3rd MRS-S Conf. on Adv. Mater., Feb., 2008, IMRE, Singapore.
3. “Nanocomposites, $(\text{SnO} \cdot \frac{1}{2} \text{VO}_x)$ as anodes for lithium ion batteries” **B. Das**, M. V. Reddy, G. V. Subba Rao, B.V.R. Chowdari, presented at Intl. Conf. on Mater. for Adv. Technol. (ICMAT), June, 2009, Singapore.

Chapter I

Introduction

Abstract

A brief account of the primary and secondary batteries, principles of operation, world market and present and future trends of lithium ion batteries (LIBs) are presented. This is followed by a comprehensive literature survey on cathode, anode and electrolyte materials for LIBs. Motivation for the present studies on the anode materials for LIB are mentioned.

I.1. Definition of Battery

A battery is a device, which converts the chemical energy stored within its active material to electrical energy during operation. This may be series and/or parallel combination of cells. The maximum electrical energy that can be delivered is a function of the active materials forming the electrodes. The amount of electrical energy per unit weight (Wh/kg) or per unit volume (W h/ l) depends on the nature, amount and chemistry of the electrodes constituting the cell. The battery consists of three major components: positive electrode (cathode), electrolyte which behaves as the conducting medium for the ions, and negative electrode (anode). The electrochemical processes that occur at both the electrodes generate movement of electrons through the external circuit. Depending on the principle of operation, batteries are classified as primary (disposable) and secondary (re-chargeable) batteries [1-5].

I.1.1. Primary (Disposable) batteries

Primary batteries (disposable) can produce electric energy during discharge via an irreversible electrochemical reaction. These are intended to be used once and discarded, since the chemical reactions are irreversible and the active materials may not return to

their original forms. These are most commonly used in portable devices that have low current drain. They represent 80% of the total number of batteries sold in market because of less maintenance, availability in large number, light weight, good shelf- life, high safety level, reasonably high energy density at low discharge conditions and low cost [1,2,4,6]. Different shapes and sizes of primary batteries are manufactured depending on their applications. The primary batteries, like zinc-MnO₂ (1.5 V) and Li-MnO₂ (3.0 V) are mostly available in the market [1, 4, 6].

I.1.2. Secondary (Rechargeable) battery

The rechargeable batteries, commonly known as storage batteries can be recharged to generate the active materials after discharging, by passing an external current in opposite direction of the flow of electrons. They are the ultimate eco-friendly product as they place no strain on the earth's limited resources and can be used repeatedly, thus reducing waste. They show high power density, high discharge rates, flat discharge curves and excellent low temperature performances [1, 2, 4, 6]. But they suffer from low energy density and charge retention as compared to primary batteries. The common examples are: Ni- Cd, Lead Acid, Ni-MH and lithium- ion batteries (LIBs). Li-polymer rechargeable batteries are considered as prominent ones for the next generation because of their design flexibility [1-4, 6].

I.2. Development of Li-ion batteries

The increasing demand of Li-ion batteries (LIBs) for the portable electronic devices as secondary power sources is encouraging the scientific community to continue the research and development. The idea of using battery technology based on Li- metal as negative electrode material depends upon its advantages over other materials. The Li

metal is light weight (atomic weight = 6.94 g mol^{-1} ; specific gravity = 0.53 g cm^{-3}) as well as highly electropositive (-3.04 V vs. standard hydrogen electrode) and can deliver large specific capacity, 3860 mAhg^{-1} , compared to other metals [1, 2, 6, 7-10]. However, the commercialization of rechargeable batteries based on Li-metal as anode is hindered due to various disadvantages associated with it during charge- discharge cycling. The extraction and deposition of Li during the electrochemical cycling causes roughness of the electrode and dendrite formation. During long term cycling, continuous deposition of Li causes more growth of dendrite, which can perforate the separator and can reach the cathode causing internal short circuit and battery failure [1, 2, 7, 9, 10].

In 1980s, Lazzari and Scrosati [11] and Murphy et al. [12] proposed to replace the Li-metal by a Li-insertion (intercalation) material. To compensate the increase in potential of negative electrode, a high- potential intercalation material was suggested as cathode, such that Li-ions can transfer between two electrodes. The group of Goodenough [1, 3] studied LiCoO_2 and suggested that it can be used as a 4 V- cathode. In 1990 Sony Co., Japan, introduced the first commercial LIB, where they employed specialty graphite (graphitized carbon), and later by using mesocarbon microbeads (MCMB) of graphite as negative and LiCoO_2 as positive electrode materials, respectively. In 2005, Sony introduced the 2nd generation LIB, where Sn-Co-C composite is used as negative electrode material. The development of LIBs and various aspects of electrode materials have been discussed in detail in various books and reviews [1-10].

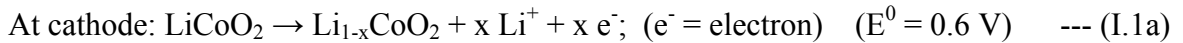
I.3. Principle of operation of LIBs

The LIB operates on the principle of Li^+ insertion/de-insertion to the electrodes via an electronically insulating and ionically conducting medium called ‘electrolyte’. This is

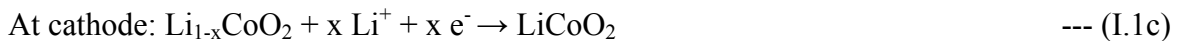
accompanied by a redox (reduction/oxidation) reaction of the host matrix with flow of electrons through external circuit, as shown in Fig. I.1. In the commercial LIB, Li-containing layer compound (LiCoO_2) is employed as cathode material whereas graphitic carbon (MCMB) is the anode material. A non-aqueous solution of 1 M LiPF_6 dissolved in ethylene carbonate (EC) + diethyl carbonate/dimethyl carbonate (DEC/DMC) (1:1 by volume) is used as the electrolyte, which is ionically conducting, but electronically insulating.

During charging of an LIB, Li-ions are extracted from cathode and inserted to anode. This process is reversed during discharging (i.e., operating the LIB under load). Due to the reversible Li-ion insertion/de-insertion through the electrolyte, the LIBs are also known as rocking chair, swing or shuttle-cock batteries. The reactions in LIB are:

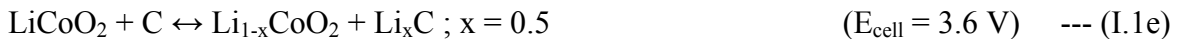
During charge



During discharge



The overall reaction is



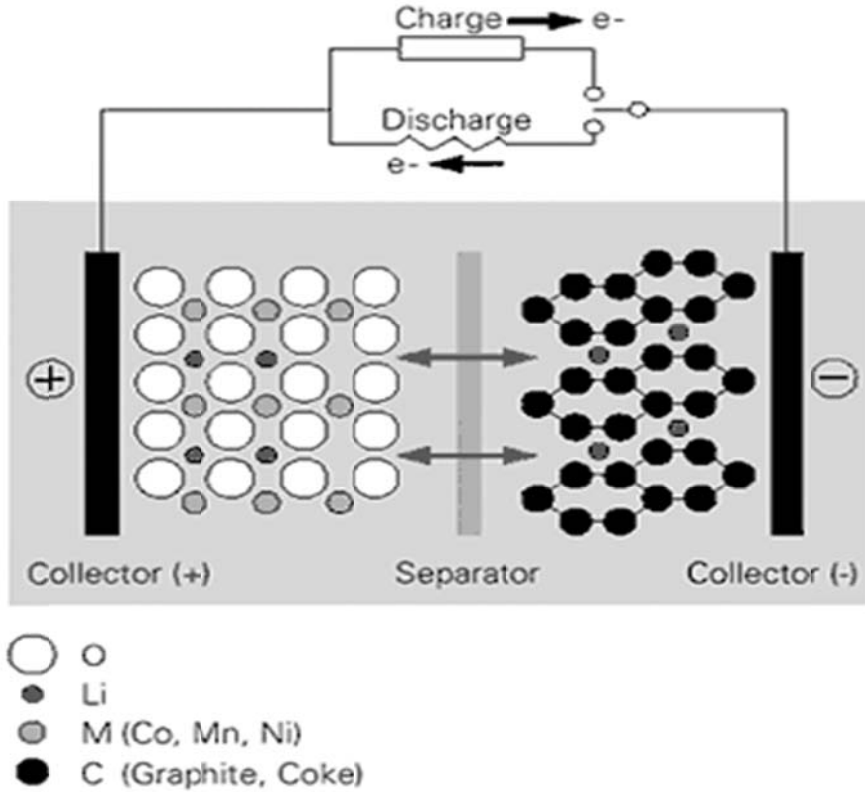


Fig.I.1 Schematic representation of the operation of LIB. Taken from [13].

The open circuit voltage (OCV) of a cell can be calculated by the equation:

$$E_{\text{cell}}^{\text{OCV}} = - (\Delta G/nF) \quad \text{--- (I.2)}$$

where ΔG = free energy change of the cell reaction, n = number of electrons involved in reaction, F = Faraday constant.

The free energy change is associated with the chemical potential (μ_i):

$$\mu_i = \partial G / \partial x \quad \text{--- (I.3)}$$

Thus, the OCV of a cell is

$$E_{\text{cell}} = - (1/nF) (\mu_{\text{Li}(c)} - \mu_{\text{Li}(a)}) \quad \text{--- (I.4)}$$

I.4 Applications and World Market

LIBs are used in portable electronic devices such as cellular phones, notebook computers, camcorders, portable hard disk drive (HDD) etc. LIBs of different shapes and sizes are available in the market. The structure of a cylindrical LIB is shown in Fig. I.2

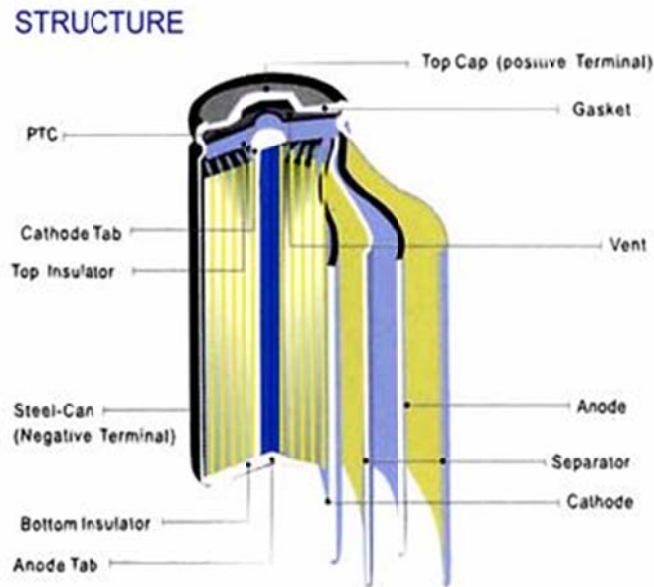


Fig. I.2 Structure of a cylindrical LIB. Taken from [14].

The global sales of LIBs reached 2.5 billion in 2006 and expected to increase to 3 billions in 2010 [1, 6].

I.5. Need of R&D and selection criterion of electrode materials for LIBs

Li-ion batteries (LIBs) are being considered for use in electric vehicles and hybrid (plug-in) electric vehicles (EV/HEV). For this purpose, there is a need for increasing the energy density and safety- in- operation. Thus, there is a need to improve the performance of the presently used electrode materials. The characteristics of an ideal cathode and anode material for LIBs are given below:

- (i) To maximize the cell potential, the transition metal ion present in the cathode should possess high redox potential. (LiCoO_2 : $\text{Co}^{3+/4+} = 4.0 \text{ V vs. Li}$). An ideal anode must have a low redox potential (graphite: $0.1\text{-}0.2 \text{ V vs. Li}$).
- (ii) The cathode should be a good host for intercalation/de-intercalation of Li-ion, so that the parent structure is retained on cycling. Thus, two- dimensional (2 D) layered or 3 D- channel type structure are favored (LiCoO_2 and graphite have 2D-structures).
- (iii) The electrode materials must not be soluble in the solvents of the electrolyte.
- (iv) The compound should possess both high gravimetric and high volumetric energy density so that the active material mass can be reduced in the LIB. Thus, low atomic weight elements in the electrodes are preferred ($\text{Co} = 60$; $\text{C} = 12$).
- (v) The electrode material should have high electronic and ionic conductivity for good current pick- up and for Li-ion mobility.
- (vi) Electrodes should show thermal stability in the charged- and discharged- state. This will ensure the safety -in-operation of the LIB.
- (vii) The intercalation and de-intercalation potential of the cathode should not be higher than the decomposition potential of electrolyte, so that oxidation of the solvent in the electrolyte can be avoided. Similarly, the opposite holds for anode (low intercalation potential and reduction of the solvent).
- (viii) The synthesis procedure for the electrode material should be easy and cost effective for manufacture of kg- quantities.
- (ix) Finally, the electrode materials should be environmentally benign.

In addition to the above criterion, electrolyte also plays an important role in the performance of LIBs. The high Li- ionic conductivity and stability at high operating voltages are the essential features of electrolyte. The cell design to dissipate the heat and maximize the available space in the gadget are also to be considered. This is especially the case for use of LIBs in EV/HEV.

The presently used cathode, LiCoO_2 and the specialty anode, mesocarbon microbeads (MCMB) graphite satisfy many of the characteristics of the ideal electrode materials. However, there are shortcomings:

- (i) LiCoO_2 contains Co, which is toxic and expensive in comparison to Mn, Fe or Ni. Also, only half of the theoretical capacity is being used during charge-discharge cycling of the LIBs. This is due to the instability of $\text{Li}_{1-x}\text{CoO}_2$ ($x < 0.5$).
- (ii) The electrolyte (LiPF_6 dissolved in EC + DEC) has a low ionization potential and can not be used for voltages > 5 V vs. Li. This hinders the possibility of using 5 V- cathodes in LIBs.
- (iii) The theoretical capacity of the presently used graphite anode is 372 mAhg^{-1} , whereas practically obtainable value is $\sim 310 \text{ mAhg}^{-1}$. The charged anode is a strong reducing agent and can decompose the solvent of the electrolyte. Hence, there is a need to develop alternative anodes which can deliver higher capacities and ensure safety-in-operation.
- (iv) Similarly, there is a need to search for cheaper and less-toxic oxide cathode materials to replace the LiCoO_2 .

I.6. Prospective second generation cathode materials for LIBs

As a result of extensive researches during the past twenty years, a good number of second- generation oxide cathode materials have been discovered and perfected and this includes improvements on the LiCoO_2 . These developments have been reported in books [1, 3, 5] and in several review articles [7-10, 15-21]. A brief account is given here.

I.6.1. Modified LiCoO_2

The layer- structured LiCoO_2 , can be prepared by solid state reaction at $800\text{ }^\circ\text{C}$ of the constituent oxides (Li_2O and Co_3O_4) or hydroxides, carbonates or other precursors in air. It is black in color. As mentioned earlier, LiCoO_2 can deliver a specific theoretical capacity of 274 mAhg^{-1} corresponding to insertion/de-insertion of $x = 1$ in $\text{Li}_{1-x}\text{CoO}_2$. But, practically only ~ 0.5 moles of Li can be reversibly cycled in voltage range of $2.7 - 4.2\text{ V}$, which corresponds to a reversible capacity of $120\text{-}140\text{ mAhg}^{-1}$ [1- 3]. The Co^{3+} oxidizes to Co^{4+} and vacancies are formed when Li-ions are extracted from the layered LiCoO_2 . For $x > 0.5$, Co^{4+} causes oxidative decomposition of the non-aqueous solvent in electrolyte, which leads to evolution of gases and deterioration of the performance of LIB. Also, the phase transformations associated during the cycling are: Hexagonal (H1) - Monoclinic (M) - Hexagonal (H2) – Hexagonal (H1-3) – Hexagonal (O1) for $x \geq 0.5$ in $\text{Li}_{1-x}\text{CoO}_2$ and causes large changes in the unit cell volume, except for $\text{H1} \leftrightarrow \text{M}$ which is smaller. These volume variations during cycling cause deterioration of the composite cathode and thereby, causing capacity fading.

The capacity- fading and structural instability of LiCoO_2 have been addressed by doping of certain metals (both electrochemically- active and -inactive) at the Co- site such as Cr, Mg, Al, Ti and excess lithium at the Li-site. These dopants suppress the

H1 \leftrightarrow M transition and enable cycling to $V > 4.2$ V and yielded higher capacities. Studies have also shown that surface coating on LiCoO₂ by oxides such as FePO₄, TiO₂, Al₂O₃, ZrO₂, SiO₂, AlPO₄ is a promising way to suppress the structural instability and capacity loss when cycled to > 4.2 V. The coated oxide or compound forms a thin layer which suppress the phase transformation and also it prevents the electrolyte decomposition by forming a physical barrier between the surface of the particles (LiCoO₂) and electrolyte. In favorable cases, stable capacities of 170-180 mAhg⁻¹ were obtained when cycled up to 4.5 V vs. Li.

1.6.2. Layered LiNiO₂

Another well known member of layered compounds, namely LiNiO₂ which is isostructural to LiCoO₂ has been explored as prospective cathode material because of less toxicity, lower cost in comparison to Co, and it can deliver capacities larger than 160 mAhg⁻¹. The Ni^{3+/4+} redox couple is 3.8 V vs. Li, slightly smaller than that of LiCoO₂.

However, there are many problems with this oxide cathode. Preparation of stoichiometric composition, LiNiO₂ can only be done in a flowing O₂- atmosphere, and inter-site mixing (cation-mixing) occurs where some Ni²⁺ ions occupy the Li-layer and vice versa. Slight Li-deficiency and stability of Ni²⁺ ions in the structure are the main reason for the deviation caused from the ideal composition. Similar to LiCoO₂, LiNiO₂ also undergoes reversible structural transformation, H1 \leftrightarrow M \leftrightarrow H2 \leftrightarrow H3 and these cause unit cell volume variations during cycling. The above factors cause extensive of capacity-fading in LiNiO₂ [1, 3, 16, 18, 21].

In order to improve the performance of LiNiO₂, partial replacement of nickel by transition elements, like Co, Mn, Fe and non-transition elements, like as Al, Mg have

been carried out and the Li- cycling has been thoroughly studied. The solid solution, $\text{LiNi}_{1-x}\text{Co}_x\text{O}_2$ was found to be the best among all the dopants studied. Particularly, the composition with both Co and Al at the Ni- site, namely $\text{Li}(\text{Ni}_{0.85}\text{Co}_{0.1}\text{Al}_{0.05})\text{O}_2$ showed good stability and cyclability for long- term cycling and has been commercialized [16, 18].

I.6.3. Layered LiMnO_2 , $\text{Li}(\text{Ni}_{1/2}\text{Mn}_{1/2})\text{O}_2$ and $\text{Li}(\text{Ni}_{1/3}\text{Mn}_{1/3}\text{Co}_{1/3})\text{O}_2$

The layered compound, LiMnO_2 can be a potential cathode material for LIBs, because of its low cost, low toxicity and high theoretical capacity (277 mAhg^{-1}) [1, 3, 15, 16, 18]. It crystallizes in two different polymorphs namely, orthorhombic (zigzag layered structure; space group, Pmmn) and monoclinic (layered structure; space group, C2/m) [1, 3]. However, the cathodic performance of LiMnO_2 is not satisfactory and capacity-fading occurs on cycling. The layered LiMnO_2 can only be prepared by the ionic exchange of Na- analogue and converts to a spinel- like structure during the charge/discharge cycling. According to the structural relation between layered and spinel symmetries, it is believed that such a phase transition occurs by the migration of Mn-ions from their octahedral sites to the interlayer Li vacancies and the Li-ion occupies the tetrahedral site ($\text{Li}_{0.5}\text{MnO}_2 \equiv \text{LiMn}_2\text{O}_4$) [1, 3, 16, 18].

To address the problem associated with LiMnO_2 , attempts were made to stabilize the layer structure by partial substitution of Mn by more electron- rich elements like Co and Ni. The compositions, $\text{Li}(\text{Ni}_{0.5}\text{Mn}_{0.5})\text{O}_2$ and $\text{Li}(\text{Co}_{0.33}\text{Ni}_{0.33}\text{Mn}_{0.33})\text{O}_2$ were first prepared and studied in 2001 [18, 21] and showed a high capacity and very good rate capability. In both cases, a high capacity of $\sim 160 \text{ mAhg}^{-1}$ is noticed with good reversibility and rate capability in the voltage range of 2.0-4.6 V vs. Li. In addition, these

compounds exhibit good thermal stability in the charged- state in comparison to LiCoO_2 and were extensively studied in this decade. It is now recognized that $\text{Li}(\text{Co}_{0.33}\text{Ni}_{0.33}\text{Mn}_{0.33})\text{O}_2$ is one of the second generation cathodes for LIBs and has been commercialized.

I.6.4. Spinel LiMn_2O_4

The compound, LiMn_2O_4 , is an attractive 4 V- cathode for LIBs because of advantages such as low cost, environmentally compatible, good-rate capability and good thermal stability in the charged- state. It has been studied extensively for the last 20 years. LiMn_2O_4 has a cubic spinel structure with the space group, $\text{Fd}3\text{m}$, in which Li- ions are located at the 8a tetrahedral sites and the Mn-ions are at the 16d octahedral sites [1, 3,16, 21, 22]. The crystal structure of LiMn_2O_4 is shown in Fig. I. 3

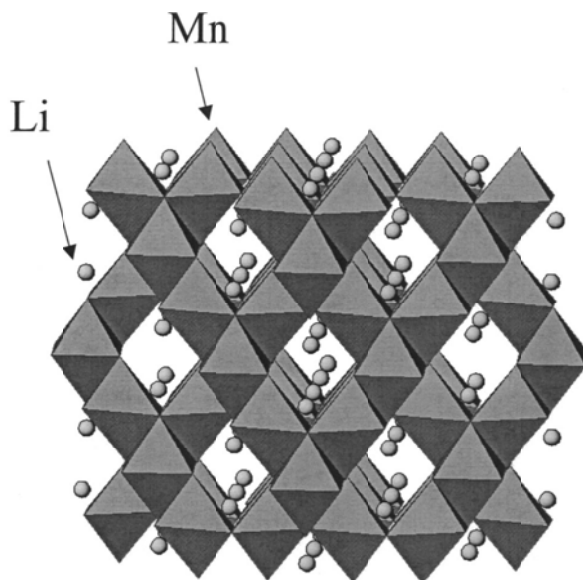


Fig.I.3 The spinel structure of LiMn_2O_4 showing the MnO_6 octahedra and the Li 8a tetrahedral positions. Taken from [22].

The LiMn_2O_4 has a theoretical specific capacity of 148 mAhg^{-1} , but practically it delivers between $105\text{-}120 \text{ mAhg}^{-1}$. During charging, theoretically one mole of Li^+ can be

extracted at about 4 V (4.05 V and 4.15 V vs. Li) from the tetrahedral sites of LiMn_2O_4 , leading to the de-lithiated $\lambda\text{-MnO}_2$. But practically, it is not possible to extract all the Li^+ and hence only $\lambda\text{-Li}_x\text{MnO}_2$ ($x \leq 0.1\text{-}0.2$) is obtained. Studies have shown that LiMn_2O_4 shows severe capacity- fading, especially when cycled at 55°C . The capacity- fading is due to several factors: (i) Lattice distortion due to Jahn- Teller effect because of large concentration of Mn^{3+} ion during high C-rate insertion of Li at the particle surface. (ii) The dissolution of Mn^{2+} ion in the solvents of the electrolyte due to disproportionation of Mn^{3+} ($2 \text{Mn}^{3+} \rightarrow \text{Mn}^{4+} + \text{Mn}^{2+}$) thereby reducing the concentrations of Mn^{3+} in the lattice. (iii) Instability of cubic structure for $x \leq 0.2$ in $\text{Li}_x\text{Mn}_2\text{O}_4$ during the extraction of Li from the lattice [1, 3, 16, 21, 22].

Tremendous efforts are put to improve the Li- cycling behavior of LiMn_2O_4 by several ways: (i) the partial substitution of Mn- ion by different metal ions such as $\text{M} = \text{Li}, \text{Co}, \text{Ni}, \text{Cr}, \text{Fe}, \text{Ru}, \text{Al}$ and mixed Co-Al. This leads to some improved electrochemical behavior at the cost of the obtainable capacity. (ii) Surface- coating by oxides and mixed-oxides, such as nano- SiO_2 , MgO , ZnO , ZrO_2 , Al_2O_3 , and AlPO_4 . These coatings help in reducing the Mn dissolution during cycling by avoiding direct contact of LiMn_2O_4 particles with the electrolyte. The surface- coated pure and doped LiMn_2O_4 have shown a better electrochemical performance at room and elevated temperature. (iii) The synthesis procedure to obtain nano-size particles and meso- and micro- porous LiMn_2O_4 has also played a vital role in improving the electrochemical performance [1, 17, 21].

A suitably doped and surface modified LiMn_2O_4 is now considered as a prospective second generation cathode for LIBs due to the low cost and environmental

friendliness. Cell packs for EV/HEV have been fabricated and tested by several companies.

I.6.5. Olivine- LiMPO_4 ($M = \text{Fe, Co, Ni, Mn}$)

The olivine- LiMPO_4 ($M = \text{Fe, Mn}$) are considered as promising cathode materials for use in the next generation of LIBs, because of its low cost, low toxicity, safety-in-operation and very good thermal stability in the charged state [1, 5, 9, 10, 16, 19, 20, 21]. The compound LiFePO_4 is extensively studied. It has a theoretical capacity of 170 mAhg^{-1} and a flat voltage at $\sim 3.5 \text{ V vs. Li}$ [16, 20]. It has an orthorhombic crystal structure with Pnma space group. The metal ions occupy half of the octahedral sites, whereas P ions are in one-eighth of the tetrahedral sites of a hexagonal closed packed (hcp) array of oxygens. This gives rise a two dimensional (2D-) pathway for Li- ion diffusion as shown in Fig.I.4.

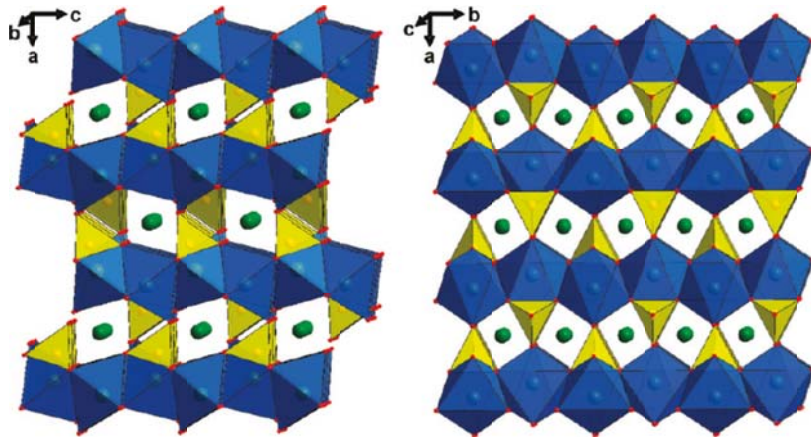
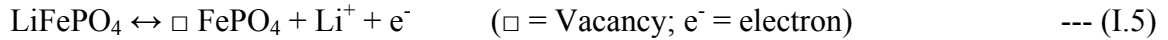


Fig. I.4 Polyhedral representation of the structure of LiFePO_4 (space group, Pnma) viewed (a) along the b-axis and (b) along the c-axis. The FeO_6 octahedra are shown in blue, the PO_4 tetrahedra in yellow, and the Li- ions in green. Taken from [20].

The LiFePO_4 undergoes a two phase reaction unlike the layered compounds, LiCoO_2 or LiNiO_2 :



During charging, the vacancies are created when Li^+ ions are extracted from the crystal structure. The structural similarity between the two phases during charging/discharging leads to a good capacity retention. Padhi et al [23] first reported the electrochemical behavior of LiFePO_4 in 1997, who showed that ~ 0.6 Li can be reversibly extracted/inserted from/to the crystal structure at a voltage of ~ 3.5 V vs. Li. Since then, many attempts were made to improve the electrochemical properties of LiFePO_4 .

There are problems associated with LiFePO_4 : (i) low electronic conductivity (1×10^{-7} S cm^{-1}), (ii) slow Li- kinetics due to two- phase reaction and (iii) poor C- rate capability. Many attempts were made to improve the electronic conductivity of LiFePO_4 . The various approaches are: (i) Doping foreign metal atoms such as Nb, Al, Ti, Mg, Zr, W at the Li- or Fe- site, (ii) carbon- coating or co-synthesizing the compound with carbon and (iii) reducing the particle size. The other olivine structures studied are LiMPO_4 ($M = \text{Co, Mn, Ni}$) [19, 20, 21]. But, none of them showed superior electrochemical performance compared to LiFePO_4 and the redox potentials for $M = \text{Mn}$ is ~ 4 V and for $M = \text{Co}$ is ~ 4.7 V. The carbon- coated LiFePO_4 is a second- generation cathode material for LIBs due to its low cost, stable cycling behavior and eco- friendliness. The LIBs with LiFePO_4 cathode have been fabricated and tested.

I.6.6. LiVPO_4F and $\text{Li}_3\text{V}_2(\text{PO}_4)_3$

The triclinic LiVPO_4F was prepared and studied as prospective 4 V cathode material by Barker et al. [24] as an alternative to LiCoO_2 . The interesting features of LiVPO_4F made its way to be commercialized and tested along with mesoporous microbeads (MCMB) graphite as counter electrode, which showed stable cycling

performance for long term cycling. The theoretical capacity of LiVPO_4F is 156 mAhg^{-1} based on the two phase reaction (i.e. $\text{LiVPO}_4\text{F} \leftrightarrow \square(\text{VPO}_4\text{F})$) similar to that of LiFePO_4 . The average operating potential corresponding to the redox couple $\text{V}^{3+/4+}$ during discharge/charge cycling was reported as $\sim 4.2 \text{ V}$, which is higher than that of LiCoO_2 and LiFePO_4 . The better thermal stability of charged- cathode compared to LiCoO_2 added to its potential application as prospective cathode [20]. Recently, Reddy et al. [25] reported a stable capacity of $\sim 120 \text{ mAhg}^{-1}$ at 0.92 C-rate in the voltage window of 2.5 – 4.3 V up to at least 800 cycles. The inherent poor electronic conductivity of LiVPO_4F is a disadvantage and carbon- coating of the particles was found to be effective in improving the cycling performance.

The lithium vanadium phosphate, $\text{Li}_3\text{V}_2(\text{PO}_4)_3$ is another member of the phosphate family, first introduced by the group of Nazar [20] as a 4V- cathode. Its structure is related, but not identical to the Nasicon (Sodium super ion conductor), $\text{Na}_3\text{Zr}_2\text{Si}_2\text{PO}_{12}$. On the other hand, $\text{Na}_3\text{V}_2\text{P}_3\text{O}_{12}$ has the Nasicon structure, with 3D-channels occupied by the Na- ions. The theoretical capacity depends on the amount of Li- ions that can be removed from the crystal structure during charging and corresponds to 192 mAhg^{-1} upon complete removal of Li-ions at 4.6 - 4.8 V vs. Li. The Li- intercalation/de-intercalation involved the two- phase reactions at different potentials are: $\text{Li}_3\text{V}^{3+}_2(\text{PO}_4)_3 \leftrightarrow \text{Li}_2(\text{V}^{3+}, \text{V}^{4+})(\text{PO}_4)_3$ at $\sim 3.6 \text{ V}$ and $\text{Li}_2(\text{V}^{3+}, \text{V}^{4+})(\text{PO}_4)_3 \leftrightarrow \text{Li}(\text{V}^{4+}, \text{V}^{4+})(\text{PO}_4)_3$ at $\sim 4.1 \text{ V}$ and finally $\text{Li}(\text{V}^{4+}, \text{V}^{4+})(\text{PO}_4)_3 \leftrightarrow \square(\text{V}^{4+}, \text{V}^{5+})(\text{PO}_4)_3$ at $\sim 4.6 \text{ V}$ [20, 25]. LIBs with MCMB graphite anode have been tested.

I. 6.7. Heavily- doped LiMn₂O₄ as 5- V cathodes

The increasing demand of LIBs for high energy applications such as electric vehicle/hybrid-electric vehicle (EV/HEV) motivated the search for high energy density electrode materials. Hence, the electrodes with an operating voltage > 4.0 V are of great interest. Several cathodes based on heavily doped spinel, Li(M,Mn)O₄ with M = Co, Ni, Cr and Fe were studied as 5 V cathodes [1, 3, 5, 26]. These compounds showed voltage plateaus during charging at ~4.7 to 5.0 V, which correspond to the redox couple of M^{3+/4+} or M^{2+/3+} [1].

West et al. [26] found that the Co-doped spinels, such as Li(Co_{0.4}Mn_{1.6})O₄ and LiCoMnO₄ performed well as ~5 V cathodes ascribed to the redox potential Co^{3+/4+}. However, a voltage plateau at ~4.0 V indicated the presence of Mn^{3+/Mn⁴⁺}. The reversible capacity of these compounds was found to be 135 and 105 mAhg⁻¹, respectively. Sigala et al. [27] reported that much of the reduced capacity of Cr- doped LiMn₂O₄ appears in 4.9 V plateau and the size of the plateau increases with Cr content. It was found that Ni-doped composition, Li(Ni_{1/2}Mn_{3/2})O₄ is the most promising and attractive cathode material because of its excellent cycling performance and relatively high capacity with one dominant plateau at 4.7 V[21, 28]. The theoretical capacity of Li(Ni_{1/2}Mn_{3/2})O₄ is 147 mAhg⁻¹.

The main drawbacks associated with Li(Ni_{1/2}Mn_{3/2})O₄ are: (i) the redox couple (Ni^{3+/Ni⁴⁺}) is at the potential of decomposition of the conventional battery electrolyte, (ii) difficulties in preparation due to formation of LiNi_{1-x}O as second phase, which deteriorates the electrochemical cycling. So, many attempts were made in terms of, (i) cationic substitution, (ii) surface modifications and (iii) synthesis method to overcome

these difficulties. The cation- substituted spinel, $\text{Li}(\text{Ni}_{1/2-y}\text{Mn}_{3/2-z}\text{M}_{y+z})\text{O}_4$ ($\text{M} = \text{Co}, \text{Fe}, \text{Cr}$) showed better electrochemical performance and rate capability in the 5 V region compared to the $\text{Li}(\text{Ni}_{1/2}\text{Mn}_{3/2})\text{O}_4$. Coating of nanosized Al_2O_3 , ZnO , AlPO_4 on to $\text{Li}(\text{Ni}_{1/2}\text{Mn}_{3/2})\text{O}_4$ enhanced the Li- cycling. Recently, Liu at al. [29] reported that the sol-gel prepared $\text{Li}(\text{Cr}_{0.1}\text{Ni}_{0.4}\text{Mn}_{1.5})\text{O}_4$ showed discharge capacities of 141, 125, 95 mAhg^{-1} at 0.5, 1 and 5 C- rate in the voltage range of 3.5 – 5.0 V.

I. 6.8. Theoretical studies on cathode materials

In the last decade, the research on cathodes for LIBs has been focused on lithium transition metal oxides (LiMO_2 ; $\text{M} = \text{Co}, \text{Ni}, \text{Mn}$ and LiMn_2O_4) and lithium transition metal phosphates (LiMPO_4 ; $\text{M} = \text{Fe}, \text{Co}, \text{Ni}$). There are many reports on the theoretical studies of cathodes employing the well- known computational techniques such as first-principles and ab initio calculation. The first- principle is the computational approach to predict the properties of materials based on the knowledge of their constituent atoms/ ions and basic laws of physics and chemistry [30]. It can be used to calculate important properties for comparison with experimental data. The properties of interest are: (i) the open circuit voltage (OCV), (ii) the energy density, (iii) crystal structure, (iv) phase stability, (v) electronic band structure and (vi) average intercalation voltages (V_{ave}) [1, 30, 31].

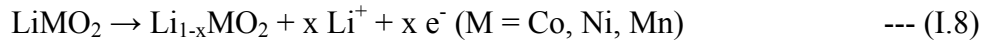
The V_{ave} of various Li- intercalated cathodes are determined by using the basic thermodynamics along with the theoretical computational tool called first- principle plane wave pseudo potential method. The V_{ave} is given as

$$V_{\text{ave}} = -\Delta G/F \quad \text{--- (I.6)}$$

where ΔG is the change in Gibbs free energy for the intercalation reaction, F is the Faraday constant. Assuming that the effects of the changes in volume and entropy associated with the intercalation on the Gibbs free energy are negligibly small, ΔG can be approximated by the internal energy term, ΔE and the V_{ave} can be expressed as

$$V_{ave} = -\Delta E/F \quad \text{--- (I.7)}$$

For the electrochemical reaction,



The ΔE is related to the total energy:

$$\Delta E = E_{total} [LiMO_2] - E_{total} [Li_{1-x}MO_2] - E_{total} [Li] \quad \text{--- (I.9)}$$

The effect of structure, metal cations and anions on the V_{ave} of $LiMO_2$ was studied by the group of Ceder et al. [30] and the group of Yamaki [31]. For example, the theoretically calculated average intercalation voltage of $LiCoO_2$, $LiNiO_2$, $LiFePO_4$ and $LiCoPO_4$ are 3.97 V, 3.14 V, 3.5 V and 4.9 V, respectively. These values compare favorably with the experimental data.

Also, the first- principle method is very useful to calculate the metal reduction potentials of layered Li_xMO_2 ($M = Co, Ni, Mn$) to investigate the possibility of metal reduction during charging. Thus, with the help of theoretical calculations and computer simulation, new cathodes can be predicted for LIBs.

I.7. Prospective Anode materials for LIBs

Increasing demand for high energy density LIBs has motivated the search for new negative electrode materials with high gravimetric and volumetric capacity and good cyclability. As mentioned earlier, the first generation of LIBs employed specialty graphite (MCMB: mesoporous microbeads) as anode material, having a theoretical

capacity of 372 mAhg^{-1} . It suffers from safety problems at high current – charge rate. In this regard, different metals and their oxides, inter-metallics and complex compounds which can react with Li via various mechanisms are explored as alternative anodes for LIBs. They are broadly classified into groups depending upon the mechanism of Li-cycling: (i) intercalation/ de- intercalation type oxides, such as TiO_2 , $\text{Li}_4\text{Ti}_5\text{O}_{12}$ etc. (ii) alloying/ de- alloying type metals, metal oxides etc. and (iii) conversion/ displacement type transition metal oxides, sulfides, nitrides etc.

1.7.1. Intercalation/ de-intercalation based anode materials

1.7.1.1. Graphitic carbon, carbon nanotubes, Fullerene and disordered carbon

Graphite has a layered rhombohedral-hexagonal structure with stacking of graphene layers. It comprises sp^2 - hybridized carbon atoms in the planar layers bound together by van der Waals forces. Fig. I. 5 shows the crystal structure of hexagonal graphite. The Li- ion can intercalate in to graphite lattice to form a graphite intercalation compound (Li-GIC) with the stoichiometry of Li_xC_6 , where $0 < x < 1$ as per Eqn. I.1. The x value is 1 for the so-called stage I GIC where Li is present in between each layer. For $x < 1$, stage II, III and IV are observed where Li is present in between one, two or three alternate layers.

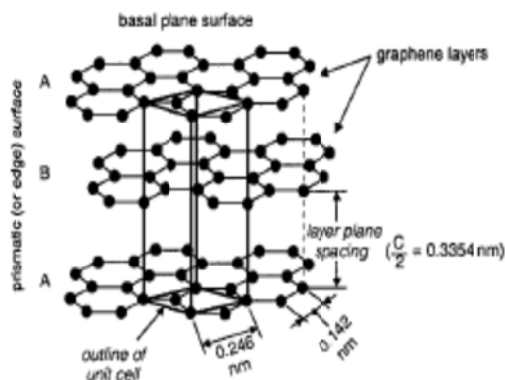


Fig. I. 5 Crystal structure of hexagonal graphite. Taken from [1].

Carbon nanotubes (CNTs) have been studied as anode materials and also as conductive additives [1, 3, 5, 32]. In the literature, various groups studied both single walled CNTs (SWCNTs) and multi walled CNTs (MWCNTs) for their Li- cycling properties. It was found that morphology, structure and synthesis procedure played an important role in the electrochemical performance [32, 33]. The reversible capacities in case of CNTs result from the diffusion of Li-ion to the 'stable sites' located on the surface or inside of the CNTs through the end cap/ side wall. Maurine et al [34] and Shin et al [35] studied the Li- cycling of MWCNTs and reported a reversible capacity of 180 and 250 mAhg⁻¹, respectively. Gao et al. [36] reported a capacity of 460 mAhg⁻¹ for bamboo like CNTs. Both raw and purified SWCNTs showed a capacity of 450-600 mAhg⁻¹ (Li_{1.2}C₆ to Li_{1.6}C₆). However, due to certain disadvantages, such as high cost, sophisticated synthesis procedure and low yield to prepare the SWCNTs and MWCNTs in gram scale and large irreversible capacity loss (ICL) in the first- cycle restrict their applicability as anodes for LIBs.

Recently, graphene has been studied as the anode material for LIBs [37, 38]. It was found to show a capacity of 540 mAhg⁻¹. This value could be increased to 730 and 784 mAhg⁻¹ by controlling the interlayer distance of graphene layers by introducing interacting molecules such as CNTs and fullerenes (C₆₀) [37]. The higher obtainable capacity as compared to graphite is ascribed to increase in interlayer spacing. Also, the various defects and large surface area are other key factors which are claimed to be responsible for higher capacity values in the case of graphene nanosheets [37, 38]. Fullerene can intercalate 3 Li per formula unit and since the theoretical capacity is fairly small (112 mAhg⁻¹), it is not of much interest as an anode for LIBs.

The disordered carbon has a planar network structure with short range crystallographic ordering. The crystalline and amorphous regions are connected by cross-linked network. The disordered carbon is broadly classified as graphitizable (soft carbon) and non- graphitizable (hard carbon). The crystallites in soft carbon are weakly linked and almost oriented in same direction (c- axis direction) and thus, can be easily ‘graphitized’ during heat treatment at temperature (T) above 2400⁰ C. The hard carbon does not show any tendency towards graphitization even at T > 3000⁰ C due to disordered crystallite orientations [1, 3, 5, 32].

Hard- carbon and soft carbon were found to deliver higher capacity compared to graphite due to additional sites for Li- storage. Values in the range of 500-1000 mAhg⁻¹ were reported [32]. The ‘additional sites’ are attributed to cavities and nanopores, interfacial/ surface storage and effect of hetero-atoms [32]. Sony Co. in early 1990s commercialized LIBs with hard- carbon anode but later discontinued due to large hysteresis during cycling and safety considerations. The specialty graphite (MCMB), prepared by patented processes by companies has been the favored anode in all the commercial LIBs for the last 15 years. The discharge- charge profiles of MCMB- graphite vs. Li are shown in Fig. I.6.

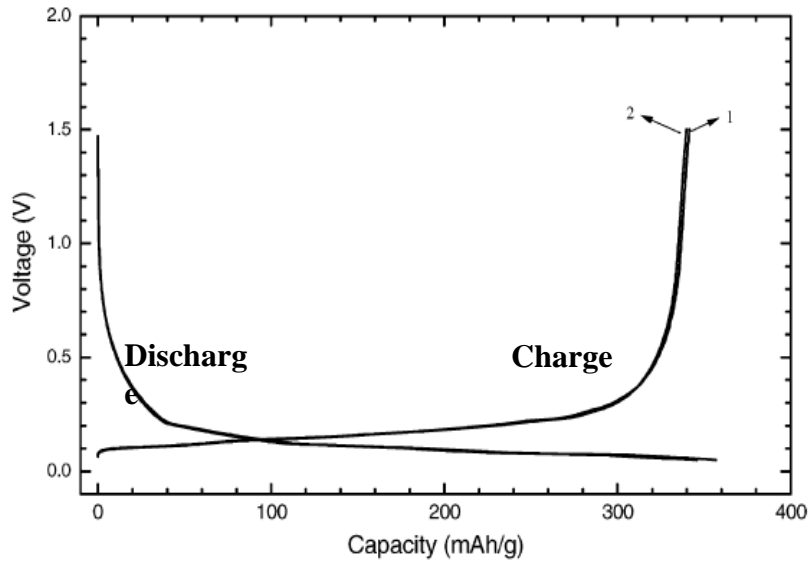


Fig.I.6. Charge-discharge cycling of MCMB graphite. Taken from [39].

I.7.1.2. Oxide Anodes based on intercalation/de-intercalation

I.7.1.2.1. $\text{Li}_4\text{Ti}_5\text{O}_{12}$

The lithium titanium oxide ($\text{Li}_4\text{Ti}_5\text{O}_{12}$) with the cubic spinel structure works as an Li insertion/de-insertion material and has been studied extensively during the last 15 years [1, 3, 5, 40, 41]. The special characteristic shown by $\text{Li}_4\text{Ti}_5\text{O}_{12}$ is small volume change during charge/discharge processes (zero-strain material), which enables a long and stable cycling. It shows Li-insertion potential of ~ 1.5 V vs. Li as a two-phase reaction, which overcomes the electrolyte reduction and solid electrolyte interphase (SEI) formation during first discharge [1, 40].

The spinel structure of $\text{Li}_4\text{Ti}_5\text{O}_{12}$ ($(\text{Li})_{8a}[\text{Li}_{1/3}\text{Ti}_{5/3}]_{16d}\text{O}_4$) consists of a cubic close packed oxygen array in which the Li- ions are located at the 8a tetrahedral sites and the Ti- ions along with some Li-ions are located at the 16d octahedral sites of a cubic unit cell with space group $\text{Fd}3\text{m}$ [1].

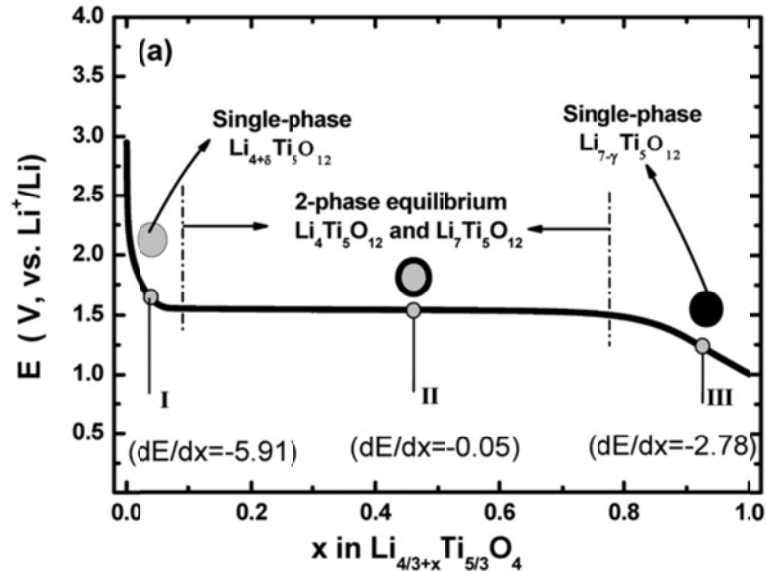


Fig. I.7 Voltage vs. capacity (x Li) of $\text{Li}_4\text{Ti}_5\text{O}_{12}$ at a current density 35 mA g^{-1} . Taken from [41].

During discharge, Li-ions intercalate in to the $\text{Li}_4\text{Ti}_5\text{O}_{12}$ to form $\text{Li}_7\text{Ti}_5\text{O}_{12}$ and revert back from $\text{Li}_4\text{Ti}_5\text{O}_{12}$ during charge (Fig. I.7). The voltage plateau during charge and discharge reaction is indicative of two- phase reaction. The theoretical capacity is 170 mAh g^{-1} , a value much smaller than that of graphite.

Although, $\text{Li}_4\text{Ti}_5\text{O}_{12}$ shows fairly high Li- ion mobility due to the spinel structure, it has poor electronic conductivity ($\sigma < 10^{-13} \text{ S cm}^{-1}$). Two approaches have been adopted in the last few years to minimize the conductivity problem; namely, using the nano-sized particles and coating of conducting metals or making composites with Ag, Cu etc. and by doping with other metals at the Ti- site. The high voltage (1.5 V vs. Li) is a great disadvantage of $\text{Li}_4\text{Ti}_5\text{O}_{12}$ as an anode in addition to the low capacity. When LiCoO_2 is used as the cathode, the net voltage of the cell is $\sim 2.0 - 2.4 \text{ V}$. Several researchers used

high voltage (~5 V) cathodes like, $\text{Li}(\text{Ni}_{0.5}\text{Mn}_{1.5})\text{O}_4$ and LiCoMnO_4 in place of LiCoO_2 and demonstrated the feasibility of the Li- ion cells [42, 43].

Other metal oxides besides $\text{Li}_4\text{Ti}_5\text{O}_{12}$, which have the ability to show Li-intercalation/de-intercalation to/from the crystal structure reported in literature are, TiO_2 , MoO_3 and Nb_2O_5 . The TiO_2 is one of the potential candidates as high- power anodes for LIBs due to its low cost, ready availability in large scale and eco- friendly. The anatase is known to be most electroactive host for Li-intercalation among all the polymorphs of TiO_2 . During the Li-insertion, the TiO_2 forms Li_xTiO_2 , thereby creating a charge compensating $x\text{Ti}^{3+}$ cations in the Ti^{4+} sublattice. The redox reaction in TiO_2 occurs in the voltage range of 1.5 -1.8 V vs. Li. Similar to $\text{Li}_4\text{Ti}_5\text{O}_{12}$, high potential makes the TiO_2 inherently safer than graphite and decrease the reactivity at the electrode/electrolyte interface and thereby minimizing the ICL [44]. But, the poor electronic and Li-ion conductivity associated with TiO_2 in its bulk form restricts its potential use as anode material for LIBs. To improve its electrochemical properties, various attempts are made to fabricate nanostructure TiO_2 to increase the Li-insertion by decreasing the diffusion length. Recently, Chen et al. [45] reported excellent Li- cycling performance of anatase- TiO_2 hollow microsphere assembled with nanotubes and showed initial insertion/de-insertion capacities of 290 and 232 mAhg^{-1} at a current rate of 0.2 C, respectively. A high reversible capacity of 150 mAhg^{-1} was noticed after 500 cycles at 1 C- rate [45].

Molybdenum oxide, MoO_3 is widely studied as anode material due to its high theoretical capacity (1117 mAhg^{-1}) and due to the layered crystal structure. But, the poor electronic and ionic conductivity limits its performance. Various attempts were made to overcome this problem: (i) doping metal ions in to MoO_3 , (ii) modifying the structure and

(iii) incorporating MoO₃ in to a composite. The Na_{0.25}MoO₃ (sodium molybdenum oxide bronze) showed a high initial capacity of 940 mAhg⁻¹ when cycled in the voltage range of 3.0 - 0.005 V, but the value degraded to 400 mAhg⁻¹ after 100 cycles [46]. However, a stable capacity was noted at a low current rate 0.05 C and when the lower cut- off voltage was increased to 0.2 V [46]. With respect to morphology and particle size, MoO₃ nanoparticles displayed a high capacity of 630 mAhg⁻¹ when cycled in the voltage range of 3.5 – 0.005 V at C/2 current rate which was stable upto 150 cycles, whereas the micron- sized MoO₃ (~5 μm) particles showed drastic capacity fading [47].

Another interesting Li-insertion material studied as anode for LIBs is niobium pentoxide, Nb₂O₅. Wei et al. [48] reported the Li- cycling of Nb₂O₅ nanobelts and showed an initial discharge (intercalation) capacity of 250 mAhg⁻¹ in the voltage range of 1.2 – 3.0 V, at 0.1 mA g⁻¹, which corresponds to x = 2.5 for Li_xNb₂O₅. A stable capacity of 180 mAhg⁻¹ was obtained at the end of 50 cycles. The CV of Nb₂O₅ at 0.1 mVs⁻¹ in the potential range 1.0-3.0 V showed the reduction of Nb⁵⁺ ↔ Nb⁴⁺ and Nb⁴⁺ ↔ Nb³⁺. The potentials correspond to these reduction are 1.62 V and 1.33 V, respectively. During oxidation, peaks at 1.73 V and 1.42 V were noticed, which correspond to Nb⁴⁺ ↔ Nb⁵⁺ and Nb³⁺ ↔ Nb⁴⁺, respectively [48].

I.7.2. Anodes based on metals undergoing alloying/ de-alloying reaction

Many elements/ metals belonging to Group II, III, IV and V elements of the Periodic Table can form alloys with Li (strictly, inter-metallics). They are Si, Ge, Sn, Pb, Zn, Cd, Al, In, Sb and Bi [1, 2, 3, 5, 49-51]. The alloying- de-alloying reaction (Eqn. I.10) which can contribute to the reversible capacity and thus, the M (M = alloying element) can act as an anode material for LIBs:



The ranges of x for different alloying elements are listed in the Table.I.1 with voltage ranges vs. Li metal. As can be expected, Sn and Si are explored as potential anode materials for LIBs due to their high capacity, low voltage for the reaction (Eqn. I.10), relatively cheap and environmentally acceptable. Since the densities of Si and Al are relatively low, the volumetric capacities are also high.

Table.I.1. Li- alloying elements. Alloying composition, x in Li_xM , voltage range vs. Li-metal and theor. capacity based on the atomic weight of M are given. Data taken from [49, 50].

Elements	Thero. Cap. (mAhg ⁻¹)	Alloying range; x in Li_xM	Voltage range vs. Li (Volt)
C	372	0-0.17	0.07-0.4
Bi	389	0-3	0.8
Zn	410	0-1	0.15-0.5
Pb	570	0-4.4	0.3-0.6
Sb	660	0-3	0.94
In	700	0-3	0.08-0.5
Cd	715	0-3	0.05-0.7
Al	990	0-1	0.4
Sn	994	0-4.4	0.4-0.8
Ge	1624	0-4.4	0.7-1.2
Ag	2982	0-12	0.0-0.25
Si	4200	0-4.4	0.0-3.0

I.7.2.1. Electrochemistry of Si-Li system

Silicon has been explored as the possible negative electrode material for LIBs, as it delivers a high theoretical capacity ($\text{Li}_{4.4}\text{Si}$; 4200 mAhg⁻¹), almost 11 times that of commercial graphite, based on alloying/de-alloying reaction mechanism. Also, it is the second most abundant element on earth which adds another advantage for the feasibility as anode material. But, severe unit cell volume change during cycling causes larger stain

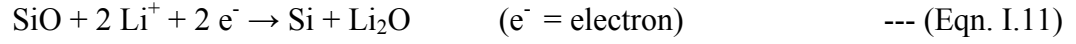
in the material and results in the loss of electrical contact with the current collector. Intensive studies have been carried out to overcome the above by various approaches: (i) reducing the particle size to nano- level, (ii) dispersing Si in other matrix materials, and (iii) using different binder [1, 2, 52, 53].

Studies have shown that Si in different nanostructures showed improvements in the capacity- retention compared to that of bulk- (micron- size) Si [54-56]. Chan et al. [54] reported the Li- cycling of Si- nanowire, which showed a reversible capacity of 2900 mAhg⁻¹ at a current rate of 0.05 C. However, only 50% of the initial capacity was obtained at 2 C- rate. Kim et al. [55] reported the Li- cycling of Si- nanoparticles of 5, 10 and 20 nm in the voltage range of 0 – 1.5 V at a current rate of 900 mAhg⁻¹. They showed that first- charge capacity of these nanoparticles are in the range of 2650 – 3770 mAhg⁻¹, with coulombic efficiencies < 85%. The Si- nanoparticle of 10 nm showed best capacity retention of 87% compared to 5 and 20 nm up to 40 cycles. Kang et al. [56] studied the Li-cycling of Si- nanowire up to 50 cycles in the voltage range of 0.01 – 2.0 V and showed an initial capacity of 4000 mAhg⁻¹ with coulombic efficiency < 98 %.

The Si-M composites (M = Co, Fe, Ca, Sn, Zn, Ag and C), have been investigated in recent years for their cycling stability [1, 2, 52, 53, 57-59]. Carbon has been shown to be a good candidate due to its good electronic conductivity and buffering effect of volume changes occurring in Si. Recently, Magasinski et al. [59] reported the Li- cycling of Si/C nanocomposite and obtained a high capacity of 1590 mAhg⁻¹ at 1 C-rate and stable up to 100 cycles.

The silicon monoxide is considered as a promising choice for high capacity anode material. During first discharge it is irreversibly reduced, resulting in the formation of

nano-sized clusters of amorphous Si surrounded by Li₂O as per Eqn. I.11. Further reaction with Li is the reversible formation of Li_{4.4}Si as per Eqn. I.12



But, the in-situ formed Li₂O is not sufficient to alleviate the large volume changes associated with the Li- cycling. Recently, Park et al. [60] reported the Li- cycling of milled- SiO, milled-SiO/graphite and nano-Si/SiO_x/graphite composites prepared by ball-milling, in the voltage range of 0.0 – 2.0 V at 100 mA g⁻¹. The nano-Si/SiO_x/graphite showed better capacity retention (70% of the initial capacity) and a reversible capacity of 710 mA h g⁻¹ was noticed after 100 cycles. Zhang et al. [61] reported the Li- cycling of core-shell Si/SiO nanocomposite prepared by sol-gel method and obtained a capacity of 540 mA h g⁻¹ at the 20th cycle.

I.7.2.2. Electrochemistry of Sn-Li system

As mentioned earlier, the Sn-metal shows a high capacity (~994 mA h g⁻¹) due to the alloying/de-alloying reaction mechanism of Li_xSn with x = 4.4. Detailed experimental studies have shown that the value of x goes through several stages (x = 0.4, 1.0, 3.3) before reaching the maximum value of 4.4. This behavior was supported by the theoretical calculations [52], as shown in Fig. I.8.

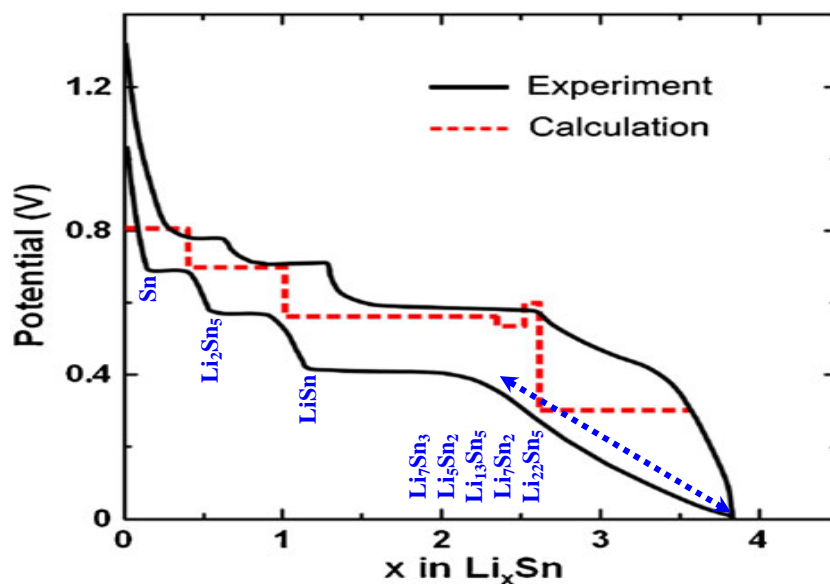


Fig.I.8. Experimental (solid line) and calculated (dashed line) voltage profile for the lithiation of tin. Taken from [51].

During the electrochemical lithiation, the Sn pulverizes rapidly when it forms $\text{Li}_{4.4}\text{Sn}$ due to the large density difference and unit cell volume change w.r.t. Sn. This is because, the crystal structures of the phases with various x are different and hence their unit cell values are different, in comparison to the pure Li and pure Sn. This volume change is as high as 300% for $x = 0$ to 4.4. It was observed that restricting the alloy formation to a stoichiometric LiSn ($x = 1$), reduces the large volume change as both Sn and LiSn are having almost the same densities.

Over the years, strategies similar to those employed for Si have been adopted to suppress or reduce the capacity- fading during Li- cycling of Sn. These are: (i) reduction of particle size to nano-meter range so that relative changes in the unit cell volumes are small, (ii) introducing electrochemically inactive/active matrix element in the form of nano-composites which will help in absorbing some of the volume changes, (iii) surface

coating of the particles with suitable materials and (iv) choosing a suitable binder for making the electrode in place of the conventional polymer (pvdf + hfp) binder.

I.7.2.3. Tin based inter-metallics and composites

The Sn-based inter-metallics and composites showed a significant improvement in Li-cyclability over that of Sn-metal [1, 3, 5, 49-51, 62-64]. The idea of using the Sn-based inter-metallics/ composites is that during Li-cycling at specific electrode potential, one phase/component is electrochemically active, i.e. expansion/ contraction of host lattice, whereas the other remains less active or inactive (called as matrix) and helps in buffering the volume expansion. To achieve satisfactory cycling performance the active materials should be in nano- size, finely distributed in the matrix, the matrix should be a good electronic conductor and preferably also an ionic conductor so that it allows both Li-ion and electron to enter into the bulk to react with the active material.

The Sn-based inter-metallics or composites containing the electrochemically-inactive matrix elements, M = Co, Ni, Fe, were extensively studied as anode materials. The M- metal does not form alloy with Li. During the Li-cycling, the M-Sn inter-metallic dissociates to M and Sn-metal. The Sn-metal participates in Li- cycling as per Eqn. I.13.



The re-formation of parental compound (M-Sn) may or may not occur at the end of charge- cycle. The use of inactive matrix (M) results in lowering of the obtainable reversible capacity for a given weight of electrode material. To achieve a high capacity, many electrochemically- active elements (M' = Si, Zn and Sb) which can also form alloy with Li, were introduced along with Sn, where they contributed to reversible capacity and mutually worked as matrix elements due to their Li-reactivity at different voltages

(Table.1). For example, in SnSb the Li- alloying potential for Sb is 0.8 – 1.0 V, whereas for Sn, the alloying potential is 0.3-0.5 V. Both Sb ($x = 3.0$ in Li_3Sb) and Sn take part in Li-cycling to give high capacity. An SnSb/C (amorphous carbon) has been found to give a stable capacity of 550 mAhg^{-1} up to 300 cycles at 2C rate [65].

The composite of Sn@C is interesting due to the dual behavior of carbon, where it provides electronic conductivity and behaves as matrix element buffering the volume variation. Hassoun et al. [64] reported a capacity of 450 mAhg^{-1} stable upto at least 100 cycles for nanostructured Sn@C composite, whereas Cui et al. [66] obtained a stable capacity of $\sim 550 \text{ mAhg}^{-1}$ for Sn encapsulated carbon. Carbon nanotube (CNT) were used as matrix and conducting additive due to their hollow core, high electrical conductivity and flexibility. A number of Sn@CNT composites were studied as anode materials, where Sn was deposited on the external wall of CNT [67, 68]. The group of Dahn [63, 69-71] extensively studied varying compositions of Sn-Co-C composites. The optimized composition, $\text{Sn}_{35}\text{Co}_{35}\text{C}_{30}$ showed a better performance, with a stable capacity of 400 mAhg^{-1} in the voltage range of 0.005-1.2 V at 0.2 C- rate up to 100 cycles. Incidentally, the above composite is very similar to the Sony. Co., second- generation anode material, Sn-Co-C.

A few Sn- and Sb- based intermetallics have been studied as anodes [72-75]. Examples are: Cu_6Sn_5 , Co and Ni- substituted Cu_6Sn_5 [72, 73], CuSb [75] and ZnSb [76].

I.7.2.4. Tin based oxides

I.7.2.4.1. Amorphous Tin composite oxides (ATCO)

A large number of Sn-based oxides, both in amorphous and crystalline form have been tested as anode materials for LIBs for the past 13 years. In 1997, Idota et al. [77]

studied the Li-cycling of amorphous tin composite oxide (ATCO). The ATCO has the general formula, SnM_xO_y , where M is a group of glass- forming elements whose total stoichiometric number is equal to or more than that of Sn ($x \geq 1$) and typically consists of mixture of B(III), P(V) and Al(III). In ATCO, Sn is the electrochemically- active ion for Li- reaction, whereas the glass network provides electrochemically- inactive species, which isolates the Sn(II) active center. During the reaction with Li, the Sn-oxide is reduced to metal, followed by the Li-Sn alloy formation. The ATCO showed initial reversible capacity 600 mAhg^{-1} , which however, slowly decreased upon cycling.

I.7.2.4.2. Sn-based binary oxides

During the past decade, various metal oxides of different particle size and morphology, such as ZnO [78], PbO [79], In_2O_3 [80], Sb_2O_3 [81], SnO [82], SnO_2 [83] were studied as prospective anode materials for LIBs, since the metals can form stable alloys with Li.

Tin oxides, SnO [82, 84- 86] and SnO_2 [83, 87-89] were extensively studied due to their high capacity in comparison to other oxides. During the first discharge (reaction with Li), the SnO or SnO_2 undergoes crystal structure destruction (amorphisation) and formation of nano Sn-metal dispersed in amorphous Li_2O as per Eqn.I.14 and I.15. This is followed by the alloy formation, $\text{Li}_{4.4}\text{Sn}$ (Eqn. I.13). During the charging process, the reverse reaction of Eqn. (I.13) occurs in the presence of Li_2O acting as a matrix.



The Eqns. I.14 and I.15 are irreversible reactions, which contribute to the irreversible capacity loss (ICL) during the first- cycle, where as Eqn. I.13 contributes to the reversible

capacity. The Li- cycling performances of Sn-based oxides were found to be superior to pure elements, due to the presence of electrochemically formed nano- Li_2O . The Li_2O behaves as buffering domain during Li-Sn alloy formation and decomposition, thereby reducing the volume variation and reducing the capacity- fading by maintaining the electrode integrity. It also provides the conducting channel for the Li-ion migration and helps in keeping the electrochemically formed nano Sn- metal particles apart and prevents agglomeration. However, Li_2O alone is not effective in completely suppressing the capacity fading during long term cycling.

Li et al [84] reported that the Li-cycling properties of SnO were influenced by the particle size, as was clear from studies on un-milled and ball-milled SnO. Uchiyama et al. [85] reported a comparative study of the cycling of SnO of different morphologies with that of commercial SnO. They found that both meshed and flat plate SnO showed initial capacities of 760 and 880 mAhg^{-1} , respectively compared to 525 mAhg^{-1} for commercial SnO in the voltage range 0.1- 1.0 V at 100 mA^{-1} . Ning et al. [82] studied the Li- cycling of nanoflower SnO in the voltage range of 0.01- 2.0 V at 0.1 C rate. A 4th cycle charge capacity of $\sim 750 \text{mAhg}^{-1}$ was noticed, but the capacity faded to 450 mAhg^{-1} with in 20 cycles.

The SnO_2 nanowires prepared by vapour- liquid- solid (VLS) method showed a high capacity of 510 mAhg^{-1} at the end of 50th cycle [83]. Wang et al. [88] reported the Li-cycling of SnO_2 of different morphology, such as nanotubes, nanotube-nanorod hybrid and nanorods. They showed that fully tubular nanostructure- SnO_2 performed well and a capacity of 654 mAhg^{-1} was retained at the end of 40 cycles. Kim et al. [87] reported the effect of critical particle size of SnO_2 on the electrochemical performance. The SnO_2 of

particle size ~ 3 nm showed a high reversible capacity of $\sim 600 \text{ mAhg}^{-1}$. The cycling performance of SnO_2 was also tested by preparing SnO_2 -CNT composites [89 - 91], CuO-CNT- SnO_2 nanocomposite [92] and coating of SnO_2 with conducting carbon [93-96]. It was found that the upper cut-off voltage w. r. t. Li- metal has a tremendous effect on cycling performance of both SnO and SnO_2 . Capacity- fading was found when cycled above the upper cut-off voltage of 1.0 V due to the formation of SnO/ SnO_2 , which led to large volume variation [97, 98]. The optimum upper cut-off voltage for best Li-cycling of Sn-oxides was found to be < 1.0 V in majority of studies. There are, however, some reports of nano- SnO_2 exhibiting high and stable capacities when cycled in the range, 0.005 – 3.0 V [89, 90].

I.7.2.4.3. Sn-based ternary oxides

Incorporating both electrochemically inactive/active matrix to the Sn-based oxides was found to be one way to buffer the unit cell volume changes and thereby minimizing the capacity- fading. During last decade, many ternary Sn-based oxides such as M_2SnO_4 (M= Zn, Co, Mn) [99-103], ASnO_3 (Ca, Ba, Sr) [104, 105], Li_2SnO_3 and SiSnO_3 [106], composites MO.SnO_2 (M = Ca [107], Mg [108]) were studied as anode materials for LIBs. The electrochemically formed M / $\text{MO-Li}_2\text{O}$ during the first discharge reaction acts as a matrix for electrochemical cycling of Sn. Sharma et al. [107] reported a high and stable capacity of 500 mAhg^{-1} for nano-composite CaO.SnO_2 and showed that the presence of CaO acts as an excellent buffering matrix to suppress the capacity- fading.

The crystal structure also plays an important role in Li- cycling of Sn-based ternary/quaternary oxides. Connor and Irvine [99, 100] reported that M_2SnO_4 (M = Mg, Mn) having SnO_4 tetrahedral O- coordination with the inverse- spinel structure showed

different Li- cycling behavior compared to SnO_2 or CaSnO_3 which have SnO_6 octahedral O-coordination. Behm and Irvine [109] found different Li- cycling behavior of SnP_2O_7 possessing different crystal structures. The cubic phase with isolated SnO_6 octahedra (and corner- linked PO_4 tetrahedra) showed higher reversible capacity and 96% capacity- retention at the end of 50 cycles, as compared to the SnP_2O_7 with the layered structure which showed only 53% capacity- retention at the end of 50 cycles. The Sn- based hollandite- type compounds containing SnO_6 octahedra with chemical formula $\text{A}_2(\text{M},\text{Sn})_8\text{O}_{16}$, where A = large size alkali or alkaline earth cations like, K or Ba and M = bivalent or trivalent metal ion, are of interest to study as anode materials. Sharma et al. [110] studies the Li- cyclability of $\text{K}_2(\text{M},\text{Sn})_8\text{O}_{16}$ (M = Li, Mg, Fe and Mn) and reported for M = Li, a capacity of 602 mAhg^{-1} at a current density of 60 mA g^{-1} , with a capacity- retention of 73 % after 50 cycles. They found that the M- ion plays a role on the Li- cyclability with M = Li and Fe acting as ‘good’ matrices, whereas M = MgO and Mn are ‘bad’ matrices and yielded drastic capacity- fading. Li- cyclability of Sn- oxides with the pyrochlore structure, $\text{A}_2\text{Sn}_2\text{O}_7$ (A = Nd, Y) are reported by Sharma et al. [111].

The reduction of particle size to nanometer scale has a tremendous effect on Li- cycling behavior of alloying- de-alloying based anode materials due to compensation of large volume variations during discharge and charge process. The capacity retention in the case of Sn-based oxides has been improved to some extent by reducing the particle size of the active material to nano- size [112, 113]. As mentioned earlier, the advantages associated with nanomaterials as electrode materials for LIBs are: (i) They enable the electrode reactions, which may not take place when micron- size particles are employed. (ii) The rate of Li-ion intercalation/de-intercalation is highly increased due to the smaller

diffusion length (L). The characteristic time (τ) for intercalation/de-intercalation is decreased due to decrease in diffusion length, since $\tau = L^2/D$, where D is the diffusion coefficient. (iii) The electron transport is enhanced within the particles due to nanometer-sized particles. (iv) The smaller particle size can modify the chemical potentials for Li-ions and electrons, thereby changing the electrode potential to some extent (\sim mV)[114, 115].

I.7.2.5. Antimony (Sb) based Anodes

Antimony (Sb) has received attention as an alternative to graphite anode, due to its high specific capacity (Li_3Sb ; 660 mAhg^{-1}) and higher operating voltage than graphite which favors for the battery safety during rapid charge/ discharge cycles. But, the inherent problem associated with Sb is the large volume variation (e.g., 137 % per Sb atom). In order to alleviate the large volume change, Sb in nanocrystalline form, containing electrochemically active/inactive counter ions and composites were studied [1, 2, 116]. Recently, Yoon and Manthiram [116] reported the Li- cycling of Sb- MO_x - C ($M = \text{Al, Ti, Mo}$) nanocomposites and showed good electrochemical performance and rate capability. For $M = \text{Al}$, they found the best result, with a capacity $>430 \text{ mAhg}^{-1}$ after 100 cycles when cycled in the voltage range of 0-2.0 V at 100 mAg^{-1} .

There are a few reports on the Li- cycling of Sb_2O_3 [117-119]. Xue et al. [118] studied the nanostructured Sb_2O_3 thin films and obtained a reversible capacity of 794 mAhg^{-1} in the voltage range of 0.01 to 3.0 V at 273 mAg^{-1} . The alloying/de-alloying voltages of Sb in Sb_2O_3 were attributed to 0.8 V and 1.05 V, respectively and these values agree with those reported by Li et al. [117].

I.7.3. Metal oxide anodes based on conversion reaction

I.7.3.1. Binary oxides

In 2000, Poizot et al. [120] reported the Li- storage and cyclability of transitional metal oxides, MO, where M = Co, Cu, Ni and Fe with rock salt structure. They showed that nano- MO showed high capacity of $\sim 700 \text{ mAhg}^{-1}$, with good capacity- retention up to 100 cycles at a high C- rate. The reaction mechanism involved during Li- cycling is different from that of intercalation/de-intercalation and alloying/de-alloying, and involves the formation and decomposition of Li_2O , along with the reduction to, and oxidation of, metal nano particles, the so called ‘conversion / displacement reaction’ (Eqn. I.16).



Normally, Li_2O is electrochemically inert, but it can participate during electrochemical cycling due to the ‘insitu’ electrochemically formed nanoparticles, as the latter catalyze the reaction [120-123].

The voltage vs. composition (x in Li_xMO) profiles of various MO (M = Co, Ni, Fe) are shown in Fig.I.9. As can be seen, for all M, a flat voltage region during the first-discharge at a voltage of 1.0- 0.8 V (R1 in Fig. I. 9) and a sloping region till to the deep discharge limit of 0.01 V are observed (R2 in Fig. I.9). CoO showed a high reversible capacity of 750 mAhg^{-1} in the voltage range of 0.01 – 3.0 V and remained stable at least up to 100 cycles [120- 123]. The voltage plateau noticed at 1.0 – 0.8 V in the region (R1) corresponds to the crystal structure destruction and formation of Co/ Li_2O , where the nano-size Co-metal particles ($\sim 4\text{-}5 \text{ nm}$) are embedded in the X-ray amorphous Li_2O . The sloping region (R2) extended up to deep discharge of 0.01 V. The extra capacity (consumption of $x > 2.0$) noticed during this first- discharge process are ascribed to the

factors, such as (i) formation of polymeric gel- type layer on the Co-metal nanoparticles due to the catalytic decomposition of the solvents of the electrolyte [120, 121] and (ii) possibly interfacial storage of extra Li in Co/Li₂O. During the charging process, re-formation of CoO is noticed, which is supported by in-situ XRD and –TEM [120, 121, 123]. Studies showed that charging to voltage > 2.0 V vs. Li is necessary in order to achieve a stable capacity as the dissolution of polymeric layer (formed during discharge) occurs above 2.0 V [124].

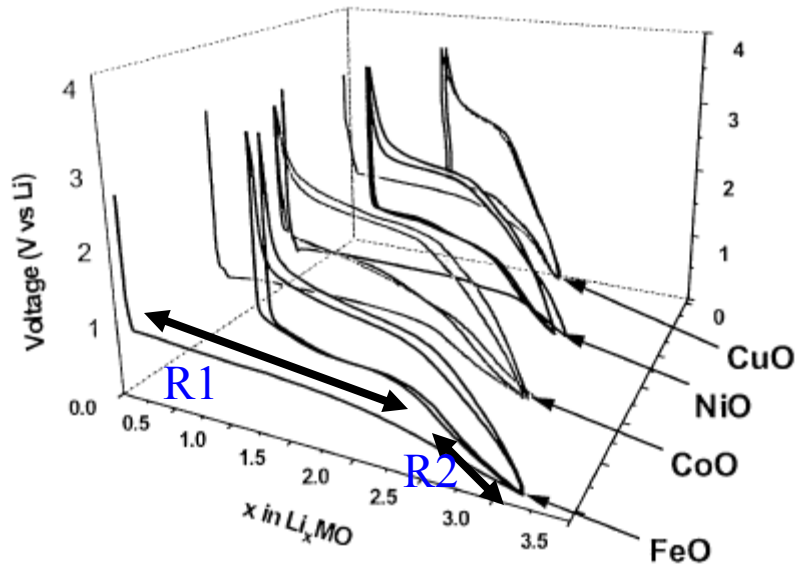
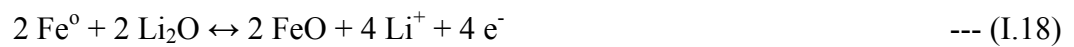


Fig. I.9 Voltage- composition profile for various MO/Li cells. The cells were cycled at C/5 rate in the voltage range, 0.01-3.0 V. Taken from [121].

Another transitional metal oxide, namely, Fe₂O₃ has been explored as anode material via conversion reaction [125-130]. During the first discharge, the Fe₂O₃ is reduced to Fe- metal particle and Li₂O as per the Eqn. I.17:



According to Eqn. I.17, 6 moles of Li per formula unit of Fe_2O_3 will be consumed. But during charging (Eqn. I.18), studies showed that re-formation of Fe- metal to FeO or Fe_2O_3 is possible depending on the particle size. Liu et al. [128] showed that Fe_2O_3 nanorods of thickness, 60-80 nm and length 300-500 nm, exhibited a stable specific capacity of 800 mAhg^{-1} . They showed that the reversible transformation of Fe^0 to Fe^{3+} at $\sim 1.8 \text{ V}$ is possible during charging. However, capacity- retention was poor due to slow kinetics. Li- cycling of Fe_2O_3 of different morphology [125,126,128] and surface- coating [129,130] were also studied. Li et al. [127] reported that significant increase in reversible capacity as well as better cycling stability of micron- size Fe_2O_3 can be achieved by heat- treating the composite electrode, containing the active material, binder and conducting carbon, at 300°C for 12 h in flowing argon gas. They found a reversible capacity of $\sim 400 \text{ mAhg}^{-1}$ in the case of bare electrode, whereas the heat- treated electrode showed a capacity of $\sim 800 \text{ mAhg}^{-1}$, stable up to at least 100 cycles, when cycled at 0.2 C-rate, in the voltage range, 0.005 – 3.0 V.

Co_3O_4 crystallizes with the inverse spinel structure, $\text{Co}^{3+}[\text{Co}^{2+, 3+}]_2\text{O}_4$ and is well studied as anode material. Lu et al. [131] reported the Li- cycling performance of Co_3O_4 of different morphologies like, nanoparticles, nanorods and macroporous platelets. They showed that macroporous platelets performed better compared to others, with a capacity of 811 mAhg^{-1} at the high current rate of 1780 mA^{-1} . Co_3O_4 in the form of nanoplatelets [132], nanoneedles [133] and nanotubes [134] were also studied for Li- cyclability and all of them showed high capacities. Li et al. [135] reported a capacity of 700 mAhg^{-1} at 1 C rate for mesoporous nanowire Co_3O_4 .

Fe_3O_4 is another binary oxide, which adopts an inverse spinel structure (similar to Co_3O_4), where Fe^{3+} ions occupy tetrahedral (8a) sites and the Fe^{2+} and Fe^{3+} ions occupy the octahedral (16d) sites in the crystal structure [136] (Fig. I.10). It has been extensively studied as anode material due to its high theoretical capacity values, low cost and environmental friendly- nature [137-140].

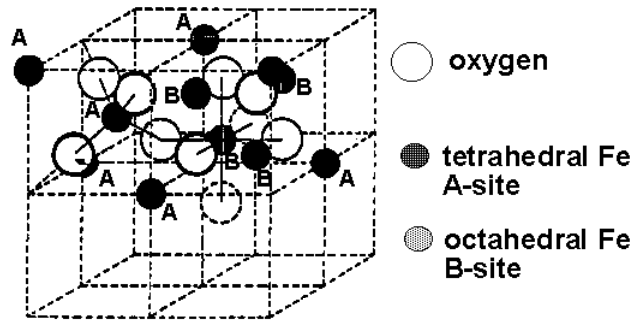


Fig. I.10 Crystal structure of Fe_3O_4 . Taken from [136].

Early studies on Fe_3O_4 showed poor capacity- retention and limited diffusion kinetics. Liu et al. [138] reported that $\text{Fe}_3\text{O}_4/\text{C}$ core- shell nanorods show a reversible capacity of $\sim 390 \text{ mAhg}^{-1}$ after 100 cycles. Wang et al. [139] reported a high capacity of 1007 mAhg^{-1} at the 80th cycle for $\text{Fe}_3\text{O}_4/\text{C}$ composite nanofiber with good rate capability.

Other binary oxides like FeO [120, 121], NiO [120, 121, 141], CuO [120, 142], ZnO [143], CdO [144] have been studied for their Li- cycling property by conversion reaction. In the latter two compounds, the metals can form alloys with Li (Table I.1), and thus larger reversible capacities are expected. However, capacity- fading is noticed in almost all the above binary oxides.

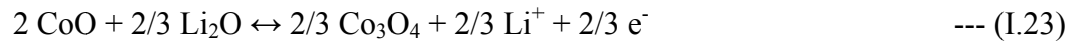
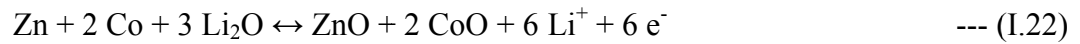
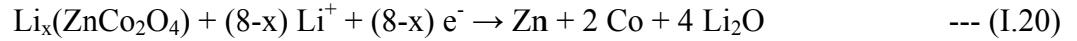
Binary oxides of rutile-type, MO_2 , $\text{M} = \text{V}$ [145], Mo [146] and Ru [147] have been studied as anode materials via conversion reactions. In the case of V and Mo , these can not be reduced to metals by Li during electrochemical cycling and they form either VO or MoO_y ($y \geq 1$). Stable capacities have been reported for nano- VO_2 [145] and MoO_2 [146]. RuO_2 can be reduced to Ru - metal by Li and the Li - cyclability of RuO_2 has been reported with 100% coulombic efficiency in the first- cycle when cycled between 0.05 – 3.0 V vs. Li [147]. Lee et al. [47] reported the Li -cycling of MoO_3 nanoparticles, which showed a stable reversible capacity of 630 mAhg^{-1} up to 150 cycles in the voltage range of 0.005-3.0 V.

I.7.3.2. Ternary oxides with spinel structure

Ternary oxides with a variety of crystal structures like, spinel, scheelite, brannerite, brownmillerite and CaFe_2O_4 - type have been investigated as anode materials. They contain at least one transition metal ion and one or more electrochemically active/ inactive ions. The Li -cycling mechanism involves ‘conversion reaction’ with the inactive- metal ions (e.g. Ca , Mg) acting as matrix. Depending on the structure, morphology, nano-size and metal ions, large and stable capacities have been reported.

Since Co_3O_4 and Fe_3O_4 adopt the inverse spinel structure and found to show good Li - cyclability with high capacities, studies have been reported, as can be expected, on the substituted- Co_3O_4 and Fe_3O_4 . Thus, MCo_2O_4 , $\text{M} = \text{Mg}$, Fe [148], Ni [149], Mn [150], Cu [151], Zn [152] have been studied either as bulk micron- size or nano-size particles. It is possible that Li - intercalation can occur, to some extent, in many of the above oxides without destroying the structure, due to the vacant sites for Li - ions in the spinel lattice. This has been noticed even though the recyclable Li - content is fairly small.

Deep discharge reaction with Li leads to structure destruction and metal- particle formation by the conversion reaction. In the case of MgCo_2O_4 , MgO will be formed which acts as the matrix. ZnCo_2O_4 is an interesting compound in that Zn can form alloy and in addition participate in the conversion reaction (Eqns. I.(19-23)).



Thus, a reversible capacity corresponding to 8.3 moles of Li per mole of ZnCo_2O_4 are expected. Indeed, Sharma et al. [152] have realized near theoretical capacity ($\sim 900 \text{ mAhg}^{-1}$) in nano- ZnCo_2O_4 stable up to 50 cycles at 60 mA g^{-1} when cycled in the range, 0.005- 3.0 V.

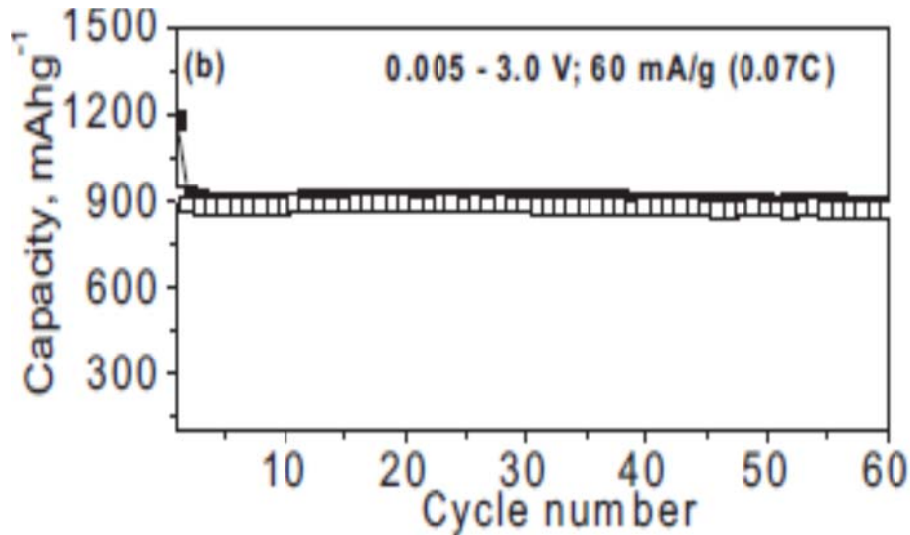


Fig. I. 11 Capacity vs. cycle number of ZnCo_2O_4 . Filled squares: Discharge; open squares: Charge. Taken from [152].

Some compounds based on Fe- oxides with the spinel structure, namely MFe_2O_4 , $M = Co, Ni$ [153], Zn [154] and Cd [155] have also been studied. Vanadium oxides with inverse- spinel structure, $LiNiVO_4$ [156, 157] and $LiCoVO_4$ [158] with V^{5+} ions at the tetrahedral sites, have been studied for their Li- cyclability both in thin film and polycrystalline form. Recently, spinel with V^{3+} at the octahedral site, ZnV_2O_4 [159] has also been investigated.

1.7.3.3. Ternary oxides with other structures

Early studies on Li- cycling of MVO_4 , $M = In, Cr, Fe$ and Al [160], $FeVO_4$ [161] were reported, but the results were not encouraging. Molybdenum oxides of the type, $MMoO_4$, $M = Mn$ [162], Cu, Zn, Ni and Fe [163] and Ca [164] have been studied, where capacity- fading was noted in all cases. Hara et al. [165, 166] studied pure and Mo- doped MnV_2O_6 with the brannerite structure and elucidated the Li- cycling mechanism. Nazar et al. [167] and Sharma et al. [168] studied $CaFe_2O_4$ and its anodic behavior, whereas Sharma et al. [169] reported on the compounds with the brownmillenite structure, $Ca_2Fe_2O_5$ and $Ca_2Co_2O_5$. It was found that Ca acts as a good matrix element, in the form of electrochemically- generated CaO and gives a good Li- cyclability. However, the observed capacities were low ($\leq 400 \text{ mAhg}^{-1}$). Hence, there is a need to continue Li- cycling studies on other and complex oxides.

1.7.4. Metal nitrides as anodes

Metal nitrides are explored as candidates for anode materials due to their high energy density as they can consume 3 moles of Li per formula unit (as Li_3N) compared to that of oxides, where only 2 moles of Li are consumed. The lower redox potential in the case of metal nitrides, as compared to the oxide for the conversion reaction, is another

advantage. The lithiated phase of metal nitrides i.e., M/Li₃N gives an excellent platform for reversible Li-reaction due to the high Li- ionic conductivity of Li₃N, which has antifluorite structure [170]. Both binary and ternary metal nitrides have been studied over the years for their Li- cyclability.

I.7.4.1. Binary metal nitrides

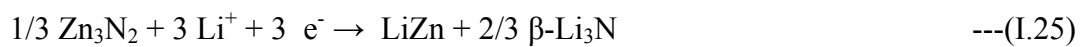
The reaction mechanism during charging and discharging cycles of M_yN_z is given in Eqn. I.24, which shows a conversion reaction by the formation of metal nanoparticles embedded in Li₃N matrix.



Binary metal nitrides in thin film form studied are: Sn₃N₄ [171, 172], Zn₃N₂ [173], Ge₃N₄ [174], Cu₃N [175], Co₃N and Fe₃N [176], Ni₃N [177], CrN [178] and VN [179].

Bates et al. [171] reported the Li-cycling of Sn₃N₄ thin films prepared by reactive sputtering and showed that during first- discharge reaction, Sn₃N₄ is reduced to Sn-metal and formation of Li₃N along with the formation of Li-Sn alloy. The reversible capacity originated from the alloying/de-alloying of Li_{4.4}Sn and, Li₃N behaved as electrochemically- inactive matrix. Capacity- fading was noticed. Recently, Baggetto et al. [172] reported the Li-intercalation to Sn₃N₄ thin film forming a ternary compound of Li-Sn-N. They showed more than 6 moles of Li can be consumed due to the formation of intermediate compound, Li-Sn-N. This is followed by the formation of Sn metal and Li₃N matrix.

Pereira et al. [173] found that the Zn₃N₂ reacts with Li to form LiZn alloy and β-Li₃N, and no evidence of formation of Zn prior to alloying (Eqn.I.25)





The reversible capacity is due to the reversible conversion of LiZn and $\beta\text{-Li}_3\text{N}$ into LiZnN (Eqn. I.26).

Ge_3N_4 was investigated as anode material by Pereira et al. [174]. The partial participation of active material of Ge_3N_4 during Li-cycling was supported by both in-situ/ex-situ XRD and -TEM and gave a reversible capacity of 500 mAhg^{-1} in the voltage range of 0- 0.8 V. The Ge- metal and $\alpha\text{-Li}_3\text{N}$ were found at the end of first discharge by SAED (selected area electron diffraction). Cu_3N was studied as anode by Pereira et al. [175], where they showed much improved cycle life and excellent rate capability based on conversion reaction. The reversible reduction to Cu- metal and Li_3N matrix and re-formation of Cu_3N during discharge and charge process are responsible for the capacity.

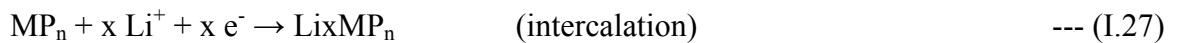
The transition metal nitrides of general formula, M_3N where $\text{M} = \text{Co}, \text{Fe}$ [176] and $\text{M} = \text{Ni}$ [177] were studied as prospective anode materials. Reversible capacities ranging from 320 to 440 mAhg^{-1} were observed up to 40 cycles. The Li- cycling performance of thin film of CrN [178] and VN [179] were studied. Films of CrN showed a first cycle discharge capacity of 1800 mAhg^{-1} when cycled at $28 \mu\text{Acm}^{-2}$, in the range 0.005-3.5 V vs. Li, whereas the first- charge capacity of 1200 mAhg^{-1} slowly degraded by 0.5% per cycle up to 30 cycles. A stable capacity of 800 mAhg^{-1} was found for the VN thin films up to 50 cycles. The reaction mechanism is the conversion reaction and reversible reduction and formation of metal nitrides during discharge and charge cycling as per Eqn. I.24.

I.7.4.2. Ternary metal nitrides

Lithium transition metal nitrides of the general formula, $\text{Li}_{3-x}\text{M}_x\text{N}$ having layered hexagonal crystal structure (same as that of Li_3N) were explored as negative electrode materials. Nishijima et al. [180, 181] and Shodai et al. [182, 183] reported the Li-cycling of $\text{Li}_{3-x}\text{M}_x\text{N}$ ($\text{M} = \text{Co}, \text{Ni}, \text{Cu}$). Among these compounds, the composition, $\text{Li}_{2.6}\text{Co}_{0.4}\text{N}$ was studied extensively, which showed a high reversible capacity of $\sim 900 \text{ mAhg}^{-1}$ in the voltage range of 0.01 to 1.5 V. There is an irreversible structure change leading to an amorphous phase in the first Li-extraction process and capacity-fading was noticed during cycling. Liu et al [184] reported the electrochemical performance of composite of $\text{Li}_{2.6}\text{Co}_{0.4}\text{N}$ and carbon prepared by ball-milling and obtained a stable capacity of 400-450 mAhg^{-1} . Liu et al. [185] also reported studies on Cu or Fe or Ni- doped $\text{Li}_{2.6}\text{Co}_{0.4}\text{N}$. The compound, $\text{Li}_{2.6}(\text{Co}_{0.2}\text{Cu}_{0.2})\text{N}$ showed a capacity of 600 mAhg^{-1} up to 60 cycles in the voltage range 0-1.3 V, whereas $\text{Li}_{2.6}(\text{Co}_{0.2}\text{Cu}_{0.1}\text{Ni}_{0.1})\text{N}$ and $\text{Li}_{2.6}(\text{Co}_{0.2}\text{Cu}_{0.15}\text{Fe}_{0.05})\text{N}$ showed 80% and 81% capacity- retention at the end of 60th cycle against the 1st cycle capacity of 717 and 781 mAhg^{-1} , respectively.

I.7.5. Metal phosphides and sulfides

Metal phosphides (MP_n) have received attention as anodes due to the high-lying mixed anion-metal bands and strong covalent characteristics of M- pnictogen bond [186, 187]. They show lower intercalation potential as compared to metal oxides and metal nitrides. The reaction mechanisms involved during the Li- cycling are:



Kishore and Vardaraju [186] studied the simple phosphides, InP and GaP with the zinc blende structure as anode materials. InP performs well with a reversible capacity of $\sim 475 \text{ mAhg}^{-1}$ when cycled between 0.2- 1.5 V. Souza et al. [187] showed that Li- intercalation to the host lattice of the layered structure MnP_4 occurs to form Li_7MnP_4 . The first discharge and charge capacities are $\sim 1150 \text{ mAhg}^{-1}$ and $\sim 700 \text{ mAhg}^{-1}$, respectively. The re-formation of MnP_4 was observed during Li- extraction in the voltage range of 0.57- 1.7 V vs. Li. However, a large volume variation associated with the above reactions during cycling led to capacity- fading.

Silva et al. [188] studied the Li- cycling property of FeP_2 . They found that during the first-discharge, 6 moles of Li are consumed to form a metastable ternary ‘Li-Fe-P’ phase, of which 5.5 moles of Li are extracted during the first- charge. The Li- reaction of CoP_3 [189] is different from that of MnP_4 and FeP_2 , where crystal structure destruction/ amorphisation occurs typical of conversion reaction (Eqn. I.29).



A reversible capacity of 487 mAhg^{-1} was observed (theoretical capacity is 536 mAhg^{-1}).

Binary metal sulfides and LiMS_2 ($\text{M} = \text{Ti}, \text{V}, \text{Cr}$) have been studied as anode materials for their Li- cyclability [190-192]. Seo et al. [190] studied the electrochemical performance of nanoplates of SnS_2 and showed that it can reversibly react with Li via conversion reaction and formation of Li-Sn alloy during the discharge reaction. The initial reversible capacity was found to be $\sim 600 \text{ mAhg}^{-1}$ but capacity- fading was noticed. Yan et al. [192] reported that CoS_2 showed first- discharge capacity as 1280 mAhg^{-1} at a current rate of 50 mA g^{-1} based on conversion reaction where CoS_2 is reduced to Co-metal and Li_2S .

I.7.6. Metal fluorides and Oxyfluorides

Metal fluorides and oxyfluorides are another class of materials which are studied as anodes for LIBs. Due to high ionic bond between M-F, these metal fluorides show electronically insulating behavior and inhibit the Li-diffusion to the host lattice. This problem was addressed by various groups by preparing nanocomposites of carbon and metal fluorides. Badway et al. [193] showed that FeF_3 mixed uniformly with carbon exhibits a reversible capacity of 600 mAhg^{-1} at 70°C . Li et al. [194] reported the Li-cycling of a number of metal fluorides, TiF_3 , VF_3 , MnF_2 , FeF_2 , CoF_2 , NiF_2 , CuF_2 . They showed that during first-discharge reaction, reduction of metal fluorides to metal and LiF is seen.

Reddy et al. [195] reported the Li-cycling of metal oxyfluorides, TiOF_2 and NbO_2F . They noticed during the first discharge, both compounds showed crystal structure destruction, in the voltage range of $0.8 - 0.9 \text{ V}$ for TiOF_2 and $1.3 - 1.4 \text{ V}$ for NbO_2F . They reported that 1.52 moles of Li/Ti in Li_xTiOF_2 and 1 mole of Li/Nb in $\text{Li}_x\text{NbO}_2\text{F}$ are cyclable between $0.005\text{-}3.0 \text{ V}$.

I.7.7. Metal Hydrides, Carbonates and Oxalates

Oumellal et al. [196] showed that metal hydrides are cyclable w. r. t. Li-metal, have an average voltage of 0.5 V and the mechanism is conversion reaction. In the case of MgH_2 , they reported a capacity of 1480 mAhg^{-1} but the capacity-retention was poor.

Metal carbonates and oxalates can show similar type of conversion reaction and can deliver a high reversible capacity. Aragon et al. [197] showed that MnCO_3 can reversibly react with Li based on conversion reaction and forms Li_2CO_3 and Mn metal particles. They obtained a reversible capacity of $\sim 600 \text{ mAhg}^{-1}$, but capacity-fading was

noted. Recently, Sharma et al. [198] reported the Li- cycling of the mixed-metal carbonate, $(\text{Cd}_{0.33}\text{Co}_{0.33}\text{Zn}_{0.33})\text{CO}_3$, where they showed that both conversion and alloying reactions (due to Li_3Cd and LiZn) are mutually beneficial to achieve a stable capacity. They obtained a stable capacity of 680 mAhg^{-1} for the mixed carbonate in the voltage range of 0.005- 3.0 V when cycled at 60 mA g^{-1} up to 60 cycles.

The Li- cyclability of mesoporous iron oxalate, FeC_2O_4 nanoribbons was studied by Aragon et al. [199]. They reported a high capacity of $\sim 700 \text{ mAhg}^{-1}$ after 50 cycles at 2C- rate based on conversion reaction. The first- discharge process involves reduction of FeC_2O_4 to Fe metal along with the formation of $\text{Li}_2\text{C}_2\text{O}_4$ matrix.

I.8. Electrolytes for LIBs

An electrolyte is an integral part of the LIBs, which provides conducting pathways to the Li- ions from cathode to anode and vice-versa during charging and discharging. The electrolyte in LIBs consists of a Li-salt dissolved in a mixture of non-aqueous (organic) solvents. The basic requirements of a suitable electrolyte for batteries, in particular, LIBs are: (i) Should have high ionic but negligibly small electronic conductivity. This is to minimize the cell short-circuit, achieve a good current (C-) rate capability and keep the self- discharge to a minimum. (ii) Should have high thermal and chemical stability. This is to reduce the decomposition of electrolyte in contact with the electrodes. Also, it should withstand temperatures, $T \geq 80 \text{ }^\circ\text{C}$. (iii) Should have wide potential window to tolerate the high voltage difference between anode and cathode ($> 3.5 \text{ V}$). (iv) Should have low reactivity towards the electrodes, namely the electrode material must not be soluble in the solvents. (v) Should have low melting point to provide sufficient conductivity at low temperature. (vi) Should have high boiling point to provide

safety and prevent explosion resulting from high pressure build up in the LIB. (vii) Should be non- toxic and cost effective.

Since the LIBs operate in the voltage range of 2.75 – 4.2 V, water can not be the solvent due to low decomposition potential (1.23 V). Depending on the nature and properties of electrolytes, they are broadly divided into three types, namely, liquid, solid and polymer electrolytes [1, 3, 4, 5, 200, 201].

I.8.1. Liquid electrolytes

Liquid electrolytes for LIBs comprise of Li- salts dissolved in non-aqueous (organic) solvents. The solvent can be one or a mixture of two or three solvents to realize the desired properties of a good electrolyte. The commonly used Li- salts are, LiPF_6 , LiBF_4 , LiAsF_6 , LiClO_4 , LiCF_3SO_3 and $\text{LiN}(\text{CF}_3\text{SO}_2)_2$. These Li- salts satisfy the criteria such as: (i) They have the ability to completely dissolve and dissociate in non-aqueous medium, and the solvated ions should be able to move in the medium with high mobility. (ii) The anions are inert and stable against oxidative decomposition at the cathode.

The LiCF_3SO_3 is a preferred choice, as it is not prone to oxidation and is also thermally stable, nontoxic compared to LiPF_6 , LiBF_4 and LiAsF_6 [1, 200- 204]. But it has major drawbacks such as poor ionic conductivity in non-aqueous solvents as compared to other Li- salts. The use of LiClO_4 as an electrolyte in LIBs is prohibited due to the high oxidation state of chlorine (VII) in the salt, which is a strong oxidant. This can make the LiClO_4 to react violently with most organic species at high temperature and high current rate of operation. The LiBF_4 is also not recommended because of its moderate ionic conductivity compared to other Li-salts and poor cycling efficiency, though it is less toxic, easy to handle and its anion, BF_4^- is stable against oxidation. The LiAsF_6 is highly

expensive and potentially carcinogenic, which restricts its use in LIBs. Thus, LiPF_6 emerged as the suitable salt for LIBs. It has a high melting point ($200\text{ }^\circ\text{C}$), high decomposition temperature ($T_d \sim 80\text{ }^\circ\text{C}$ in EC (ethylene carbonate) + DEC (diethyl carbonate)) and shows high ionic conductivity, $\sigma \sim 1 \times 10^{-2}\text{ S cm}^{-1}$ at $25\text{ }^\circ\text{C}$ for 1 M LiPF_6 in EC + DEC (50:50 vol.) [200]. However, it is toxic and expensive.

The solvents play an important role in deciding the performance of electrolytes. It has been established that organic carbonates are most suitable solvents for LIB [1, 200, 201, 204]. These carbonates are aprotic, polar and have high dielectric constant and hence can solvate the Li- salts at relatively high concentration ($> 1\text{ M}$) and provide a good ionic conduction. The solvents commonly used are propylene carbonate (PC: $\text{C}_4\text{H}_6\text{O}_3$), ethylene carbonate (EC: $\text{C}_3\text{H}_4\text{O}_3$) and other linear carbonates, like, diethyl carbonate (DEC: $\text{C}_5\text{H}_{10}\text{O}_3$), dimethyl carbonate (DMC: $\text{C}_3\text{H}_6\text{O}_3$) and ethylmethyl carbonate (EMC: $\text{C}_4\text{H}_8\text{O}_3$). Studies have shown that none of the single solvent fulfilled the requirements for LIBs and thus, a large number of solvent combinations were studied with different Li- salts. The most suitable solvent for LIB is the combination of EC with DEC, DMC or combination of both (1:1 by volume).

I.8.2. Solid Electrolytes

Solid electrolytes are also called fast ion conductors or superionic conductors in which the ion like, H^+ , Li^+ , Na^+ are highly mobile at temperature, $T \geq 25\text{ }^\circ\text{C}$. The Li- solid electrolytes are of special interest for application in LIBs. The Li- solid electrolyte contains a crystalline ceramic or a glassy network, in which the Li- ion moves through the interstitials or vacancies. The conductivity of solid electrolytes is $\sim 10^{-4} - 10^{-8}\text{ S cm}^{-1}$ at $25\text{ }^\circ\text{C}$ [1, 205-207].

The advantages of using Li- solid electrolytes for LIBs are: (i) They are single ion conductors, i.e., only Li - ion have an appreciable mobility, while the anions and other cations form a rigid network. (ii) They suppress the undesirable side reactions / decomposition of the electrolyte by eliminating the anionic concentration gradient across the electrolyte. (iii) They withstand high voltage operation (> 4.5 V) and high temperature (80 – 100 °C) operation due to the stability of ‘all-solid-state’ LIBs. Also, Li- metal can be used as the anode. (iv) The solid electrolyte - electrode interface has the added advantages of providing a dense, hard surface that maintains its integrity and inhibits roughening of the microstructure that leads to mossy or dendrite deposit of Li.

The solid electrolytes are divided into two categories, (i) ceramic (crystalline) electrolyte and (ii) glassy (amorphous) electrolyte.

I.8.2.1. Ceramic Electrolytes

Ceramic compounds in the form of oxides, halides, sulfides and nitrides with different crystal structures, are well studied as Li-ion conductors [1, 205-207]. They showed significant conductivity only at high temperature ($T > 200$ °C) due to their high activation energy. Among the oxides, perovskite (ABO_3)- type Li^+ - ion conductors attracted a lot of attention as ceramic electrolytes. ABO_3 (A, B are metal ions) compounds adopt a 3D- framework structure, with the vertex- sharing BO_6 octahedra and the A- ions occupy the 12- coordinate sites in the lattice [208]. Various cations can be substituted at the A- site without disturbing the parental crystal structure. The Li^+ - ion conductivity depends on various factors, such as: (i) degree of cationic ordering, (ii) Li^+ - ion and vacancy concentrations at the A- site, and (iii) size and symmetry of the unit cell. The perovskite compound, $La_{2/3-x}Li_{3x}\square_{1/3-2x}TiO_3$ [\square : A-site vacancy; $0 \leq x \leq 0.167$] shows

Li⁺ - ion conductivity (σ_i) as high as 10^{-3} S cm⁻¹ at room temperature. But the reduction of Ti⁴⁺ to Ti³⁺ (at $\sim 2.3 - 1.5$ V) during Li⁺-ion insertion causes predominant electronic conduction and hence may not be suitable for applications as electrolyte in LIBs [209].

The NASICON (sodium super-ionic conductor) - type Li- ion conductors of crystal structure, LiA₂(PO₄)₃ (A = Ge, Ti, Zr) are compounds of interest as electrolytes for LIBs [1, 210]. The crystal structure is made up of AO₆ octahedra and PO₄ tetrahedra, which form 3D- network with interconnected channels which are occupied by the Li- ions. The Al- doped composition, Li_{1.3}Al_{0.3}Ti_{1.7}(PO₄)₃ (LATP) showed σ_i (bulk) 3×10^{-3} S cm⁻¹ at 25 °C. The compound family with general formula, Li_{1+x}Ti_{2-x}M_x(PO₄)₃ (M = Al, Ga, In, Sc) have been investigated [211, 212]. All-solid-state LIBs with the above electrolytes have been fabricated and tested [213, 214].

The LISICON- type Li- ion conductors are another class of compounds with general formula, ABO₄ and a structure known as γ - Li₃PO₄, where BO₄ tetrahedra shares the corners with cluster of three AO₄ tetrahedra [1, 215]. The compound, Li_{2+2x}Zn_{1-x}GeO₄ was studied as electrolyte by Bruce and West [216]. The ionic conductivity of LISICON- type compounds are $\sim 10^{-6}$ S cm⁻¹ at 25 °C.

I.8.2.2. Glassy Electrolytes

The advantages of Li- containing glassy electrolytes are: (i) ease of fabrication, (ii) isotropic conductivity and (iii) absence of grain boundaries, which help in the enhancement of Li- ion conductivity. The Li- ion conducting glasses can be: oxides, oxynitrides, sulfides and oxysulfides [1, 215]. They are synthesized by adding the glass formers like SiO₂, SiS₂, B₂O₃ and P₂O₅ etc. along with the glass modifiers, such as Li₂O and Li₂S. However, the σ_i are $\sim 10^{-4} - 10^{-5}$ S cm⁻¹ at room temperature (RT). The sulfide

glasses show slightly higher σ_i ($>10^{-4}$ S cm $^{-1}$). The metastable and highly moisture-sensitive Li $_7$ P $_3$ S $_{11}$ showed $\sigma_i = 3.2 \times 10^{-3}$ S cm $^{-1}$ at RT [217].

Lithium phosphorous oxynitride (LIPON) was studied as glassy electrolyte for LIBs. The Li- ion defective γ - Li $_3$ PO $_4$ solid solution, with typical composition, Li $_{2.88}$ PO $_{3.73}$ N $_{0.14}$ in thin film form showed a $\sigma_i = 3.3 \times 10^{-6}$ S cm $^{-1}$ at RT [218]. LIBs with the above and with the sulfide solid electrolytes have been fabricated and tested [219]

I.8.3. Polymer Electrolytes

The Li- salts dissolved in polymers are of interest for LIBs. The desired properties of polymer Li- electrolytes are: (i) good mechanical stability, (ii) adequate Li- ion conductivity, (iii) high cationic mobility, (iv) good interfacial contact with electrode, (v) wide electrochemical stability, (vi) chemical and thermal stability and (vii) ease of processing. The polymer electrolytes are divided in to two groups: (a) Solid polymer electrolytes and (b) Gelled polymer electrolytes [1, 220].

I.8.3.1. Solid polymer electrolytes

Solid polymer electrolytes (SPEs) are made up of Li- salts (LiClO $_4$, LiXF $_6$ (X = As, P), LiBF $_4$, LiCF $_3$ SO $_3$ etc.) dissolved in high molecular weight polymers such as polyethylene oxide (PEO), polypropylene oxide (PPO) and polyvinylidene fluoride (PVDF), and these act as solid solvents [1, 220, 221]. Wright and co-workers were the first to discover that PEO can dissolve Li- salts and show ion conduction at ambient temperature [1, 220, 221]. The ionic motion in SPEs is closely associated with the local structural relaxations related to the glass transition temperature (T_g) of polymer [1, 220]. The lower the T_g , the better will be the σ_i since the SPE remains amorphous at RT. Many SPEs studied show $\sigma_i \sim 10^{-4}$ S cm $^{-1}$ at RT which is insignificant for applications in

LIBs. Some improvement in σ_i is reported by dispersing ceramic nano- particles such as SiO_2 , Al_2O_3 and TiO_2 in to the polymer matrix [205]. Also, the interfacial impedance present in both Li anode and composite cathode causes the ohmic losses in the electrolytes.

I.8.3.2. Gelled polymer electrolytes

To overcome the problems noticed in SPEs, gelled- polymer electrolytes (GPEs) were developed. These are obtained by incorporating a larger quantity of liquid plasticizers and/or organic solvents to the polymer matrix that is capable of forming a stable gel with the polymer host structure. They showed higher σ_i at RT due to the easier segmental motion of polymers, but poor mechanical stability compared to SPEs. The mechanical properties in GPEs are improved by addition of components, which lead to cross-linking [1, 220, 221]. These GPEs are attractive as electrolytes for plastic LIBs, as they show diffusive transport properties of liquid electrolytes and mechanical stability of SPEs. The safety-in-operation, electrochemical stability, and ionic conduction comparable to liquid electrolytes made these GPEs more closely to practical applications [205]. The commonly studied polymer systems are polymethyl methacrylate (PMMA), polyacrylonitrile (PAN), polyvinylidene fluoride (PVDF), polyvinyl chloride (PVC) and polyvinyl pyrrolidone (PVP). Among them, PAN- based polymer electrolytes have been extensively studied. The present- day LIBs found in cell phones contain the GPEs with LiPF_6 as the salt and PVDF-HFP and other polymers and some patented additives. They possess $\sigma_i \sim 10^{-3} \text{ S cm}^{-1}$ at RT.

I.9. Full cells (LIBs) with various cathodes and anodes

The first- generation commercial LIBs employed LiCoO_2 as cathode and specialty graphite (MCMB). Using the prospective second- generation cathodes and anodes described in earlier Sections, LIBs with 3.5/ 5 V- cathodes and $\text{Li}_4\text{Ti}_5\text{O}_{12}$ or Sn- based anodes have been fabricated and tested. Recently, the group of Scrosati [223] reported the fabrication and testing of $\text{Li}(\text{Ni}_{0.5}\text{Mn}_{1.5})\text{O}_4$ as the 5 V- cathode material with Sn-C as anode (~ 0.5 V vs. Li) and the gelled polymer as electrolyte. They reported a high capacity value of 120 mAhg^{-1} which is 82% of its theoretical capacity at C/3-rate ($1 \text{ C} = 0.2 \text{ Acm}^{-2}$) in the voltage range of 3.0 V- 5.0 V. The voltage vs. specific capacity profiles of the Li- ions cell are shown in Fig. I.12.

Studies were also reported in the literature using the anode material, $\text{Li}_4\text{Ti}_5\text{O}_{12}$ with the combination of cathodes like, $\text{LiNi}_{0.5}\text{Mn}_{1.5}\text{O}_4$ [224] and 3.5 V LiFePO_4 [225]. The SnO_2 was tested as anode in the cell using gel-type polymer electrolyte, and the mixed nickel-cobalt oxide cathode, $(\text{LiNi}_{0.8}\text{Co}_{0.2}\text{O}_2)$ [226].

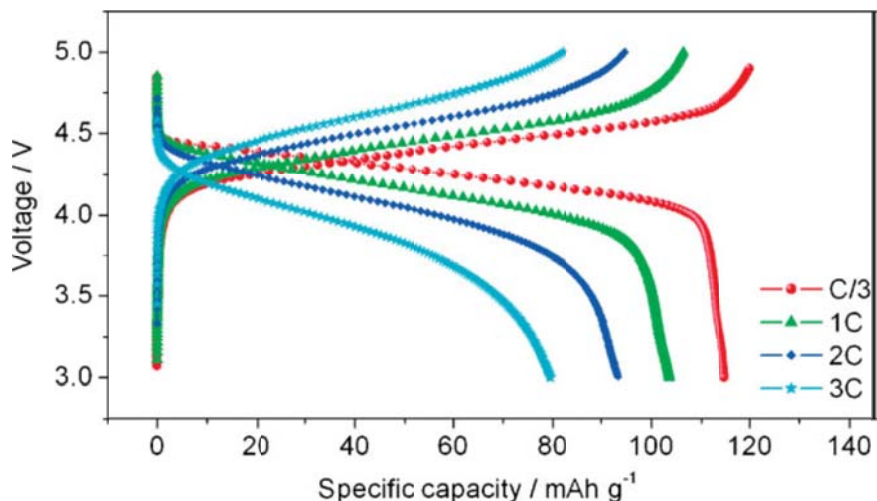


Fig. I.12 Voltage- capacity profiles of the Sn-C/GPE/ $\text{LiNi}_{0.5}\text{Mn}_{1.5}\text{O}_4$ Li- ion cell at various rates ($1\text{C} = 0.2 \text{ A cm}^{-2}$ with respect to the cathode mass) and at room temperature. Taken from [223].

Sony Co. introduced the second generation 14430- size LIB (total capacity; 900 mAh) known as ‘Naxelion’ in 2005, which has 30% higher than the MCMB- graphite. The LIB employed the amorphous Sn-Co-C as anode with the newly developed electrolyte and the mixture of $\text{Li}(\text{Ni}_{1/3}\text{Mn}_{1/3}\text{Co}_{1/3})\text{O}_2$ and LiCoO_2 as cathode.

Since the LIBs show promise for powering the hybrid electric vehicles (HEV) and plug-in hybrid vehicles (PHEVs), a wide variety of large- scale LIBs were assembled and tested (Table I.2).

Table. I.2. Selected LIB systems for PHEV. State of charge (SOC) and area specific impedance (ASI) are given. Taken from [227].

System	NCA- Graphite	LFP- Graphite	MS- TiO	MNS- TiO	MN- Graphite
Electrodes Positive Negative	$\text{LiNi}_{1/3}\text{Co}_{0.15}\text{Al}_{0.05}\text{O}_2$ Graphite	LiFePO_4 Graphite	LiMn_2O_4 $\text{Li}_4\text{Ti}_5\text{O}_{12}$	$\text{LiMn}_{1.5}\text{Ni}_{0.5}\text{O}_4$ $\text{Li}_4\text{Ti}_5\text{O}_{12}$	$\text{Li}_{1.2}\text{Mn}_{0.6}\text{Ni}_{0.2}\text{O}_2$ Graphite
Capacity, mAh/g Positive Negative	155 290	162 290	100 170	130 170	275 290
Voltage, 50% SOC	3.6	3.35	2.52	3.14	3.9
ASI for 10-s Pulse, $\text{ohm}\cdot\text{cm}^2$	25	25	9.2	100	25
Safety	Fair	Good	Excellent	Excellent	Excellent
Life Potential	Good	Good	Excellent	Unknown	Unknown
Cost	Moderate	Moderate	Low	Moderate	Moderate
Status	Pilot Scale	Pilot Scale	Develop.	Research	Research

I.10. Motivation for Present Study

As described in the previous Sections, there is a need to develop cheaper cathode and anode materials in order that the cost of LIBs can be brought down and make them easily adoptable for high energy applications like, HEV, PHEVs, power tools and

stationary power storage. The present work was undertaken to study the Li- cyclability of selected oxide materials and cobalt nitride (in thin films), which have not been reported in the literature. Specifically, hexagonal Mo_3 - cluster oxides, $\text{Li(Y/Ho)Mo}_3\text{O}_8$ and $\text{A}_2\text{Mo}_3\text{O}_8$ (A = Mn, Co, Zn) (Chapter III), hollandites- type tin oxides, $\text{K}_2(\text{M}_2\text{Sn}_6)\text{O}_{16}$ (M = Co, In) (Chapter V) and nano-composites $\text{SnO}(\text{V}_2\text{O}_3)_x$ ($x = 0, 0.25, 0.5$) and $\text{SnO}(\text{VO})_{0.5}$ (Chapter VI) and CoN thin films (Chapter IV) were examined. These compounds were synthesized by various methods and characterized by physical techniques, and their Li- storage and cycling properties were studied.

The Mo_3 - cluster compounds, $\text{Li(Y/Ho)Mo}_3\text{O}_8$ and $\text{A}_2\text{Mo}_3\text{O}_8$ (A = Mn, Co, Zn) were studied as anode materials (Chapter III), as they were expected to give a high capacity value based on the conversion reaction due to the reversible reaction of Mo and A atoms present in the compounds with Li and to know the effect of counter atoms on the Li- cycling for these iso-structural compounds. The unusual feature of these compounds is the presence of Mo_3 - cluster, in which Mo-Mo bond distance is less than that of Mo-Mo bonds in the Mo- metal. To study the Li- cycling behavior of such Mo_3 - cluster will be of interest.

The cobalt nitride, CoN (Chapter IV) was studied in thin film form as anode material due to its high theoretical capacity ($\sim 1100 \text{ mAhg}^{-1}$) based on conversion reaction and lower redox potential compared to metal oxides. The delithiated phase of CoN i.e. Co/ Li_3N is expected to give an excellent platform for reversible Li- reaction due to high Li- ion conductivity of Li_3N .

The Tin- based oxides and composites were studied as prospective anodes due to their high theoretical capacity values and lowering operating voltages. But, the large

volume variation during electrochemical cycling causes capacity degradation. This problem is addressed by various approaches: (i) reducing the particle size to nano; (ii) introducing electrochemically active/ inactive matrix elements; (iii) selecting suitable initial crystal structure and (iv) choosing a suitable upper cut-off voltage.

The Tin- hollandites (Chapter V) were studied as anodes as they have SnO_6 octahedral and tetragonal suitable crystal structure for Li- cycling. The delithiated phase of Tin- hollandites, i.e. $\text{K}_2\text{O-Co/In-Li}_2\text{O}$ was expected to provide a suitable platform for Li- cycling of Sn and buffer the large volume variation during alloy-de-alloy reaction of Sn to stabilize the capacity fading. The reduction of particle size of ball milled Tin- hollandites combined with the buffering effect of $\text{K}_2\text{O-Co/In-Li}_2\text{O}$ were expected to enhance the Li- cycling performance and help in stabilizing the capacity.

The nanocomposites, $\text{SnO}(\text{VO}_x)$ (Chapter VI) were studied as anodes as they were expected to give a high and stable capacity due to the simple formula (SnO), nanosize particles and presence of V_2O_3 and VO as matrices. The presence of V_2O_3 and VO , which show metallic nature at ambient conditions can provide a conducting pathway for Li and help in buffering the large volume variation of alloy-de-alloy reaction.

The above research work was carried out in partial fulfillment of the requirements for the Ph.D. degree. The work presented in the Thesis has been published in the open literature. The work reported by others in the literature has been duly acknowledged and the Thesis contains more than 350 references, many of them being recent. The training received by me in the research methodology is of great significance to me and I hope that the present research results will add to the existing knowledge of the materials aspects of LIB.

References

- [1] G. A. Nazri, G. Pistoia (eds.), 'Lithium batteries-science and technology', Kluwer Academic., New York, 2003.
- [2] J. O. Besenhard, in 'Handbook of batteries', John Willey, 1998.
- [3] W. A. Van Schalkwijk, B. Scrosati (eds.), 'Advances in lithium-ion batteries', Kluwer Academic /Plenum, New York, 2002.
- [4] D. Linden, T. B. Reddy (eds.), in 'Handbook of batteries', 3rd edition, McGraw Hill 2002.
- [5] K. Ozawa (ed.), in 'Lithium ion rechargeable batteries', Wiley-VCH, 2010.
- [6] <http://www.batteryuniversity.com>.
- [7] Y. Nishi, The Chemical Record 1 (2001) 406.
- [8] J.-M. Tarascon, M. Armand, Nature 414 (2001) 359.
- [9] M. Armand, J.-M. Tarascon, Nature 451 (2008) 652.
- [10] B. Scrosati, J. Garche, J. Power Sources 195 (2010) 2419.
- [11] M. Lazzari, B. Scrosati, J. Electrochem. Soc. 127 (1980) 773.
- [12] D. W. Murphy, F. J. DiSalvo, J. N. Carides, J. V. Waszczak, Mat. Res. Bull. 13 (1978) 1395.
- [13] www.varta-automotive.com.
- [14] <http://www.dimec.unisa.it>
- [15] A. Manthiram, J. Kim, Chem. Mater. 10 (1998) 2895.
- [16] M. S. Whittingham, Chem. Rev. 104 (2004) 4271.
- [17] C. Li, H.P. Zhang, L.J. Fu, H. Liu, Y.P. Wu, E. Rahm, R. Holze, H.Q. Wu, Electrochim. Acta 51 (2006) 3872.

- [18] T. Ohzuku, R. J. Brodd, *J. Power Sources* 174 (2007) 449.
- [19] J. B. Goodenough, Y. Kim, *Chem. Mater.* 22 (2010) 587.
- [20] B. L. Ellis, K. T. Lee, L. F. Nazar, *Chem. Mater.* 22 (2010) 691.
- [21] J. W. Fergus, *J. Power Sources* 195 (2010) 939.
- [22] G. Amatucci, J.-M. Tarascon, *J. Electrochem. Soc.* 149 (2002) K31.
- [23] A. K. Padhi, K. S. Nanjundaswamy, J. B. Goodenough, *J. Electrochem. Soc.* 144 (1997) 1188.
- [24] J. Barker, M. Y. Saidi, J. L. Swoyer, *J. Electrochem. Soc.* 150 (2003) A1394.
- [25] M. V. Reddy, G. V. Subba Rao, B.V.R. Chowdari, in ‘Solid State Ionics: Fundamental researches and technological applications’ [Proceedings of the 12th Asian conference on solid state ionics], (eds) B. V. R. Chowdari et al., Wuhan Univ. of Technol. Press, Wuhan, China, 2010. pp. 497-506.
- [26] K. West, G. Vitins, R. Koksang, *Electrochim. Acta* 45 (2000) 3141.
- [27] C. Sigala, D. Guyomard, A. Verbaere, Y. Piffard, M. Tournoux, *Solid State Ionics* 81 (1995) 167.
- [28] R. Santhanam, B. Rambabu, *J. Power Sources* 195 (2010) 5442.
- [29] G. Q. Liu, L. Wen, G. Y. Liu, Y. W. Tian, *J. Alloys Compnds.* 501 (2010) 233.
- [30] F. Zhou, M. Cococcioni, C. A. Marianetti, D. Morgan, G. Ceder, *Phys. Rev. B* 70 (2004) 235121.
- [31] T. Doi, H. Fukudome, S. Okada, J. Yamaki, *J. Power Sources* 174 (2007) 779.
- [32] N. A. Kaskhedikar, J. Maier, *Adv. Mater.* 21 (2009) 2664.
- [33] B. J. Landi, M. J. Ganter, C. D. Cress, R. A. DiLeo, R. P. Raffaele, *Energy Environ. Sci.* 2 (2009) 638.

- [34] G. Mourine, Ch. Bousquet, F. Henn, P. Bernier, R. Almairac, B. Simon, *Chem. Phys. Lett.* 312 (1999) 14.
- [35] H.-C. Shin, M. Liu, B. Sadanadan, A. M. Rao, *J. Power Sources* 112 (2002) 216.
- [36] B. Gao, A. Kleinhammes, X. P. Tang, C. Bower, L. Fleming, Y. Wu, O. Zhou, *Chem. Phys. Lett.*, 307 (1999) 153.
- [37] E. Yoo, J. Kim, E. Hosono, H.-S. Zhou, T. Kudo, I. Honma, *Nano Lett.* 8 (2008) 2277.
- [38] D. Pan, S. Wang, B. Zhao, M. Wu, H. Zhang, Y. wang, Z. Jiao, *Chem. Mater.* 21 (2009) 3136.
- [39] J. Yao, G. X. Wang, J.-H. Ahn, H. K. Liu, S. X. Dou, *J. Power Sources* 114 (2003) 292.
- [40] Y. F. Tang, L. Yang, Z. Qiu, J. S. Huang, *Electrochem. Commun.* 10 (2008) 1513.
- [41] Y. Wang, H. Liu, K. Wang, H. Eiji, Y. Wang, H. Zhou, *J. Mater. Chem.* 19 (2009) 6789.
- [42] H. F. Xiang, Q. Y. Jin, R. Wang, C. H. Chen, X. W. Ge, *J. Power Sources* 179 (2008) 351.
- [43] K. Ariyoshi, S. Yamamoto, T. Ohzuku, *J. Power Sources* 119-121 (2003) 959.
- [44] Z. Yang, D. Choi, S. Kerisit, K. M. Rosso, D. Wang, J. Zhang, G. Graff, J. Liu, *J. Power Sources* 192 (2009) 588.
- [45] J. Chen, L. Yang, Y. Tang, *J. Power Sources*, 195 (2010)6893
- [46] N. A. Chernova, M. Roppolo, A. C. Dillon, M. S. Whittingham, *J. Mater. Chem.*, 19 (2009) 2526.
- [47] S-H. Lee, Y.-H. Kim, R. Deshpande, P. A. Parilla, E. Whitney, D. T. Gillaspie, K. M.

- Jones, A. H. Mahan, S. Zhang, A. C. Dillon, *Adv. Mater.* 20 (2008) 3627.
- [48] M. Wei, K. Wei, M. Ichihara, H. Zhou, *Electrochem. Commun.* 10 (2008) 980.
- [49] R.A. Huggins, *J. Power Sources* 81-82 (1999) 13.
- [50] M. Winter, J.O. Besenhard, *Electrochem. Acta* 45 (1999) 31.
- [51] A. D. W. Todd, P.P. Ferguson, M. D. Fleischauer, J. R. Dahn, *Int. J. Energy Res.* 34 (2010) 535.
- [52] U. Kasavajjula, C. Wang, A. J. Appleby, *J. Power Sources* 163 (2007) 1003.
- [53] D. Larcher, S. Beattie, M. Morcrette, K. Edstrom, J.-C. Jumas, J.-M. Tarascon, *J. Mater. Chem.* 17 (2007) 3759.
- [54] C. K. Chan, H. Peng, G. Liu, K. Mcilwrath, X. F. Zhang, R. A. Huggins, Y. Cui, *Nat. Nanotechnol.* 3 (2008) 31.
- [55] H. Kim, M. Seo, M.-H. Park, J. Cho, *Angew. Chem. Int. Ed.* 49 (2010) 2146.
- [56] K. Kang, H.-S. Lee, D.-W. Han, G.-S. Kim, D. Lee, G. Lee, Y.-M. Kang, M.-H. Jo, *Appl. Phys. Lett.* 96 (2010) 053110.
- [57] J. Wolfenstine, *J. Power Sources* 124 (2003) 241.
- [58] T.D. Hatchard, M. N. Obrovac, J. R. Dahn, *J. Electrochem. Soc.* 153 (2006) A282.
- [59] A. Magasinski, P. Dixon, B. Hertzberg, A. Kvit, J. Ayala, G. Yushin, *Nature Mater.* 9 (2010) 353.
- [60] C. M. Park, W. Choi, Y. Hwa, J.-H. Kim, G. Jeong, H.- J. Sohn, *J. Mater. Chem.* 20 (2010) 4854
- [61] T. Zhang, J. Gao, H.P. Zhang, L.C. Yang, Y.P. Wu, H.Q. Wu, *Electrochem. Commun.* 9 (2007) 886.
- [62] R. Alcántara, G. Ortiz, I. Rodríguez, J. L. Tirado, *J. Power Sources* 189 (2009) 309.

- [63] P. P. Ferguson, M. L. Martine, R. A. Dunlap, J. R. Dahn, *Electrochim. Acta* 54 (2009) 4534.
- [64] J. Hassoun, G. Derrien, S. Panero, B. Scrosati, *Adv. Mater.* 20 (2008) 3169.
- [65] C.-M. Park, H.-J. Sohn, *Electrochim. Acta* 54 (2009) 6367.
- [66] G. Cui, Y. -S. Hu, L. Zhi, D. Wu, I. Lieberwirth, J. Maier, K. Mullen, *Small* 3 (2007) 2066.
- [67] Y. Wang, M. Wu, Z. Jiao, J. Y. Lee, *Chem. Mater.* 21 (2009) 3210.
- [68] J. W. Zheng, S. M. L. Nai, M.-F. Ng, P. Wu, J. Wei, M. Gupta, *J. Phys. Chem. C* 113 (2009) 14015.
- [69] P. P. Ferguson, M. Rajora, R. A. Dunlap, J. R. Dahn, *J. Electrochem. Soc.* 156 (2009) A204.
- [70] A. D. W. Todd, R. E. Mar, J. R. Dahn, *J. Electrochem. Soc.* 154 (2007) A597.
- [71] Y. Tian, A. Timmons, J. R. Dahn, *J. Electrochem. Soc.* 156 (2009) A187.
- [72] L. Trahey, J. T. Vaughey, H. H. Kung, M. M. Thackeray, *J. Electrochem. Soc.* 156 (2009) A385.
- [73] J.-J. Zhang, X. Zhang, Y. Xia, *J. Electrochem. Soc.* 154 (2007) A7.
- [74] J.-J. Zhang, Y. M. Zhang, X. Zhang, Y. Xia, *J. Power Sources* 167 (2007) 171.
- [75] S. Matsuno, M. Noji, T. Kashiwagi, M. Nakayama, M. Wakihara, *J. Phys. Chem. C* 111 (2007) 7548.
- [76] C. M. Park, H. J. Sohn, *Adv. Mater.* 22 (2010) 47.
- [77] Y. Idota, T. Kubota, A. Matsufuji, Y. Maekawa, T. Miyasaka, *Science* 276 (1997) 1395.
- [78] C. Li, Z. Yu, S. Fang, H. Wang, Y. Gui, J. Xu, R. Chen, *J. Alloys Compds.* 475

- (2009) 718.
- [79] Q. Pan, Z. Wang, J. Liu, G. Yin, M. Gu, *Electrochem. Commun.* 11 (2009) 917.
- [80] W.-H. Ho, C.-F. Li, H.-C. Liu, S.-K. Yen, *J. Power Sources* 175 (2008) 897.
- [81] H. Bryngelsson, J. Eskhult, L. Nyholm, M. Herranen, O. Alm, K. Edstrom, *Chem. Mater.* 19 (2007) 1170.
- [82] J. Ning, Q. Dai, T. Jiang, K. Men, D. Liu, N. Xiao, C. Li, D. Li, B. Liu, B. Zou, G. Zou, W. W. Yu, *Langmuir* 25 (2009) 1818.
- [83] Y. D. Ko, J. G. Kang, J. G. Park, S. Lee, D. W. Kim, *Nanotechnol.* 20 (2009) 455701.
- [84] H. Li, X. Huang, L. Chen, *Electrochem. Solid-State Lett.* 1 (1998) 241.
- [85] H. Uchiyama, E. Hosono, I. Honma, H. Zhou, H. Imai, *Electrochem. Commun.* 10 (2008) 52.
- [86] D. Aurbach, A. Nimberger, B. Markovsky, E. Levi, E. Sominski, A. Gedanken, *Chem. Mater.* 14 (2002) 4155.
- [87] C. Kim, M. Noh, M. Choi, J. Cho, B. Park, *Chem. Mater.* 17 (2005) 3297.
- [88] Y. Wang, M. Wu, Z. Jiao, J. Y. Lee, *Nanotechnol.* 20(2009) 345704.
- [89] C. L. Zhu, M. L. Zhang, Y. J. Qiao, P. Gao, Y. J. Chen, *Mater. Res. Bull.* 45 (2010) 437.
- [90] G. Du, C. Zhong, P. Zhang, Z. Guo, Z. Chen, H. Liu, *Electrochim. Acta* 55(2010) 2582.
- [91] S. Yang, H. Song, H. Yi, W. Liu, H. Zhang, X. Chen, *Electrochim. Acta* 55 (2009) 521.
- [92] C. Li, W. Wei, S. Fang, H. Wang, Y. Zhang, Y. Gui, R. Chen, *J. Power Sources* 195

- (2010) 2939.
- [93] N. H. Zhao, L. C. Zhang, G. J. Wang, B. D. Yao, Y. P. Wu, *Mater. Lett.* 64 (2010) 972.
- [94] X. Ji, X. Huang, J. Liu, J. Jiang, X. Li, R. Ding, Y. Hu, F. Wu, Q. Li, *Nanoscale Res. Lett.* 5 (2010) 649.
- [95] J. S. Chen, Y. L. Cheah, Y. T. Chen, N. Jayaprakash, S. Madhavi, Y. H. Yang, X. W. Lou, *J. Phys. Chem. C* 113 (2009) 20504.
- [96] F. M. Courtel, E. A. Baranova, Y. A. Lebdeh, I. J. Davidson, *J. Power Sources* 195 (2010) 2355.
- [97] I. Sandu, T. Brousse, D. M. Schleich, M. Danot, *J. Solid State Chem.* 177 (2004) 4332.
- [98] Y. Sharma, N. Sharma, G. V. Subba Rao, B. V. R. Chowdari, *J. Power Sources* 192 (2009) 627.
- [99] P. A. Connor, J. T. S. Irvine, *J. Power Sources* 97-98 (2001) 223.
- [100] P. A. Connor, J. T. S. Irvine, *Electrochim. Acta* 47 (2002) 2885.
- [101] X. Hou, Q. Cheng, Y. Bai, W.F. Zhang, *Solid State Ionics* 181 (2010) 631.
- [102] G. Wang, X.P. Gao, P.W. Shen, *J. Power Sources* 192 (2009) 719.
- [103] S. Lei, K. Tang, C. Chen, Y. Jin, L. Zhou, *Mater. Res. Bull.* 44 (2009) 393.
- [104] N. Sharma, K. M. Shaju, G. V. Subba Rao, B. V. R. Chowdari, *Electrochem. Commun.* 4 (2002) 947.
- [105] N. Sharma, K. M. Shaju, G. V. Subba Rao, B. V. R. Chowdari, *J. Power Sources* 139 (2005) 250.
- [106] I. A. Courtney, J. R. Dahn, *J. Electrochem. Soc.* 144 (1997) 2045.

- [107] Y. Sharma, N. Sharma, G. V. Subba Rao, B. V. R. Chowdari, *Chem. Mater.* 20 (2008) 6829.
- [108] F. Huang, Z. Yuan, H. Zhan, Y. Zhou, J. Sun, *Mater. Chem. Phys.* 83 (2004) 16.
- [109] M. Behm, J. T. S. Irvine, *Electrochim. Acta* 47 (2002) 1727.
- [110] N. Sharma, J. Plevert, G. V. Subba Rao, B. V. R. Chowdari, T. J. White, *Chem. Mater.* 17 (2005) 4700.
- [111] N. Sharma, G. V. Subba Rao, B. V. R. Chowdari, *J. Power Sources* 159 (2006) 340
- [112] D. Deng, J. Y. Lee, *Chem. Mater.* 20 (2008) 1841.
- [113] X. W. Lou, D. Deng, J. Y. Lee, L. A. Archer, *Chem. Mater.* 20 (2008) 6562.
- [114] P. G. Bruce, B. Scrosati, J.-M. Tarascon, *Angew. Chem. Int. Ed.* 47 (2008) 2930.
- [115] J. Graetz, C. C. Ahn, R. Yazami, B. Fultz, *Electrochem. Solid State Lett.* 6 (2003) A194.
- [116] S. Yoon, A. Manthiram, *Chem. Mater.* 21 (2009) 3898.
- [117] H. Li, X. Huang, L. Chen, *Solid State Ionics* 123 (1999) 189.
- [118] M.-Z. Xue, Z.-W. Fu, *Electrochem. Commun.* 8 (2006) 1250.
- [119] Y. Hu, H. Zhang, H. Yang, *J. Alloys Compds.* 428 (2007) 327.
- [120] P. Poizot, S. Laruelle, S. Grugeon, L. Dupont, J.-M. Tarascon, *Nature* 407 (2000) 496.
- [121] P. Poizot, S. Laruelle, S. Grugeon, L. Dupont, J.-M. Tarascon, *J. Power Sources* 97-98 (2001) 235.
- [122] F. Badway, I. Plitz, S. Grugeon, S. Laruelle, M. Dolle, A. S. Gozdz, J.-M. Tarascon, *Electrochem. Solid-State Lett.* 5 (2002) A115.
- [123] S. Grugeon, S. Laruelle, L. Dupont, J.-M. Tarascon, *Solid State Sci.* 5 (2003)

895.

- [124] S. Laruelle, S. Grugeon, P. Poizot, M. Dolle, L. Dupont, J.-M. Tarascon, J. Electrochem. Soc. 149 (2002) A 627.
- [125] J. Chen, L. Xu, W. Li, X. Gou, Adv. Mater. 17 (2005) 582.
- [126] M. V. Reddy, T. Yu, C. H. Sow, Z. X. Shen, C. T. Lim, G. V. Subba Rao, B. V. R. Chowdari, Adv. Funct. Mater. 17 (2007) 2792.
- [127] J. Li, H. M. Dahn, L. J. Krause, D.-B. Le, J. R. Dahn, J. Electrochem. Soc. 155 (2008) A812.
- [128] H. Liu, G. Wang, J. Park, J. Wang, H. Liu, C. Zhang, Electrochim. Acta 54 (2009) 1733.
- [129] M. F. Hassan, M. M. Rahman, Z. P. Guo, Z. X. Chen, H. K. Liu, Electrochim. Acta 55 (2010) 5006.
- [130] M.-S. Wu, Y.-H. Ou, Y.-P. Lin, Electrochim. Acta 55 (2010) 3240.
- [131] Y. Lu, Y. Wang, Y. Zou, Z. Jiao, B. Zhao, Y. He, M. Wu, Electrochem. Commun. 12 (2010) 101.
- [132] J. Wang, G. Du, R. Zeng, B. Niu, Z. Chen, Z. Guo, S. Dou, Electrochim. Acta 55 (2010) 4805.
- [133] X. W. Lou, D. Deng, J. Y. Lee, L. A. Archer, J. Mater. Chem. 18 (2008) 4397.
- [134] W.-Y. Li, L.-N. Xu, J. Chen, Adv. Funct. Mater. 15 (2005) 851.
- [135] Y. Li, B. Tan, Y. Wu, Nano Lett. 8 (2008) 265.
- [136] <http://www.irm.umn.edu>
- [137] P. L. Taberna, S. Mitra, P. Poizot, P. Simon, J.-M. Tarascon, Nature Mater. 5 (2006) 567.

- [138] H. Liu, G. Wang, J. Wang, D. Wexler, *Electrochem. Commun.* 10 (2008) 1879.
- [139] L. Wang, Y. Yu, P. C. Chen, D. W. Zhang, C. H. Chen, *J. Power Sources* 183 (2008) 717.
- [140] T. Muraliganth, A.V. Murugan, A. Manthiram, *Chem. Commun.* (2009) 7360.
- [141] B. Varghese, M. V. Reddy, Z. Yanwu, C. S. Lit, T. C. Hoong, G. V. Subba Rao, B. V. R. Chowdari, A. T. S. Wee, C. T. Lim, C.-H. Sow, *Chem. Mater.* 20 (2008) 3360.
- [142] M. A. Dar, S. H. Nam, Y. S. Kim, W. B. Kim, *J. Solid State Electrochem.* 2010 (In press).
- [143] C. Q. Zhang, J. P. Tu, Y. F. Yuan, X. H. Huang, X. T. Chen, F. Mao, *J. Electrochem. Soc.* 154 (2007) A65.
- [144] Y. Li, B. Tan, Y. Wu, *Chem. Mater.* 20 (2008) 567.
- [145] R. Li, C.- Y. Liu, *Mater. Res. Bull.* 45 (2010) 688.
- [146] Q.Gao, L. Yang, X. Lu, J. Mao, Y. Zhang, Y. Wu, Y. Tang, *J. Mater. Chem.* 20 (2010) 2807.
- [147] P. Balaya, H. Li, L. Kienle, J. Maier, *Adv. Funct. Mater.* 13 (2003) 621.
- [148] Y. Sharma, N. Sharma, G. V. Subba Rao, B. V. R. Chowdari, *Solid State Ionics* 179 (2008) 587.
- [149] A. Thissen, D. Ensling, F. J. F. Madrigal, W. Jaegermann, R. Alcantara, P. Lavela, J. L. Tirado, *Chem. Mater.* 17 (2005) 5202.
- [150] P. Lavela, J.L. Tirado, C. Vidal-Abarca, *Electrochim. Acta* 52 (2007) 7986.
- [151] Y. Sharma, N. Sharma, G. V. Subba Rao, B. V. R. Chowdari, *J. Power Sources* 173 (2007) 495.
- [152] Y. Sharma, N. Sharma, G. V. Subba Rao, B. V. R. Chowdari, *Adv. Funct. Mater.*

17 (2007) 2855.

- [153] P. Lavela, J.L. Tirado, *J. Power Sources* 172 (2007) 379.
- [154] Y. Sharma, N. Sharma, G. V. Subba Rao, B. V. R. Chowdari, *Electrochim. Acta* 53 (2008) 2380.
- [155] Y. Sharma, N. Sharma, G. V. Subba Rao, B. V. R. Chowdari, *Bull. Mater. Sci. (India)* 32 (2009) 295.
- [156] M. V. Reddy, A. Levasseur, *J. Electroanal. Chem.* 639 (2010) 27.
- [157] X. Han, W. Tang, Z. Yi, J. Sun, *J. Appl. Electrochem.* 38 (2008)1671.
- [158] J. Shirakawa, M. Nakayama, H. Ikuta, Y. Uchimoto, M. Wakihara, *Electrochem. Solid-State Lett.* 7 (2004) A27.
- [159] L. Xiao, Y. Zhao, J. Yin, L. Zhang, *Chem. Eur. J.* 15 (2009)9442.
- [160] S. Denis, E. Baudrin, M. Touboul, J.- M. Tarascon, *J. Electrochem. Soc.* 144 (1997) 4099.
- [161] P. Poizot, E. Baudrin, S. Laruelle, L. Dupont, M. Touboul, J. M. Tarascon, *Solid State Ionics* 138 (2000) 31.
- [162] S. S. Kim, S. Ogura, H. Ikuta, Y. Uchimoto, M. Wakihara, *Solid State Ionics* 146 (2002) 249.
- [163] N. N. Leyzerovich, K. G. Bramnik, T. Buhrmester, H. Ehrenberg, H. Fuess, *J. Power Sources* 127 (2004) 76.
- [164] N. Sharma, K. M. Shaju, G. V. Subba Rao, B. V. R. Chowdari, Z. L. Dong, T. J. White, *Chem. Mater.* 16 (2004) 504.
- [165] D. Hara, H. Ikuta, Y. Uchimoto, M. Wakihara, *J. Mater. Chem.* 12 (2002) 2507.
- [166] D. Hara, J. Shirakawa, H. Ikuta, Y. Uchimoto, M. Wakihara, T. Miyanaga, I.

- Watanabe, J. Mater. Chem. 13 (2003) 897.
- [167] L. F. Nazar, G. Goward, F. Leroux, M. Duncan, H. Huang, T. Kerr, J. Gaubicher, Intl. J. Inorg. Mater. 3 (2001) 191.
- [168] N. Sharma, K. M. Shaju, G. V. Subba Rao, B. V. R. Chowadari, J. Power Sources 124 (2003) 204.
- [169] N. Sharma, K. M. Shaju, G. V. Subba Rao, B. V. R. Chowadari, Electrochim. Acta 49 (2004) 1035.
- [170] T. Lapp, S. Skaarup, A. Hooper, Solid State Ionics 11 (1983) 97.
- [171] J.B. Bates, N.J. Dudney, B. Neudecker, A. Ueda, C.D. Evans, Solid State Ionics 135 (2000) 33.
- [172] L. Baggetto, N. A. M. Verhaegh, R. A. H. Niessen, F. Roozeboom, J. C. Jumas, P. H. L. Notten, J. Electrochem. Soc. 157 (2010) A340.
- [173] N. Pereira, L. C. Klein, G. G. Amatucci, J. Electrochem. Soc. 149 (2002) A262.
- [174] N. Pereira, M. Balasubramanian, L. Dupont, J. McBreen, L. C. Klein, G. G. Amatucci, J. Electrochem. Soc. 150 (2003) A1118.
- [175] N. Pereira, L. Dupont, J.- M. Tarascon, L. C. Klein, G. G. Amatucci, J. Electrochem. Soc. 150 (2003) A1273.
- [176] Z.-W. Fu, Y. Wang, X.-L. Yue, S.-L. Zhao, Q.-Z. Quin, J. Phys. Chem. B, 108 (2004) 2236.
- [177] Y. Wang, Z.-W. Fu, X.-L. Yue, Q.-Z. Quin, J. Electrochem. Soc. 151 (2004) E162.
- [178] Q. Sun, Z.-W. Fu, Electrochem. Solid-State Lett. 10 (2007) A189.
- [179] Q. Sun, Z.-W. Fu, Electrochem. Acta 54 (2008) 403.
- [180] M. Nishijima, T. Kagohashi, M. Imanishi, Y. Takeda, O. Yamamoto, S. Kondo,

- Solid State Ionics 83 (1996) 107.
- [181] N. Nishijima, T. Kagohashi, Y. Takeda, M. Imanishi, O. Yamamoto, J. Power Sources 68 (1997) 510.
- [182] T. Shodai, S. Okada, S. Tobishima, J. Yamaki, Solid State Ionics 86-88 (1996) 785.
- [183] T. Shodai, S. Okada, S. Tobishima, J. Yamaki, J. Power Sources 68 (1997) 515.
- [184] Y. Liu, T. Mastumura, Y. Ono, N. Imanishi, A. Hirano, Y. Takeda, Solid State Ionics 179 (2008) 2069.
- [185] Y. Liu, T. Matsumura, N. Imanishi, T. Ichikawa, A. Hirano, Y. Takeda, Electrochem. Commun. 6 (2004) 632.
- [186] M. V. V. M. S. Kishore, U. V. Varadaraju, J. Power Sources 156 (2006) 594.
- [187] D. C. S. Souza, V. Pralong, A. J. Jacobson, L. F. Nazar, Science 296 (2002) 2012.
- [188] D. C. C. Silva, O. Crosnier, G. Ouvrard, J. Greedan, A. S.-Sefat, L. F. Nazar, Electrochem. Solid-State Lett. 6 (2003) A162.
- [189] R. Alcantara, J.L. Tirado, J.C. Jumas, L. Monconduit, J. O-. Fourcade, J. Power Sources 109 (2002) 308.
- [190] J. -W. Seo, J.-T. Jang, S.-W. Park, C. Kim, B. Park, J. Cheon, Adv. Mater. 20 (2008) 4269.
- [191] Y. Kim, K.-S. Park, S.-H. Song, J. Han, J. B. Goodenough, J. Electrochem. Soc. 156 (2009) A703.
- [192] J. M. Yan, H. Z. Huang, J. Zhang, Z. J. Liu, Y. Yang, J. Power Sources 146 (2005) 264.
- [193] F. Badway, N. Pereira, F. Cosandey, G. G. Amatucci, J. Electrochem. Soc. 150

- (2003) A1209.
- [194] H. Li, P. Balaya, J. Maier, *J. Electrochem. Soc.* 151 (2004) A1878.
- [195] M. V. Reddy, S. Madhavi, G. V. Subba Rao, B. V. R. Chowdari, *J. Power Source* 162 (2006) 1312.
- [196] Y. Oumellal, A. Rougier, G. A. Nazri, J.-M. Tarascon, L. Aymard, *Nature Mater.* 7 (2008) 916.
- [197] M. J. Aragon, C. P. –Vicente, J. L. Tirado, *Electrochem. Comm.* 9 (2007) 1744.
- [198] Y. Sharma, N. Sharma, G. V. Subba Rao, B. V. R. Chowdari, *J. Mater. Chem.* 19 (2009) 5047.
- [199] M. J. Aragon, B. Leon, C. P. Vicente, J. L. Tirado, *Inorg. Chem.* 47 (2008) 10366.
- [200] K. Xu, *Chem. Rev.* 104 (2004) 4303.
- [201] D. Aurbach (ed.), ‘Non-aqueous electrochemistry’, Marcel Dekker, Inc., New York, 1999.
- [202] D. Aurbach, Y. Talyosef, B. Markovsky, E. Markevich, E. Zinigrad, L. Asraf, J. S. Gnanaraj, H.-J. Kim, *Electrochim. Acta* 50 (2004) 247.
- [203] A. Lewandowski, A. S.-Mocek, *J. Power Sources* 194 (2009) 601.
- [204] M. Armand, F. Endres, D. R. McFarlane, H. Ohno, B. Scrosati, *Nature Mater.* 8 (2009) 621.
- [205] J. W. Fergus, *J. Power Sources* 195 (2010) 4554.
- [206] A. D. Robertson, A. R. West, A. G. Ritchie, *Solid State Ionics* 104 (1997) 1.
- [207] T. Minami, M. Tatsumisago, M. Wakihara, C. Iwakura, S. Kohjiya, I. Tanaka (eds.), ‘Solid State Ionics for Batteries’, Springer-Verlag, Tokyo, 2005.
- [208] J. L. Fourquet, H. Duroy, M. P. Crosnier-Lopez, *J. Solid State Chem.*, 127 (1996)

283.

- [209] V. Thangadurai, W. Weppner, *J. Am. Ceram. Soc.* 88 (2005) 411.
- [210] V. Thangadurai, W. Weppner, *Ionics* 12 (2006) 81.
- [211] C. J. Leo, G. V. Subba Rao, B. V. R. Chowdari, *J. Mater. Chem.* 12 (2002) 1848.
- [212] K. Arbi, J. M. Rojo, J. Sanz, *J. Eur. Ceram. Soc.* 27 (2007) 4215.
- [213] M. Kotobuki, Y. Suzuki, H. Munakata, K. Kanamura, Y. Sato, K. Yamamoto, T. Yoshida, *J. Power Sources* 195 (2010) 5784.
- [214] J. E. Trevey, Y. S. Jung, S.-H. Lee, *J. Power Sources* 195 (2010) 4984.
- [215] P. Knauth, *Solid State Ionics* 180 (2009) 911.
- [216] P. G. Bruce, A. R. West, *J. Solid State Chem.* 53 (1984) 430.
- [217] F. Mizuno, A. Hayashi, K. Tadanaga, M. Tatsumisago, *Adv. Mater.* 17 (2005) 918.
- [218] J. B. Bates, N. J. Dudney, G. R. Gruzalski, R. A. Zuhr, A. Choudhury, C. F. Luck, *Solid State Ionics* 53-56 (1992) 647.
- [219] S. H. Jee, M.- J. Lee, H. S. Ahn, D.- J. Kim, J. W. Choi, S. J. Yoon, S. C. Nam, S. H. Kim, Y. S. Yoon, *Solid State Ionics* 181 (2010) 902.
- [220] W. H. Mayer, *Adv. Mater.* 10 (1998) 439.
- [221] A. M. Stephan, *Eur. Polymer J.* 42 (2006) 21.
- [222] J. Y. Song, Y. Y. Wang, C. C. Wan, *J. Power Sources* 77(1999) 183.
- [223] J. Hassoun, S. Panero, P. Reale, B. Scrosati, *Adv. Mater.* 21 (2009) 4807.
- [224] H. F. Xiang, Q. Y. Jin, R. Wang, C. H. Chen, X. W. Ge, *J. Power Sources* 179 (2008) 351.
- [225] A. Jaiswal, C. R. Horne, O. Chang, W. Zhang, W. Kong, E. Wang, T. Chern, M. M. Doeff, *J. Electrochem. Soc.* 156 (2009) A1041.

[226] S. Panero, G. Savo, B. Scrosati, *Electrochem. Solid- State Lett.* 2 (1999) 365.

[227] <http://www.transportation.anl.gov>

Chapter II

Experimental Techniques

Abstract

The experimental techniques used and their principle there of, in the synthesis and characterization of compounds as anode materials are described in this Chapter. The details of coin cell fabrication incorporating these materials as the test electrodes and the electrochemical characterization are also presented.

II.1. Introduction

In this Chapter, a brief description of methods and principle involved in synthesis, characterization of metal oxides, metal nitrides and composites are presented. Conventional high temperature solid-state reaction, nitridation, carbothermal reduction, high energy ball-milling of component oxides and RF magnetron sputtering have been adopted for the synthesis of compounds. The physical characterization by way of powder X-ray diffraction (XRD), scanning electron microscopy (SEM), high- resolution transmission electron microscopy (HR-TEM), X-ray photoelectron spectroscopy (XPS), Fourier transform infrared spectroscopy (FT-IR), Raman spectroscopy, density measurement and BET surface area measurement were carried out. In selected cases, elemental analysis was conducted by inductively coupled plasma- optical emission spectroscopy (ICP-OES) technique. The electrochemical characterizations like galvanostatic cycling, cyclic voltammetry and electrochemical impedance spectroscopy (EIS) were performed.

II.2. Synthesis of Materials

The conventional high temperature solid- state reaction method was employed to prepare the Sn-based hollandite oxides [1]. The stoichiometric quantities of metal oxides/ carbonates (SnO_2 , MnCO_3 and K_2CO_3) were mixed thoroughly in a mechanical grinder followed by pelletizing using a stainless steel die and a hydraulic press. The pellets (size: 2 cm dia.) were heated to temperature ($T = 900\text{-}1150\text{ }^\circ\text{C}$) in air using the box furnace (Carbolite, UK) and cooled to ambient temperature by furnace shut- off. Repelletizing and reheating is necessary to obtain pure phases of the products. The Sn-based hollandite oxides, $\text{K}_2\text{M}_2\text{Sn}_6\text{O}_{16}$ ($M = \text{Co}, \text{In}$) were thus prepared. The Mo-cluster oxide compounds have been prepared by carbothermal reduction method [2]. This method is generally used to prepare the transition metal oxides of a reduced valency. Here, super P carbon black (MMM, Ensaco) is used as the source of reducing agent, which reduces the valency of metal in the compound to its lower valency by forming CO at $T \geq 650\text{ }^\circ\text{C}$. The synthesis was carried out in inert (flowing Ar-gas) atmosphere in order to avoid the oxidation of the product. The compounds prepared by carbothermal reduction method are, $\text{Li}(\text{Y}/\text{Ho})\text{Mo}_3\text{O}_8$, $\text{A}_2\text{Mo}_3\text{O}_8$ ($A = \text{Mn}, \text{Zn}, \text{Co}$).

The RF magnetron sputtering technique was used to prepare the CoN thin films [3]. The CoN thin films were deposited on Cu- foil substrates (16 mm dia, and 20 μm thick discs, 99.9%) and on surface oxidized Si- substrates (SHE, Japan; 6.25 cm^2 area and 380 μm thick) by using RF magnetron sputtering unit (Denton Vacuum Discovery 18 system) in N_2 atmosphere. Both the substrates were contained in the sputtering chamber. The Co- metal disc (Angstrom Sciences, USA, 99.9%) was used as the target. The

deposition conditions are: RF power at 150 W, total N₂ partial pressure at 10 mTorr, sputtering time, 120 min and substrate temperature, 27⁰C.

The nitridation of many metal oxides to form metal nitrides was carried in the flowing ammonia gas at T < 350 °C [4]. Presently, polycrystalline CoN was prepared from Co₃O₄ (obtained from the high temperature decomposition of cobalt oxalate) powder at 335°C for 2 h in flowing ammonia gas (NH₃:15% + N₂:85%) in a tubular furnace.

High energy ball-milling (HEB) is an effective method for the preparation of nanomaterials [5]. The composites of SnO(VO_x) (x = 1.0 and 1.5) were prepared by HEB at 1400 rpm using the equipment, Spex, 8000D, USA from the starting oxides, SnO and VO_x. The materials were weighed and sealed inside a stainless steel vial (capacity, 25 ml) in the Ar- containing glove box (MBraun, Germany), the vial was taken out and ball milled for 18 h, in three steps of 6 h each, to avoid significant rise in temperature of the vial. Stainless steel balls (½ inch dia.) were used for milling with a ball to active mass ratio as 4:1. Also, nano-K₂(M₂Sn₆)O₁₆ (M = Co, In) were prepared from the pre-synthesized compounds under similar HEB conditions.

II.3. Characterization techniques

II.3.1. X-ray Diffraction

Powder X-ray diffraction (XRD) is a very common tool to characterize the materials to identify crystal structure, space group and in many cases to evaluate the crystallite size [6]. Since in many crystalline materials, the inter-atomic (ionic) distance is of the same order of X-ray wavelength, the principle behind the XRD is the Bragg's Law. According to Bragg's Law, when X-rays of wavelength λ are incident at an angle θ to the crystal of

inter-planar distance d , the X-rays are diffracted as shown in Fig.II.1. The path difference noticed between two X-rays introduces a constant phase difference as per the Eqn.II.1:

$$\text{Phase difference} = 2\pi/\lambda \times \text{Path difference} \quad \text{--- (II.1)}$$

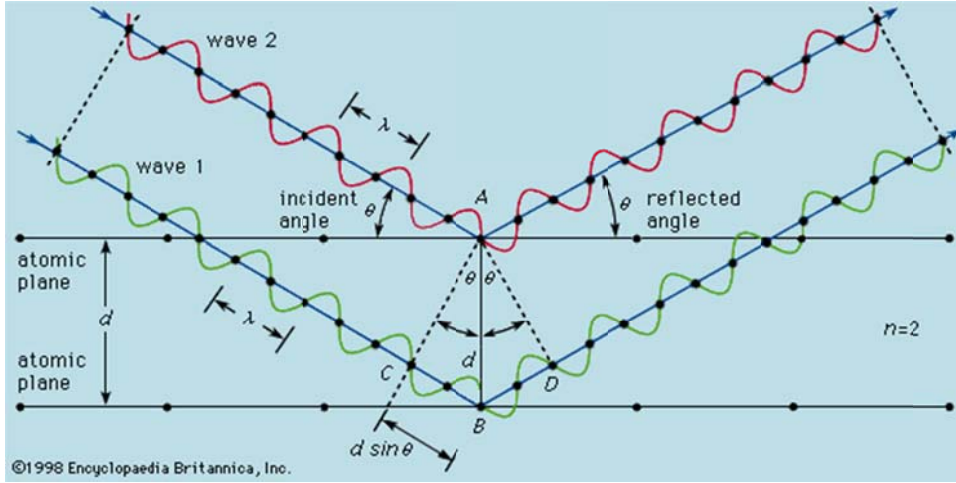


Fig. II.1 Schematic diagram of X-ray diffraction by crystalline material. Taken from [7].

The path difference between the two rays is $(BC + BD) = 2d \sin \theta$. Hence, for the constructive interference, the path difference should be a multiple of λ , stating the Bragg condition for diffraction as

$$2 d \sin \theta = n \lambda \quad (n = \text{order of diffraction} = 1) \quad \text{--- (II.2)}$$

The d - values can be calculated by using the above Eqn. II.2. For a single crystal, there is only one orientation of crystal whereas various random orientations of crystallites are found in polycrystalline materials. So, the positions of the diffracted X-rays are measured in a broad range of angle by moving the detector. The patterns for the XRD are obtained as plot of intensity (in arb. units) (Y-axis) vs. 2θ (in degree) (X-axis). In the present studies, Siemens D5005 or Philips X' PERT MPD diffractometer equipped with X-ray monochromatic source as $\text{Cu K}\alpha$ - radiation ($\lambda = 1.54 \text{ \AA}$) was routinely used. The XRD

patterns were analyzed and information about the lattice parameters, space groups, crystal structures are evaluated by comparing the available standard data in the form of JCPDS (Joint Committee on Powder Diffraction Standards) provided by International Center for Diffraction Data (ICDD), USA. Software such as least square fitting (FINAX) and Rietveld refinement (TOPAS R 2.1) were used to analyze the raw data.

The crystallite size (P) of the oxides and other materials can be calculated from the observed XRD pattern by employing the Scherrer formula [6]:

$$P = K \lambda / \beta_{1/2} \cos \theta \quad \text{--- (II.3)}$$

where $\beta_{1/2}$ is the Full Width at Half Maximum (FWHM), K is the Scherrer constant (~0.9), λ is the wavelength (Cu K α - radiation; 1.54 Å), θ is the angle at maximum intensity. The XRD- instrumental broadening was calculated by using the nano-TiO₂ (anatase) (Evonik Degussa; 99.5%) of ~25 nm particle size as the standard and was found to be 0.08°. This value was subtracted from the θ values from the XRD pattern containing two or more high- intensity peaks.

II.3.2. Fourier transform infrared spectroscopy

Fourier transform infrared spectroscopy (FT-IR) is a well known technique for materials analysis and used to identify the known and unknown materials, their quality or consistency of the sample, the amount of components in a mixture, the bonding of the ions/ atoms/ molecules in a solid/ liquid/gas [8]. The principle is based on the absorption of a frequency, same as the frequency of internal vibration of group of atoms/ ions. When an infrared (IR) radiation is passed through a sample, some of it gets absorbed by the sample corresponding to the vibration frequency of the chemical bonds and some of it is transmitted. The absorbed radiation is measured by the spectrometer and the resulting

spectrum of energy in the Fourier- transformed mode (% transmittance) vs. frequency (wave number, cm^{-1}) is the FT-IR spectrum of the material. The FTIR spectrum is the fingerprint of each material and reveals the characteristic vibrational frequencies. In the present study, Varian 3100 FT-IR, Excalibur 97 series, Canada, was used to record the FTIR spectra.

II.3.3. Raman spectroscopy

Raman spectroscopy is a complementary tool of the FT-IR spectra and is used to characterize solid, liquid and gas species. It is based on inelastic scattering of monochromatic light from a laser source. When a laser light of frequency (ν_0) falls on the sample, the photons are absorbed and some of them are re-emitted. The corresponding frequencies of emitted photons are either smaller or greater than the incident frequency. The effect of shifting of frequency to higher or lower values is named as ‘Raman effect’ [9]. The shift of frequencies provides the information about vibrational, rotational, and other low frequency transitions in the molecules. This is generally based on the deformation of the molecules in the electric field \mathbf{E} (laser light is considered as the oscillating electromagnetic wave with electric field vector \mathbf{E}) determined by the molecular polarizability α . The interaction of light with the sample induces electric dipole moment $\mathbf{P} = \alpha \mathbf{E}$, which deforms the molecules and causes molecular vibrations. Generally, the molecules emit three different frequencies, such as: (i) Rayleigh frequency, which is same as the incident frequency due to elastic scattering. (ii) Stokes frequency, which is lower than the incident frequency and (iii) Anti-Stokes frequency, which is higher than the incident frequency.

In the present work, micro-Raman measurements of the samples of LiYMo_3O_8 and $\text{Mn}_2\text{Mo}_3\text{O}_8$ were performed using 514.5 nm Ar ion LASER, and a triple monochromator system (JY-T64000) attached to a liquid N_2 -cooled charge-coupled device detector. Raman spectra at various temperatures were recorded by using the OXFORD microstat (liquid N_2 -cooled cryostat).

II.3.4. Scanning electron microscopy

Scanning electron microscopy (SEM) is one type of electron microscope, which is used to study the surface morphology or topography of powder or thin films. This gives information on the particle morphology, size, texture, surface-structure and surface defects [10]. The principle behind the SEM is based on the detection and visualization of secondary and back-scattered electrons as a result of the interaction of electron beam with the sample surface. It gives three-dimensional (3 D-) micrographs of the image by scanning the surface of the sample. Generally, the basic components of SEM instrument are: (i) electron column containing lenses, electron gun etc., (ii) vacuum system containing specimen chamber and (iii) detector.

During the SEM recording, the electron gun emits a beam of high-energy electrons, and the beam moves towards the sample in presence of series of magnetic lenses designed to focus the beam to a very fine spot on the sample. The focused beam scans the surface of the sample. The secondary and back-scattered electrons generated due to interaction of electron beam and sample are detected. The secondary electrons of low energy give the surface information of the sample, whereas the back-scattered electrons give chemical content distribution of the sample. For the SEM recording to get good micrographs, conducting samples are preferred to reduce the electrical-charging of

the sample. For non-conducting samples, a thin layer of metal such as Au / Pt is coated on the sample surface by the dc- sputtering technique.

In the present study, the SEM (JEOL JSM-6700 F) was used. Measurements were done on of polycrystalline powders.

II.3.5. Transmission electron microscopy

Transmission electron microscopy (TEM) is another type of electron microscope. This is a well known technique for imaging solid materials at atomic resolution. The morphological and structural information can be obtained both by high resolution imaging as well as by electron diffraction [10]. The elemental analysis down to the sub-nanometer scale can be performed by the TEM instrument employing additional detectors. The principle behind the TEM is the detection of transmitted beam of electrons through an ultra- thin specimen, interacting with the specimen as it passes through. An image is formed from the interaction of the electrons transmitted through the specimen. The high-energy (~300 kV) electrons and electromagnetic lenses are used in a TEM. The electron beam passes an ultra- thin electron-transparent sample and a magnified image is formed using a set of lenses. This image is projected onto a fluorescent screen or a CCD camera. The smaller wavelength of electrons allows for a resolution of 0.2 nm in a TEM. There are two different modes of TEM imaging: bright- field image (the transmitted beam intensity) and the dark- filed image (diffracted beam intensity).

Selected area electron diffraction (SAED) is a valuable technique which is carried out in dark- field mode with the help of TEM. The structural characterization of materials is performed in this mode. A high- energy parallel electron beam is focused on the selected area of the specimen and diffracted by the ions/atoms present in the sample of

the selected area. The diffracted electrons create a pattern when projected onto the CCD camera. It shows a bright dotted pattern for single crystals, whereas concentric diffuse rings are noticed for amorphous material. Nano-crystalline materials show the concentric circles with diffused spots. The SAED pattern is used to evaluate the d- spacing (inter-planar distance) by measuring the diameter of the concentric circles and thereby identifying the crystal structure by assigning the Miller indices (hkl) to the corresponding d- values.

Energy dispersive analysis X-rays (EDAX) can also be carried out by TEM by characterizing the energies of X-rays emitted from the atoms/ ions as a result of the interaction of the incident electron beam with the sample. The X-ray spectrum that is obtained allows for quantification of the elemental composition of the irradiated area in the sample. In the present work, HR-TEM (JEOL JEM-3010 operating at 300 kV) was used.

The sample preparation for TEM study has a great significance in image formation by using electrons transmitted through the sample [10]. The characteristics of a good TEM sample are: (i) the sample thickness should be $< 5 \mu\text{m}$ and surface should be free of contamination. (ii) The thickness of the sample should be comparable or less than the mean free path of the electron beam to avoid scattering. The following procedures are adopted to prepare a TEM sample: (i) the powders are ground to fine particles by agate mortar and pestle. (ii) A small quantity of the powder is suspended in an organic solvent (ethanol) and milled with ultrasonic miller for homogeneous dispersion. (iii) The latter is deposited onto the copper grid coated with holy-carbon.

II.3.6. Elemental Analysis

Inductively coupled plasma- optical emission spectroscopy (ICP-OES) is a valuable technique to analyze the elements present in the samples [11]. In the course of measurement, first the powder sample is dissolved either in an acid (like HNO₃) or aqua regia and then mixed with water before being fed into the plasma. The plasma consists of a hot, partially ionized gas, containing an abundant concentration of cations and electrons that make the plasma a conductor. In case of ICP-OES, the UV and visible spectrometry are being used to image the plasma at the exact wavelength of ionic excitation of the element of interest. In the present work, ICP-OES system (Perkin Elmer Dual-View Optima 5300 DV) was used. The samples were dissolved in an acid mixture using Milestone microwave laboratory system for the analysis.

II.3.7. Density measurement

The density of the polycrystalline sample is measured both in powder and pellet form based on the Archimedes principle of fluid displacement [12, 13]. In this experiment, He- gas is used as the fluid and the mass of the displaced He- gas by the sample is measured by using the Pycnometer, Accupyc 1330 (Micromeritics, USA). At least, 20-30 runs are performed for one sample and the observed experimental density is an averaged value. The pycnometer is calibrated with standards. The observed densities are compared with the theoretical density, calculated from the XRD data.

II.3.8. BET surface area measurement

The BET- method is a well known technique to measure the surface area of the amorphous/ polycrystalline powders and this method was first proposed by Braunauer, Emmett and Teller. The principle is based on the physisorption of gas species on the

surface of the sample [12, 13]. The adsorbed gas molecules are free to move around the surface of the sample and form a thin (mono) layer covering the surface when more and more gas species are introduced. The volume of the gas species are measured at the boiling point of the N_2 . The amount of the adsorbed gas species gives an approximate number of molecules (N_m) required to cover the surface of the sample with a monolayer of adsorbed molecules. Thus, multiplying N_m by the cross-sectional area of an adsorbate molecule gives the surface area of the sample. Here, N_2 is used as the adsorbate gas. In the present work, Micromeritics Tristar 3000 (USA) apparatus was used for BET surface area measurement.

II.3.9. Fabrication of Li-ion coin cells

The electrochemical properties of the materials were studied in the form of coin cells consisting of metal oxides/ nitrides as active material. The various steps adopted to fabricate the coin cells are described below.

II.3.9.1. Preparation of composite electrode

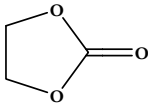
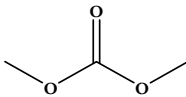
In order to prepare the composite electrode material, the powder of active material is mixed with the super P carbon black (MMM, Ensaco), which is an electronically conducting additive and the Kynar 2801 (Vinylidene fluoride- hexafluoro propylene) polymer as binder in the weight ratio of 75-15-15. The polymer binder helps the coating to adhere the current collector. The N-methyl pyrrolidinone (NMP, Merck) is used as the solvent for the Kynar binder to prepare the slurry. The thick and uniform slurry is coated onto the etched Cu- foil (15 μm thick, Alpha Industries Co. Ltd., Japan) of $\sim 15 \mu\text{m}$ thickness by doctor blade technique. The Cu- foil is used as the current collector due to its excellent electronic conductivity and inability to form alloy with Li. The thick coated

film is dried in an air oven at $\sim 80^{\circ}\text{C}$ for 12 h to evaporate the NMP. The film is pressed between the stainless steel twin rollers (Soei Singapore Scientific Quartz Co.) at 2 MPa pressure to ensure the good adherence of composite electrode materials to the current collector. The thick film is then cut in to circular discs of 16 mm diameter and dried in a vacuum oven at $\sim 70 - 80^{\circ}\text{C}$ for 12 h and then transferred to glove box for cell fabrication.

II.3.9.2. Assembly of coin cells

The sequence of steps for coin cell fabrication is given in Fig. II.2. The cells are fabricated inside the glove box (MBraun, Germany), which maintains <1 ppm of H_2O and O_2 . The coin cells of size 2016 (20 mm diameter; 1.6 mm thickness) are assembled from commercial stainless steel cup and lid fitted with plastic ring by pressing with crimping unit (Hohsen Corp., Japan). The coin cell contains composite electrode material as cathode, Li- metal (Kyokuto Metal Co., Japan) foil cut into disc as anode and glass microfiber filter (GF/F) (Whatman Int. Ltd, Maidstone, England) as separator. The solution of 1M LiPF_6 dissolved in a mixture of ethylene carbonate (EC) and dimethyl carbonate (DMC) (1:1 by volume, Merck Selectipur LP40) is used as electrolyte (The physical properties of the solvents EC and DMC are listed in Table II.1). The composite electrode is placed at the center of the bottom cup with few drops of the electrolyte. The bottom cup is treated as positive (cathode) terminal. This is covered by micro- porous separator that is permeable for Li-ions but prevent the short- circuiting between the two electrodes. A few drops of electrolyte are again added and circular disc of 13 mm diameter and 0.6 mm thick Li- metal is placed on it. To ensure a thorough electronic contact between the top cup (lid), a stainless steel spring is welded to the lid.

Table. II.1 Physical properties of EC and DMC. Taken from [14].

Solvent	Structure	Melting point ($^{\circ}\text{C}$)	Boiling point ($^{\circ}\text{C}$)	Co-efficient of viscosity (cP)	Dielectric constant	Density (g cm^{-3}) (25°C)
EC		36.4	248	1.90 (40°C)	89.78	1.321
DMC		4.6	91	0.59 (20°C)	3.107	1.063

The lid fitted with the plastic ring is rested on the Li-metal and forms the negative terminal. Finally, the sealing is done with the crimping machine. The assembled cell is taken out from the glove box and aged for ~ 12 h to ensure the percolation of electrolyte to the electrode before the electrochemical characterization is carried out. Here, the Li-metal acts as the counter (anode) and reference electrode whose voltage is arbitrarily considered as zero.

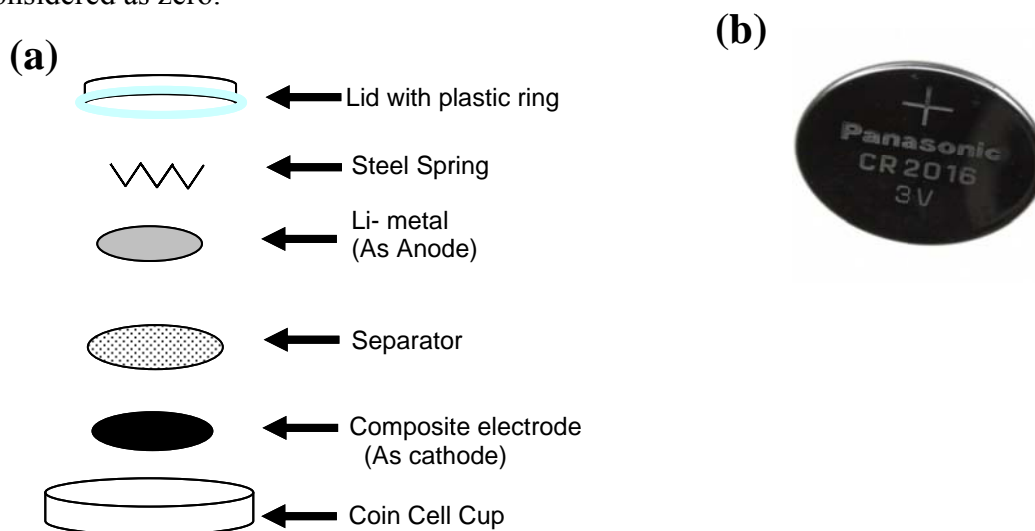


Fig. II.2 (a) Schematic diagram of cell assembly and (b) photograph of 2016 type fabricated coin cell.

II.3.10. Electrochemical studies

The electrochemical studies on the coin cell are carried out in two different modes, such as (i) at constant current (galvanostatic cycling) and (ii) at constant potential rate (potentiostatic cycling).

II.3.10.1. Galvanostatic cycling

Galvanostatic cycling is the technique to obtain the voltage – composition relationship of an electrochemical cell at a constant current. The voltage of the cell varies as a function of the state of discharge/ charge of electrode w.r.t. Li- metal, which is used as counter electrode [15, 16]. While performing galvanostatic cycling, the voltage of the cell is decreased (during discharge)/ increased (during charge) at a constant current. The output result is plotted as a function of voltage vs. time or state of discharge/ charge. The information of specific capacity (ability of charge storage per unit weight of active material) in terms of mAhg^{-1} of an electrode can be derived from the voltage-composition plot. In the present work, the galvanostatic cycling of the cells is carried out at ambient (room) temperature ($RT = 25^\circ\text{C}$) by computer controlled Bitrode multiple battery tester (model SCN, Bitrode, USA) for a good number of cycles. The data are plotted as a function of voltage vs. discharge/ charge time or the specific capacity.

The theoretical specific capacity, also called, gravimetric capacity of an electrode material is calculated as follows. Specific capacity (mAhg^{-1}) = $\frac{(F \times n_{\text{Li}})}{M \times 3600} \times 1000$ --- (II.4)

where F is the Faraday's constant (96,500 coulombs per gram equiv.), n_{Li} is the number of Li-ions (and electrons) involved in the chemical reaction per formula weight of the compound and M is the formula weight (g) of the compound.

For example, the theoretical capacity of graphite (C) is calculated as:

$$[(96500 \times 1/6) / (12 \times 3600)] \times 1000 = 372 \text{ mAhg}^{-1} \quad \text{---}$$

(II.5)

Here, carbon can take 1/6 Li-ion per formula weight to form LiC_6 based on intercalation mechanism. The specific capacity can also be calculated in mAh cm^{-3} by knowing the density of the electrode material. This is called volumetric capacity. The suitability of the electrode material for use in LIBs is evaluated after a comparison of the theoretical and experimental specific capacity (both gravimetric and volumetric).

II.3.10.2. Cyclic voltammetry

Cyclic voltammetry (CV) is a commonly used technique for electrochemical measurement that gives the qualitative/ quantitative information about the reversibility of electrode reaction, redox potential and electrode reaction kinetics [15, 16]. The quantitative information of diffusion coefficient of the species, like Li- ion that takes part in the electrochemical reactions can be estimated from the CV data. The theoretical aspect of CV was first reported by Randles in 1938. The technique involves flow of current between the electrodes by varying the potential of the working electrode at a constant potential sweep rate (μVs^{-1}) with respect to the counter electrode both in forward and reverse direction. The current measured during the voltage sweep is plotted vs. voltage and the result is referred to as a cyclic voltammogram. The parameters observed from the CV are the peak potentials, i.e. both anodic and cathodic potential (E_a and E_c) and the corresponding current (I_a and I_c). When the electron transfer rate in both the forward and reverse directions at the electrode is high, the reaction is described as reversible, and the cathodic and anodic peaks are separated by a potential of

approximately $59/n$ mV, where n is the number of electrons transferred. The peak current is given by the Randles- Sevcik equation:

$$I_p = 2.686 \times 10^5 n^{3/2} A c^0 D^{1/2} v^{1/2} \quad \text{--- (II.6)}$$

where I_p is the peak current in mA, n is the number of electrons taking part in the reaction, A is the area of the electrode in cm^2 , D is the diffusion coefficient ($\text{cm}^2 \text{s}^{-1}$), c^0 is the concentration of electroactive species (mol cm^{-3}) and v is the potential sweep rate (Vs^{-1}).

In the present work, the CV on the coin cells containing composite electrode as cathode and Li-metal as counter/ reference electrode, was carried out at a low potential sweep rate of $58 \mu\text{Vs}^{-1}$ by using the computer controlled MacPile II (Biological, France) unit at room temperature.

II.3.10.3. Electrochemical Impedance Spectroscopy

The electrochemical impedance spectroscopy (EIS) is a non-destructive technique, which is used to understand the interfacial behavior in electrochemical cell at various voltages [17 - 19]. The cell is equilibrated at a fixed voltage for 2-3 h prior to the measurement. The cell impedance is determined in response to a small amplitude (10 mV) of ac signal superimposed during the measurement. The small perturbation from the equilibrium due to the application of ac signal is measured in terms of amplitude and phase of the resultant current induced by the applied voltage and gives information of overall impedance of the cell. The frequency of the ac signal is varied from high (1 MHz) to low (3 mHz) and the characteristic change in cell impedance as a function of frequency is studied. The total cell impedance (Z) is a complex number,

$$Z = Z' + i Z'' \quad \text{--- (II.7)}$$

where, Z' is the real part and Z'' is the imaginary part and $i = \sqrt{-1}$. The cell impedance is presented by a vector diagram called Nyquist plot, where the real part (Z' , in phase) is presented in X-axis and negative of imaginary part (Z'' , out of phase by 90°) in Y-axis (Fig. II.3).

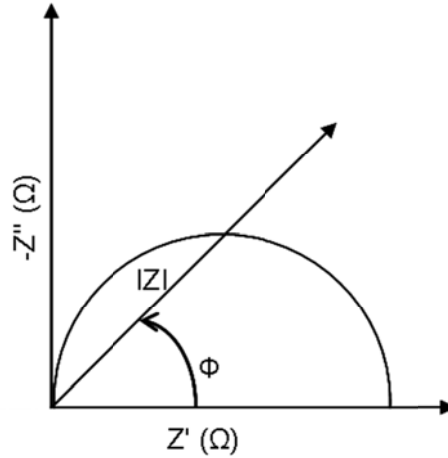


Fig. II.3 Vector diagram of the Cell impedance (Z).

In EIS, the total impedance obtained during measurement is the contribution from individual impedance of various factors, such as passivating layer (surface film), charge (ions) transfer, bulk impedance, Warburg impedance and intercalation capacitance. The contribution of impedance from the aforementioned factors varies as a function of frequency. The surface film and charge transfer impedances ($R_{(sf + ct)}$) dominate at high frequency range (1 MHz to 1 kHz), whereas bulk (R_b) and Warburg (W_s) impedances dominate at lower frequency range. Thus, the EIS has to be carried out in a wide range of frequency.

The observed data of the Nyquist plots are analyzed by fitting with an equivalent electrical circuit and the quantitative information of impedance are obtained. The equivalent electrical circuits are designed with series or parallel combinations of resistors and capacitors or constant phase elements. Each of the circuit element corresponds to the

individual components in the electrochemical cell. The impedance due to the solution (electrolyte) is represented by the resistor, whereas the semicircle is represented by the parallel combination of resistor and capacitor. The Nyquist plot and its equivalent circuit is shown in Fig. II.4

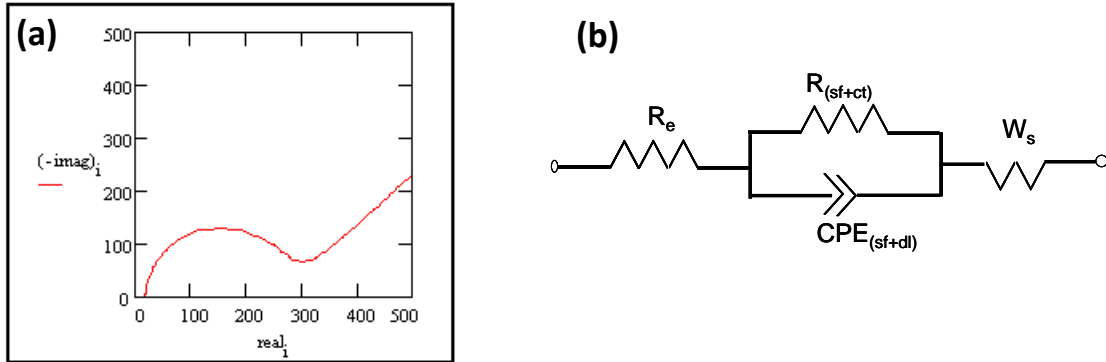


Fig. II.4 (a) Nyquist plot of an electrochemical cell with one semicircle and (b) Equivalent electrical circuit. Taken from [20].

The constant phase element (CPE) is used instead of a pure capacitor, when the electrode deviates from its ideal behavior and presents a depressed semicircle (which does not touch the X-axis) instead of a perfect semicircle (which touches the X-axis) in the Nyquist plot. The impedance due to the CPE is given as $Z'' = 1/C (\omega)^{-n}$, where C is the capacitance, ω is the applied frequency and n is a number which defines the magnitude of deviation from a pure capacitor. For CPE, the value of n is always < 1 .

In the present study, the Solatron Impedance/gain-Phase Analyzer (SI 1260)(UK) coupled with a battery Test Unit (1286) (UK) was used. An ac signal with an amplitude of 10 mV is used to measure the impedance response over the frequency range varying

from 0.18 MHz to 3 mHz. The data acquisition and analysis were carried out using Z-plot and Z-view software (Version 2.2, Scribner Associates Inc., USA).

II.3.10.3.1. Determination of Li- ion diffusion coefficient from EIS

The Li-ion diffusion coefficient (D_{Li^+}) of polycrystalline and thin film electrode can be derived at different charge- discharge voltages from the detailed analysis of impedance spectra (Nyquist plots) [19, 21-23]. The D_{Li^+} can be calculated from formula,

$$D_{Li^+} = \pi f_L L^2 \quad \text{--- (II.8)}$$

where f_L is the limiting frequency determined from the impedance spectrum where the Warburg region (a straight line with a slope $\sim 45^\circ$ from the real axis in the Nyquist plot) gives way to a vertical line, $\geq 80^\circ$. Generally, the f_L is realized at low- frequency region. The L is the maximum diffusion length for the Li-ions in the active material in the electrode. As a first approximation, L is the particle size or crystallite size in nanometer range. The latter can be estimated from the XRD and TEM data on the material. In the case of thin- film, the thickness is taken as the value of L . In the present work, EIS was used to estimate D_{Li^+} at various voltages of selected nanometer- size oxides. There are many other (and more accurate) methods for obtaining the D_{Li^+} of the electrode materials, like galvanostatic intermittent titration technique (GITT), potentiostatic intermittent titration technique (PITT), CV and DC polarization [23]. The GITT is considered to be the best method. In this case, the D_{Li^+} is given by:

$$D_{Li^+} = \frac{1}{2} \left[\left(\frac{V_m}{FAA_w} \right) \frac{dE}{dx} \right]^2 \quad \text{--- (II.9)}$$

where V_m is the molar volume of the electrode material, F is the Faraday constant, A is the electrode area, A_w is the Warburg coefficient obtained from the Warburg region of the

Nyquist plot. The (dE/dx) is the change in the voltage of the cell due to the change in the Li- content (x) which is obtained by passing a known quantity of current and stabilize the voltage to its equilibrium value. The process is repeated to cover the entire range of voltage of interest.

References

- [1] A.R. West, 'Solid state chemistry and its applications' John Wiley, Singapore, New York, 1989.
- [2] J. Barker, M.Y. Saidi, J. L. Swoyer, Solid State Ionics 158 (2003) 261.
- [3] K. Suzuki, T. Kaneko, H. Yoshida, H. Morita, H. Fujimori, J. Alloys Compds 224 (1995) 232
- [4] Y. Shi, Y. Wan, R. Zhang, D. Zhao, Adv. Funct. Mater. 18 (2008) 2436.
- [5] W.J. Botta F., R. Tomasi, E.M.J.A. Pallone, A.R. Yavari, Scripta Mater. 44 (2001) 1735.
- [6] B. D. Cullity, S. R. Stock, 'Elements of X-ray diffraction' (3rd edition), Prentice Hall, New York, 2001.
- [7] www.britannica.com
- [8] D. L. Pavia, G. M. Lampman, G. S. Kriz, 'Introduction to Spectroscopy' (3rd edition), Thomson Learning, Inc., USA, 2001.
- [9] J. R. Ferraro, K. Nakamoto, C. W. Brown, 'Introductory Raman Spectroscopy' (2nd edition), Elsevier, 2003.
- [10] P. J. Goodhew, J. Humphreys, R. Beanland, 'Electron microscopy and analysis', Taylor and Francis, London, 2001.
- [11] J. Nolte, 'ICP emission spectrometry: a practical guide', Wiley-VCH, Weinheim, 2003.
- [12] J. E. Shields, M. A. Thomas, M. Thommes, 'Characterization of porous solids and powders: surface area, pore size and density', Kluwer Academic, New York, 2004.
- [13] J. B. Condon, 'Surface area and porosity determinations by physisorption:

measurements and theory' (1st edition), Elsevier, British Library Cataloguing publication data, 2006.

[14] K. Xu, Chem. Review 104 (2004) 4303.

[15] C. M. A. Brett, A. M. O. Brett, 'Electrochemistry: principles, methods and applications', Oxford Univ. Press, New York, 1993.

[16] V. S. Bagotsky, 'Fundamentals of electrochemistry' (2nd edition), John Wiley & Sons, Inc., New Jersey, 2006.

[17] D. Aurbach, A. Nimberger, B. Markovsky, E. Levi, E. Sominski, A. Gedanken, Chem. Mater. 14 (2002) 4155.

[18] M. V. Reddy, T. Yu, C. H. Sow, Z. X. Shen, C. T. Lim, G. V. Subba Rao, B. V. R. Chowdari, Adv. Funct. Mater. 17 (2007) 2792.

[19] Y. Sharma, N. Sharma, G. V. Subba Rao, B. V. R. Chowdari, Chem. Mater. 20 (2008) 6829.

[20] <http://www.gamry.com>

[21] B. Garcia, J. Farcy, J. P. Pereira-Ramos, N. J. Baffier, J. Electrochem. Soc. 144 (1997) 1179.

[22] G. X. Wang, D. H. Bradhurst, S. X. Dou, H. K. Liu, J. Power Sources 83 (1999) 156.

[23] J. Xie, N. Imanishi, T. Matsumura, A. Hirano, Y. Takeda, O. Yamamoto, Solid State Ionics 179 (2008) 362.

Chapter III

Carbothermal synthesis, spectral and magnetic characterization and Li- cyclability of the Mo- cluster compounds, LiYMo_3O_8 , $\text{LiHoMo}_3\text{O}_8$ and $\text{A}_2\text{Mo}_3\text{O}_8$ (A = Mn, Co, Zn)*

Abstract

The molybdenum cluster compounds, LiYMo_3O_8 , $\text{LiHoMo}_3\text{O}_8$ and $\text{A}_2\text{Mo}_3\text{O}_8$ (A = Mn, Co, Zn) are prepared by the carbothermal reduction method and characterized by X-ray diffraction (XRD), scanning electron microscopy (SEM), high resolution transmission microscopy (HR-TEM), selected area electron diffraction (SAED), fourier transform infrared spectroscopy (FT-IR) and Raman techniques. The FT-IR at ambient temperature (RT), and Raman spectra at various temperatures (78-450 K) of LiYMo_3O_8 and $\text{Mn}_2\text{Mo}_3\text{O}_8$ are reported for the first time and results are interpreted. Magnetic studies on $\text{Mn}_2\text{Mo}_3\text{O}_8$ in the temperature range, 10-350 K confirm that it is ferrimagnetic, with $T_C = 39$ K. Magnetic hysteresis and magnetization data at various fields and temperatures are presented. The Li- cyclability is investigated by galvanostatic cycling in the voltage range, 0.005-3.0 V vs. Li at 30mA g^{-1} (60 mA g^{-1}). At 30 mA h g^{-1} , LiYMo_3O_8 and $\text{LiHoMo}_3\text{O}_8$ show a total first-discharge capacity of 305 and 275 (± 5) mA h g^{-1} , respectively whereas the first-charge capacity is only 180 mA h g^{-1} for both at room temperature (RT). However, both values increased systematically with an increase in the cycle number and yielded a reversible capacity of 385 and 290 (± 5) mA h g^{-1} at the end of 120th and 70th cycle, respectively. The Li-cyclability behavior of $\text{A}_2\text{Mo}_3\text{O}_8$ is entirely different from that of $\text{LiY}(\text{Ho})\text{Mo}_3\text{O}_8$. The total first-discharge and charge capacities for A = Mn at 30 mA g^{-1} are 710 (± 5) and 565 (± 5) mA h g^{-1} . For A = Zn and Co at 60 mA g^{-1}

* Two papers have been published and two papers were presented at two Intl. Conferences based on the work described in this Chapter.

the corresponding values are 775 and 1250(± 5) mAhg⁻¹ (first- discharge capacity) and 350 and 900 (± 5) mAhg⁻¹ (first- charge capacity). The coulombic efficiency of all the compounds ranges from 94-96%. Plausible reaction mechanisms are proposed and discussed based on the galvanostatic cycling, cyclic voltammetry, ex-situ -XRD, ex-situ -TEM and impedance spectral data.

III. 1. Introduction

Binary and ternary transition metal oxides are of interest as prospective anode materials to replace the graphite anode in the present day lithium ion batteries (LIBs). Fairly high reversible capacities are obtained by the formation and decomposition of Li₂O by the redox ('conversion') reaction [1-5]. Optimization of the Li- cycling behavior has been possible by employing nano-size particles of the oxides, modifying their morphology, adjusting the composition and by using the 'matrix' elements which are either electrochemically active or inactive. Some of the metal oxides well-studied are, nano-sized MO, M= Fe, Co, Ni, Cu [6], Fe₃O₄ [7], Co₃O₄ [8, 9], Fe₂O₃ [10], Cr₂O₃ [11, 12], and ZnCo₂O₄ [13]. In addition to the metal oxides, conversion reactions with Li involving transition metal fluorides [14] and oxyfluorides [15] have also been studied.

Molybdenum (Mo) containing mixed oxides have received attention as possible negative electrodes for use in LIBs. This is due to the ability of the above metal ion to exist in several oxidation states in oxides, ranging from 3+ to 6+ and reversibly reacting with Li. Further, the high density of Mo-oxides can give rise to higher volumetric energy density of the electrode as compared to the graphite. The compounds of the type Na_{0.23}MoO₃ [16, 17], Mn_{1-x}(V_{1-x}Mo_x)₂O₆ (x = 0 and 0.4) [18,19] and solid solutions, SnO₂-MoO₂[20] have been investigated. Other Mo- containing oxides studied are

MnMoO₄ [21], CaMoO₄ [22], MMoO₄, M= Cu, Zn, Ni, Fe [23], and recently MoO₂ [24] and (VO)MoO₄ [25].

Li(Y/Ho)Mo₃O₈ and A₂Mo₃O₈ (A = Mn, Zn, Co) are examples of a large number isostructural hexagonal layer-type compounds in which the Mo-ions and (Li, Y/Ho) and (Mn / Zn / Co) -ions occupy the alternate O-ion layers perpendicular to the *c*-axis [26, 27]. The Mo is in 4+ oxidation state and is in an octahedral environment of oxide ions, whereas the (Li-, Y/Ho)- ions adopt a tetrahedral and octahedral O-coordination, respectively. For A₂Mo₃O₈ (A = Mn, Zn, Co), one of divalent A- ion occupies tetrahedral and other in octahedral O- coordination alternatively. The Ho ion can be replaced by other rare earth (Ln= Sm→Lu), Sc, Ga or In, to give rise to isostructural compounds [26, 27]. An unusual feature in all these compounds is the existence of triangular Mo₃ – clusters in which the Mo-Mo distance is less than that of the of Mo-Mo distance in Mo-metal. Since the two 4d-electrons of each Mo⁴⁺ ion are trapped in the Mo-Mo bonds, the Mo₃ –cluster does not possess a net magnetic moment. The structure of LiYMo₃O₈ and Mn₂Mo₃O₈ are shown in Fig.III.1a, b. These are drawn using the commercial software (Material studio company, Japan), assuming the space group, P3m1 for LiYMo₃O₈ and P6₃mc for Mn₂Mo₃O₈ and the atom positions reported in the literature [27-29]. There are two formula units per unit cell in which two bivalent Mn ions adopt the octahedral oxygen coordination, whereas the other two bivalent Mn ions adopt the tetrahedral O-coordination. All the tetravalent Mo-ions adopt the octahedral oxygen coordination. In LiYMo₃O₈, the Li and Y ions adopt the tetrahedral and octahedral O- coordination, respectively and hence, the space group changes to P3m1, even though the structure remains hexagonal [27,29]. In the present work, the preparation, physical characterization

and electrochemical studies on the cluster compounds, LiYMo_3O_8 , $\text{LiHoMo}_3\text{O}_8$ and $\text{A}_2\text{Mo}_3\text{O}_8$ are described and discussed.

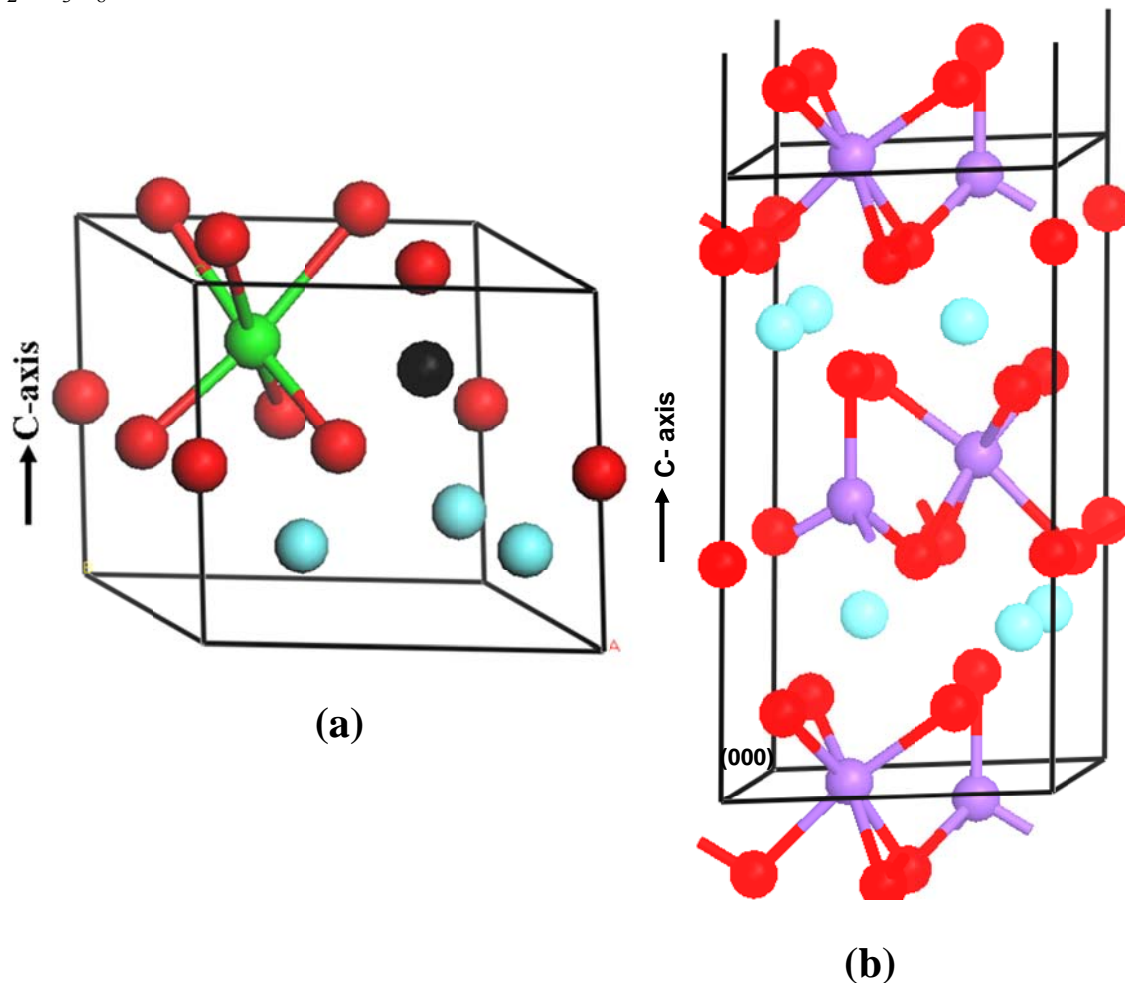


Fig.III.1. The crystal structure of hexagonal (a) LiYMo_3O_8 and (b) $\text{Mn}_2\text{Mo}_3\text{O}_8$. Li: black sphere; Y: green sphere; Mn: Pink spheres; Mo: Light blue sphere; O: Red spheres. For clarity, all the ions are given the same size.

III.2. Experimental

The compounds, $\text{Li(Y/Ho)Mo}_3\text{O}_8$ were prepared by using stoichiometric mixture of LiOH (Merck, 98%), $\text{Y}_2\text{O}_3/\text{Ho}_2\text{O}_3$ (Acros, 99.99%), MoO_3 (Alfa Aesar, 99.95%) and Super P carbon (C) (MMM, Ensaco; an electrically conducting and structurally amorphous (low crystallinity) with the BET surface area of $230 \text{ m}^2\text{g}^{-1}$). Calculated amount of carbon was employed according to the reaction, $\text{MoO}_3 + \text{C} \rightarrow \text{MoO}_2 + \text{CO}\uparrow$.

The mixture was ground in a mechanical grinder for 15 min, and pressed into a pellet. The pellet was kept in a carbon crucible (10 × 2.5 cm) and heated at 750 °C for 8 h in flowing argon gas inside a tubular furnace (Carbolite, UK) and cooled to room temperature. The pellet was ground to a fine powder and stored in a desiccator. The compounds, $A_2Mo_3O_8$ (A = Mn, Zn) were prepared by using stoichiometric mixture of MnO_2/ZnO (Merck, 99.9%), MoO_3 and C and heat treatment as above. However, two more steps of regrinding- pelletizing- heat treatment were found to be necessary to obtain the pure phase. For the compound A = Co, the stoichiometric amount of pre-synthesized $CoMoO_4$ was mixed with C and the above procedure was followed.

Powder X-ray Diffraction (XRD) data were collected using Philips X'PERT MPD instrument (Cu K_{α} radiation) and analyzed to identify the crystal structure. Rietveld refinement of the XRD data to obtain the unit cell lattice parameters were carried out by using the TOPAS software version 2.1 and atomic positions and space group reported in literature. The Brunauer, Emmett and Teller (BET) surface area of the powders was measured by using NOVA 3000, USA and the densities were determined by using AccuPyc 1330 pycnometer, Micromeritics (USA). The morphology of the powders was examined by Scanning Electron Microscopy (SEM) (JEOL JSM-6700F). High Resolution Transmission Electron Microscopy (HR-TEM) and Selected Area Electron Diffraction (SAED) images were taken by using JEOL JEM 3010 operating at 300 kV. Infrared spectra were recorded using IR spectrophotometer (Varian 3100 FT-IR, Excalibur series, Canada) and Micro Raman measurements were performed using 514.5 nm Ar ion LASER, and a triple monochromator system (JY-T64000) attached to a liquid N_2 cooled charge-coupled device detector. Raman spectra at various temperatures were

recorded by using the OXFORD microstat (liquid N₂ cooled cryostat). Magnetic measurements were carried out using vibrating sample magnetometer (VSM, Quantum Design, USA) which is attached to the physical property measuring system (PPMS, Quantum Design, USA) in the temperature range, 350-10K under applied magnetic fields up to 5 T. For zero field cooled (ZFC) measurements, the sample was cooled to low temperature in the absence of magnetic field and then data were collected in the presence of required magnetic field during warming- up of the sample. For field cooled (FC) measurements, the sample was cooled to low temperature in the presence of applied magnetic field and then data were collected in the same magnetic field during warming.

Fabrication of the electrodes for electrochemical studies was done using a mixture of the following composition: active material, super P carbon black (MMM, Ensaco; electronically conducting additive) and polymer binder (Kynar 2801) in the weight ratio 70:15:15. N-methyl-pyrrolidinone (NMP) was used as the solvent for the binder. The homogeneous and viscous slurry obtained after thorough mixing was then cast on to an etched Cu-foil (15 μm thick, Alpha Industries Co. Ltd., Japan) to form a thick layer (~15 μm) by doctor-blade method. The Cu- substrate acts as the current collector. The active mass in the electrode is typically 3- 4 mg and geometrical area of the electrode is 2.0 cm². The electrode discs were vacuum dried at 70 °C for 12 h before being transferred into an argon filled glove box (MBraun, Germany) for cell assembly. The atmosphere in the glove-box was maintained at <1 ppm of H₂O and O₂. For the coin-cell (size 2016) assembly, a glass microfiber filter (GF/F) (Whatman Int. Ltd, Maidstone, England) was used as the separator for the electrodes and the electrolyte used was 1M LiPF₆ in ethylene carbonate (EC) + diethyl carbonate (DEC) in the ratio of 1:1 volume (Merck). The Li-

metal foil (Kyokuto Metal Co., Japan) was cut in to circular disc (16 mm diameter) and used as the counter electrode. Cyclic voltammetry and galvanostatic cycling tests on the coin-cells were conducted at room temperature (24°C) using a potentiostat system (Macpile II, Bio-logic, France) and Bitrode multiple battery tester (Model SCN, Bitrode, USA), respectively. The cells were aged for 12 h before testing. For the ex-situ XRD patterns of discharged and cycled electrodes, the cells were disassembled in the glove box, the electrodes were recovered, washed with DEC and dried. To avoid exposure to air/moisture, the electrodes were covered with paraffin film (American National Can™) and mounted on the X- ray diffractometer. For ex-situ TEM studies the electrode material was scraped from the Cu- foil in the glove box and the powder was dispersed in ethanol by ultrasonic miller (Transsonic, 660/H, Germany) and deposited on a holey carbon grid. For measurements at 50 °C, the cells were kept in a temperature controlled oven (± 3 °C). Impedance measurements were carried out with the computer controlled Solartron Impedance/gain-phase analyzer (model SI 1255) coupled with a computer controlled battery test unit (model 1470) at room temperature (RT). The frequency range was varied from 0.35 MHz to 3 mHz with ac signal amplitude of 5 mV. The collected data were analyzed using Z plot and Z view software (Version 2.2, Scribner associates Inc., USA) to obtain the Nyquist plots (Z' vs. $-Z''$).

III.3. Results and Discussion

III. 3.1. Structure and morphology

Compounds containing the molybdenum in a reduced valency state, like MoO₂ are usually prepared by heating MoO₃ at high temperature in a hydrogen atmosphere or by heating the mixture of MoO₃ and Mo-metal in suitable proportions in evacuated and

sealed quartz tubes. In recent years, Barker et al. [30, 31] have been able to prepare MoO_2 , $\text{LiMo}^{3+}\text{O}_2$ and other Mo-oxides by the high-temperature carbothermal reduction method in an inert atmosphere. Presently, this method was adopted to prepare LiYMo_3O_8 , $\text{LiHoMo}_3\text{O}_8$ and $\text{A}_2\text{Mo}_3\text{O}_8$. It must be mentioned however, that further optimization of synthesis conditions is necessary, since small amounts of MoO_2 were found as an impurity in the XRD patterns of all the compounds except for $\text{A} = \text{Co}$, in which Co-metal impurity was noted. Residual carbon, if any, is not detected by XRD.

The LiYMo_3O_8 , $\text{LiHoMo}_3\text{O}_8$ and $\text{A}_2\text{Mo}_3\text{O}_8$ are black and crystalline compounds. The Rietveld refined XRD patterns show the lines characteristic of the hexagonal structure (Fig. III. 2). The Rietveld refined lattice parameters, space groups of all the compounds are given in Table III.1. The evaluated values are in good agreement with the reported values in literature for all the compounds. From the XRD data, the MoO_2 impurity is calculated to be 5-7% for all the compounds except for $\text{A} = \text{Co}$.

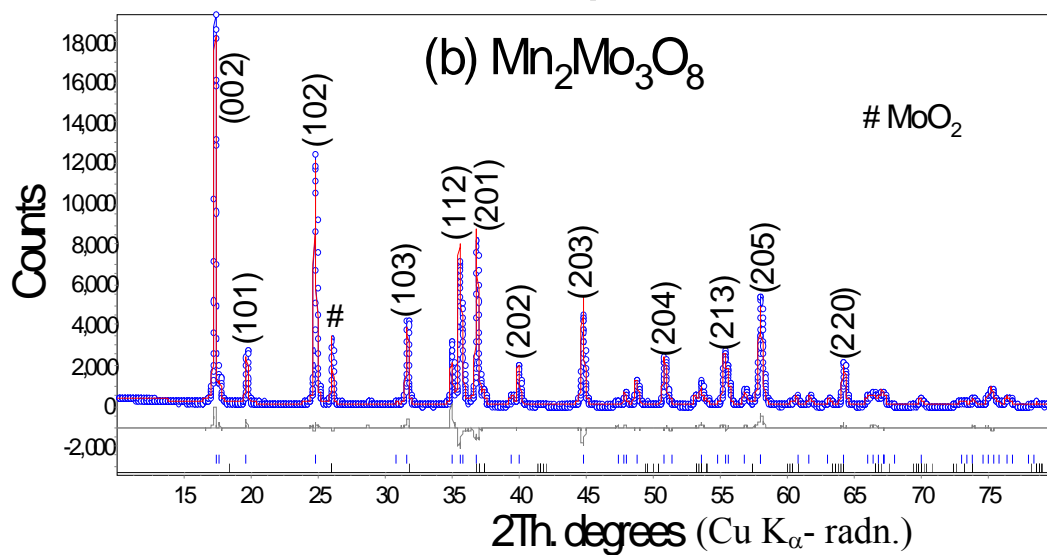
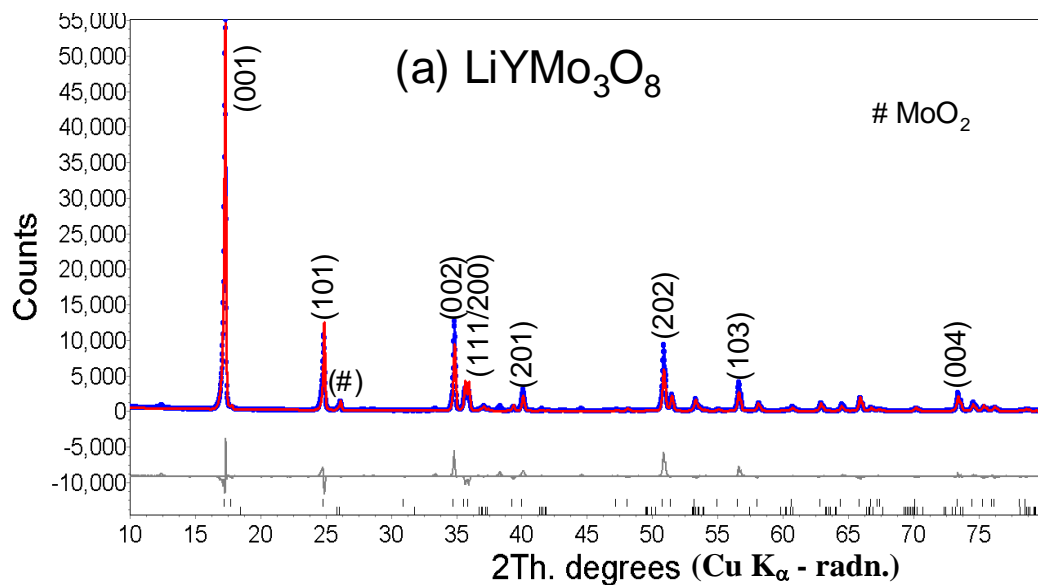


Fig. III.2 (Caption in next page)

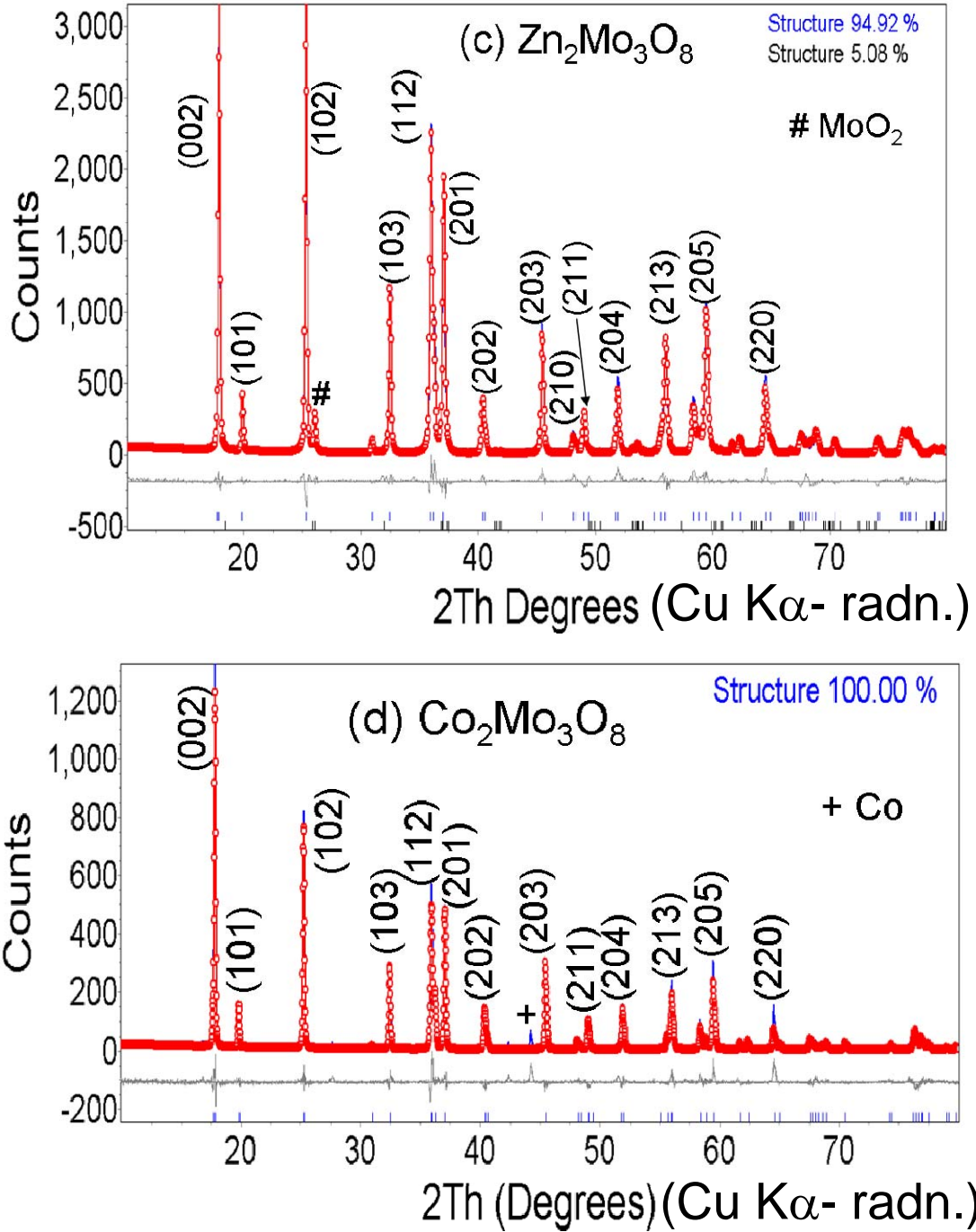


Fig.III.2. Rietveld refined X-ray diffraction pattern of (a) $LiYMo_3O_8$, (b) $Mn_2Mo_3O_8$, (c) $Zn_2Mo_3O_8$ and (d) $Co_2Mo_3O_8$. Miller indices (hkl) are shown. Symbols represent experimental data and continuous line represents the refined data. The difference pattern and positions of reflections (vertical lines) of $LiYMo_3O_8$ and $A_2Mo_3O_8$ and lines due to MoO_2 , Co (impurities) are also shown.

Table III. 1 Crystal lattice parameters, space groups and reported values with JCPDS card no. for LiYMo₃O₈, LiHoMo₃O₈ and A₂Mo₃O₈.

Compounds	LiHoMo ₃ O ₈	LiYMo ₃ O ₈	Mn ₂ Mo ₃ O ₈	Co ₂ Mo ₃ O ₈	Zn ₂ Mo ₃ O ₈
Evaluated Lattice parameter (±0.002) Å	<i>a</i> = 5.776 <i>c</i> = 5.150 (Least Square Fitted)	<i>a</i> = 5.783 <i>c</i> = 5.160	<i>a</i> = 5.795 <i>c</i> = 10.254	<i>a</i> = 5.771 <i>c</i> = 9.904	<i>a</i> = 5.774 <i>c</i> = 9.913
Space group	P3m1	P3m1	P6 ₃ mc	P6 ₃ mc	P6 ₃ mc
Lattice parameters, Å Ref.: JCPDS card No.	<i>a</i> = 5.771 <i>c</i> = 5.156 32-0562	<i>a</i> = 5.790 <i>c</i> = 5.160 18- 0757	<i>a</i> = 5.798 <i>c</i> = 10.268 71-1424	<i>a</i> = 5.767 <i>c</i> = 9.916 71- 1423	<i>a</i> = 5.775 <i>c</i> = 9.915 76- 1737

The measured BET surface area of LiYMo₃O₈ and Mn₂Mo₃O₈ are 4.1 and 4.6 m²/g, respectively. The experimental densities of LiYMo₃O₈ and Mn₂Mo₃O₈ are 5.451 g/cm³ and 5.741 g/cm³, respectively and compare well with the calculated X-ray densities of 5.68 g/cm³ and 5.85 g/cm³. The SEM photographs of all the compounds showed the submicron-range of the particle size, with agglomerated morphology (Fig. III.3).

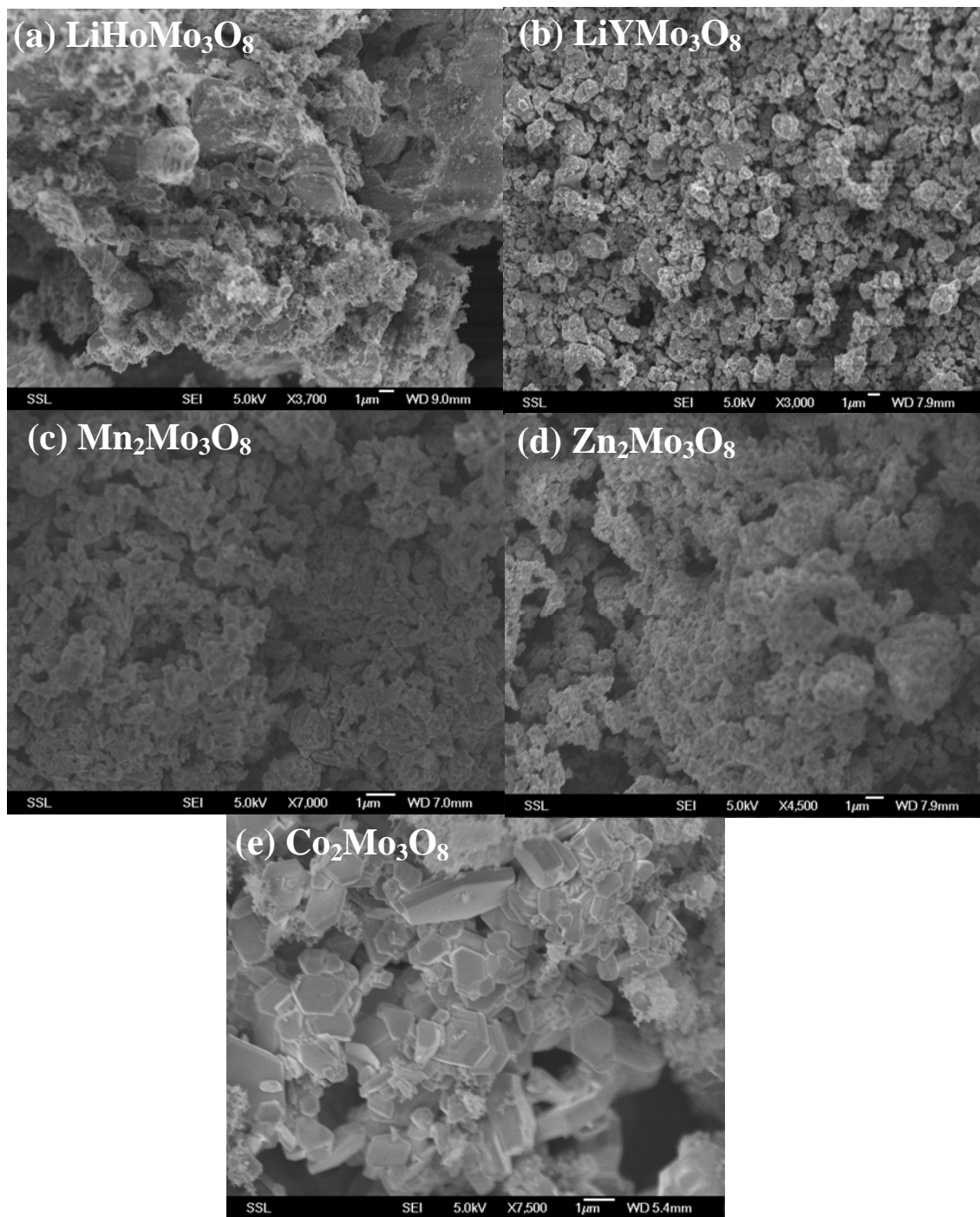


Fig. III.3. SEM micrographs of (a) $\text{LiHoMo}_3\text{O}_8$, (b) LiYMo_3O_8 , (c) $\text{Mn}_2\text{Mo}_3\text{O}_8$, (d) $\text{Zn}_2\text{Mo}_3\text{O}_8$ and (e) $\text{Co}_2\text{Mo}_3\text{O}_8$. Scale bars are shown.

The HR-TEM lattice images and SAED patterns of LiYMo_3O_8 , $\text{LiHoMo}_3\text{O}_8$ and $\text{A}_2\text{Mo}_3\text{O}_8$ are shown in Fig. III.4. The d-values are derived and the Miller indices are shown in the SAED patterns.

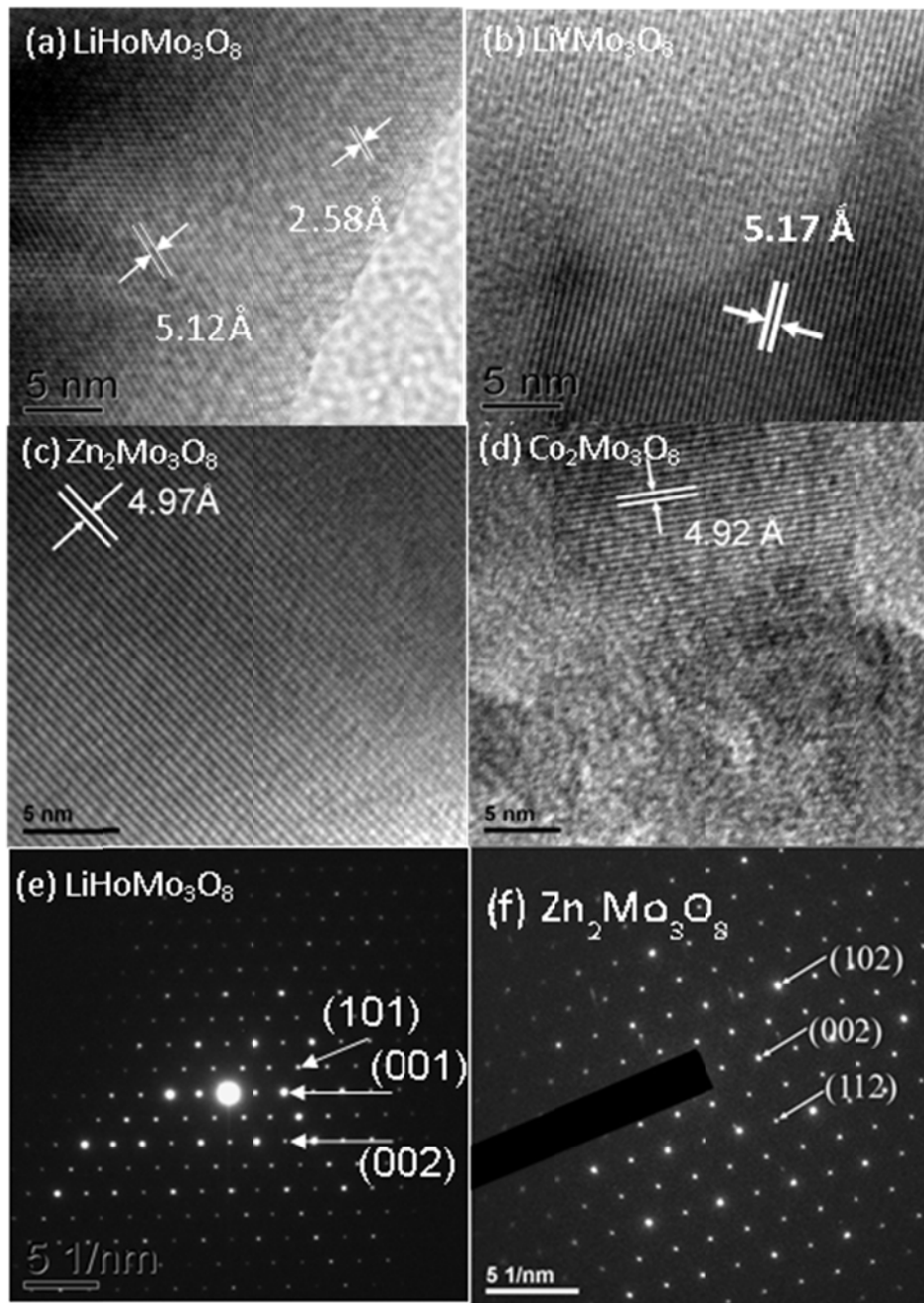


Fig. III.4. HR- TEM lattice image of (a) $\text{LiHoMo}_3\text{O}_8$, (b) LiYMo_3O_8 , (c) $\text{Zn}_2\text{Mo}_3\text{O}_8$ and (d) $\text{Co}_2\text{Mo}_3\text{O}_8$. SAED patterns of (e) $\text{LiHoMo}_3\text{O}_8$ and (f) $\text{Zn}_2\text{Mo}_3\text{O}_8$. Miller indices (hkl) and scale bars are shown.

III.3.2. Infrared and Raman spectra of LiYMo_3O_8 and $\text{Mn}_2\text{Mo}_3\text{O}_8$

The infrared (IR) and Raman spectra of the Mo_3 - cluster compounds have not been reported in the literature. The Fourier transform infrared (FT-IR) spectra of LiYMo_3O_8 and $\text{Mn}_2\text{Mo}_3\text{O}_8$ at ambient temperature in the transmission mode in the range, 400-1400 cm^{-1} are shown in Fig. III. 5. The relative intensities are normalized for better comparison and the band positions are accurate to $\pm 3 \text{ cm}^{-1}$. The spectrum of LiYMo_3O_8 shows well-defined bands at 723, 526, 474 and 447 cm^{-1} . Minor low-intensity bands at 841, 805 and 630 cm^{-1} , and two shoulder bands at ~ 560 and $\sim 430 \text{ cm}^{-1}$ are also seen. The IR spectrum of $\text{Mn}_2\text{Mo}_3\text{O}_8$ bears good resemblance to that of LiYMo_3O_8 , as can be expected, but shows minor shifts in the positions of the main high-intensity bands due to the replacement of Li and Y ions by Mn. Thus, the well-defined high- intensity bands in $\text{Mn}_2\text{Mo}_3\text{O}_8$ now appear at 733, 522, 484 and 454 cm^{-1} and the low- intensity bands at 838 and 636 cm^{-1} . In addition, two medium-intensity bands are also seen at 798 and 561 cm^{-1} in $\text{Mn}_2\text{Mo}_3\text{O}_8$ which were either low-intensity or shoulder bands in the spectrum of LiYMo_3O_8 (Fig. III.5).

From group theoretical considerations, we can expect nine IR -active modes of symmetry, ($3A_1 + 6E_1$) in both LiYMo_3O_8 and $\text{Mn}_2\text{Mo}_3\text{O}_8$. The observed spectra indeed show many of the expected IR-bands. The bands in the region of 725-735 cm^{-1} must be due to the stretching vibrations involving Mo-O bonds in these cluster compounds, whereas those in the region of 445-560 cm^{-1} must be due to Y-O/ Mn-O stretching and bending vibrations. The Li-O stretching vibrations are expected below 300 cm^{-1} , and thus not seen in the present study. It may be noted that a detailed factor group analysis and

temperature variation of the IR spectra, preferably on single crystals, are needed for a complete band -assignment in the above cluster compounds.

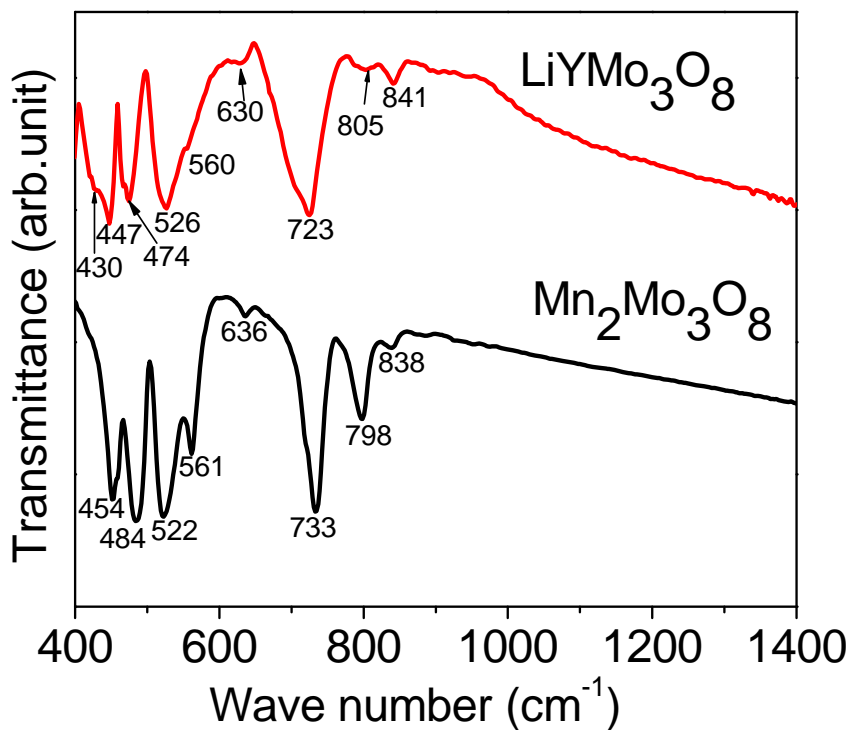


Fig. III. 5. The FT- IR spectra of LiYMo₃O₈ and Mn₂Mo₃O₈ recorded at room temperature. The numbers refer to band positions in cm⁻¹.

Raman scattering technique is a useful tool to non- destructively probe the lattice vibrational modes of metal oxides. The Raman peaks can also be correlated to the dielectric properties of ternary oxides. Presently, the temperature dependent Raman spectra on LiYMo₃O₈ and Mn₂Mo₃O₈ are reported for the first- time (Fig. III.6). The relative intensities are normalized for better comparison and the band positions are accurate to ± 3 cm⁻¹. Several first-order Raman active modes are expected from the Mo₃- cluster compounds under visible Raman excitation. For crystalline LiYMo₃O₈ (sp.gr., P3m1), maximum nine Raman- active modes ($3A_1 + 6E$) are allowed under group- theory selection rules, whereas for crystalline Mn₂Mo₃O₈ (sp.gr., P6₃mc), maximum 15 Raman-

active modes ($3A_1 + 6E_1 + 6E_2$) are allowed. However, due to lack of data on single crystals, it is difficult to carry out a detailed group theoretical analysis and assignment of peaks to particular phonon mode of a given symmetry. Furthermore, polycrystalline compounds do not obey Raman polarization selection rules, since the directions of the phonon wave vectors are randomly distributed with respect to the crystallographic axes.

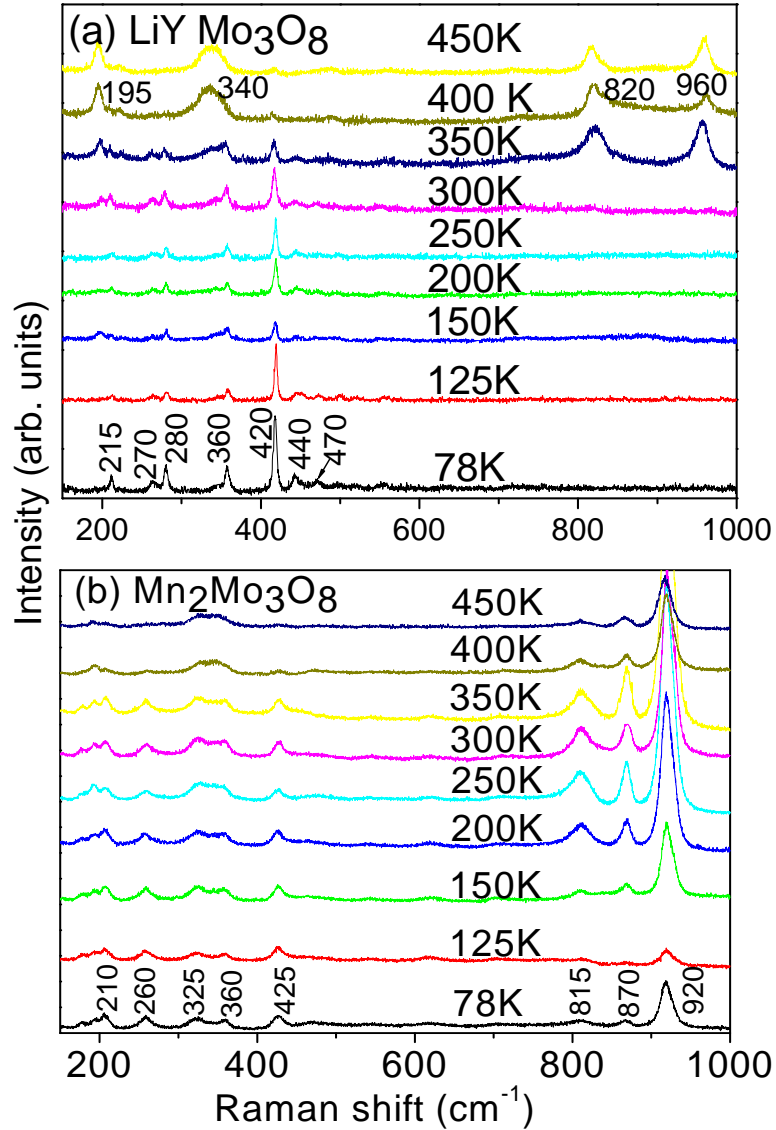


Fig.III.6. Raman spectra at various temperatures (78 – 450 K): (a) LiYMo_3O_8 and (b) $\text{Mn}_2\text{Mo}_3\text{O}_8$. The numbers refer to band positions in cm^{-1} .

The spectra in Fig. III.6 show first- order peaks within 100- 600 cm^{-1} along with some combinational or higher order modes in the range of 800- 1000 cm^{-1} . It may be noted that due to lattice disorder- induced broadening, only few Raman bands are prominent. The Raman line broadening can occur due to the doping/ alloying- induced compositional fluctuations arising from a random distribution of ions in the lattice. However, in the present case of LiYMo_3O_8 and $\text{Mn}_2\text{Mo}_3\text{O}_8$, there is no structural disorder since all the cations occupy specific crystallographic positions, as discussed earlier (Fig.III.1). Since a selected Raman mode frequency is related to the force constant and the reduced mass of the compound, the observed peaks due to the selected lattice modes below 450 cm^{-1} are due to the different crystal symmetries and the differences in the masses of (Li,Y) vs. Mn ions in the two compounds.

The spectrum of LiYMo_3O_8 at 78 K clearly shows peaks at 215, 280, 360 and 420 cm^{-1} of which the latter peak has the highest relative intensity. In addition, low intensity peaks are noted at 270, 440 and 470 cm^{-1} (Fig.III.6a). Thus, only seven modes are observed out of the nine expected Raman modes. With an increase in the temperature (T), the low-intensity peaks gradually disappear, and there is a decrease in the relative intensity of the main peaks along with some peak-broadening, as expected. But, no new peaks appear till 300 K is reached, where an additional low intensity peak at $\sim 195 \text{ cm}^{-1}$ is observed. Also, no higher-order combinational modes are seen till 300 K. The spectra in the range, 350-450 K clearly show that with an increase in T, the peak at $\sim 195 \text{ cm}^{-1}$ grows in intensity, the peak at 360 cm^{-1} is broadened and shifted to $\sim 340 \text{ cm}^{-1}$ and grows in intensity, whereas the 420 cm^{-1} peak intensity drastically decreases. Also, at T=350 K, the higher-order combinational modes are seen at ~ 820 and $\sim 960 \text{ cm}^{-1}$, whose intensity

increases with an increase in T. It is to be noted that the new peak at $\sim 195 \text{ cm}^{-1}$ seen at $T \geq 350 \text{ K}$ may be due to a specific Li-O vibration, enabled due to a minor structural phase transition to a different crystal symmetry in LiYMo_3O_8 . More detailed studies, especially on single crystals, are needed to clarify this aspect.

The Raman spectrum of $\text{Mn}_2\text{Mo}_3\text{O}_8$ at 78 K shows peaks at 210, 260, 325, 360 and 425 cm^{-1} of moderate relative intensity. In addition, two low-intensity peaks are noted at around 185 and 195 cm^{-1} (Fig.III.6b). Thus, only seven of the expected 15 Raman modes are observed in $\text{Mn}_2\text{Mo}_3\text{O}_8$. It may be noted that the 360 and 425 cm^{-1} bands are also seen in the spectra of LiYMo_3O_8 (viz., at 360 and 420 cm^{-1}), and thus possibly represent the $(\text{O}-(\text{Mo}-\text{Mo})_{\text{cluster}}-\text{O})$ and $(\text{Mo}-\text{O}-\text{Mo})$ bending vibrations. The peaks at and below 325 cm^{-1} might be due to the Mn-O bending vibrations, of the MnO_4 -tetrahedra and MnO_6 -octahedra in the structure. Unlike the case of LiYMo_3O_8 , the higher-order combinational modes are seen in $\text{Mn}_2\text{Mo}_3\text{O}_8$ even at 78 K, at 815, 870 and 920 cm^{-1} , the latter peak having a high relative-intensity. With an increase in the temperature, no new peaks appear and the relative-intensity of all the peaks with the wave number, $\omega \leq 425 \text{ cm}^{-1}$ remains almost the same in the T-range, 78-350 K. However, there is a decrease in the relative intensity of the main peaks along with some peak-broadening in the spectra at 400 and 450 K. Also, the intensities of all the higher-order combinational modes show a systematic increase with an increase in the temperature from 78-to-350 K, above which temperature, a decrease in intensity is clearly seen in the spectra at 400 and 450 K (Fig.III.6b). From the Raman spectral data it may be concluded that there are no phase transformations in $\text{Mn}_2\text{Mo}_3\text{O}_8$ in the T-range, 78-450 K.

III.3.3. Magnetic properties of $\text{Mn}_2\text{Mo}_3\text{O}_8$

Many years ago, magnetic studies on $\text{Mn}_2\text{Mo}_3\text{O}_8$ were carried out on single crystals [32, 33, 34] and on polycrystalline powders [35] prepared by reactions in sealed silica tubes. Results showed that the compound exhibits strongly anisotropic magnetic behavior, as expected of the compound with a layer structure, and at low temperatures, it orders ferrimagnetically with a Curie temperature, $T_C = 41.5$ K. It is known that in $\text{Mn}_2\text{Mo}_3\text{O}_8$, the two magnetic ions (Mn^{2+}) occupy tetrahedral and octahedral sites in the structure, and thus there are two magnetic sublattices, the interactions in each being ferromagnetic [32]. The magnetic field dependence below T_C showed that the moments are parallel to the crystallographic c-axis, but the value of spontaneous magnetization (M_s) was small at liq. He-temperatures, and interestingly it was found that, $M_s \rightarrow 0$ as $T \rightarrow 0$ K, an unusual behavior of a magnetic oxide system. This showed that the ferrimagnetic order in $\text{Mn}_2\text{Mo}_3\text{O}_8$ arises mainly due to the Mn-ions, whereas the Mo^{4+} ions do not carry any magnetic moment, possibly due to the trapping of the $4d^2$ -electrons in the strong Mo-Mo bonds in the structure.

The magnetic behavior of $\text{Mn}_2\text{Mo}_3\text{O}_8$ presently studied is shown in Fig. III.7a in the form of temperature (T) dependent magnetization data collected while cooling the sample under 1 kOe applied field. A paramagnetic behavior from 300 K to 50 K is seen followed by a strong peak at 39 K corresponding to the T_C . This value matches well with the reported T_C of 41.5 K on single crystal as well as on polycrystalline samples [32,35]. The inverse magnetic susceptibility (χ) as a function of T is well fitted to Curie-Weiss law ($\chi^{-1} = (T - \theta) / C$) above T_C , shown in the inset of Fig. III.7a. The fitted value of θ (paramagnetic Curie temperature) is -255 K and C, the Curie constant is 16.5 emu K/mol.

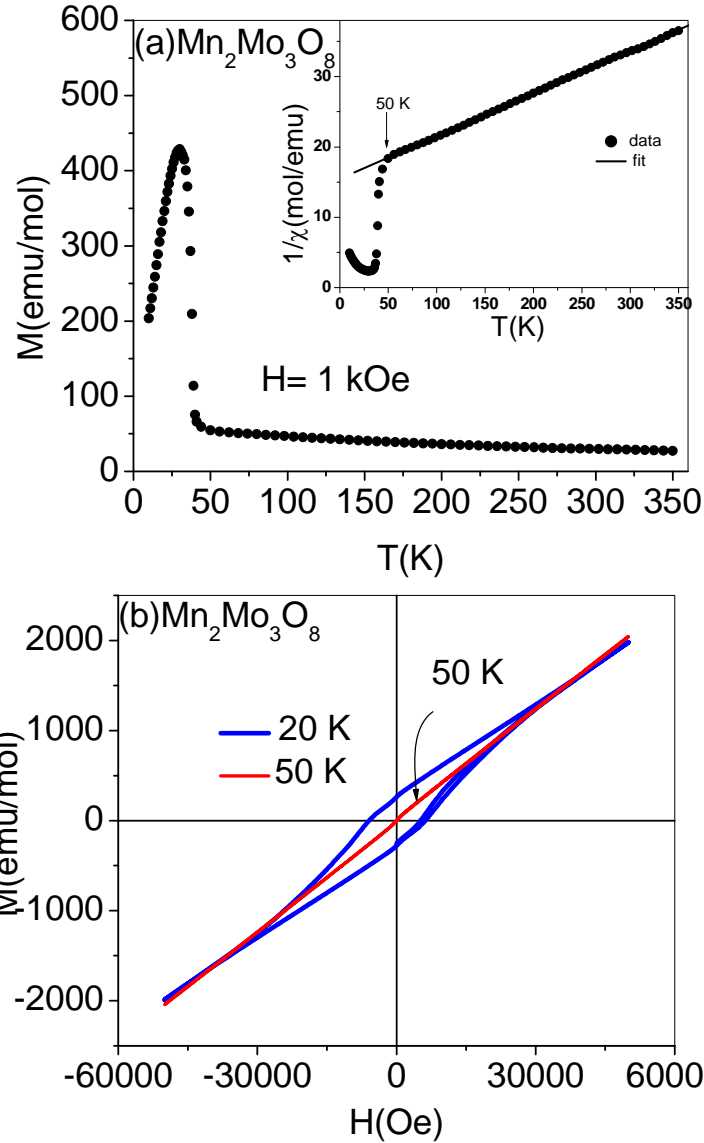


Fig. III.7. (a) Temperature dependent magnetization of $\text{Mn}_2\text{Mo}_3\text{O}_8$ at 1kOe applied magnetic field. The inset shows inverse magnetic susceptibility as a function of temperature and Curie- Weiss law fit to data. (b) Magnetic field dependent magnetization hysteresis loop at $T = 20$ and 50 K. The arrow shows the loop at 50 K which has minimum coercive field.

From this, the effective magnetic moment (μ_{eff}) is calculated from the equation, $\mu_{\text{eff}} = (2.828 \sqrt{C}) \mu_{\text{B}}$, where μ_{B} is Bohr magneton. Since there are two Mn-ions in one formula unit of $\text{Mn}_2\text{Mo}_3\text{O}_8$, the μ_{eff} per Mn ion is $5.74\mu_{\text{B}}$. This value agrees within 3% with the spin-only value for Mn^{2+} ion, viz., $5.92 \mu_{\text{B}}$. It is pertinent to compare the corresponding

value reported for $\text{Mn}_2\text{Mo}_3\text{O}_8$ by McAlister and Strobel [32]. They found anisotropic μ_{eff} $\perp c$ and $\mu_{\text{eff}} \parallel c$ values of $6.6 \mu_{\text{B}}$ and $7.4 \mu_{\text{B}}$, for measurement with $H \perp c$ and $H \parallel c$ axes, respectively. Thus, the expected μ_{eff} for the polycrystalline compound of $\text{Mn}_2\text{Mo}_3\text{O}_8$ will be $6.87 \mu_{\text{B}}$, which is 16% higher than the spin-only value. It must be mentioned that the impurity of 7.2 wt. % MoO_2 and disordered carbon, if any, present in the $\text{Mn}_2\text{Mo}_3\text{O}_8$ do not affect the above magnetic behavior. This is because both disordered carbon [36] and MoO_2 [37] show T-independent weak (Pauli-type) paramagnetism whose magnetic moments, in the 50-300 K range, are two orders of magnitude smaller than that measured for $\text{Mn}_2\text{Mo}_3\text{O}_8$ (~ 0.1 emu/g; Fig.III.7a). The presence of MnO , if any, also will not have any effect since it is known to be antiferromagnetic with a Neel temperature, $T_{\text{N}} = 118$ K [38], and we did not see an indication of that in the $1/\chi$ -T plot (Fig. III.7a, inset).

The isothermal magnetization at different temperatures ($T = 10, 20, 30, 40$ and 50 K) up to a maximum field of 50 kOe has been measured. For clarity, the M-H hysteresis loops only at $T = 20$ K and 50 K are shown in Fig.III.7b. The M-H plot at $T \geq 50$ K is linear without hysteresis up to the highest applied field, whereas the hysteresis loop develops below 40 K. However, the magnetization at $T = 20$ K does not saturate even at 50 kOe. A small remnant magnetization ($= 262$ emu/mol) and a large coercive field ($H_{\text{C}} = 5.9$ kOe) is seen at $T = 20$ K. Strangely, the hysteresis loop does close only for $H > 30$ kOe $> H_{\text{c}}$. The possible Mn-O impurities like MnO , Mn_3O_4 contributing to hysteresis loop is ruled out. Since, MnO is antiferromagnetic with $T_{\text{N}} = 118$ K, the possible contribution to hysteresis from MnO is avoided. Another possibility could be Mn_3O_4 , which shows ferrimagnetic behavior at $T_{\text{c}} = 42$ K. Since, the compound was prepared by carbothermal reduction method at 750 °C, Mn_3O_4 can't exist in these conditions. Hence,

it is clear that the hysteresis is due to the cluster compound, $\text{Mn}_2\text{Mo}_3\text{O}_8$. From M-H loops measured at different temperatures, the coercive field (H_C) and the magnetization at 50 kOe have been evaluated (Fig.III.8a). As can be seen, the H_C initially increases with lowering of temperature below 40 K, shows a peak at $T= 20$ K and then decreases. It is difficult to understand this behavior but it is possibly due to change in magnetic domain structure or domain wall pinning. The magnetization at 50 kOe does not increase, but decreases, below T_C . This behavior indicates that the magnetic anisotropy is probably strong in this material and the applied field of 50 kOe is unable to destroy the ferrimagnetic order completely. A strong magnetic anisotropy also leads to difference in zero field cooled (ZFC) and field cooled (FC) magnetization as shown in Fig. III.8b. As is clear, the FC- magnetization decreases up on lowering the temperature below 40 K and the difference between ZFC and FC- magnetization values persists even at 20 kOe ($> H_C$).

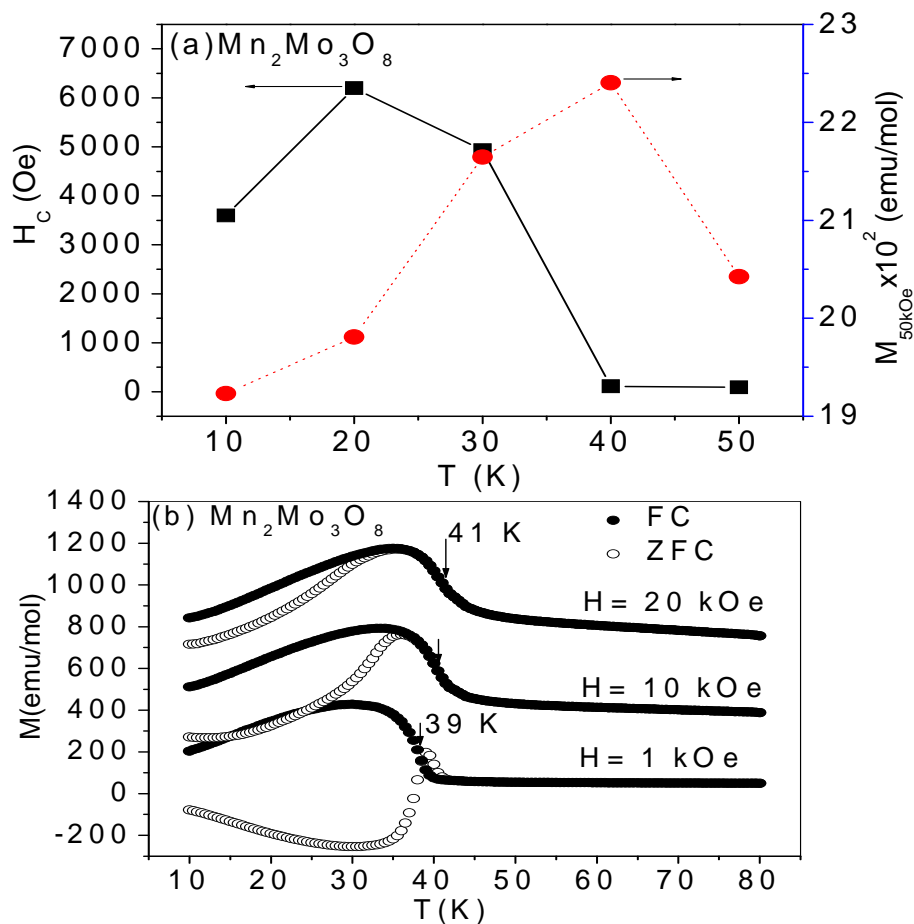


Fig.III.8. Magnetization data on $Mn_2Mo_3O_8$. (a) Temperature dependent coercive magnetic field (H_c) (left hand scale) and magnetization at 50 kOe (right hand scale). (b) Temperature dependent zero field cooled (ZFC) and field cooled (FC) magnetization under different magnetic fields. The inflexion point (arrow) refers to the T_C .

III.3.4. Electrochemical properties

III. 3.4.1. Li- cycling behavior of $LiYMo_3O_8$ and $LiHoMo_3O_8$

III.3.4.1.1. Galvanostatic cycling of $LiYMo_3O_8$

Fig. III.9a-c show the voltage vs. capacity profiles of $LiYMo_3O_8$ at the ambient temperature (24°C) and 50 °C. The galvanostatic cycling was carried out at a current density of 30 mA g^{-1} (0.08 C rate), in the voltage window of 0.005 - 3.0 V vs. Li. For $LiYMo_3O_8$, the cycling was carried out up to 120 and 60 cycles at 24 °C and 50 °C, respectively. The cells showed an open circuit voltage (OCV) ~ 2.6 V. The first-discharge

curve of LiYMo_3O_8 corresponding to the reaction with Li at 24 °C showed minor voltage plateau ~ 1.6 V and large plateau region at ~ 1.0 V extending up to a capacity of 170 (± 5) mAhg^{-1} (consumption of 3.2 moles of Li per mole of LiYMo_3O_8) (Fig. III.9 a). The existence of plateau is indicative of the two-phase region. In the range, 1.0 – 0.005 V, the profile shows a continuous decrease, indicating a single phase reaction. At the end of first-discharge cycle, the capacity is 305 (± 5) mAhg^{-1} (5.82 moles of Li per mole of LiYMo_3O_8) (Fig. III.9a).

During the first-charge cycle (Li-extraction), fairly large voltage plateau is seen at ~ 1.0 V, which coincides with that observed during the discharge-cycle. In addition, small but distinct voltage plateaux are seen at 1.4, 1.7 and 2.2 V for LiYMo_3O_8 (Fig. III.9a). However, except for the 1.0 V and 2.2. V plateaus, the capacity associated with the 1.4 and 1.7 V plateaus are very small, 5-15 mAhg^{-1} .

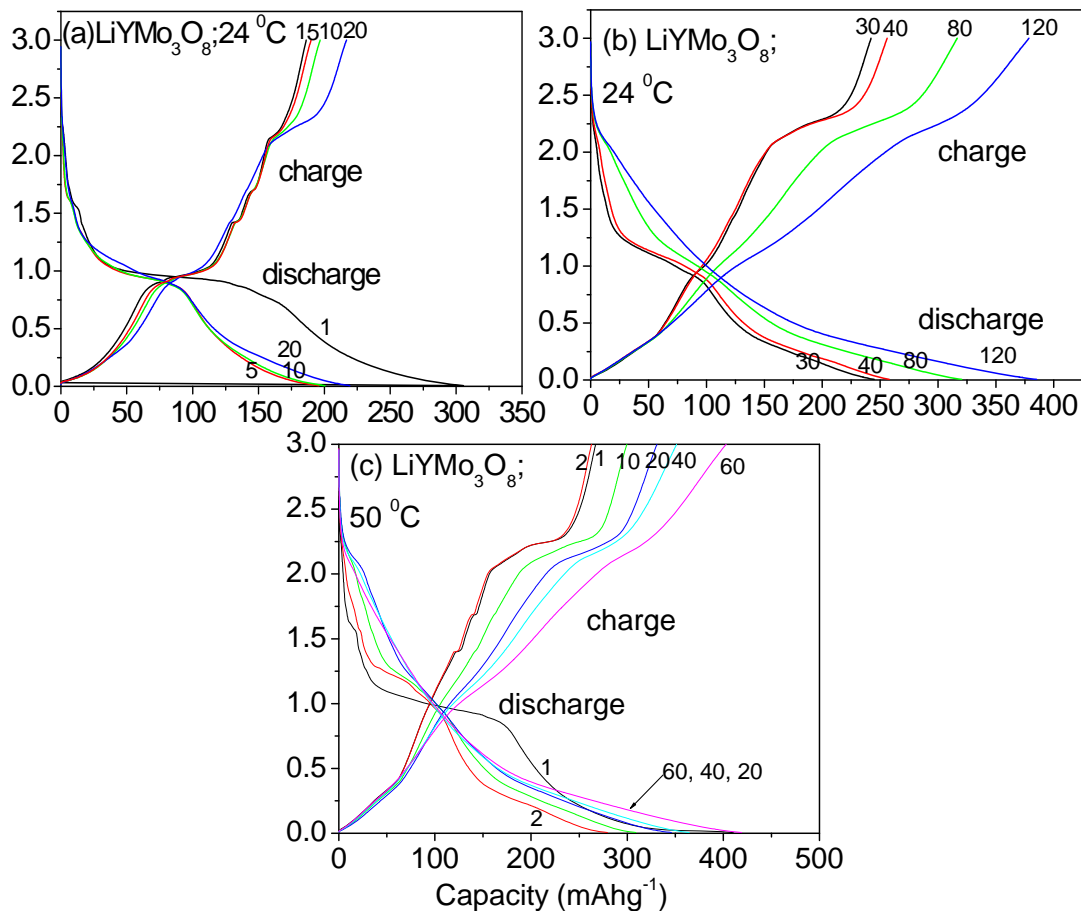


Fig. III.9. Galvanostatic charge-discharge curves. LiYMo_3O_8 (at 24 °C): (a) 1-20 cycles; (b) 30-120 cycles. At 50 °C: (c) LiYMo_3O_8 ; 1-60 cycles. The numbers indicate cycle number. Voltage range, 0.005-3.0 V vs. Li, at a current rate of 30 mA g^{-1} (0.08C).

The total first-charge capacities are $180 (\pm 5) \text{ mAhg}^{-1}$ (3.43 moles of Li per mole of LiYMo_3O_8). The irreversible capacity loss (ICL) during the first discharge – charge cycle is 2.39 moles of Li for LiYMo_3O_8 . During the 2 to 20 cycles, the charge and discharge profiles follow a similar pattern to that of the first cycle. However, the width of the 1 V-plateau region during discharge as well as the charge operation decreases with an increase in the cycle number. In the range 25-120 cycles, there is a qualitative change in the voltage – capacity profiles as shown in Fig. III.9b. The plateau region at ~1 V in the

discharge- profile and a broad plateau at ~ 2.2 V in the charge- profile are only noticeable, and all other minor voltage plateaus are eliminated.

The voltage- capacity curves at 50°C closely resemble those obtained at 24°C , but higher discharge and charge capacities were obtained. At 50°C , the first – discharge capacities are $410 (\pm 5) \text{ mAhg}^{-1}$ (~ 7.82 moles of Li), whereas the first- charge capacity is $267 (\pm 5) \text{ mAhg}^{-1}$ (~ 5.1 moles of Li) leading to an ICL of $143 (\pm 5) \text{ mAhg}^{-1}$ (2.72 moles of Li) for LiYMo_3O_8 (Fig. III.9c). The ICL noticed at 50°C is larger than the ICL measured at 24°C . In general, the ICL arises due to intrinsic nature of the oxide material, electrolyte decomposition followed by the formation of the solid electrolyte interphase (SEI) and the formation of a ‘polymeric film’ covering the nano-sized particles of metal or metal-oxide composites under the deep discharge (to 0.005 V vs. Li) conditions [6, 7, 8, 10, 13].

The capacity vs. cycle number plots of LiYMo_3O_8 , at 24° and at 50°C are shown in Fig.III.10. Both the discharge and charge capacities overlap well. The reversible capacity of LiYMo_3O_8 at 24°C increases from $200 (\pm 5) \text{ mAhg}^{-1}$ at the 10^{th} cycle to $385 (\pm 5) \text{ mAhg}^{-1}$ at the end of the 120^{th} . The latter of the two values corresponds to ~ 7.35 moles of Li. Assuming that $1\text{C} = 385 \text{ mAhg}^{-1}$, the current rate of 30 mAhg^{-1} corresponds to ~ 0.08 C. The coulombic efficiency (η) reaches 96-98%. For the LiYMo_3O_8 cycled at 50°C , the reversible capacity increases from $300 (\pm 5) \text{ mAhg}^{-1}$ (~ 5.7 moles of Li) at the 10^{th} cycle to $418 (\pm 5) \text{ mAhg}^{-1}$ (~ 8.0 moles of Li) at the end of the 60^{th} . The η is 94-98% in the range of 10-60 (40 cycles) cycles. The observed larger reversible capacity of LiYMo_3O_8 cycled at 50°C is due to the better electronic conductivity of the compound, larger ionic conductivity of the electrolyte and hence better electrode kinetics in comparison to the

performance at 24 °C. Possible reasons for the consistent increase in the reversible capacity on cycling, both at 24 °C and 50 °C are discussed later.

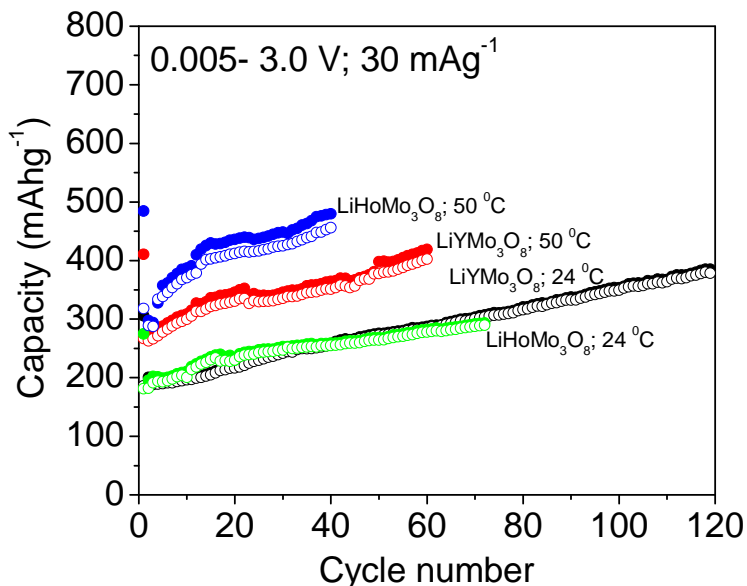


Fig.III.10. Capacity vs. cycle number plots of Li(Y/Ho)Mo₃O₈ at 24°C and 50°C (0.005-3.0 V; 30 mA g⁻¹). Closed symbol: Discharge capacity; Open symbol: Charge capacity.

III.3.4.1.2. Galvanostatic cycling of LiHoMo₃O₈

Galvanostatic charge-discharge cycling profiles of LiHoMo₃O₈ at 24 °C and 50 °C are shown in Fig III.11a-c. The cycling was carried out at a current density of 30 mA g⁻¹, in the voltage window, 0.005-3.0V vs. Li up to 70 and 40 cycles at 24 °C and 50 °C, respectively. The cells showed an open circuit voltage (OCV) about ~2.9 V. The first-discharge curve (Li-insertion reaction) at 24 °C showed minor voltage plateau ~1.51 V and a large plateau at ~1.0 Vs followed by a continuous decrease of the voltage up to the deep discharge limit, 0.005 V similar to that of LiYMo₃O₈. As can be seen, the capacity up to the end of the ~1 V- plateau region is 120 (±5) mAhg⁻¹ (~2.3 moles of Li per mole of LiHoMo₃O₈). The total first-discharge capacity is 275 (±5) mAhg⁻¹(~5.3 moles of Li).

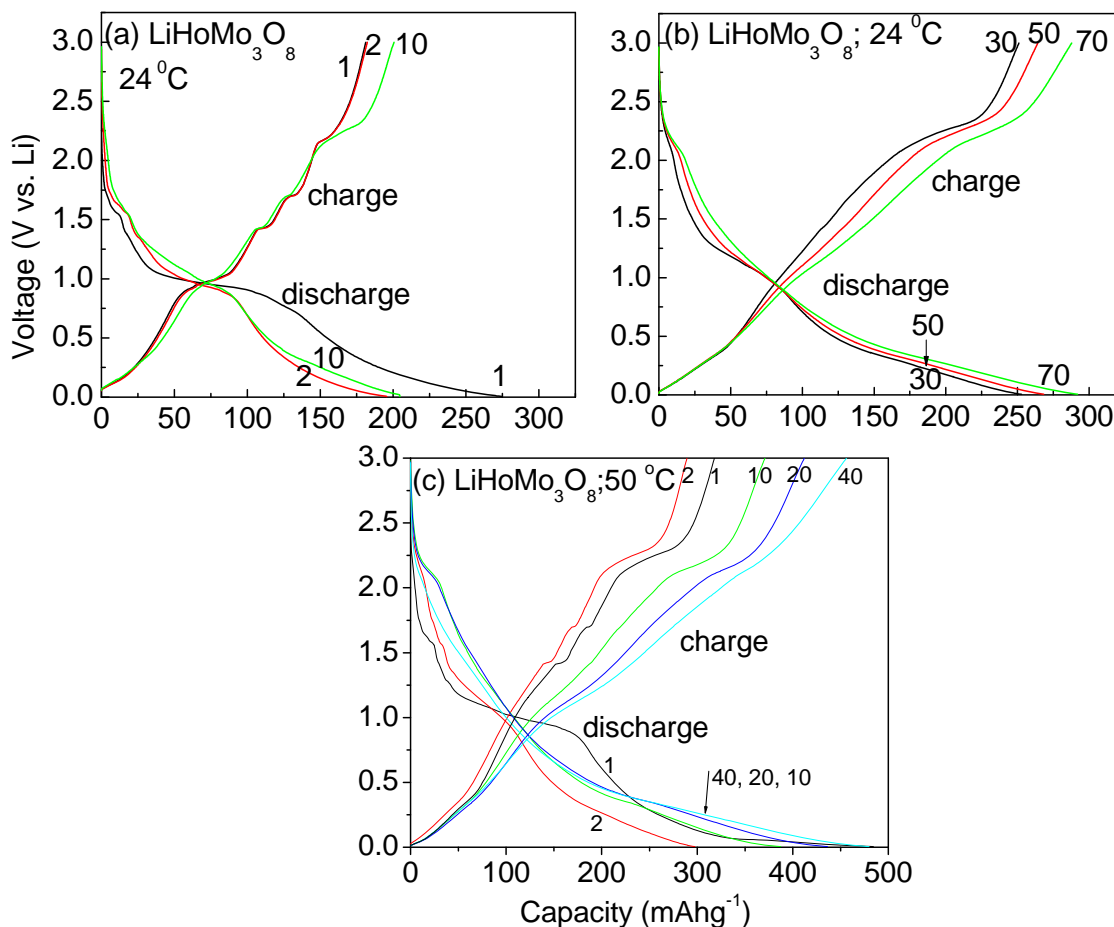


Fig. III.11. Galvanostatic charge-discharge curves. $\text{LiHoMo}_3\text{O}_8$ (at 24°C): (a) 1-10 cycles; (b) 30-70 cycles. At 50°C : (c) $\text{LiHoMo}_3\text{O}_8$; 1-40 cycles. The numbers indicate cycle number. Voltage range, 0.005-3.0 V vs. Li, at a current rate of 30 mA g^{-1} (0.1C).

During the first –charge cycle (Li-extraction) the voltage plateau regions at ~ 1.0 , 1.4, 1.7 and 2.2 V are clearly seen, as noticed in the case of LiYMo_3O_8 . However, except for the 1.0V and 2.2V voltage plateaus, the capacities associated with the 1.4V and 1.7V plateau regions are small ($\leq 20\text{ mAhg}^{-1}$). The total first-charge capacity is $180 (\pm 5)\text{ mAhg}^{-1}$ (~ 3.5 moles of Li). Thus, the irreversible capacity loss (ICL) during the first discharge – charge cycle is ~ 1.8 moles of Li. During the 2-20 cycles, the charge and discharge profiles follow a similar pattern with the voltage plateau regions clearly

reproduced as in the first cycle. However, the width of the 1 V-plateau region during discharge and charge operation decreases with an increase in the cycle number. The reversible capacities show an increasing trend from 180 (± 5) mAhg⁻¹. In the range 25-70 cycles, there is a qualitative change in the profiles as shown in Fig. III.11b. The plateau region at ~1 V in the discharge- profiles and at ~2.2 V in the charge- profiles are only noticeable and all other minor voltage plateaus are eliminated. The capacity vs. cycle number plot (Fig. III.10) shows that the reversible capacity increases and reaches 290(± 5) mAhg⁻¹ (5.6 moles of Li) at the end of 70 cycles. Assuming that 1C = 290 mAg⁻¹, the current rate corresponds to ~0.1 C. The coulombic efficiency (η) reaches 96-98 %.

Voltage vs. capacity profiles of LiHoMo₃O₈ recorded at 50 °C up to 40 cycles are shown in Fig.III.11c. The observed voltage plateaus during cycling are similar to those encountered at 24°C in the range 1-10 cycles. The first – discharge capacity is 480 (± 5) mAhg⁻¹ (9.2 moles of Li), whereas the first – charge capacity is 315 (± 5) mAhg⁻¹ (6.03 moles of Li) leading to an ICL of 165 mAhg⁻¹ which is larger than the ICL measured at 24 °C. From Fig. III.10, it is clear that the reversible capacity continuously increases with the cycle number and reaches 470 (± 5) mAhg⁻¹ (9.1 moles of Li) at the end of 40 cycles and almost matches with the first discharge capacity (9.2 moles of Li). The current rate of 30 mAg⁻¹ corresponds to ~0.06 C assuming that 1C = 470 mAg⁻¹. The coulombic efficiency (η) is 92-96% in the range of 12-40 cycles.

III. 3.4.1.3. Cyclic voltammetry of LiYMo₃O₈ and LiHoMo₃O₈

Cyclic voltammograms (CV) were recorded on cells with LiYMo₃O₈ and LiHoMo₃O₈ as the cathode at the slow scan rate of 58 μ Vs⁻¹, in the range 0.005-3.0 V, at 24 °C. The counter and reference electrode was Li-metal. During the first- cathodic scan

(reaction of LiYMo_3O_8 with Li), which started from OCV ~ 2.6 V, low intensity peaks are observed at 1.52 V, 1.34 V and 1.24 V (Fig.III.12a). In addition, an intense cathodic current peak, at 0.81 V with an onset at ~ 1.0 V appears followed by a shoulder peak at 0.69 V. During the first anodic scan (Li extraction), the CV shows a peak at 1.0 V preceded by a minor shoulder at 0.92 V. At higher potentials, three low intensity peaks are seen at 1.44, 1.71 and 2.20 V (Fig. III.12a).

The second cathodic scan of LiYMo_3O_8 slightly differs from the first cathodic scan. A low intensity split peak at 1.61 V and a well-defined peak at 0.88 V are clearly seen. The second cathodic and anodic peaks overlap well showing good reversibility. The hysteresis between the main cathodic and anodic potentials (at ~ 1 V) is fairly small, $\Delta V \sim 0.12$ V. The CVs overlap well up to the 10th cycle, and for clarity, the 5th cycle CV is shown in Fig. III.12b. The peaks in CV are the indication of existence of two-phase reaction and /or phase transformation occurring in the active material during cycling. As can be expected, the shape of the CV as well as the peak potentials in Figs.III.12a,b agree very well with the differential capacity (dQ/dV) vs. V plots extracted from the galvanostatic capacity vs. voltage profiles (of Fig. III.9 a, b). These are shown in Figs. III.12c, d.

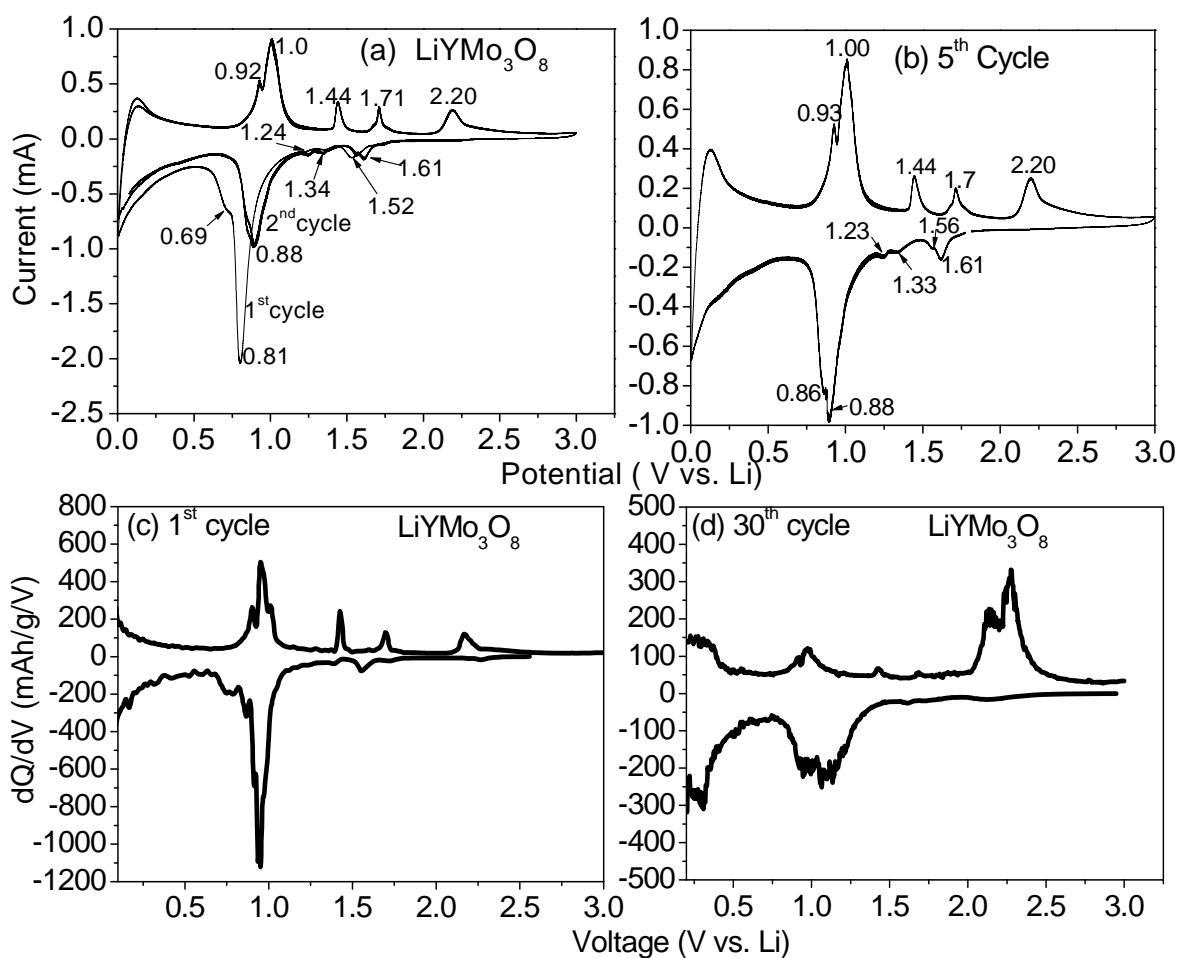


Fig. III.12. Cyclic voltammograms of LiYMo_3O_8 . (a) 1st and 2nd cycle, and (b) 5th cycle. Scan rate, $58 \mu\text{Vs}^{-1}$. Li- metal anode was the counter and reference electrode. Numbers represent the potentials in volts. (c) Differential capacity (dQ/dV) vs. Voltage plot extracted from the galvanostatic capacity- voltage profiles of Fig.III.9a for the 1st cycle. (d) Differential capacity vs. Voltage plot extracted from the galvanostatic capacity- voltage profiles of Fig.III.9b for the 30th cycle.

The CV-behavior of $\text{LiHoMo}_3\text{O}_8$ is exactly similar to the iso-structural compound LiYMo_3O_8 , and is in tune with the galvanostatic cycling properties (Fig. III.13 a, b). This is because both are Mo-cluster compounds with a similar crystal structure and differ only in terms of the counter ions, Y vs. Ho. During the first- cathodic scan minor peaks at

potentials 2.28, 1.72 and 1.51 V are seen followed by the increase of current with an onset of peak at ~ 1.0 V and an intense peak at ~ 0.81 V (Fig.III.13a).

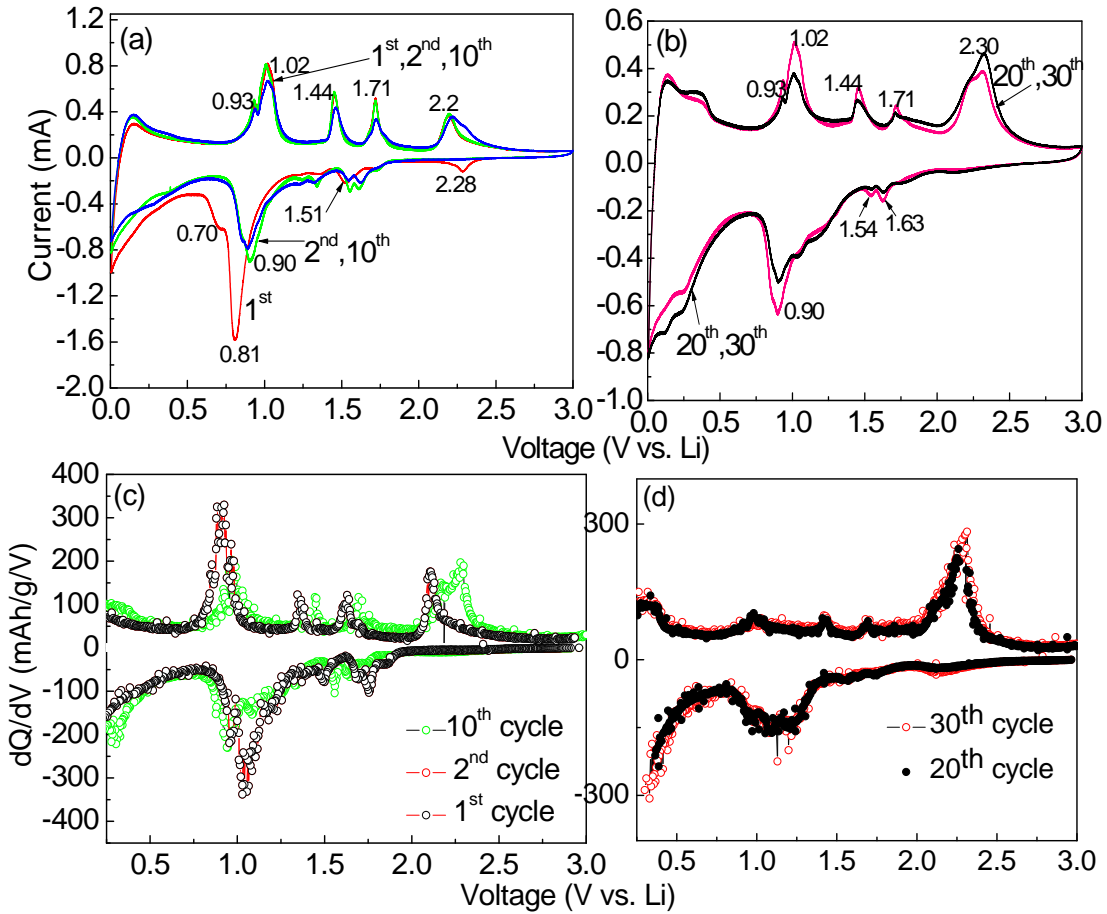


Fig. III.13. Cyclic voltammograms of $\text{LiHoMo}_3\text{O}_8$. (a) 1st, 2nd and 10th cycle, and (b) 20th and 30th cycle. Scan rate, $58 \mu\text{Vs}^{-1}$. Li- metal anode was the counter and reference electrode. Numbers represent the potentials in volts. (c) Differential capacity (dQ/dV) vs. Voltage plot extracted from the galvanostatic capacity- voltage profiles of Fig.III.11a for the 1st, 2nd, 10th cycle. (d) Differential capacity vs. Voltage plot extracted from the galvanostatic capacity- voltage profiles of Fig.III.11b for the 20th and 30th cycle.

During the first-charge cycle (anodic) curve a split peak at ~ 1.0 V is seen followed by peaks at 1.44, 1.71 and 2.2 V. The second cathodic sweep slightly differs from the first cathodic scan; the 2.28 V peak disappears and split peaks at ~ 1.6 V and a well-defined peak at ~ 0.90 V are clearly seen. The CVs remain essentially unchanged during the 10th,

20th and 30th cycle (Fig.III.13 a, b). The peaks in the CV are an indication of two-phase reaction and/or phase transformation taking place in the material during cycling. The differential capacity (dQ/dV) vs. voltage plots extracted from the voltage-capacity profiles of Fig.III.11a, b are analogous to the CV- profiles and these are shown in Fig.III.13c, d. As can be seen, there is very good correspondence between the respective peak voltages in both the CV and (dQ/dV) vs. V plots up to 10 cycles. However, there is a marked difference in the (dQ/dV) vs. V plots at the 20th and 30th cycle in that the anodic peak at ~1.0 V is absent. It is clear from Fig.III.13d that the average discharge-voltage for Li - insertion is ~1.1 V and the corresponding charge- voltage for Li- extraction is ~2.2 V.

III. 3.4.2. Li- cycling behavior of A₂Mo₃O₈ (A = Mn, Zn, Co)

III. 3.4.2.1. Galvanostatic cycling

III.3.4.2.1.1. Mn₂Mo₃O₈

The voltage vs. capacity profiles of Mn₂Mo₃O₈ at the current rate, 30 mA g⁻¹ up to 50 cycles at 24 °C are shown in Fig.III.14a. The cell showed an OCV of ~3.0 V. The first-discharge profile (Li-insertion reaction) for Mn₂Mo₃O₈ showed a rapid decrease in voltage with a minor voltage plateau at ~0.8 V. This is followed by a continuous decrease of the voltage up to ~0.3 V and a capacity of ~140 mAhg⁻¹ is reached. Thereafter, a slow and steady decrease of voltage occurs up to the deep discharge limit, 0.005 V. The total first-discharge capacity is 710(±5) mAhg⁻¹ (consumption of ~14 moles of Li per formula unit of Mn₂Mo₃O₈). The first-charge curve smoothly increases in voltage up to ~1.3 V, giving a capacity of ~200 mAhg⁻¹, followed by a broad plateau extending up to ~1.8 V, giving an additional ~220 mAhg⁻¹. Thereafter, the voltage rises fairly continuously up to the charge limit of 3.0 V. The total first-charge capacity is 565 (±5) mAhg⁻¹

corresponding to the extraction of ~ 11 moles of Li per formula unit. Thus, the ICL is 3 moles of Li ($\sim 145 \text{ mAhg}^{-1}$). During the second discharge, the voltage continuously decreases up to $\sim 0.5 \text{ V}$, followed by a large plateau extending up to a capacity of $\sim 450 \text{ mAhg}^{-1}$, and thereafter it decreases smoothly up to 0.005 V . The total second-discharge capacity is $560 (\pm 5) \text{ mAhg}^{-1}$ (~ 11 moles of Li), and matches well with the first-charge capacity. The second-charge profile is similar to that of the first-charge profile, and gives a total extraction capacity of $530 (\pm 5) \text{ mAhg}^{-1}$, slightly smaller than the first-charge capacity.

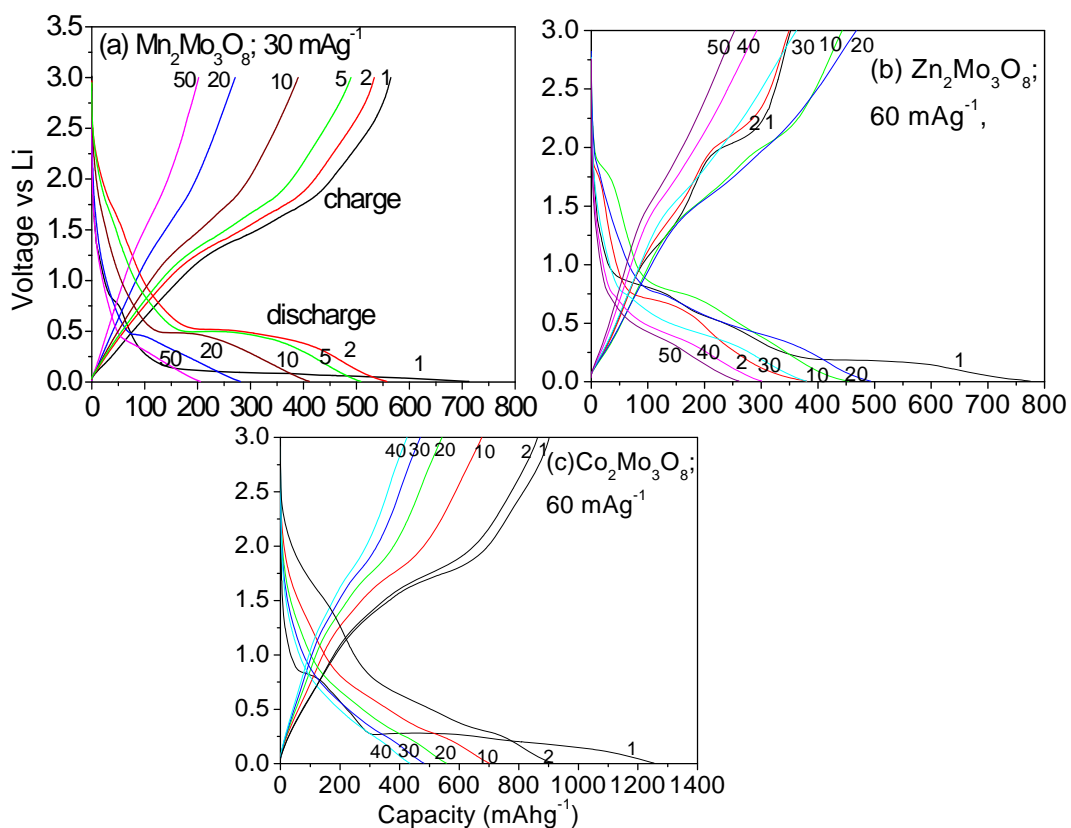


Fig. III.14. Galvanostatic charge-discharge curves. (a) $\text{Mn}_2\text{Mo}_3\text{O}_8$; 1-50 cycles, (b) $\text{Zn}_2\text{Mo}_3\text{O}_8$; 1-50 cycles and (c) $\text{Co}_2\text{Mo}_3\text{O}_8$; 1-40 cycles. The numbers indicate cycle number. Voltage range, 0.005-3.0 V vs. Li.

With an increase in the cycle number, the voltage plateau regions during both discharge and charge operations decrease continuously, signifying a continuous loss of capacity as is clear in Fig. III.14a. The capacity vs. cycle number plot indicates a drastic capacity-fading in $\text{Mn}_2\text{Mo}_3\text{O}_8$ up to about 25 cycles, followed by a smaller decrease in the range 25-50 cycles (Fig. III.15a). The reversible capacity at the 50th cycle is only 205 (± 5) mAhg^{-1} (~ 4 moles of cyclable Li). The coulombic efficiency is $\sim 94-96\%$ during the first 25 cycles, and approaches $\sim 98\%$ at the 50th cycle.

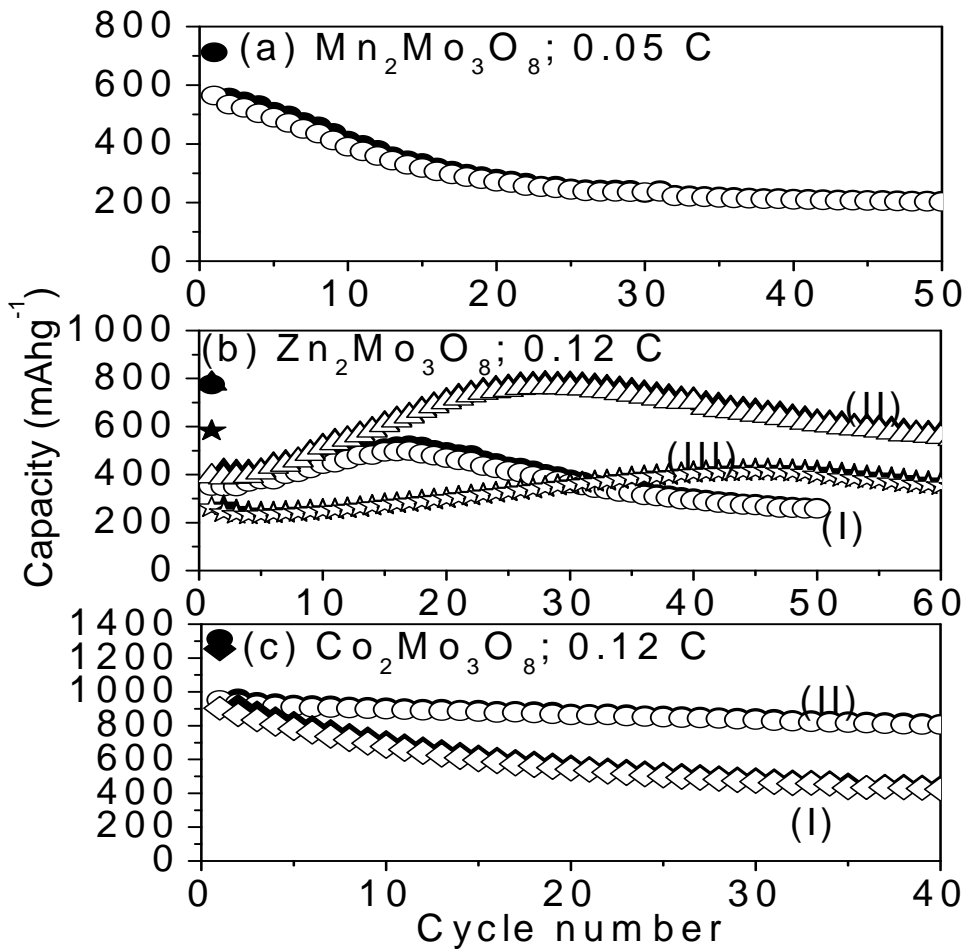


Fig. III.15. Capacity vs. cycle number plots. (a) $\text{Mn}_2\text{Mo}_3\text{O}_8$, (b) $\text{Zn}_2\text{Mo}_3\text{O}_8$: (I) Bare electrode; (II) Electrode heat-treated at 300°C for 12 h in Ar- atm. and (III) Bare electrode at 180 mAhg^{-1} . (c) $\text{Co}_2\text{Mo}_3\text{O}_8$: (I) Bare electrode and (II) Electrode heat-treated at 300°C for 12 h in Ar- atm. Voltage range: 0.005- 3.0 V vs. Li. Closed symbol: Disch. capacity; Open symbol: Charge capacity.

III.3.4.2.1.2. $\text{Zn}_2\text{Mo}_3\text{O}_8$

The galvanostatic discharge- charge cycling of $\text{Zn}_2\text{Mo}_3\text{O}_8$ was carried out at a current density of 60 mA g^{-1} , in the voltage range of 0.005-3.0 V up to 50 cycles at room temperature (Fig. III.14b). During the first discharge cycle, the voltage drops from the open circuit voltage (OCV $\sim 2.5 \text{ V}$) to $\sim 0.9 \text{ V}$ in a smooth fashion which indicates the intercalation of Li- ions up to a capacity of $\sim 50 \text{ mAh g}^{-1}$ ($\sim 1.0 \text{ Li}$ per formula unit of $\text{Zn}_2\text{Mo}_3\text{O}_8$). This is followed by two different voltage plateaus at 0.7 and 0.4 V, indicating a two- phase reaction with a net capacity of $400 (\pm 5) \text{ mAh g}^{-1}$ (8.2 moles of Li). A sloping region starting from $\sim 0.2 \text{ V}$ extends up to the deep discharge of 0.005 V vs. Li. The total first- discharge capacity is $775 (\pm 5) \text{ mAh g}^{-1}$ ($\sim 15.8 \text{ moles of Li}$) (Fig. III.14b).

During the first-charge cycle (Li-extraction), a small voltage plateau is seen at $\sim 1.3 \text{ V}$, followed by a fairly large voltage plateau at $\sim 2.1 \text{ V}$ (two-phase reaction; (Fig. III.14b)). The total first-charge capacity is $350 (\pm 5) \text{ mAh g}^{-1}$ ($\sim 7.1 \text{ moles of Li}$). Thus, the irreversible capacity loss (ICL) during the first discharge – charge cycle is 8.7 moles of Li . The discharge- charge profiles from 2 - to - 10 cycles behave similarly to that of the first cycle. However, the profiles from 10-to-50 cycles are different from the first cycle, in that the extent of voltage plateaus noticed at ~ 1.3 and $\sim 2.1 \text{ V}$ in the charge- profile decrease with an increase in the cycle number.

The capacity vs. cycle number plots of $\text{Zn}_2\text{Mo}_3\text{O}_8$ and the electrode heat- treated at 300°C for 12 h in Ar- gas are shown in Fig.III.15b. The reversible capacity of $\text{Zn}_2\text{Mo}_3\text{O}_8$ increases from $350(\pm 5) \text{ mAh g}^{-1}$ ($\sim 7.1 \text{ moles of Li}$) at the 2nd cycle to $500 (\pm 5) \text{ mAh g}^{-1}$ ($\sim 10.2 \text{ moles of Li}$) at the 17th cycle. After this, capacity- fading is noticed and reaches $255 (\pm 5) \text{ mAh g}^{-1}$ ($\sim 5.2 \text{ moles of Li}$) at the end of 50th cycle. The capacity- fading

is 48% in the range of 17-50 cycles. Assuming that $1C = 500 \text{ mA g}^{-1}$, the current rate of 60 mA g^{-1} corresponds to 0.12 C. For the heat-treated electrode of $\text{Zn}_2\text{Mo}_3\text{O}_8$, the reversible capacity increases from $390 (\pm 5) \text{ mA h g}^{-1}$ (~ 8.0 moles of Li) at the 2nd cycle to $760 (\pm 5) \text{ mA h g}^{-1}$ (~ 15.5 moles of Li) at the end of the 30th cycle. A decrease in capacity is noticed in the range 30- 50 cycles (20% drop) and reaches $610 (\pm 5) \text{ mA h g}^{-1}$ (~ 12.4 moles of Li) at the end of 50th cycle.

The observed larger reversible capacity of the heat-treated electrode of $\text{Zn}_2\text{Mo}_3\text{O}_8$ is due to the homogeneous distribution of active material in the electrode and better inter-particle contact and with the current collector. A similar enhancement of reversible capacity and better cycling stability was observed in Fe_2O_3 by Li et al [39]. At a higher current density of 180 mA g^{-1} (0.36 C), the $\text{Zn}_2\text{Mo}_3\text{O}_8$ shows a first-discharge capacity of $580 (\pm 5) \text{ mA h g}^{-1}$ (~ 11.8 Li) and first-charge capacity of $260 (\pm 5) \text{ mA h g}^{-1}$ (~ 5.3 Li). The reversible capacity increases from $240 (\pm 5) \text{ mA h g}^{-1}$ (~ 4.9 Li) at the 7th cycle to $415 (\pm 5) \text{ mA h g}^{-1}$ (~ 8.5 Li) at the end of 45th cycle. A decrease in capacity is noticed after 45th cycle and the value reaches $365 (\pm 5) \text{ mA h g}^{-1}$ (~ 7.4 Li) at the end of 60th cycle (Fig. III.15b). In all cases, the coulombic efficiency is 96-98 %.

III.3.4.2.1.3. $\text{Co}_2\text{Mo}_3\text{O}_8$

The voltage vs. capacity profiles of $\text{Co}_2\text{Mo}_3\text{O}_8$ at the current rate, 60 mA g^{-1} up to 40 cycles are shown in Fig.III.14c. The first-discharge profile (Li-insertion reaction) showed a rapid decrease in voltage from OCV (~ 2.5 V) to ~ 0.8 V, followed by a continuous decrease of the voltage up to ~ 0.25 V. Thereafter, a slow and steady decrease of voltage occurs up to the deep discharge limit, 0.005V. The total first-discharge capacity is $1250 (\pm 5) \text{ mA h g}^{-1}$ (~ 25 moles of Li per mole of $\text{Co}_2\text{Mo}_3\text{O}_8$). The first-charge

curve smoothly increases in voltage up to ~ 1.5 V, followed by a broad plateau extending up to ~ 1.8 V. Thereafter, the voltage rises fairly continuously up to the charge limit of 3.0 V. The total first-charge capacity is $900(\pm 5)$ mAhg⁻¹ (extraction of ~ 18 moles of Li). Thus, the ICL is 7 moles of Li (~ 350 mAhg⁻¹). During the second discharge, the voltage continuously decreases up to ~ 0.75 V, followed by a large plateau, and thereafter it decreases smoothly up to 0.005 V. The total second- discharge capacity is $915 (\pm 5)$ mAhg⁻¹ (18.3 moles of Li), which is almost same as the first- charge capacity thereby showing good reversibility. The discharge-charge profiles during 2- 40 cycles are similar to that of the first discharge-charge profile, except that the voltage plateau noticed at ~ 1.8 V in the first- charge profile slowly disappears with an increase in the cycle number.

The capacity vs. cycle number plots of the bare and heat- treated (300 °C; 12 h; Ar) electrodes of Co₂Mo₃O₈ up to 40 cycles are shown in Fig. III.15c. As can be seen, continuous capacity-fading occurs in both cases. For the bare electrode, the reversible capacity decreases from $900 (\pm 5)$ mAhg⁻¹ (~ 18 moles of Li) at the first- cycle to $425 (\pm 5)$ mAhg⁻¹ (~ 8.5 moles of Li) at the end of 40th cycle (capacity- fading is 52%), where as for the heat- treated electrode the capacity decreases from $950 (\pm 5)$ mAhg⁻¹ (~ 19 moles of Li) at the first- cycle to $805 (\pm 5)$ mAhg⁻¹ (~ 16.1 moles of Li) at the end of 40th cycle (capacity- fading is 15%). The coulombic efficiency is 96-98 % for both the cases.

III. 3.4.2.2. Cyclic voltammetry

III. 3.4.2.2.1. Mn₂Mo₃O₈

The cyclic voltammograms (CVs) of Mn₂Mo₃O₈ in the range 1-28 cycles are shown in Figs. III.16a, b. As can be seen, during the first cathodic scan three feeble-intensity current peaks are observed in the range 1.7-1.25 V, and a medium intensity peak

at 0.77 V. This is followed by a large increase in the cathodic current starting at ~ 0.5 V, and extending up to the deep discharge limit, 0.005 V. During the first anodic scan, three low intensity peaks at 1.42 V, 1.71 V and 1.79 V are seen.

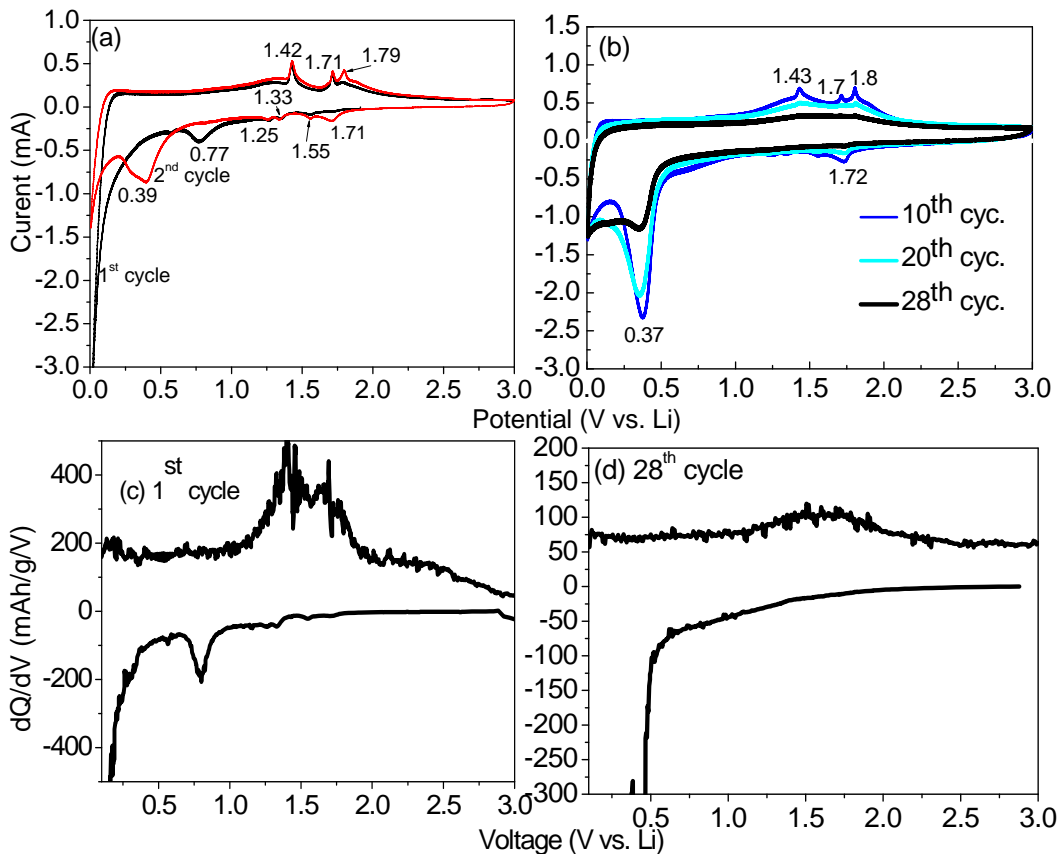


Fig. III.16. Cyclic voltammograms of $\text{Mn}_2\text{Mo}_3\text{O}_8$. (a) 1st and 2nd cycle, and (b) 10th, 20th, and 28th cycle. Scan rate, $58 \mu\text{Vs}^{-1}$. Li- metal anode was the counter and reference electrode. Numbers represent the potentials in volts. (c) Differential capacity (dQ/dV) vs. Voltage plot extracted from the galvanostatic capacity- voltage profiles of Fig.III.14a for the 1st cycle. (d) Differential capacity vs. Voltage plot extracted from the galvanostatic capacity- voltage profiles of Fig. III.14a for the 28th cycle.

In the second cathodic scan, the three feeble-intensity current peaks in the range 1.7-1.25 V are still observed, but the medium intensity peak is now shifted from 0.77 V to 0.39 V (Fig.III.16a). On the other hand, the second anodic scan is almost identical to the first anodic scan. The CV profiles remain the same for the 10th and 20th cycles. However, as can be seen in Fig.III.16b, there is a qualitative change in the CV profile of the 28th cycle

in that while the cathodic scan still shows the peak at 0.37 V, but with small intensity, the anodic scan shows only a broad and feeble hump in the range, 1.4-1.8 V. Thus, the decrease in the area under the cathodic and anodic peaks is an indication of the capacity-fading. This is also reflected in the differential capacity vs. voltage plots extracted from the galvanostatic profiles (Fig.III.14a), shown in Figs.III.16c, d, respectively for the 1st and 28th cycle.

III. 3.4.2.2.2. $Zn_2Mo_3O_8$

The CVs of $Zn_2Mo_3O_8$, up to 10 cycles, were recorded at the slow scan rate of 58 $\mu V s^{-1}$, in the range 0.005-3.0 V, at ambient temperature and are shown in Fig.III.17a. During the first- cathodic scan (reaction of $Zn_2Mo_3O_8$ with Li), which started from OCV ~ 2.0 V, two medium- intensity peaks are observed at 0.75 V and 0.42 V. This is followed by a peak with an onset at ~ 0.3 V and extending up to the deep discharge limit of 0.005 V. During the first anodic scan (Li extraction), the CV shows a low- intensity peak at ~ 1.2 V followed by a peak at 2.04 V (Fig. III.17a). The second cathodic scan of $Zn_2Mo_3O_8$ slightly differs from the first cathodic scan, in that there is a peak at ~ 1.84 V and the peak at 0.75 V is absent and the intensity of the peak at 0.42 V increases. The cathodic peak at 0.42 V is shifted to a higher potential (0.65 V) with an increase in the cycle number. The second anodic scan is analogous to the first anodic scan. The CVs of 1-6 cycles overlap well showing good reversibility of the system (Fig. III.17a). The hysteresis between the main cathodic and anodic potentials (at ~ 2 V) is fairly small, $\Delta V \sim 0.2$ V.

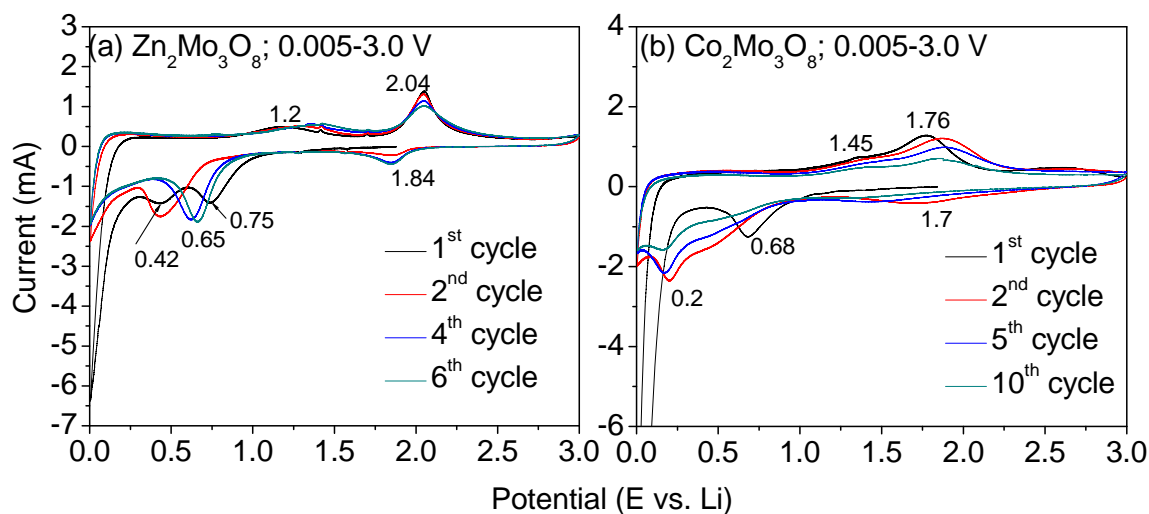


Fig.III.17. Cyclic voltammograms. (a) $\text{Zn}_2\text{Mo}_3\text{O}_8$; 1-6 cycles. (b) $\text{Co}_2\text{Mo}_3\text{O}_8$; 1-10 cycles. Scan rate is $58 \mu\text{Vs}^{-1}$. Numbers represent the potentials in volts.

III. 3.4.2.2.3. $\text{Co}_2\text{Mo}_3\text{O}_8$

The CVs of $\text{Co}_2\text{Mo}_3\text{O}_8$ from 1-10 cycles are shown in Fig. III.17b. During the first cathodic scan, a broad intense peak is noticed at 0.68 V, followed by a large increase in cathodic current starting at ~ 0.25 V and extending up to the deep discharge limit, 0.005 V. During the first anodic scan, a low-intensity peak at ~ 1.45 V is noticed, followed by a broad and intense peak at ~ 1.76 V. In the second cathodic scan, a broad peak is seen at ~ 1.7 V and the broad peak at 0.68 V observed during the first cathodic scan, is absent and a new peak developed at ~ 0.2 V (Fig. III.17b). On the other hand, the second anodic scan is almost identical to the first anodic scan with a slight shift of the anodic peak towards higher potential. The CV profiles remain the same for the 2–10 cycles. However, the observed decrease in the area under the cathodic and anodic peaks is an indication of the capacity-fading in the system. From Figs. III.17a and b, it is clear that the CV-behavior of $\text{Co}_2\text{Mo}_3\text{O}_8$ differs from that of $\text{Zn}_2\text{Mo}_3\text{O}_8$, and is in tune with the galvanostatic cycling properties, where continuous capacity-fading was noted in the case of $\text{Co}_2\text{Mo}_3\text{O}_8$. This

peculiar behavior of $\text{Zn}_2\text{Mo}_3\text{O}_8$ and $\text{Co}_2\text{Mo}_3\text{O}_8$ is some what surprising as both the compounds are iso-structural and only differ in terms of different metal cations. We note that the CV-behavior and galvanostatic cycling properties of $\text{Co}_2\text{Mo}_3\text{O}_8$ are similar to the iso-structural compound, $\text{Mn}_2\text{Mo}_3\text{O}_8$.

III.3.5. Ex-situ XRD

III.3.5.1. LiYMo_3O_8 and $\text{LiHoMo}_3\text{O}_8$

The XRD patterns of the bare and discharged/charged electrodes to selected voltages during the first-discharge, and in the charged-state (at 3.0 V) after the 1st and 32nd cycle are shown in Fig.III.18 for the LiYMo_3O_8 and $\text{LiHoMo}_3\text{O}_8$ vs. Li systems. The y- axis values are normalized for all patterns except for the bare electrode, Cu- and Al- metals, to allow comparison after discharge/ charge at various voltages. As can be seen, the lines due to the Cu-foil substrate and Al-sample holder are predominantly noticed. However, many lines due to the active material are clearly delineated and the Miller indices are shown.

From Fig. III.18A, it is clear that the intensities of the lines corresponding to Miller indices, (101), (002), (003) and (103) are affected during the discharge/charge reaction with Li. Thus, during the first-discharge, at voltage 0.5 V, there is a significant decrease in the intensity and /or broadening of the lines, (101) and (002) and disappearance of lines (003) and (103). In addition, two new lines appear at $2\theta = 33.8^\circ$ and 55.0° and grow in intensity. In addition, the (001)- peak is split into two peaks, though it is not clearly seen in Fig. III.18A due to the overlapped high- intensity peaks at $2\theta = 17^\circ$. This indicates the formation of a Li-intercalated phase, $\text{Li}_x(\text{LiYMo}_3\text{O}_8)$, and agrees with the voltage plateau observed at ~ 1 V in the galvanostatic voltage-capacity profile (Fig. III.9a)

and a well-defined peak at ~ 0.8 V in the CV (Fig. III.12a). In the XRD pattern taken after discharging to 0.005 V, the lines due to the parent compound are not seen, and the peak at $2\theta \sim 33.8^\circ$ is slightly broadened and retained. The pattern taken at the end of the 1st charge, at 3.0 V, shows lines due to the parent compound, LiYMo_3O_8 and that of the Li-intercalated phase ($2\theta = 33.8^\circ$ and 55.0°). The pattern taken after the 32nd charge is similar to the above (Fig. III.18A).

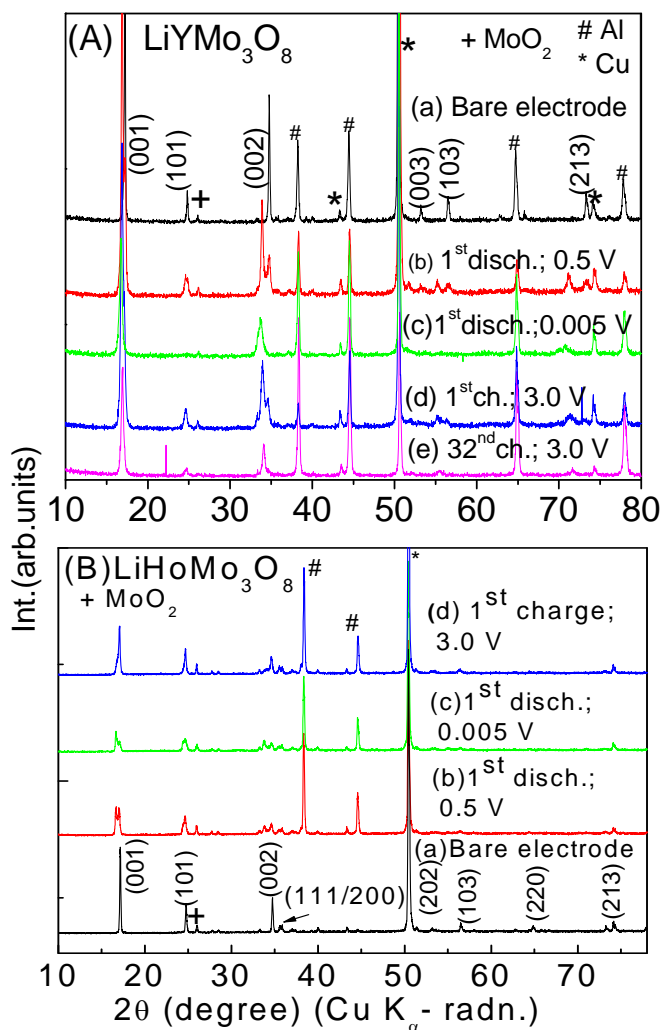


Fig.III.18. XRD patterns of the cycled electrodes: (A) LiYMo_3O_8 and (B) $\text{LiHoMo}_3\text{O}_8$. Discharge/charge voltages and the cycle number are indicated. Miller indices assigned to the peaks are shown. The symbols (*,#) represent the lines due to Cu-metal (substrate of the electrode) and Al -metal (sample holder). MoO_2 impurity (+) is also shown. The y-axis values are normalized for better comparison at various voltages.

For $\text{LiHoMo}_3\text{O}_8$, as can be seen in Fig.III.18B, the (001), (101) and (002) peaks in the XRD pattern of the bare electrode are split in to doublet peaks in the patterns of the electrode recorded after the first-discharge to 0.5 V and 0.005 V. This can be interpreted as due to the coexistence of two phases, a Li-intercalated, $\text{Li}_{(1+x)}\text{HoMo}_3\text{O}_8$ with $x \leq 1$, and the host compound. At first- discharge (0.005 V), it is clear that the intensity of the (001) peak is smaller than that of the Li-intercalated phase. The pattern recorded after the first-charge (3.0 V) shows only the lines due to the host compound and those due to the Li-intercalated phase are practically absent. Thus, the results show that, contrary to the expectations, the host crystal structure is not completely destroyed during the first – discharge to 0.005 V vs. Li. This is probably due to the highly insulating nature of the compound and Li is not able to penetrate completely in to the bulk of the sub-micron size particles.

III.3.5.2. $\text{A}_2\text{Mo}_3\text{O}_8$ (A = Mn, Co)

Ex-situ XRD data on the $\text{A}_2\text{Mo}_3\text{O}_8$ (A = Mn, Co) during the 1st discharge, and in the charged-state, at 3.0V, at the end of the 1st cycle are shown in Fig. III.19. The XRD patterns of the bare electrode, along with the Miller indices are also shown. It is clear that the behavior is completely different from that of the LiYMo_3O_8 -Li system. No additional line(s) due to Li-intercalation are evident in the patterns taken at 1.5 V (1.0 V for A = Co) and at 0.5 V but only a decrease in intensity and slight broadening of the major lines of the parent compounds. On the other hand, the XRD patterns taken at the end of the 1st discharge (0.005 V), as well as at the end of the 1st charge (3.0V), are completely devoid of lines of the parent compound, $\text{A}_2\text{Mo}_3\text{O}_8$ indicating complete amorphization (crystal

structure destruction) of the lattice. Li-cycling must be occurring in this system via ‘conversion reaction’ involving Mo-oxides.

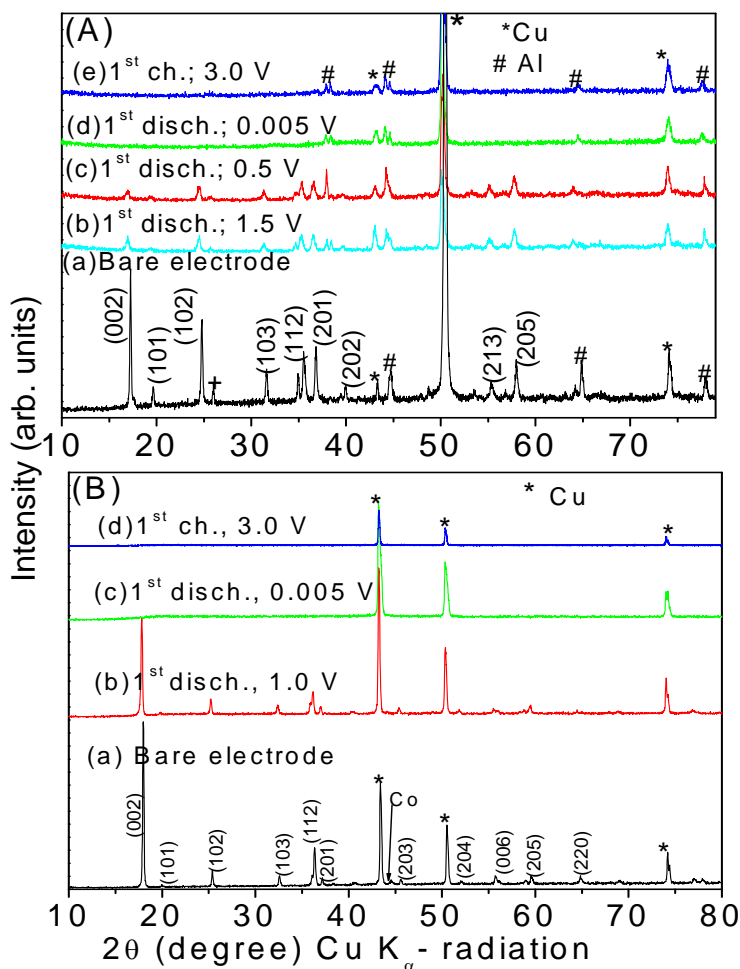


Fig.III.19. XRD patterns of the cycled electrodes: (A) Mn₂Mo₃O₈ and (B)Co₂Mo₃O₈. Discharge/charge voltages and the cycle number are indicated. Miller indices assigned to the peaks are shown. The symbols (*,#) represent the lines due to Cu-metal (substrate of the electrode) and Al –metal (sample holder) and + represents lines due to MoO₂. The y-axis values are normalized for better comparison at various voltages.

III.3.6. Ex-situ TEM of LiYMo₃O₈ and LiHoMo₃O₈

Figs.III.20 a-d show the TEM photographs and HR-TEM lattice images of the LiYMo₃O₈ and LiHoMo₃O₈ electrode material in the charged-state (3.0V) after the 1st and 70th cycle, respectively. As can be seen, due to the well-known ‘electrochemical-grinding

effect' during cycling, the active material particles have been reduced to nm-size (Figs.III.20 a, c). The lattice images show that the crystal structure has not been destroyed, and the d-spacings 5.18 and 5.15 (± 0.002) Å evaluated from the lattice fringes agree with that corresponding to Miller index, (001) of the host compound, LiYMo_3O_8 and $\text{LiHoMo}_3\text{O}_8$, respectively. Hence, it is concluded that in the LiYMo_3O_8 and $\text{LiHoMo}_3\text{O}_8$ -Li systems, only some portion of the parent compound is involved in the Li-cycling via intercalation/de-intercalation and 'conversion reaction', whereas some other portion is not at all affected.

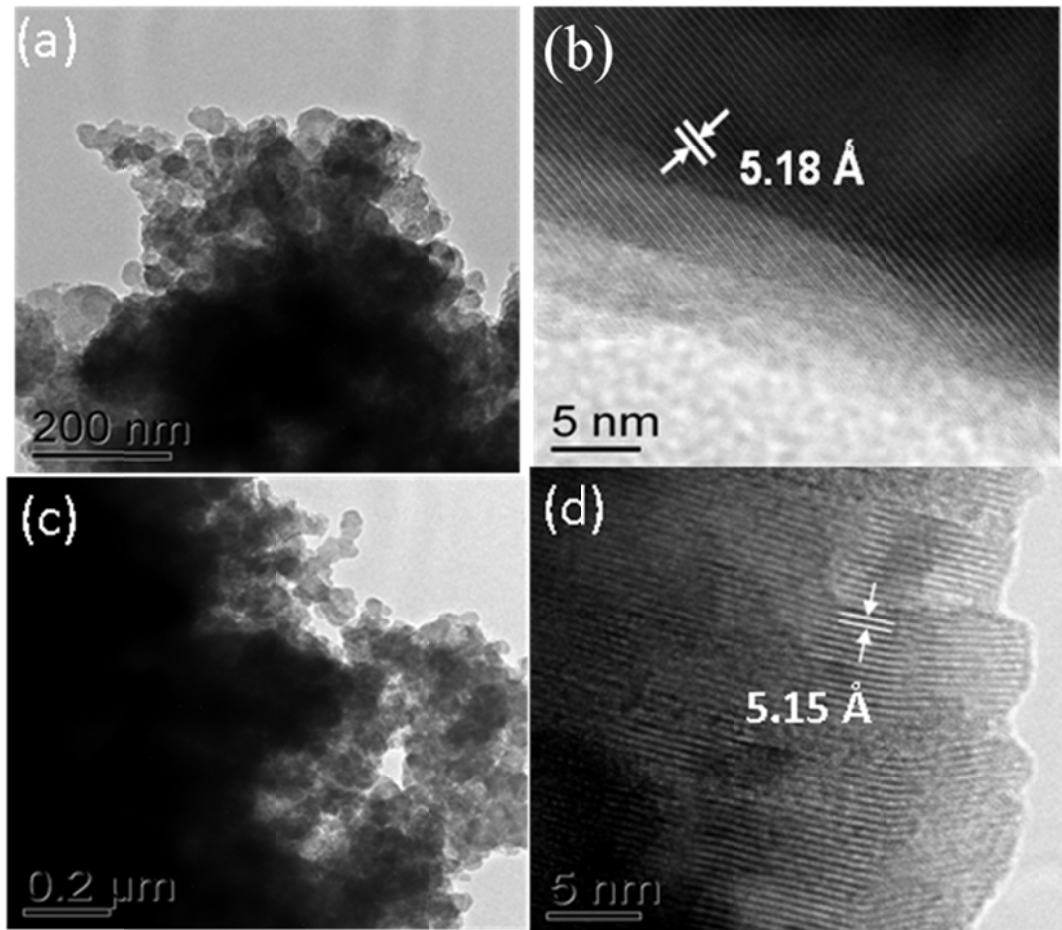


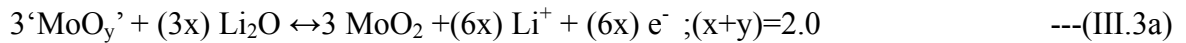
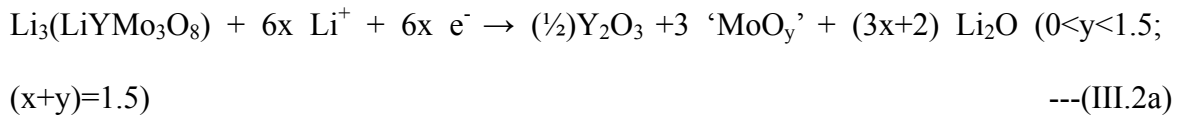
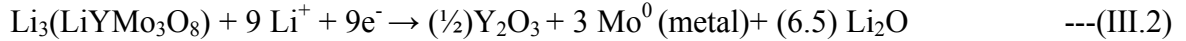
Fig.III.20. (a, b) TEM photograph and HR-TEM lattice image of LiYMo_3O_8 cycled electrode in the charged state (3.0V; 1st cycle). (c, d) TEM photograph and HR-TEM lattice image of $\text{LiHoMo}_3\text{O}_8$ cycled electrode (charged to 3.0 V after 70 cycles). Scale bars are shown.

III.3.7. Li-cycling mechanism

As mentioned in the introduction, many binary and ternary Mo-oxides have been studied in the literature for the Li-storage and electrochemical cyclability. This is due to the fact that molybdenum can adopt several valency states in oxides, and in the ideal case, 4 moles of Li can be cycled per mole of Mo-ion ($\text{Mo}^0 \leftrightarrow \text{Mo}^{4+}$). The reaction mechanism involves the formation/decomposition of an amorphous/nano-phase 'Li-Mo-O' complex [17, 20 – 22, 24]. However, it is known that the amount of reversible capacity and its long-term stability towards cycling and (current) rate-capability are determined by the crystallite-size (micron or nano-size) and morphology of the starting material, the initial crystal structure of the binary/ternary Mo-compound, and the nature and amount of the 'matrix' element with respect to Mo-content (ratio, M/Mo). The M-ion can be either electrochemically-active or -inactive towards Li.

III.3.7.1. LiYMo₃O₈-Li system

It is known that LiYMo₃O₈ is diamagnetic and an electronic insulator, due to the triangular Mo₃- cluster present in it, where all the Mo 4d-electrons, two per Mo⁴⁺ ion, are trapped to form Mo-Mo bonds. Hence, reactivity towards Li can be expected to be sluggish. However, due to the hexagonal layer structure, intercalation by Li in to the lattice can be expected, even though to the best of our knowledge, this aspect has not been studied in the literature on any of the above Mo₃- cluster compounds. Under electrochemical deep discharge conditions, usually amorphization of the crystal lattice can occur, as happens in the other M-Mo-O systems studied in the literature. Based on the observed galvanostatic cycling, CV, and ex-situ XRD/HR-TEM data, and also based on the Li-cycling mechanism proposed for Mo-oxides like, Na_xMoO₃ [17], MnMoO₄ [21], CaMoO₄ [22], the following reaction mechanism can be proposed:



Support for the reversible reaction of Eqn.(III.1) comes from the fact that Figs.III.9a shows a voltage plateau at ~1.0 V, during both forward and reverse reactions. From the voltage vs. capacity profile, it is clear that the voltage plateau ends after the consumption of 3.2 moles of Li per mole of LiYMo_3O_8 (~170 mAh/g) during the first discharge. The Mo adopts an effective valency of 3+ in the intercalated compound, $\text{Li}_3(\text{LiYMo}_3\text{O}_8)$. The CV data also show the reversible peak at ~1.0 V indicating a two-phase reaction with Li, the coexistence of intercalated and virgin phases. Under deep discharge to 0.005 V during the first cycle, some of the intercalated product undergoes amorphization, leading to either Mo-metal nano-particles (Eqn.(III.2)) or a nano-phase 'MoO_y' (0 < y < 1.5; Eqn.(III.2a)), embedded in an amorphous matrix composed of Y₂O₃ and Li₂O. Y₂O₃ will not be reduced to Y-metal by Li under the ambient temperature electrochemical conditions, due to the large Y-O bond strength [14]. The Eqns. (III.1 and III.2 or III.2a) predict that the total first-discharge capacity to be ≤ 12 moles of Li per mole of LiYMo_3O_8 , whereas the experimental value at 24°C is only 5.82 moles of Li (Fig.III.9a). At 50°C the measured total first-discharge capacity is 7.82 moles of Li. This shows that only some of the top layers (a few hundred unit cell lengths) of the active material have participated during the first-discharge, possibly due to the highly-insulating nature of the

LiYMo₃O₈. The fact that the ex-situ XRD pattern after the first-discharge shows mainly the lines due to the parent compound, and the ex-situ TEM-lattice image after the first-cycle also shows the parent compound, gives credence to the above argument.

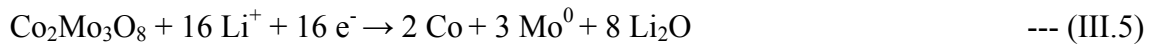
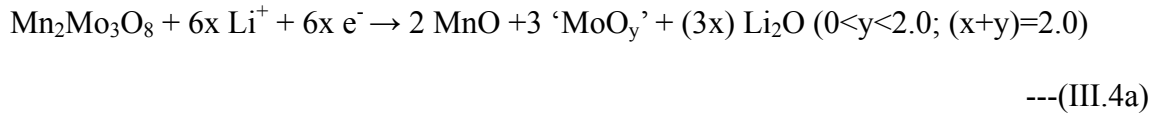
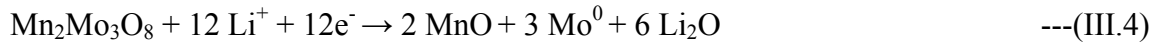
The observed total first-charge capacities of the LiYMo₃O₈ at 24 °C is 3.43 moles of Li (180 mAhg⁻¹) (Fig. III.9a), and at 50°C, the value is 5.1 moles (267 mAhg⁻¹) of Li. This is contributed by the reverse reactions of Eqns.(III.1 and III.3 or III.3a). With an increase in the number of discharge-charge cycles, more and more of the parent compound is able to react with Li, resulting in an increase in the observed discharge, as well as charge capacities, both at 24 °C and at 50 °C (Figs.III.9a,b and Fig.III.10). It is pertinent to mention here that an increase in the reversible capacity with an increase in the cycle number has also been observed in other oxide systems, like nano Fe₃O₄ [7], LiMVO₄ (M = Ni, Co, Cd, Zn) [40]. Interestingly, after 30-40 cycles, the voltage-capacity profiles of LiYMo₃O₈ undergo a qualitative change in that the voltage plateau at ~1.0 V is barely noticeable, and the reversible capacity is contributed mainly by reverse reactions of Eqns.(III.3 or III.3a). This means that the intercalated phase underwent almost complete amorphization. As can be seen from Figs. III.9a, the average discharge potential is ~1 V, whereas the average charge potential is ~2.3 V in LiYMo₃O₈. It may be pointed out that the above potential values are in tune with those measured on other Mo-oxides, like MnMoO₄ [21], CaMoO₄ [22]. A similar Li- cycling mechanism can be given for the isostructural LiHoMo₃O₈.

III.3.7.2. A₂Mo₃O₈-Li system (A = Mn, Co)

The compounds, A₂Mo₃O₈ (A = Mn, Co) differ from the iso-structural LiYMo₃O₈ and LiHoMo₃O₈ in that A is a 3d-transition element and Mn²⁺ ion is paramagnetic, and

hence the reactivity towards Li is expected to be different from that of LiYMo_3O_8 and $\text{LiHoMo}_3\text{O}_8$. The observed galvanostatic cycling, CV and ex-situ XRD data show that indeed this is the case with the $\text{A}_2\text{Mo}_3\text{O}_8$ -Li system. No Li-intercalation was noticed at ~ 1 V, and crystal structure destruction and amorphization occurs during the first-discharge to 0.005 V vs. Li. The observed total first discharge capacities correspond to 14 and 25 moles of Li (Fig.III.14a, c), whereas the first-charge capacities are 11 and 18 moles of Li per mole of $\text{Mn}_2\text{Mo}_3\text{O}_8$ and $\text{Co}_2\text{Mo}_3\text{O}_8$, respectively. However, due to drastic capacity-fading, only ~ 4 and 8.5 moles of Li are cyclable at the end of the 50th and 40th cycle.

Based on the above data, the following reaction mechanism can be proposed at the end of the first-discharge:

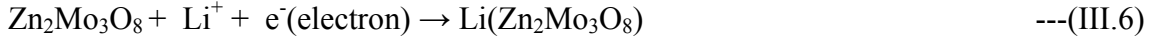


It is unlikely that under the ambient electrochemical conditions, Mn^{2+} ion is reduced to Mn-metal, because only 14 moles of Li were consumed at the end of the first-discharge reaction with Li, instead of the expected 16 moles of Li as is the case with $\text{A} = \text{Co}$ (Eqn. III.5). Studies on MnMoO_4 by Kim et al. [21] and on Mn_2SnO_4 by Connor and Irvine [41] have shown that Mn-ion may not be reduced to Mn-metal, and only Mo in MnMoO_4 , and Sn ions in Mn_2SnO_4 are reduced under ambient electrochemical conditions. Since the observed first-charge capacities (and the second discharge capacities) corresponds to 11

and 18 moles of Li for A = Mn and Co, respectively, it is assumed that Eqns. (III.4a and III.5) are more plausible.

III.3.7.3. Zn₂Mo₃O₈-Li system

Based on the observed galvanostatic cycling, CV, the following reaction mechanism can be proposed:



Support for the forward reaction of Eqn. (III.6) comes from the fact that Fig.III.14b shows voltage plateaus at ~0.9 V (consumption of 1 mole of Li for Zn₂Mo₃O₈). The voltage plateau at 0.2 V in Fig.III.14b extends up to the consumption of ~13.2 moles of Li per mole of Zn₂Mo₃O₈ during the first discharge indicating that reactions of Eqns. (III.7) and (III.8) are in operation and are completed at the voltage 0.005 V. According to the Eqns. (III.6, III.7 and III.8), the theoretical first-discharge capacity is 18 moles of Li per mole of Zn₂Mo₃O₈ (880 mAhg⁻¹), whereas the experimental value is only 15.8 moles of Li (775 mAhg⁻¹) (Fig.III.14b). Of course, part of this capacity is to be accounted for the SEI formation due to the decomposition of the electrolyte and polymeric layer formation under deep discharge conditions. This shows that the whole compound does not take part during the first- discharge reaction.

The observed total first-charge capacity of the Zn₂Mo₃O₈ is ~7.1 moles of Li (Fig. III.14b). The first- charge process can be presented by the reverse reaction of Eqn.III.8 and forward reactions of Eqns. (III.9 and III.3 or III.4a with A = Zn). Thus, the

theoretical capacity is 18 moles of Li. It is proposed that with an increase in the number of discharge-charge cycles, more and more of the parent compound is able to react with Li, resulting in an increase in the observed discharge, as well as charge capacities up to 17 cycles and 30 cycles, for bare and heat-treated electrodes of $Zn_2Mo_3O_8$, respectively (Fig.III.15b: I, II). The corresponding reversible capacities of 17th and 30th cycle are $500(\pm 5) \text{ mAhg}^{-1}$ (10.2 moles of Li) and $760 (\pm 5) \text{ mAhg}^{-1}$ (15.5 moles of Li). The latter value is only 2.5 moles of Li smaller than the theoretical capacity.

III.3.8. Electrochemical Impedance spectroscopy

Electrochemical impedance spectroscopy (EIS) is a well established technique to study electrode kinetics for cathode and anode electrode materials [10, 42-46]. EIS can give information on the surface film, charge-transfer and bulk resistances of the electrode, the associated capacitances and their variation with the applied voltage during the charge or discharge cycle. Impedance studies were carried out on $LiYMo_3O_8$ at room temperature at selected voltages in the range of 0.005 -3.0V vs. Li, at the current rate of 30 mAg^{-1} (0.08 C) during the 1st and 5th cycle and also in the discharged- state at the end of selected cycles. The cells were discharged or charged to the selected voltage values, relaxed for 3 h at that voltage and the impedance spectra were measured. Fig. III.21 shows the Nyquist plots (Z' vs. $-Z''$) during the 1st and 5th cycle at various voltage values. The impedance data were analyzed by fitting to an equivalent electrical circuit shown in Fig.III.22c similar to the circuits reported in the literature [10, 42-46]. It consists of the electrolyte resistance (R_e), surface film (R_{sf}) and charge transfer (R_{ct}) resistances, a constant phase element, CPE_i (instead of pure capacitance, due to the observation of a depressed semicircle in the spectra) along with diffusional components like Warburg

impedance (W_s). The symbols in Figs.III.21 and III.22a and b are the experimental data whereas the continuous lines represent the fitted curves. The derived impedance parameters at various voltages are given in Table III.2.

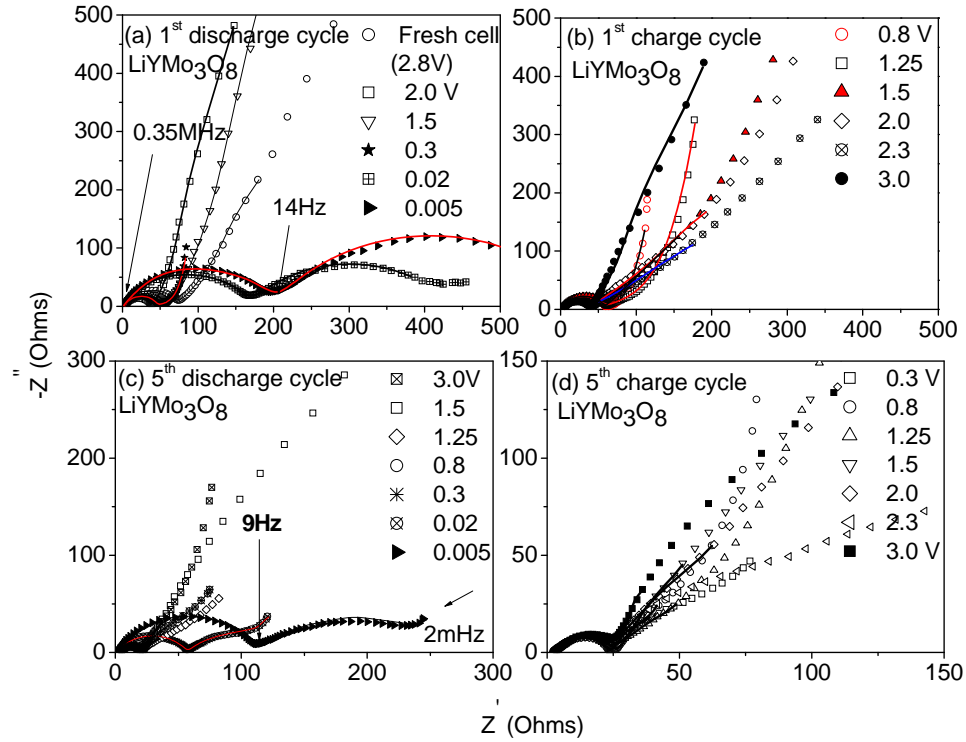


Fig.III.21. Nyquist plots (Z' vs. $-Z''$) of LiYMo_3O_8 at different voltages. (a) During the 1st discharge reaction from 2.8 to 0.005 V, (b) 1st charge reaction from 0.8 to 3.0 V, (c) 5th discharge reaction from 3.0 to 0.005 V and (d) 5th charge reaction from 0.3 to 3.0 V vs. Li. Symbols represents experimental data and continuous lines represent the fitted curve using the equivalent circuit of Fig. III.22 c. Geometric area of the electrode is 2 cm².

The fresh cell (OCV \sim 2.8 V) shows a single semicircle in the frequency region 0.35MHz-11Hz, followed by Warburg- type slope in the low- frequency region. The fitted value of impedance is 67 (\pm 5) Ω , attributed mainly to the surface-film resistance (R_{sf}). The associated capacitance (CPE_{sf}) is 26 (\pm 5) μF . The impedance spectra measured

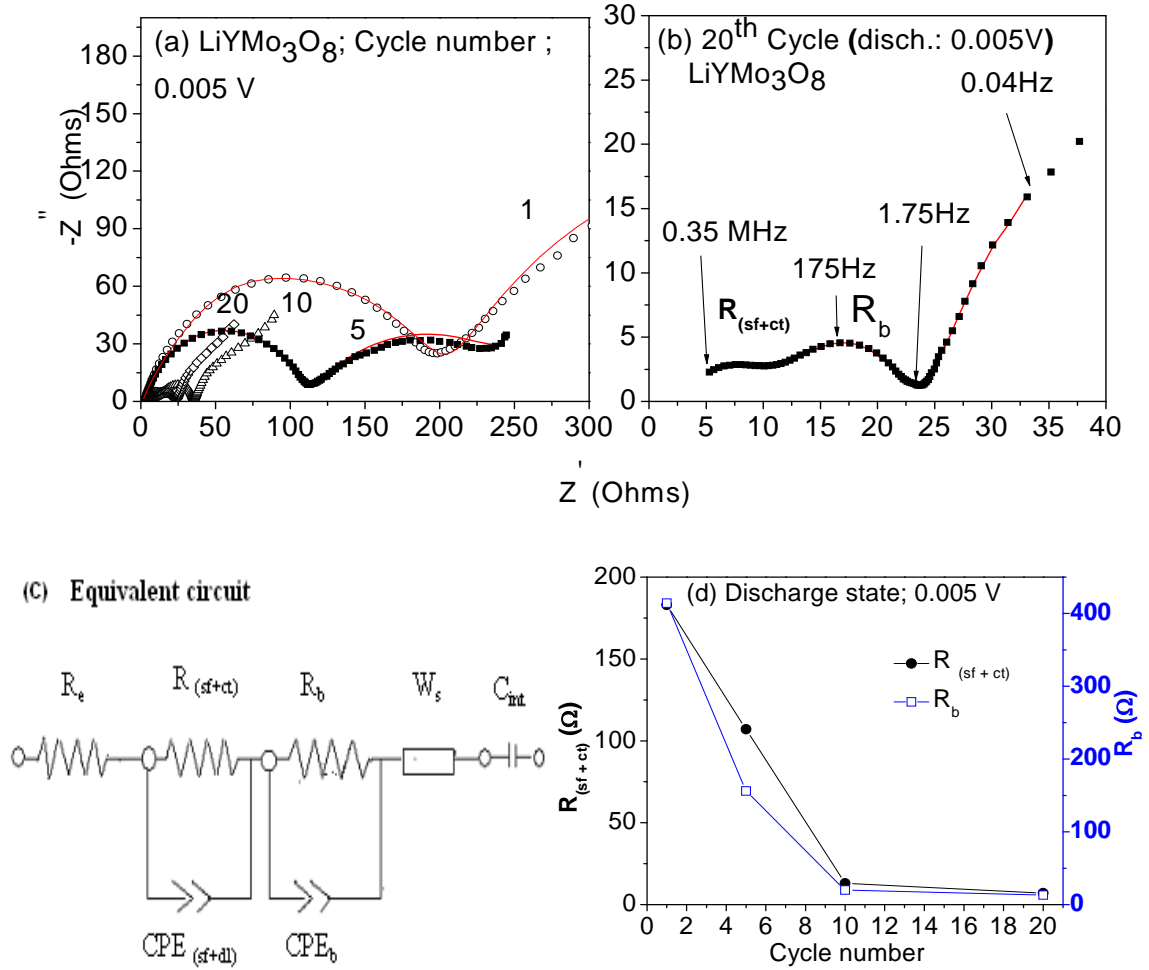


Fig.III.22. (a) Nyquist plots (Z' vs. $-Z''$) of LiYMo_3O_8 in the discharged state (0.005 V vs. Li) at various discharge-charge cycles. The numbers represent the cycle number. (b) The Nyquist plot at the 20th cycle in an expanded scale. Selected frequencies are indicated. (c) The equivalent electrical circuit consisting of resistances (R_i), constant phase elements (CPEs), Warburg impedance (W_s) and intercalation capacitance (C_{int}). (d) Variation of $R_{(sf+ct)}$ and R_b vs. cycle number of LiYMo_3O_8 , obtained by fitting the spectra of (a) with the circuit in (c).

at the voltages of 2.0, 1.5 V and 0.3 V also show only a single semicircle, similar to the spectrum at OCV (Fig.III.21a). Here the curve fitting was carried out using $R_{(sf+ct)}$ combination since electronic and ionic charge transfer are involved in the discharge process. As can be seen from Table III.2, the $R_{(sf+ct)}$ values decrease to 52 and 34 (± 5) Ω at 2.0 and 1.5 V, respectively, and then increase to 40 (± 5) Ω at 0.3 V. The corresponding

Table III.2 Impedance parameters of the LiYMo_3O_8 during the 1st and 5th discharge-charge cycles at various voltages.

Parameter values: Cell voltage, V vs Li	First-discharge cycle						
	3.0	2.0	1.5	0.3	0.02	0.005	
$R_{(\text{sf+ct})}$ (± 5) Ω	67	52	34	40	159	183	
R_b (± 5) Ω					265	414	
$\text{CPE}_{(\text{sf+dl})}$ (± 5) μF	26	22	27	29	20	24	
CPE_b (± 2) mF					6	4.4	
α (± 0.02)	0.83	0.79	0.86	0.87	0.72	0.70	
					0.63	0.66	
Parameter values : Cell voltage, V vs Li	First-charge cycle						
	0.8	1.25	1.5	2.0	2.3	3.0	
$R_{(\text{sf+ct})}$ (± 5) Ω	54	45	53	31	28	30	
$\text{CPE}_{(\text{sf+dl})}$ (± 5) μF	35	22	28	18	19	35	
α (± 0.02)	0.84	0.92	0.87	0.94	0.95	0.87	
Parameter values: Cell voltage, V vs Li	5 th discharge cycle						
	3.0	1.5	1.25	0.8	0.3	0.02	0.005
$R_{(\text{sf+ct})}$ (± 5) Ω	18	12	17	18	17	55	107
R_b (± 5) Ω						58	156
$\text{CPE}_{(\text{sf+dl})}$ (± 5) μF	233	151	210	151	127	31	15
CPE_b (± 2) mF						51	14
α (± 0.02)	0.72	0.8	0.73	0.77	0.79	0.70	0.76
						0.56	0.52
Parameter values : Cell voltage, V vs Li	5 th charge cycle						
	0.3	0.8	1.25	1.5	2.0	2.3	3.0
$R_{(\text{sf+ct})}$ (± 5) Ω	20	22	18	21	17	20	20
$\text{CPE}_{(\text{sf+dl})}$ (± 5) μF	105	108	100	109	87	99	105
α (± 0.02)	0.8	0.8	0.8	0.8	0.87	0.8	0.8

$\text{CPE}_{(\text{sf+dl})}$ (dl = double layer) range from 22 to 29 (± 5) μF in the voltage range 2.0-0.3V.

The spectra measured at 0.02V and 0.005V differ from the spectrum at 0.3V and show two large-diameter semicircles indicating the onset of contribution from the bulk resistance (R_b) in addition to $R_{(\text{sf+ct})}$. Accordingly, the R_b and CPE_b components in the circuit (Fig.III.22c) were used to fit the spectrum. The fitted values of $R_{(\text{sf+ct})}$ and R_b are: 159 and 183 (± 5) Ω , and 265 and 414 (± 5) Ω respectively, at $V = 0.02$ and 0.005 V. The

corresponding $CPE_{(sf+dl)}$ values are 20 and 24 (± 5) μF . The extracted CPE_b are fairly large and are 6 and 4.4 (± 2) mF (Table III.2). The impedance of the constant phase element, Z_{CPE} is related to the angular frequency, ω by the relation, $Z_{CPE} = 1/[C_i (j\omega)^\alpha]$, where $j = \sqrt{-1}$ and C_i is the capacitance and α is a constant. The value of α (< 1) is an estimate of the degree of distortion from the pure capacitor behavior. As can be seen from Table III.2, the values of α range from 0.83 to 0.63 during the first-discharge process. The Nyquist plots during the first-charge cycle at various voltages are shown in Fig.III.21b, and they resemble the spectra during the discharge cycle. The $R_{(sf+ct)}$ values remain almost constant at 50 (± 5) Ω in the voltage range, 0.8-1.5 V, and decrease to 30 (± 2) Ω in the voltage range, 2.0-3.0 V. The corresponding $CPE_{(sf+dl)}$ values show a decrease from 35 to 18 μF in the voltage range, 0.8-2.0 V, but increase to 35 μF at 3.0 V. The α values range from 0.84 to 0.95 depending on the voltage (Table III.2).

The impedance spectra of $LiYMo_3O_8$ during 5th discharge-charge cycle are shown Fig. III.21 c,d and the fitted impedance parameters are given in Table III.2. The spectra during the 5th discharge cycle as well as the charge cycle are qualitatively similar indicating good reversibility of the electrode, as can be expected from the cycling data shown in Fig. III.10. As can be seen from Table III.2, the $R_{(sf+ct)}$ values in the 5th discharge cycle vary from 12-18 (± 5) Ω in the range 3.0 to 0.3V. The spectra at 0.02 and 0.005 V show two semicircles indicating the contribution from the R_b , similar to the spectra during the first discharge. Accordingly, the fitted values of $R_{(sf+ct)}$ and R_b at 0.02 V are 55 and 58 (± 5) Ω , respectively. These values increase to 107 and 156 (± 5) Ω at 0.005 V. The $CPE_{(sf+dl)}$ and CPE_b values also change, but in an opposite manner when the voltage changes from 0.02 to 0.005 V. During the corresponding 5th charge cycle,

only one semicircle is seen and the fitted $R_{(sf+ct)}$ values vary from 20 to 22 (± 5) Ω in the voltage range, 0.3- 3.0 V. These are smaller in comparison to those measured during the first charge cycle, but almost similar to those observed during the 5th discharge- cycle, indicating good reversibility of the electrode. The corresponding $CPE_{(sf+dl)}$ values are in the range 87- 109(± 5) μF in the voltage range, 0.3- 3.0 V (Table III.2).

Impedance spectra were measured in the discharged-state (0.005 V) after 10 and 20 cycles. The data along with those after the 1st and 5th cycles in the discharged- states are plotted in Fig.III.22a. The 20th cycle spectrum in an enlarged scale is shown in Fig. III.22b, which clearly delineates the contributions from the surface-film + charge transfer ($R_{(sf+ct)}$) and bulk (R_b) resistances, as two well-defined semicircles. The data have been analyzed using the circuit of Fig.III.22c and the R_b -values are plotted as a function of cycle number in Fig.III.22d. As can be seen, both $R_{(sf+ct)}$ and R_b decrease drastically up to 10th cycle, and appear to stabilize by the 20th cycle to 10 (± 3) Ω , indicating good reversibility and stability of the $LiYMo_3O_8$ –Li system for Li-cycling. The $CPE_{(sf+dl)}$ and CPE_b values also show a similar drastic decrease by the end of 10th cycle. The fitted resistance value due to the electrolyte and cell components (R_e) is 4 (± 1) Ω during all the cycles. These values are similar to those measured on other oxide anode materials [10, 15, 46]. Thus, the impedance data corroborate the galvanostatic cycling data.

III.4. Conclusions

The triangular molybdenum cluster compounds, $Li(Y/Ho)Mo_3O_8$ and $A_2Mo_3O_8$ (Mn, Zn, Co) have been prepared by the carbothermal reduction method at 750°C in argon atmosphere. They were characterized by XRD, SEM, HR-TEM, density and surface area methods. The crystal lattice parameters agree well with those synthesized

using other more-involved methods, thereby establishing that the carbothermal reduction is a viable technique to prepare other iso-structural compounds in the series. The FT-IR at ambient temperature (RT), and Raman spectra at various temperatures (78-450 K) of LiYMo_3O_8 and $\text{Mn}_2\text{Mo}_3\text{O}_8$ are reported for the first time, and results interpreted. Magnetic measurements in the temperature range, 10-350 K on $\text{Mn}_2\text{Mo}_3\text{O}_8$ confirm that it is a ferrimagnet, with a Curie temperature, $T_C=39$ K, in good agreement with the value of 41.5 K reported in the literature. Magnetic hysteresis and magnetization data at various fields and temperatures were interpreted.

Li-cyclability of these compounds has been evaluated galvanostatically in the voltage range, 0.005-3.0 V vs. Li at a current of 30 mA g^{-1} and 60 mA g^{-1} at RT and at 50°C . Clear evidence of intercalation of Li-ion to the host crystal structure of LiYMo_3O_8 and $\text{LiHoMo}_3\text{O}_8$ is seen during the first-discharge reaction. At RT, the total first-discharge capacities are 305, 275 (± 5) mAh g^{-1} whereas the first-charge capacities are 180, mAh g^{-1} for LiYMo_3O_8 and $\text{LiHoMo}_3\text{O}_8$, respectively. However, for both the compounds the values increased systematically with an increase in the cycle number and yielded a reversible capacity of 385(± 5) mAh g^{-1} (at the 120th for LiYMo_3O_8) and 290(± 5) mAh g^{-1} (70th cycle for $\text{LiHoMo}_3\text{O}_8$), respectively. At 50°C , the reversible capacities are 418 and 470 (± 5) mAh g^{-1} at the end of 60 and 40 cycles for LiYMo_3O_8 and $\text{LiHoMo}_3\text{O}_8$, respectively. The coulombic efficiency ranges from 94-96%. Complementary cyclic voltammetry data showed that the average charge potential is 2.2 V whereas the average discharge potential is 1.0V for both LiYMo_3O_8 and $\text{LiHoMo}_3\text{O}_8$ during 30-120 cycles. The impedance spectral data of LiYMo_3O_8 have been analyzed to obtain the impedance parameters and suitably interpreted in terms of changes in the surface-film + charge

transfer resistance and bulk resistance as a function of the voltage. The Li-cyclability behavior of $A_2Mo_3O_8$ ($A = Mn, Zn, Co$) are entirely different from that of $LiYMo_3O_8$ and $LiHoMo_3O_8$: No evidence of Li- intercalation is seen for $A = Mn$ and Co , whereas 1 mole of Li-intercalation is seen up to 1.0 V for $A = Zn$. However, drastic capacity-fading is observed for $A = Mn$ and Co up to 25 cycles. This is followed by a smaller decrease up to 50 cycles for $A = Mn$ and up to 40 cycles for $A = Co$. For $A = Mn$, the reversible capacity at the end of 50th cycle is $205 (\pm 5) \text{ mAhg}^{-1}$, whereas for $A = Co$ is $425 (\pm 5) \text{ mAhg}^{-1}$. For $A = Zn$, the first-charge capacity is 350 mAhg^{-1} . This value increased continuously with an increase in the cycle number up to 17 cycles, and then decreased to the values of $260 (\pm 5) \text{ mAhg}^{-1}$ at the end of 50th cycle. At a higher current density of 0.36 C, a reversible capacity of $415 (\pm 5) \text{ mAhg}^{-1}$ is noticed at the end of 45th cycle. For $A = Zn, Co$, the heat-treated electrode showed an improved performance under similar cycling conditions. The coulombic efficiency ranges from 96-98% for $A = Mn, Zn, Co$. A plausible mechanism of Li-cyclability in the compounds is proposed in terms of formation/decomposition of an amorphous oxide nano-composite, 'Li-Y (A)-Mo-O_y' to explain the observed data, and it is supported by ex-situ XRD and ex-situ TEM of the electrodes.

References

- [1] G-A. Nazri, G. Pistoia, Eds, 'Lithium Batteries: Science and Technology',
Kluwer Acad. Publ., New York, USA (2003).
- [2] J. L. Tirado, *Mater. Sci. & Engg. R* 40 (2003)103.
- [3] A. S. Arico, P. Bruce, B. Scrosati, J.-M. Tarascon, W. V. Schalkwijk, *Nature Mater.* 4 (2005) 366.
- [4] P. G. Bruce, B. Scrosati, J.-M. Tarascon, *Angew. Chem. Int. Ed.* 47 (2008) 2930.
- [5] H. Li, Z. Wang, L. Chen, X. Huang, *Adv. Mater.* 21 (2009) 4593.
- [6] P. Poizot, S. Laruelle, S. Grugeon, L. Dupont, J.-M. Tarascon, *Nature* 407 (2000)
496.
- [7] P. L. Taberna, S. Mitra, P. Poizot, P. Simon, J.-M. Tarascon, *Nature Mater.* 5 (2006)
567.
- [8] S. Laruelle, S. Grugeon, P. Poizot, M. Dolle, L. Dupont, J.-M. Tarascon,
J. Electrochem. Soc. 149 (2002) A627.
- [9] Y.-M. Kang, M.-S. Song, J.-H. Kim, H.-S. Kim, M.-S. Park, J.-Y. Lee, H. K. Liu,
S.X. Dou, *Electrochim. Acta* 50 (2005) 3667.
- [10] M. V. Reddy, Y. Ting, C. H. Sow, Z. X. Shen, C.T. Lim, G.V. Subba Rao,
B.V.R. Chowdari, *Adv. Funct. Mater.* 17 (2007) 2792.
- [11] S. Grugeon, S. Laruelle, L. Dupont, F. Chevallier, P.L. Taberna, P. Simon,
L. Gireaud, S. Lascaud, E. Vidal, B. Yrieix, J.-M. Tarascon, *Chem. Mater.* 17 (2005)
5041.
- [12] J. Hu, L. Hong, X. Huang, *Electrochem. & Solid-State Lett.* 8 (2005) A66.
- [13] Y. Sharma, N. Sharma, G.V. Subba Rao, B.V.R. Chowdari, *Adv. Funct. Mater.*

- 17 (2007) 2855.
- [14] H. Li, P. Balaya, J. Maier, *J. Electrochem. Soc.* 151 (2004) A1878.
- [15] M.V. Reddy, S. Madhavi, G.V. Subba Rao, B.V. R. Chowdari, *J. Power Sources* 162 (2006) 1312.
- [16] F. Leroux, G. R. Goward, W. P. Power, L.F. Nazar, *Electrochem. Solid-State Lett.* 1 (1998) 255.
- [17] F. Leroux, L. F. Nazar, *Solid State Ionics* 133 (2000) 37.
- [18] D. Hara, H. Ikuta, Y. Uchimoto, M. Wakihara, *J. Mater. Chem.* 12 (2002) 2507.
- [19] D. Hara, J. Shirakawa, H. Ikuta, Y. Uchimoto, M. Wakihara, T. Miyanaga, I. Watanabe, *J. Mater. Chem.* 13 (2003) 897.
- [20] M. Martos, J. Morales, L. Sanchez, *J. Mater. Chem.* 12 (2002) 2979.
- [21] S. S. Kim, S. Ogura, H. Ikuta, Y. Uchimoto, M. Wakihara, *Solid State Ionics* 146 (2002) 249.
- [22] N. Sharma, K. M. Shaju, G. V. Subba Rao, B. V. R. Chowdari, Z. L. Dong, T. J. White, *Chem. Mater.* 16 (2004) 504.
- [23] N. N. Leyzerovich, K. G. Bramnik, T. Buhrmester, H. Ehrenberg, H. Fuess, *J. Power Sources* 127 (2004) 76.
- [24] Y. Liang, S. Yang, Z. Yi, X. Lei, J. Sun, Y. Zhou, *Mater. Science & Eng. B* 121 (2005) 152.
- [25] M. Anji Reddy, M. Satya Kishore, V. Pralong, V. Caiganaert, U. V. Varadaraju, B. Raveau, *J. Power Sources* 168 (2007) 509.
- [26] J. Debeneditis, L. Katz, *Inorg. Chem.* 4 (1965) 1836.
- [27] W. H. McCarroll, *Inorg. Chem.* 16 (1977) 3351.

- [28] W.H. McCarroll, L. Katz, R. Ward, *J. Am. Chem. Soc.* 79 (1957) 5410.
- [29] W.H. McCarroll, C. Darling, G. Jakubicki, *J. Solid State Chem.* 48 (1983) 189.
- [30] J. Barker, M.Y. Saidi, J. L. Swoyer, *Solid State Ionics* 158 (2003) 261.
- [31] J. Barker, M.Y. Saidi, J. L. Swoyer, *Electrochem. & Solid State Lett.* 6 (2003) A252.
- [32] S.P. McAlister, P. Strobel, *J. Mag. & Mag. Mater.* 30 (1983) 340.
- [33] F. Varret, H. Czeskleba, F. Hartmann-Boutron, P. Imbert, *J. de Physique (Paris)* 33 (1972) 549.
- [34] B. Lippold, J. Herrmann, W. Reichelt, H. Oppermann, *Phys. Stat. Sol.(a)* 121 (1990) K91.
- [35] D. Bertrand, H. Kerner-Czeskleba, *J. de Physique (Paris)* 36 (1975) 379.
- [36] P. Esquinazi, R. Hohne, *J. Mag. & Mag. Mater.* 290-291 (2005) 20.
- [37] J. Ghose, N. N. Greenwood, G.C. Hallam, D. A. Read, *J. Solid State Chem.* 19 (1976) 365.
- [38] D. A. O. Hope, A. K. Cheetham, *J. Solid State Chem.* 72 (1988) 42.
- [39] J. Li, H. M. Dahn, L. J. Krause, D.-B. Le, J. R. Dahn, *J. Electrochem. Soc.* 155 (2008) A812.
- [40] D. Guyomard, C. Sigala, A. Le Gal La Salle, Y. Piffard, *J. Power Sources* 68 (1997) 692.
- [41] P.A. Connor, J.T.S. Irvine, *J. Power Sources* 97-98 (2001) 223.
- [42] F. Nobili, R. Tossici, R. Marassi, F. Croce, B. Scrosati, *J. Phys. Chem. B.* 106 (2002) 3909.
- [43] K.M. Shaju, G.V. Subba Rao, B.V.R. Chowdari, *J. Electrochem. Soc.* 151 (2004) A1324.

- [44] M.D. Levi, D. Aurbach, J. Phys. Chem. B. 101 (1997) 4630.
- [45] D. Aurbach, A. Nimberger, B. Markovsky, E. Levi, E. Sominski, A.Gedanken, Chem. Mater. 14 (2002) 4155.
- [46] N. Sharma, J. Plévert, G.V. Subba Rao, B.V.R. Chowdari, T.J. White, Chem. Mater. 17 (2005) 4700.

Chapter IV

Nanoflake CoN as a high capacity anode for Li- ion batteries *

Abstract

CoN films with nanoflake morphology are prepared by RF magnetron sputtering on Cu and oxidized Si substrates and characterized by X- ray diffraction (XRD), field-emission scanning electron microscopy (FE- SEM), high resolution transmission electron microscopy (HR- TEM) and selected area electron diffraction (SAED) techniques. The thickness and composition of the films are determined by the Rutherford back scattering (RBS) technique confirming the stoichiometric composition of CoN with a thickness, 200 (± 10) nm. Li- storage and cycling behavior of nanoflake CoN have been evaluated by galvanostatic discharge- charge cycling and cyclic voltammetry (CV) in cells with Li-metal as counter electrode in the range of 0.005- 3.0 V at ambient temperature. Results show that a first- cycle reversible capacity of 760 (± 10) mAhg⁻¹ at a current rate 250 mA g⁻¹ (0.33 C) increases consistently to yield a capacity of 990 (± 10) mAhg⁻¹ after 80 cycles. The latter value corresponds to 2.7 moles of cyclable Li per mole of CoN vs. the theoretical, 3.0 moles of Li. Excellent rate capability is shown when cycled at 0.59 C (up to 80 cycles) and at 6.6 C (up to 50 cycles). The coulombic efficiency is found to be >96 % in the range of 10-80 cycles. The average charge and discharge potentials are 0.7 and 0.2 V, respectively for the decomposition/formation of Li₃N as determined by CV. However, cycling to an upper cut- off voltage of 3.0 V is essential for the completion of the ‘conversion reaction’. Based on the ex- situ -XRD, -HR- TEM and -SAED data, the plausible Li- cycling mechanism is discussed.

* One paper has been published based on the work described in this Chapter.

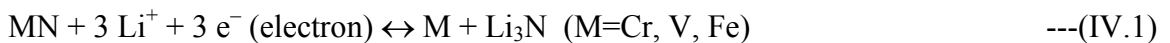
IV.1. Introduction

Lithium ion batteries (LIBs) as dominant dc power sources for the mobile communication devices and portable computers, have attracted attention due to their high energy density and rechargeability over a large number of discharge-charge cycles [1-4]. Specialty graphite is used as the anode (negative electrode) with a theoretical capacity of 372 mAhg^{-1} in the commercial first-generation LIBs. Graphite works on the basis of Li-ion intercalation-deintercalation reaction during the charge-discharge operation, the Li-ions coming from the cathode, a mixed oxide, LiCoO_2 . However, for the application of LIBs to portable power tools and electric vehicles/hybrid electric vehicles (EV/HEV), a higher energy density and safety-in-operation are needed, and hence a lot of research effort has been expended during the last decade to find alternative anode materials which can yield high reversible capacities and which may work on a reaction mechanism which is different from the intercalation-deintercalation process. As a result, metals or their compounds which can form alloys with Li (e.g., $\text{Sn} + 4.4 \text{ Li} \leftrightarrow \text{Li}_{4.4}\text{Sn}$), and compounds which can reversibly react with Li via ‘conversion’ reaction (e.g., $\text{CoO} + 2 \text{ Li} \leftrightarrow \text{Co} + \text{Li}_2\text{O}$), have been found to give reversible capacities which are higher, by a factor two or three, than the theoretical capacity of graphite [1,2,4].

Recent studies have shown that the conversion reactions occur not only with CoO [5], but also with other transition metal oxides like, Fe_2O_3 [6], Fe_3O_4 [7], complex oxides like, MnV_2O_6 [8], ZnCo_2O_4 [9], and nano-size particles of these oxides were found to be beneficial in sustaining large number of discharge-charge cycles at various current rates. Also, transition metal compounds with other anions like, fluorides [10, 11, 12],

oxyfluorides [13], sulphides [14], carbonates [15], phosphides [16, 17], and antimonides [14, 18] do undergo conversion reactions.

Metal nitrides are attractive materials as prospective anodes since the Li_3N that is formed by the conversion reaction, is an excellent ionic conductor [19], and satisfies one of the essential criteria for a desirable anode. In the literature, ternary metal nitrides of the general formula, $(\text{Li}_{3-x}\text{M}_x)\text{N}$, $\text{M}=\text{Fe}, \text{Co}, \text{Ni}, \text{Cu}$ [20-24] and LiNiN [25] have been explored for their Li-cyclability. Many binary metal nitrides, in thin film form, have been examined by the group of Fu: Ni_3N [26] and Fe_3N [27] showed reversible capacities ranging from 324 to 420 mAhg^{-1} . Studies on thin films of CrN [28] and recently, $(\text{Cr}_{1-x}\text{Fe}_x)\text{N}$, $x = 0 - 1$ [29] and of VN [30] by the same group showed initial reversible capacities in excess of 1000 mAhg^{-1} when cycled in the voltage range, 0.01-3.5 V vs Li. While CrN retained $\sim 1000 \text{mAhg}^{-1}$ after 30 cycles, with significant electrode-polarization, films of the composition, $x = 0.17$ in $(\text{Cr}_{1-x}\text{Fe}_x)\text{N}$ and VN showed a stable capacity of $\geq 800 \text{mAhg}^{-1}$ in the range 10-50 cycles. The proposed Li-cycling reaction mechanism, substantiated by complementary ex-situ studies, involves the conversion reaction:



It will be of interest to examine other binary metal nitrides for their Li-cyclability. Presently, thin films of CoN on Cu -substrates were prepared, characterized and their Li-cyclability was studied at various current (C) rates up to 80 cycles. Results show reversible capacities over 950 mAhg^{-1} after 80 cycles at 0.33 C and at 0.59 C rates, whereas a capacity of 650 mAhg^{-1} is shown after 50 cycles at 6.6 C rate. Complementary cyclic voltammetry and ex-situ X-ray diffraction and HR-TEM data are also presented.

IV.2. Experimental

The CoN thin films were deposited on Cu- foil substrates (16 mm dia, and 20 μm thick discs, 99.9%) and on surface oxidized Si- substrates, (SHE, Japan; 6.25 cm^2 area and 380 μm thick) by using RF magnetron sputtering (Denton Vacuum Discovery 18 system) in N_2 atmosphere. Both the substrates were contained in the sputtering chamber. The Co- metal disc (Angstrom Sciences, 99.9%) was used as the target. The deposition conditions are: RF power at 150 W, total N_2 partial pressure at 10 mTorr, sputtering time, 120 min and substrate temperature, 27 $^\circ\text{C}$. Several duplicate films of CoN, of thickness \sim 200 nm were deposited on the above substrates. The structural and morphological characterizations of CoN films were carried out as discussed in Chapters II and III.

The Rutherford back scattering measurements were carried out using the accelerator facility at the Centre for Ion Beam Applications laboratory of the Physics Department. A 2 MeV He^+ beam with a 2 mm diameter and a current of 10 nA was used for the measurements at room temperature. The energy of the backscattered particles were recorded using the 50 mm^2 passivated implanted planar silicon (PIPS) detectors with an energy resolution of \sim 18 keV. The detector was positioned at 170 $^\circ$ scattering angle. The experimental data were analyzed using the simulation software XRUMP [31] to determine the composition and thickness of the films.

For electrochemical measurements, the virgin CoN films grown on Cu- substrate were used as the electrodes. The active mass of the electrode was calculated by using the theoretical density of CoN (6.106 gcm^{-3}) and the geometrical area of the electrode, 2 cm^2 and was found to be, typically, \sim 0.24 mg. The cell fabrication, electrochemical

characterization and ex-situ –XRD and –TEM study of CoN films were carried out as described in Chapters II and III.

IV.3. Results and Discussion

IV.3.1. Structural and morphological characterization

Suzuki et al [32] have prepared thin films of CoN by dc reactive sputtering and studied their crystal structure and magnetic properties. They found that CoN adopts a cubic zinc blende- type structure with $a = 4.297 \text{ \AA}$. Fig.IV.1 shows the XRD pattern of CoN thin film deposited on surface oxidized Si (111) substrate. The Miller indices (h k l) correspond to the cubic structure with the space group, $F\bar{4}3m$. The lattice parameter was calculated by using least square fitting of 2θ and (h k l) values and found to be $a = 4.291(5) \text{ \AA}$, in good agreement with the reported value of 4.297 \AA [32] [JCPDS card no. 83-0831].

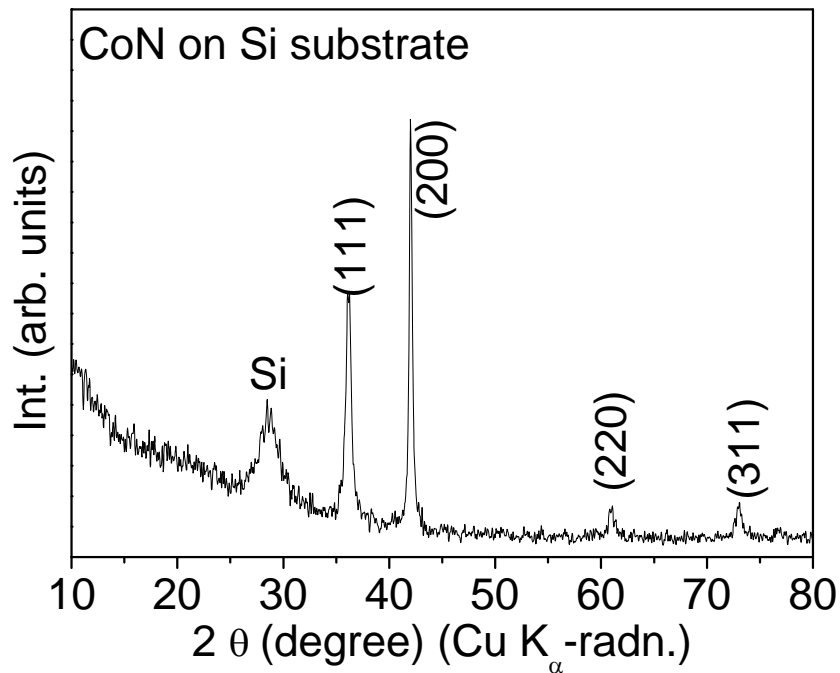


Fig.IV.1. X-ray diffraction pattern of nanoflake CoN grown on surface- oxidized Si substrate. The line due to Si substrate is shown. Miller indices (h k l) of CoN are shown.

The XRD pattern of the CoN film deposited on the Cu-substrate is shown in Fig.IV.2. Because of the preponderance of the intensities of the lines due to the Cu-substrate and the Al-sample holder, the characteristic lines due to CoN are of low relative-intensity. However, the lines due to Miller indices (111) and (200) can be clearly seen, which are in agreement with those shown in Fig.IV.1.

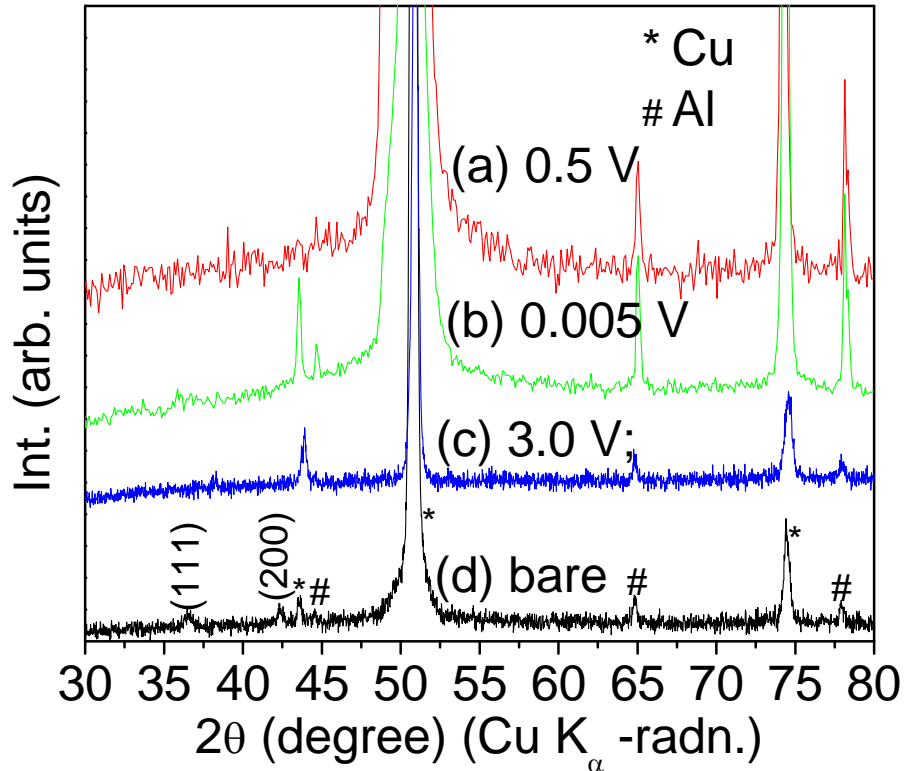


Fig.IV.2. XRD patterns of the bare CoN electrode grown on Cu- substrate and those of the electrodes of CoN discharged to 0.5 and 0.005 V, and charged to 3.0 V at the end of 1st cycle are shown. Miller indices assigned to the peaks of bare CoN are shown. The symbols (*,#) represent the lines due to Cu-metal (electrode substrate) and Al –metal (sample holder). The y- axis values are normalized for better comparison of the XRD patterns.

Rutherford back scattering (RBS) or more accurately, elastic back scattering is a valuable technique that can give information on the chemical composition, and in the case of thin films, their thickness [33]. Briefly, in a typical experiment the sample (e.g., thin film deposited on a substrate) is exposed to a beam of fast ions, like He⁺ ions. The

ions will collide with both the surface atoms as well as those present in the bulk, up to a certain depth, and get back-scattered. The mass ratio of the ions and the colliding target atom together with scattering angle (170°) will determine the kinetic energies of the back-scattered ions. The RBS spectrum displays the number of backscattered ions vs. energy or channel number. Because the scattering probability is quantitatively known, with an appropriate simulation code (XRUMP), one can extract composition and thickness of thin film systems. Fig. IV.3 shows a typical 2 MeV RBS spectrum obtained for the CoN film on surface oxidized Si- substrate. In the figure, the full circles are the experimental data and the continuous and dotted lines denote the simulated data using the XRUMP [31].

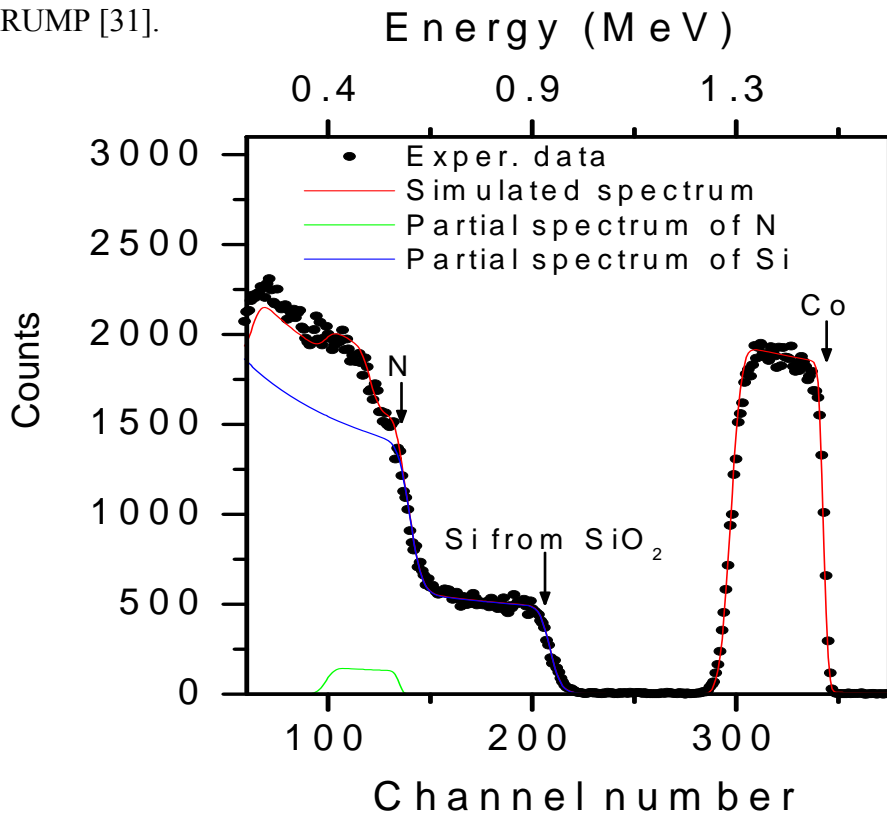


Fig.IV.3. Rutherford back scattering (RBS) spectrum of nanoflake CoN grown on surface- oxidized Si substrate. The simulated partial spectra due to the individual elements are indicated.

The back scattering surface energies of different elements present in the sample are indicated in the spectrum. Apart from the total simulated spectrum, the partial spectra of silicon and nitrogen are also shown indicating the components of the overlapped region. The atomic percentage values obtained for cobalt (50 at. %) and nitrogen (50 at. %) from the simulations confirm the stoichiometry of the CoN films. The thickness of the film was found to be 200 (± 10) nm. The bulk density of 6.106 gcm⁻³ of CoN was used in calculating the thickness. It can be assumed that the chemical composition and thickness of the CoN films deposited on Cu- substrate are identical to those deposited on oxidized Si- substrates, since both the films were deposited under the same conditions in the sputtering chamber.

The field emission (FE) - SEM photographs of the CoN nanoflakes grown on Cu-foil are shown in Fig. IV.4 a, b. As can be seen, nanoflakes of size ≤ 100 nm are densely packed but are randomly oriented with an aspect ratio, 10:1. The HR- TEM lattice image and selected area electron diffraction (SAED) pattern of the CoN film on holey carbon-coated Cu grids are shown in Fig. IV.4 c,d. Randomly oriented crystalline- regions and some amorphous regions are clearly seen. The d- spacings (inter planar distances) of the planes in Fig. IV.4c are 2.50 (± 0.02) and 2.12 (± 0.02) Å and these correspond to the Miller indices (111) and (200), respectively of CoN (Fig. IV.1). The SAED pattern shows highly resolved concentric diffuse rings and some bright spots (Fig. IV.4d). The diffuse rings indicate the nano- phase nature of CoN. The calculated d- values from the rings are: 2.50, 2.12 and 1.49 (± 0.02) Å and these correspond to the (h k l) values (111), (200) and (220), respectively. Thus, from the above data, we conclude that the CoN films consist of nanoflakes of size ≤ 100 nm, densely packed with a total layer thickness, 200 (± 10) nm.

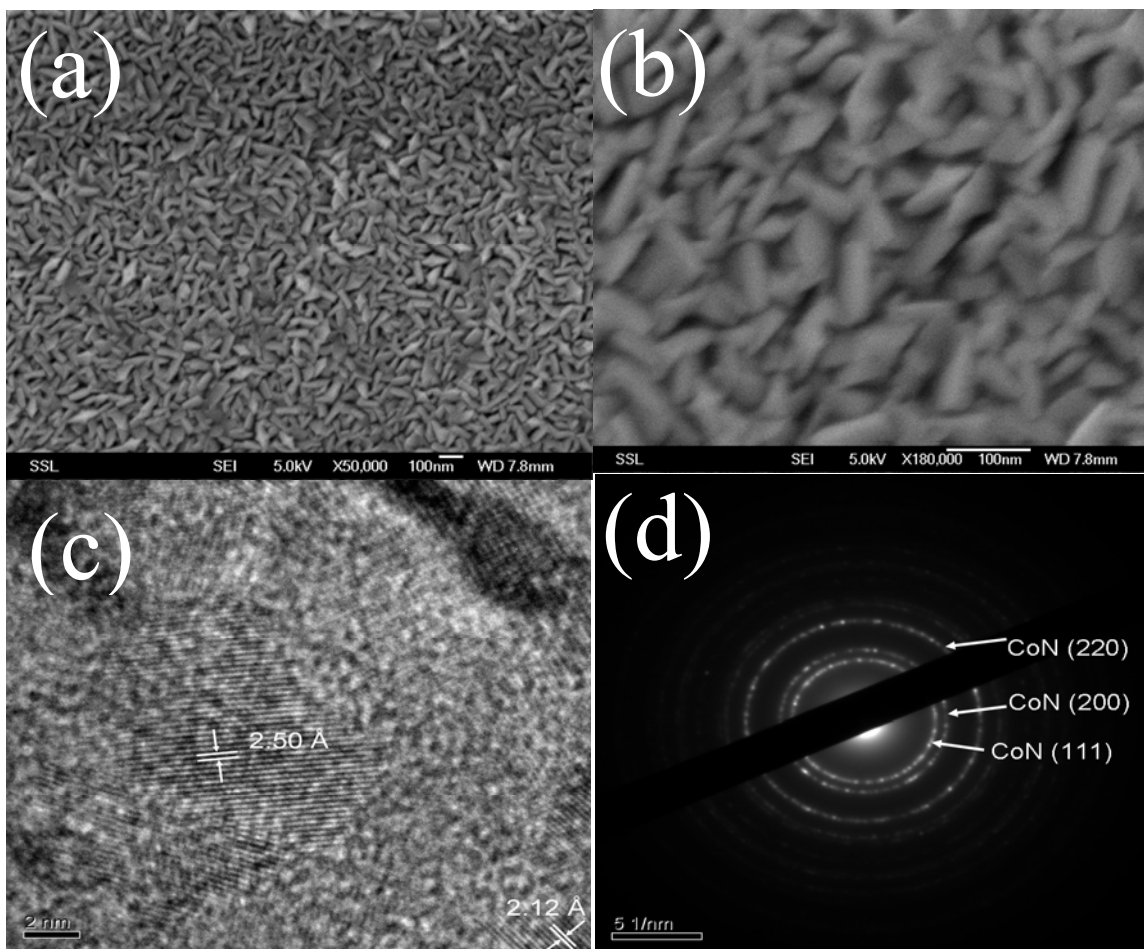


Fig.IV.4. (a, b) FE- SEM photographs of nanoflake CoN grown on Cu- substrate at two different magnifications showing randomly oriented nanoflakes of size ≤ 100 nm. (c) HR- TEM lattice image of nanoflake CoN. The interplanar (d-) spacings are indicated by arrows. (d) The SAED pattern of nanoflake CoN. Miller indices are indicated. Scale bars are shown.

IV.3.2. Electrochemical properties

IV.3.2.1. Galvanostatic cycling

The discharge- charge profiles (voltage vs. capacity curves) of nanoflake CoN at a current density 250 mA g^{-1} (0.33 C) in the voltage window, $0.005\text{-} 3.0 \text{ V}$ vs. Li, up to 80 cycles are shown in Fig. IV.5a, b. During the first discharge, that is, reaction with Li, the voltage drops from the open circuit voltage (OCV $\sim 2.6 \text{ V}$) continuously with small and

broad plateaus at ~ 1.3 and at ~ 0.8 V. At this point, the capacity is $\sim 300 \text{ mAhg}^{-1}$ which corresponds to the consumption of ~ 0.8 mole of Li per mole of CoN. After this, a large voltage plateau is observed at ~ 0.6 V up to a capacity of 570 mAhg^{-1} (1.6 moles of Li) followed by a gradual decrease in voltage up to the deep discharge limit, 0.005 V. The total first discharge capacity is $1080 (\pm 10) \text{ mAhg}^{-1}$ (2.94 moles of Li). This value is close to the theoretical capacity of 1102 mAhg^{-1} (3 moles of Li as per Eqn. (IV.1) with $M = \text{Co}$) expected from the complete reaction of CoN with Li and formation of Co- metal nano particles and Li_3N [26-30]. The first charge profile (extraction of Li) comprises a fairly large voltage plateau at ~ 0.7 V, with capacity $\sim 350 \text{ mAhg}^{-1}$ (~ 0.95 mole of Li) followed by a smaller plateau at ~ 1.3 V. The overall first charge capacity is $760 (\pm 10) \text{ mAhg}^{-1}$ (2.07 moles of Li) and thus, the irreversible capacity loss (ICL) observed during the first cycle is 320 mAhg^{-1} (0.87 mole of Li).

The second discharge profile shows a variation from the first- discharge profile indicating a slightly different electrode reaction. The plateau at ~ 0.6 V noticed during the first- discharge is not observed and the plateau at ~ 0.8 V becomes more prominent (Fig. IV.5 a). The total second- discharge capacity observed is $780 (\pm 10) \text{ mAhg}^{-1}$ (2.12 moles of Li). The second- charge profile is analogous to the first- charge profile showing a similar cycling behavior and the charge capacity is $755 (\pm 10) \text{ mAhg}^{-1}$, almost the same as the first- charge capacity. With an increase in the cycle number, the reversible capacity decreases slightly. However, after 5 cycles, it increases slowly but consistently to $990 (\pm 10) \text{ mAhg}^{-1}$ at the end of 80th cycle (Figs. IV.5b, c). Assuming $1 \text{ C} = 760 \text{ mAhg}^{-1}$, the current rate of 250 mAhg^{-1} corresponds to 0.33 C [34]. There is also a qualitative change in

the discharge- charge profiles in the cycling range, 20- 80 cycles: The well- defined voltage plateau regions are absent and show somewhat smoothly varying curves (Fig.

IV.5b).

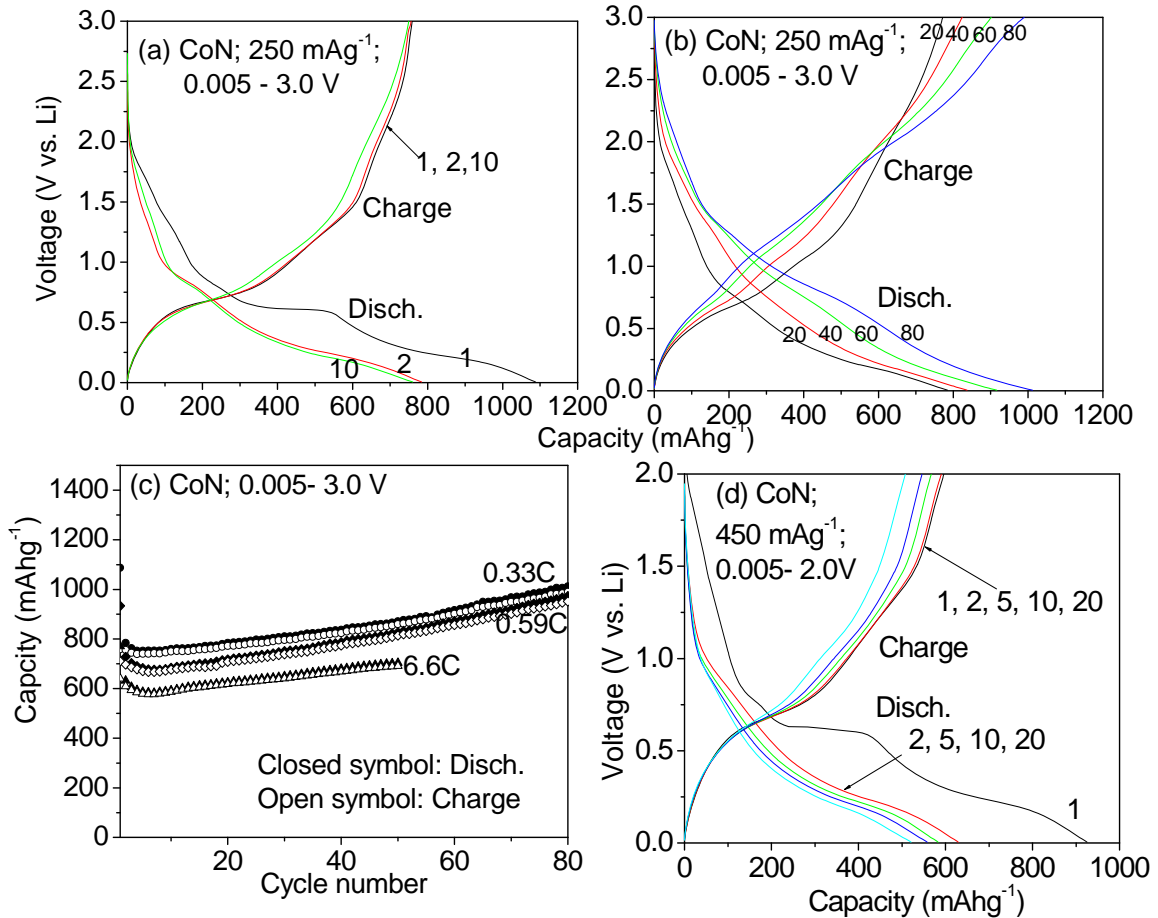


Fig.IV.5. Galvanostatic discharge- charge curves of nanoflake CoN: (a) 1-10 cycles (b) 20- 80 cycles, at 250 mA g⁻¹ (0.33 C) in the range 0.005- 3.0 V. Only selected cycles are shown for clarity. Numbers indicate cycle number. (c) Capacity vs. cycle number (up to 80 cycles) plots of nanoflake CoN, at C- rates of 0.33, 0.59 and 6.6 C. (d) Discharge-charge profiles of nanoflake CoN up to 20 cycles at 450 mA g⁻¹ (0.59 C) in the voltage range 0.005- 2.0 V. The numbers indicate cycle number.

In order to establish the rate capability of the nanoflake CoN films, galvanostatic cycling was carried out on duplicate cells at 450 mA g⁻¹ (0.59 C) up to 80 cycles, and at 5000 mA g⁻¹ (6.6 C) up to 50 cycles at room temperature. The voltage- capacity profiles are similar to those shown in Fig. IV.5 a, b. The capacity vs cycle number plots are

shown in Fig.IV.5c. As can be expected, the reversible capacities are smaller in comparison to those measured at 0.33 C. However, the general trend of the cycling behavior is similar. That is, there is an initial decrease in the capacity up to a few cycles, followed by a consistent increase up to the end of cycling. Thus, at 0.59 C-rate, the capacity increases from 670 mAhg⁻¹ at the 5th cycle to 950 (±10) mAhg⁻¹ (2.6 moles of Li) at the 80th cycle. Similarly, at 6.6 C-rate, the reversible capacity increases from 570 mAhg⁻¹ at the 5th cycle to 690 (±10) mAhg⁻¹ (1.9 moles of Li) at the 50th cycle. From Fig.IV.5c, it can be seen that the discharge and charge capacities overlap well and the coulombic efficiency (η) is 97-98 %.

Galvanostatic cycling was also carried out on duplicate cells at 450 mAhg⁻¹ (0.59 C) up to 20 cycles, in the voltage window 0.005 - 2.0 V vs. Li, in order to see the effect of reducing the upper cut-off voltage. The voltage– capacity profiles, shown in Fig.IV.5d, are qualitatively similar to those in Fig.IV.5a, b. The total first-discharge capacity is 925 (±10) mAhg⁻¹ (~2.5 moles of Li), whereas the first-charge capacity is 595 (±10) mAhg⁻¹. The ICL is thus 330 mAhg⁻¹ and compares well with the value of 320 mAhg⁻¹ obtained at 0.33C, with the upper voltage cut-off of 3.0 V (Fig.IV.5a). However, the capacity decreased consistently in the range 2-20 cycles, reaching a value of 505 (±10) mAhg⁻¹ (1.4 moles of Li) at the 20th cycle. Hence, we conclude that cycling to an upper cut-off voltage of 3.0V is necessary in order to realize the high capacities over extended number of cycles.

It is well-known that the ICL during the first-cycle arises due to the extra consumption of Li, in addition to that needed for the reduction of metal oxide, fluoride, nitride etc to the respective metal nano-particles (e.g., Eqn.(IV.1)), for the formation of

solid electrolyte interphase (SEI), and a polymeric layer, under deep discharge conditions, 0.005 V vs Li [5, 9, 14, 35]. The solvents present in the electrolyte, namely ethylene carbonate (EC) and diethyl carbonate (DEC) participate in the reaction with Li to form the above SEI and polymeric layer. During subsequent discharge and charge cycling, at least up to a certain number of cycles, the SEI and polymeric layer re-form and decompose respectively, till a stable structuring of the electrode is attained. This is called ‘formatting’ of the electrode, after which the SEI gets stabilized and the reversibility of the electrode as well as the η are improved. Studies on oxides like CoO [5, 14, 35] and ZnCo₂O₄ [9] have shown that in order to realize the maximum obtainable reversible capacities during cycling, it is essential to employ an upper cut-off voltage of ≥ 3.0 V vs Li. This is to enable the decomposition of the polymeric layer formed (or re-formed under deep discharge) on the nano-particles of the active material. As can be seen from Figs. IV.5b, c and d, cycling up to 3.0 V is essential to obtain high and reversible capacities in CoN. We note that the group of Fu employed an upper cut-off voltage of 3.5 V vs Li for CrN [28], (Cr_{1-x}Fe_x)N [29] and VN [30] and obtained high reversible capacities.

IV.3.2.2. Cyclic Voltammetry

Cyclic voltammetry studies act as complementary tool to the galvanostatic cycling data in establishing the voltages at which the reactions occur and the existence of two-phase region. The cyclic voltammograms (CV) were recorded in the potential range 0.005- 3.0 V, at the slow scan rate of 58 μ Vs⁻¹ up to 20 cycles and are shown in Fig. IV.6a, b. The Li metal is used as the counter and reference electrode. As can be seen in Fig. IV.6a, during the first cathodic scan (reaction of Li with CoN), starting from OCV

(~2.6 V) a smooth sloping curve up to ~1.7 V is observed with low intensity peaks at 1.68 V and 0.84 V. This is an indication of single phase reaction and reduction of Co^{3+} in CoN forming $\text{Li}_x(\text{CoN})$. The low- intensity peaks may represent phases with different values of x or phase transitions in $\text{Li}_x(\text{CoN})$. An intense cathodic (reduction) peak is observed at 0.58 V, followed by another strong peak at 0.2 V. As will be discussed later, these peaks represent the structure- destruction followed by the formation of Co- metal and Li_3N , respectively. During the first anodic scan (Li extraction), the CV shows a strong peak at 0.7 V followed by minor peaks at 1.37 and 2.32 V (Fig. IV.6a). These peaks are the indication of de- nitridation reaction of Li_3N and formation of CoN.

The second cathodic scan differs from the first one in that the peak at 0.58 V is absent and all the other cathodic peaks show minor shifts in potentials (Fig. IV.6b). In the second anodic scan, the intense peak at 0.7 V appears as in the first anodic scan and the minor anodic peaks now appear at 1.05 V and 2.10 V. With an increase in the cycle number, the CVs overlap well showing good reversibility. However, development of minor additional peaks at ~1.45 V and ~1.0 V in the cathodic scans, and a peak at ~1.45 V in the anodic scans are clearly noted. The low- intensity multiple peaks in the cathodic/ anodic scans are an indication of intermediate step- reactions for the decomposition/ formation of CoN during cycling. The differential capacity (dQ/dV) vs. voltage plots for the first and 20th cycle are shown in Figs. IV.6c and d. These are extracted from the galvanostatic capacity vs. voltage profiles of Figs. IV.5 a and b, respectively. The voltage plateau regions in the latter curves appear as peaks in Figs. IV.6c and d. As is clear, they show an excellent resemblance to the CVs in Figs. IV.6a and b, both in the shape as well as the values of the peak potentials, thereby confirming the complementary nature of the

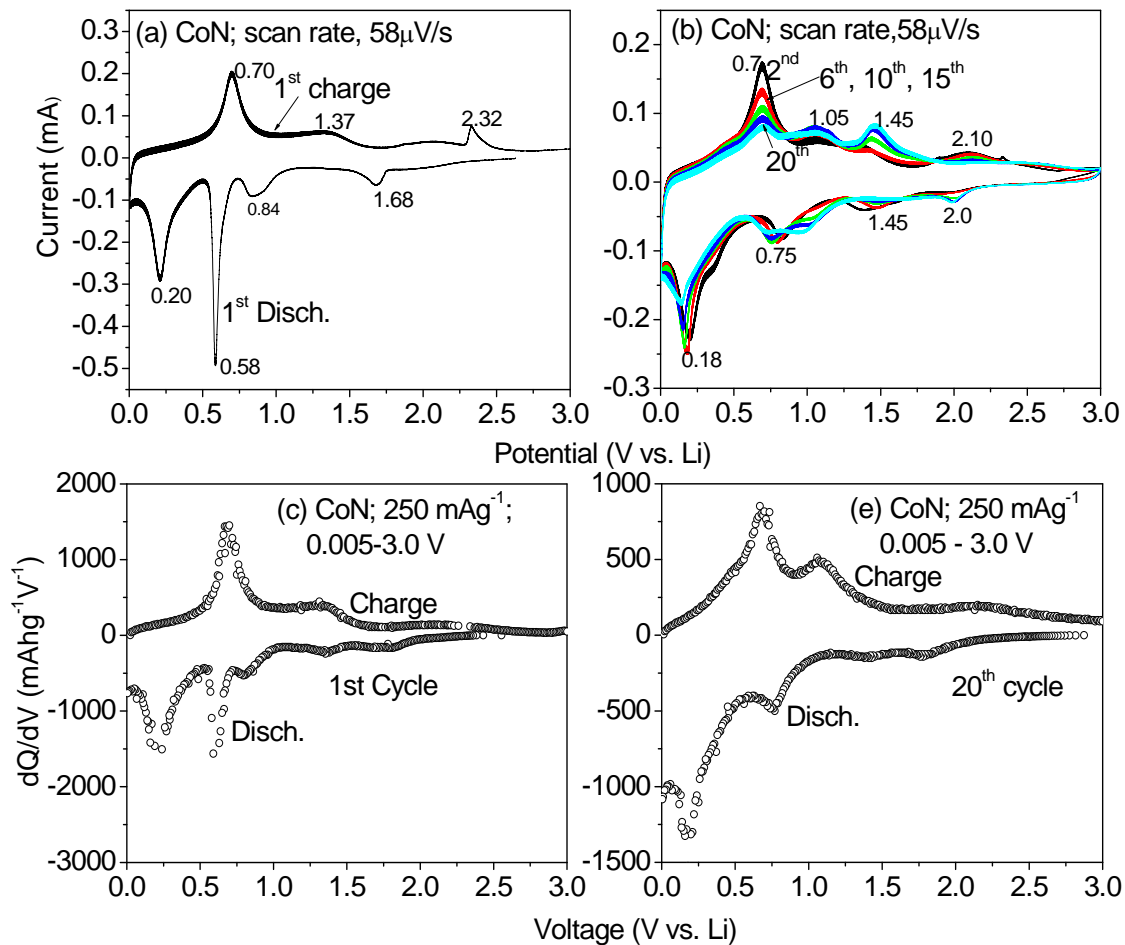


Fig.IV.6. Cyclic voltammograms of nanoflake CoN: (a) 1st cycle and (b) 2 – 20 cycles. Only selected cycles are shown for clarity. Scan rate is $58 \mu\text{Vs}^{-1}$. Li- metal anode is the counter and reference electrode. Numbers represent the potentials in Volts. (c) Differential capacity (dQ/dV) vs. Voltage plot for the first- cycle extracted from the galvanostatic capacity- voltage profiles of Fig.IV.5a. (d) Differential capacity (dQ/dV) vs. Voltage plot for the 20th -cycle extracted from the galvanostatic capacity- voltage profiles of Fig.IV.5b.

CVs, and reproducibility of the electrochemical properties of the CoN-Li system. From the data of Fig.IV.6, we note that the formation and decomposition of Li_3N occurs at potentials ~ 0.2 and ~ 0.7 V, respectively. The decomposition and formation of CoN occurs mainly at potentials ~ 0.75 and ~ 1.05 V, respectively (Fig. IV.6a,b). However, the existence of several low-intensity peaks in the range, 1.0- 2.1 V, both in the cathodic and

anodic scans indicate that the ‘conversion’ reaction involves the formation of intermediate compositions, $(\text{Li}_{3-x}\text{Co}_x)\text{N}$ (e.g., $x = 0.1-0.44$ [20, 21]), and cycling up to 3.0 V is essential for the realization of full reversible capacity. It may be mentioned here that Gillot et al [36] and Boynov et al [37] have shown that in the NiP_2 - Li system, Li-cyclability occurs through the formation/ decomposition of an intermediate phase, Li_2NiP_2 .

IV.3.2.3. ex- situ XRD, TEM and SAED

Studies by the group of Fu on CrN [28], $(\text{Cr}_{1-x}\text{Fe}_x)\text{N}$ [29] and VN [30] have shown that the crystal structure destruction occurs during the first discharge due to the reaction of Li with the starting materials followed by the formation of nano- size metals and Li_3N . Subsequent charging will re-form VN releasing Li- ions and electrons (reverse reaction of Eqn. (IV.1)). In order to confirm the crystal structure destruction in the case of CoN, several duplicate cells were assembled and then discharged /charged to selected voltages. After stabilizing for about 2 h, the cells were disassembled in the glove box and treated for XRD and TEM studies as described in Chapters II and III. The XRD patterns of the electrodes during the first cycle are shown in Fig. IV.2. The relative intensities (y-axis) have been normalized for better comparison. The XRD pattern of electrode discharged to 0.5 V did not show any peaks of CoN and peaks due to Cu- substrate and Al- sample holder only are seen. This shows the structure destruction started slightly above 0.5 V and corroborates the galvanostatic and CV data where a large voltage plateau sets in at ~ 0.58 V indicating two- phase reaction. The XRD pattern at 0.005 V during the first- discharge also is devoid of any peaks indicating that the electrochemically- formed species (Co- metal and Li_3N) are not noticeable, due to their

nano size nature [9, 15, 28, 30]. Similarly, the XRD pattern taken at 3.0 V at the end of first- charge also does not show any characteristic peaks due to CoN.

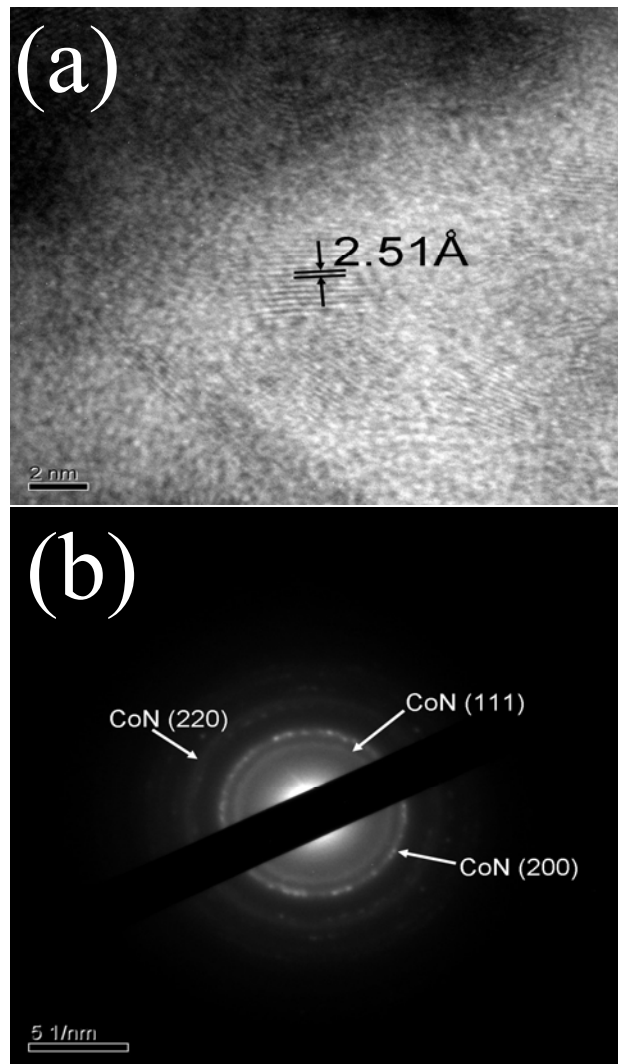


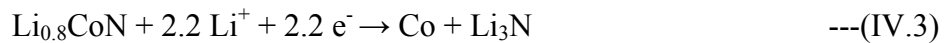
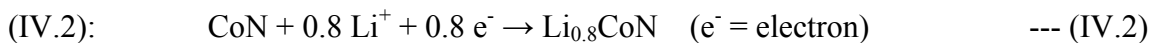
Fig.IV.7. (a) HR- TEM lattice image and (b) SAED pattern of cycled nanoflake CoN in the charged state (3.0 V) after 80 cycles in the range, 0.005- 3.0 V vs. Li. Scale bars are shown.

The ex-situ HR- TEM lattice image and the SAED pattern of the CoN electrode in the fully charged state (3.0 V) after 80 cycles are shown in Fig.IV.7a and b, respectively. Fig. IV.7a compares well with the lattice image of virgin CoN film of Fig. IV.4c and shows the nano- crystalline grains (~3- 5 nm) embedded in an amorphous matrix. The

interplanar d- spacing is found to be $2.51(\pm 0.02)$ Å, which corresponds to the (111) plane of CoN. The grain- size reduction of the embedded particles in an amorphous matrix is due to the so called ‘electrochemical grinding’ effect [14]. The SAED pattern comprises a diffuse set of concentric rings with some bright spots indicating low- crystallinity of CoN (Fig. IV.7b). The d- values calculated from the rings are 2.51, 2.13 and $1.45 (\pm 0.02)$ Å and correspond to the (hkl) values (111), (200) and (220), respectively of CoN. These values are in good agreement with the d- values calculated from the XRD pattern and the SAED of virgin material shown in Fig. IV.4d. Thus, from the ex- situ XRD, -HR- TEM and -SAED data, we conclude that during the discharge process, CoN decomposes to Co and Li_3N whereas during the charging process, re-formation of CoN occurs. We note, however, that some un-reacted CoN may also be contributing to the observed data, and hence, ex-situ HR-TEM and SAED on the discharged-product after 80 cycles, is also necessary to substantiate the above statement.

IV.3.3. Reaction mechanism

Based on ex- situ XRD, HR- TEM and SAED patterns and the observed galvanostatic cycling and CV data, a Li- cycling mechanism can be proposed similar to that established by Fu and co- workers for the metal nitrides, CrN [28] and VN [30] except for an intermediate step during the first- discharge involving Li- intercalation, Eqn.



The reaction in Eqn. (IV.2) is supported by the galvanostatic cycling (Fig. IV.5a) and CV (Fig. IV.6a), where a smoothly varying voltage profile is noted up to ~ 0.6 V during the

first- discharge, with minor voltage plateaus observed at ~ 1.3 V and ~ 0.8 V, and consumption of 0.8 mole of Li (capacity of ~ 300 mAhg⁻¹). The broad voltage plateau appearing both in the galvanostatic profile (Fig. IV.5a), and as a peak in CV (Fig. IV.6a) at 0.58 V indicates the crystal structure destruction (amorphisation) followed by Eqn. (IV.3), indicating the co- existence of intercalated phase (Li_{0.8}CoN), Co and Li₃N. This is well- supported by the ex- situ XRD (Fig. IV.2). The XRD peaks due to Co and Li₃N are not seen due to their nano size nature.

The theoretical reversible capacity based on the reaction mechanism Eqn. (IV.4) is 1102 mAhg⁻¹ (3 moles of Li), but the experimental first- discharge capacity observed is 1080 (± 10) mAhg⁻¹ (2.94 moles of Li). As discussed earlier, considerable amount of Li will also be consumed during the first- discharge for the formation of SEI and polymeric layer on the freshly generated Co- metal nano- particles. Hence, it is assumed that an incomplete participation of the active material during the first- discharge is taking place. The first-charge process can be represented by the forward reaction of Eqn.(4), analogous to Eqn.(IV.1). The first-charge capacity is only 760 mAhg⁻¹ (2.06 moles of Li) which indicates that ~ 0.9 mole of Li might have been consumed for the formation of SEI and polymeric layer. The second and subsequent cycling involve only Eqn.(IV.4) and do not appear to go through Eqn.(IV.2), due to the continuous decrease in the width of the voltage plateau at ~ 0.6 V (Figs.IV.5a,b and d). Eventhough, there is possibility of formation and decomposition of Li_{2.6}Co_{0.4}N during the first- charge operation, as studied by Shodai et al. [38] in the voltage range, 0 to 1.5 V, upon charging to 3.0 V, CoN formation occurs as per Eqn. (IV.4) , as shown by the SAED pattern (Fig. IV7b).

With an increase in the cycle number, both the discharge and charge capacities show a systematic increase, indicating an increase in the participation of the 'active material' in each cycle, ultimately reaching 990 mAhg^{-1} (2.7 moles of Li) at 0.33 C rate, at the end of 80th cycle. It must be pointed out, however, that neither the theoretical reversible capacity nor the measured first-discharge capacity has been achieved till the 80th cycle, indicating that full participation of the 'active material' possibly needs cycling beyond 80 cycles. The same trend is shown when cycled at both 0.59C and 6.6 C rates (Fig.IV.5c). An increase in the reversible capacity with an increase in the cycle number has been observed in several oxide systems in the literature, like LiMVO_4 (M = Co, Ni, Zn, Cd) [39], nano- Fe_3O_4 [7], $\text{LiHoMo}_3\text{O}_8$ and LiYMo_3O_8 (described in Chapter III). An explanation similar to that for CoN can be given for the observed cycling behavior of the above compounds.

It is relevant to compare the present data on nanoflake CoN with those reported by Fu and co-workers on thin films of CrN [28], FeN [29] and VN [30]. Their thin films varied in thickness from 400 to 700 nm, and TEM showed smooth films without any characteristic morphology. They found that, when cycled at $28 \mu\text{Acm}^{-2}$ ($\sim 230 \text{ mA g}^{-1}$, based on the weight of the film) in the range 0.005-3.5 V vs Li, CrN showed a first cycle charge capacity of 1200 mAhg^{-1} (2.96 moles of Li vs. theoretical 3 moles of Li per formula unit) which slowly degraded at 0.5% per cycle up to 30 cycles. Under similar conditions, films of VN gave a first cycle charge- capacity of 1156 mAhg^{-1} , which degraded slowly, but stabilized to 800 mAhg^{-1} (1.94 moles of Li per formula unit) in the range, 15 to 50 cycles. On the other hand, FeN films showed a first-cycle charge-capacity of 1020 mAhg^{-1} , which degraded drastically to 40 mAhg^{-1} after 30 cycles. Thus,

it may be concluded that the cycling performance of nanoflake CoN is comparable to those of thin films CrN and VN, and in addition, shows very good rate-capability.

IV.4. Conclusions

Nanoflake CoN is prepared by RF magnetron sputtering technique and characterized by XRD, RBS, FE- SEM, HR- TEM and SAED techniques. The thickness and composition, analyzed by RBS, confirm the formation of CoN with a thickness, 200 (± 10) nm. The Li- cycling behavior of nanoflake CoN is evaluated by galvanostatic discharge- charge cycling and cyclic voltammetry (CV) with Li as the counter electrode at room temperature. When cycled at a current density 250 mA g^{-1} (0.33 C) in the voltage window 0.005- 3.0 V, nanoflake CoN film showed an initial reversible capacity of $760 (\pm 10) \text{ mA h g}^{-1}$ which increases consistently to 990 mA h g^{-1} (2.7 moles of Li per mole of CoN) at the end of 80th cycle. Excellent rate capability is also shown: At 0.59 C, a capacity of $950 (\pm 10) \text{ mA h g}^{-1}$ (2.6 moles of Li) after 80 cycles, and at 6.6 C, a capacity of 690 mA h g^{-1} (1.9 moles of Li) at the end of 50 cycles, are observed. The coulombic efficiency is found to be $>96 \%$ in the range of 10-80 cycles. The average charge potential for the decomposition of Li_3N is 0.7 V whereas the average discharge potential for the formation of Li_3N is 0.2 V vs. Li. However, complete reversibility of Eqn. (IV.4) requires cycling to an upper cut- off voltage of 3.0 V and the reaction appears to go through intermediate phases, $(\text{Li}_{3-x}\text{Co}_x)\text{N}$. The Li- cycling performance of nanoflake CoN films is compared with those of CrN, FeN, and VN reported in the literature. Thus, the present study shows that nanoflake CoN film can be a prospective anode material for the future generation LIBs.

References

- [1] Lithium Batteries: Science and Technology, Eds: G.-A. Nazri, G. Pistoia, Kluwer Academic Publ., New York, 2003.
- [2] A. S. Arico, P. Bruce, B. Scrosati, J.-M. Tarascon, W. V. Schalkwijk, *Nature Mater.* 4 (2005) 366.
- [3] P. G. Bruce, B. Scrosati, J.-M. Tarascon, *Angew. Chem. Int. Ed.* 47 (2008) 2930.
- [4] A. K. Shukla, T. Prem Kumar, *Current Sci. (India)* 94 (2008) 314.
- [5] P. Poizot, S. Laruelle, S. Grugeon, L. Dupont, J.-M. Tarascon, *Nature* 407(2000) 496.
- [6] M. V. Reddy, T. Yu, C. H. Sow, Z. X. Shen, C. T. Lim, G. V. Subba Rao, B. V. R. Chowdari, *Adv. Funct. Mater.* 17 (2007) 2792.
- [7] P. L. Taberna, S. Mitra, P. Poizot, P. Simon, J.-M. Tarascon, *Nature Mater.* 5 (2006) 567.
- [8] D. Hara, J. Shirakawa, H. Ikuta, Y. Uchimoto, M. Wakihara, T. Miyayama, I. Watanabe, *J. Mater. Chem.* 12 (2002) 3717.
- [9] Y. Sharma, N. Sharma, G. V. Subba Rao, B. V. R. Chowdari, *Adv. Funct. Mater.* 17 (2007) 2855.
- [10] H. Li, P. Balaya, J. Maier, *J. Electrochem. Soc.* 151 (2004) A1878.
- [11] G. G. Amatucci, N. Pereira, *J. Fluorine Chem.* 128 (2007) 243.
- [12] R. E. Doe, K. A. Persson, Y. S. Meng, G. Ceder, *Chem. Mater.* 20 (2008) 5274.
- [13] M.V. Reddy, S. Madhavi, G.V. Subba Rao, B.V. R. Chowdari, *J. Power Sources* 162 (2006)1312.
- [14] S. Grugeon, S. Laruelle, L. Dupont, J.-M. Tarascon, *Solid State Sci.* 5 (2003) 895.
- [15] Y. Sharma, N. Sharma, G. V. Subba Rao, B. V. R. Chowdari, *J. Mater. Chem.*

- 19 (2009) 5047.
- [16] D. C. C. Silva, O. Crosnier, G. Ouvrard, J. Greedan, A. S.-Sefat, L. F. Nazar, *Electrochem. & Solid-State Lett.* 6 (2003) A162.
- [17] F. Gillot, M. Menetrier, E. Bekaert, L. Dupont, M. Morcrette, L. Monconduit, J.- M. Tarascon, *J. Power Sources* 172 (2007) 877.
- [18] L. M. L. Fransson, J. T. Vaughey, K. Edstrom, M. M. Thackeray, *J. Electrochem. Soc.* 150 (2003) A86.
- [19] T. Lapp, S. Skaarup, A. Hooper, *Solid State Ionics* 11 (1983) 97.
- [20] J.B. Ducros, S. Bach, J.P. P.-Ramos, P. Willmann, *Electrochem. Commun.* 9 (2007) 496.
- [21] J.B. Ducros, S. Bach, J.P. P.-Ramos, P. Willmann, *J. Power Sources* 175 (2008) 517.
- [22] J.B. Ducros, S. Bach, J.P. P.-Ramos, P. Willmann, *Electrochim. Acta* 52 (2007) 7035.
- [23] Y. Liu, T. Mastumura, Y. Ono, N. Imanishi, A. Hirano, Y. Takeda, *Solid State Ionics* 179 (2008) 2069.
- [24] S. Bach, J. P. P.-Ramos, J. B. Ducros, P. Willmann, *Solid State Ionics* 180 (2009) 231.
- [25] J. Cabana, Z. Stoeva, J. J. Titman, D. H. Gregory, M. R. Palacin, *Chem. Mater.* 20 (2008) 1676.
- [26] Y. Wang, Z.-W. Fu, X.-L. Yue, Q.-Z. Qin, *J. Electrochem. Soc.* 151 (2004) E162.
- [27] Z.-W. Fu, Y. Wang, X.-L. Yue, S.-L. Zhao, Q.- Z. Quin, *J. Phys. Chem. B* 108 (2004) 2236.
- [28] Q. Sun, Z.-W. Fu, *Electrochem. & Solid-State Lett.* 10 (2007) A189.

- [29] Q. Sun, Z.-W. Fu, *Electrochem. & Solid-State Lett.* 11 (2008) A233.
- [30] Q. Sun, Z.-W. Fu, *Electrochim. Acta* 54 (2008) 403.
- [31] L. R. Doolittle, *Nucl. Instrum. Methods Phys. Res. B* 9 (1985) 344.
- [32] K. Suzuki, T. Kaneko, H. Yoshida, H. Morita, H. Fujimori, *J. Alloys Compds* 224 (1995) 232.
- [33] G. De Roos, J. M. Fluit, L. A. M. Hermans, J. W. Geus, *Z. Anorg. Allgem. Chem.* 449 (1979) 115.
- [34] Many reports in the literature defined the 1C-rate as the full discharge or charge capacity corresponding to insertion/extraction of one mole of Li in 1h. While this is valid for the case of LIB-cathode materials like, LiCoO_2 , LiMn_2O_4 and LiFePO_4 , we feel that in the case of prospective anode materials which can deliver more than 1Li in 1 h, like CoO , Fe_3O_4 , SnO_2 , MN (M = V, Cr, Fe and Co), the first-cycle reversible capacity, or in favorable cases, where the reversible capacity which is stable over a large number of cycles, must be used to calculate the C-rate. Thus, we use $1\text{ C} = 760\text{ mA g}^{-1}$ in the case of CoN, since the observed first- cycle reversible capacity is 760 mA h g^{-1} , which means that the maximum capacity can be delivered in 1h during cycling.
- [35] S. Laruelle, S. Grugeon, P. Poizot, M. Dolle, L. Dupont, J.-M. Tarascon, *J. Electrochem. Soc.* 149 (2002) A627.
- [36] F. Gillot, S. Boyanov, L. Dupont, M.-L. Doublet, M. Morcrette, L. Monconduit, J.-M. Tarascon, *Chem. Mater.* 17 (2005) 6327.
- [37] S. Boyanov, J. Bernardi, E. Bekaert, M. Menetrier, M.-L. Doublet, L. Monconduit, *Chem. Mater.* 21 (2009) 298.
- [38] T. Shodai, S. Okada, S. Tobishima, J. Yamaki, *J. Power Sources* 68 (1997) 515.

[39] D. Guyomard, C. Sigala, A. Le Gal La Salle, Y. Piffard, J. Power Sources 68 (1997)
692.

Chapter V

Part I

Li- cyclability and storage of tin hollandites, $K_2(M_2Sn_6)O_{16}$ (M = Co, In) *

Abstract

Micron- size polycrystalline powders of the compounds, $K_2(In_2Sn_6)O_{16}$ (K-In) and $K_2(Co_2Sn_6)O_{16}$ (K-Co) are prepared by the high temperature solid state reaction and characterized by X-ray diffraction, scanning electron microscopy (SEM) and density methods. Electrochemical studies were carried out by galvanostatic cycling and cyclic voltammetry (CV) in the voltage window of 0.005-0.8V vs. Li, at room temperature. The first-charge capacities of (K-In) and (K-Co) at the current density of 60 mA g^{-1} ($\sim 0.1C$) are $600 (\pm 10)$ and $465 (\pm 10) \text{ mAh g}^{-1}$, respectively. For (K-Co), 91% of the 5th cycle reversible capacity was retained at the end of 40th cycle, whereas for (K-In), the capacity-retention was 80% in the range 5-40 cycles, with a coulombic efficiency, 96-97% for both the compounds. From the CV, the average charge and discharge potentials for both (K-Co) and (K-In) are $\sim 0.47 \text{ V}$ and $\sim 0.2 \text{ V}$, respectively. The ex- situ XRD data for (K-Co) are presented and Li-cycling mechanism is discussed.

* One paper has been submitted for publication and one paper was presented at an Intl. Conference based on the work described in this Chapter.

V. 1. Introduction

The increase in demand for lithium ion batteries (LIBs) as secondary power sources for portable electronic appliances and for use in high energy applications, such as electric vehicle (EV)/hybrid electric vehicle (HEV) motivated the search for new anode (negative electrode) materials with high volumetric and gravimetric capacity [1-4]. The limited capacity value of graphite (theoretical, 372 mAhg^{-1} ; LiC_6), which is employed as anode in the present-day LIBs, operates on the basis of reversible Li- intercalation/ de-intercalation reaction and may not be suitable for use in high energy applications. During the last decade, tin (Sn), Sn- alloys and Sn-based oxides and composites were extensively studied as alternative anode materials due to their high capacity ($\sim 990 \text{ mAhg}^{-1}$) based on alloying-de-alloying reaction mechanism and low charge/discharge potential vs. Li [1, 3, 4]. But the inherent problem associated with Sn is the large volume variation ($\sim 300\%$) during electrochemical cycling, which leads to the generation of strong internal mechanical stresses and cracking of the particles, resulting in the loss of electrical contact with the current collector causing capacity fading. The capacity retention in the case of Sn has been improved to some extent by various approaches, such as (i) reducing the particle size of the active material to nano-size, (ii) addition of one or more electrochemically active/ inactive counter (matrix) atoms/ions, (iii) proper choice of the starting crystal structure, morphology and restricting the voltage range of cycling vs. Li [4-9].

A large number of Sn-based ternary oxides of various crystal structures, namely, perovskite type, ASnO_3 (A = Ca, Sr, Ba) [10-12], ilmenite-type, CdSnO_3 [13], inverse-spinel-type, M_2SnO_4 (M=Mg, Mn, Co, Zn) [14-19], pyrochlore-type, $\text{A}_2\text{Sn}_2\text{O}_7$, A=Nd,Y

[20], CaFe_2O_4 -type, NaFeSnO_4 [21], ramsdellite-type, LiMSnO_4 , $\text{M}=\text{Fe}$, In [22], Nasicon-type, $\text{LiSn}_2\text{P}_3\text{O}_{12}$ [23] and hollandite-type, $\text{K}_2(\text{M}_x, \text{Sn}_{8-x})\text{O}_{16}$ ($\text{M}=\text{Li}$, Mg , Fe , Mn) [24] have been studied for their Li-cycling behavior. Results showed that indeed the starting crystal structure, the nature and amount of the matrix element (A or M), and morphology and particle-size (micron-size or nano-size) play a role in determining the obtainable reversible capacity, due to the alloying-de-alloying reaction of Sn-metal, and the long-term Li-cycling stability at various current (C)-rates. Thus, compounds containing SnO_6 - octahedra, either isolated or linked to other octahedra, as in perovskite, hollandite and Nasicon structures, matrix elements like, Ca, Co, Li or Fe were found to give high and stable capacities. Also, nano-size particles of the above compounds and/or spherical morphology of nano-size aggregates invariably are found to give good long-term Li-cyclability. High surface area and short diffusion lengths for the Li-ion diffusion of the nano-size particles will help to buffer, in the presence of the matrix elements, the unit cell volume variations during Li-cycling.

It must be pointed out that the initial electrochemical discharge reaction of the above oxides with Li-metal leads to the formation of the nano-Sn metal, other matrix elements (Fe, Co, In), Li_2O , and other oxides, like, CaO, MgO and K_2O . These will be present either in the form of X-ray amorphous or nano-crystalline composite. Subsequent electrochemical charge-reaction (extraction of Li) and cycling involves the alloying-de-alloying reaction of Sn-metal, but the 'local structure' of the nano-composite is governed by the starting crystal structure, and this influences the Li-cycling behavior [10-12, 14, 23-24].

Hollandite-type compounds possess a one-dimensional tunnel-like framework structure, have a local stoichiometry of $M^{IV}O_2$ and are bounded by rutile-type MO_6 linked octahedra. The tunnels in the structure are occupied by large-size alkaline (K, Rb) or alkaline earth (Ba) elements in conjunction with the charge compensating partial replacement of M^{IV} with di- or tri-valent cations. $K_2M_2Sn_6O_{16}$ ($M = Fe$) and $K_2(M_1Sn_7)O_{16}$ ($M = Mg, Mn, Ni$) are typical hollandite-type compounds with Sn providing the framework cation and the K occupying the tunnels (Fig. V.1).

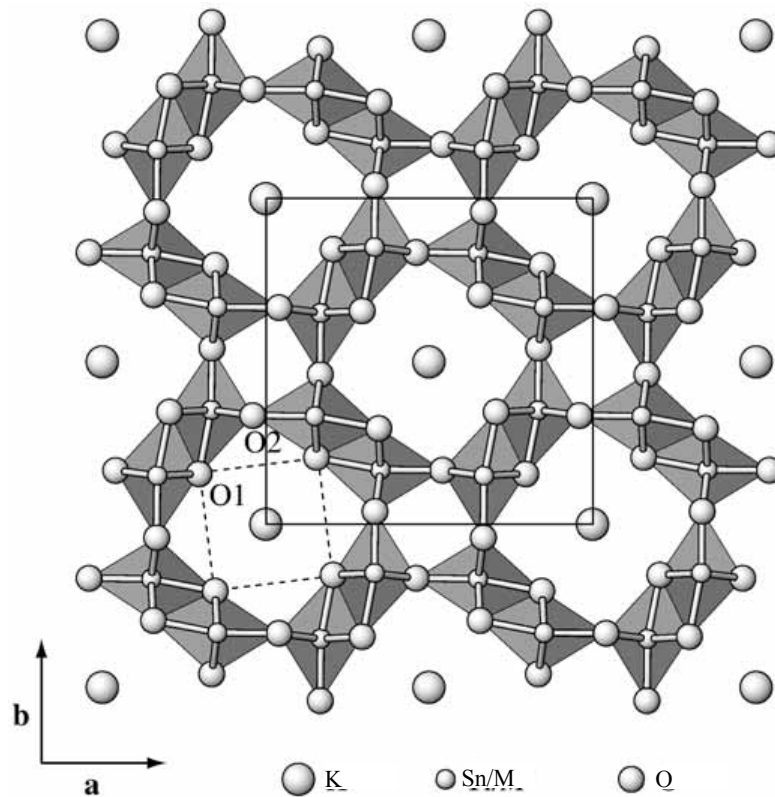


Fig.V.1. The structure of $K_2(M,Sn)_8O_{16}$ hollandite projected along the c - axis. Taken from Michiue et al. [25]

Sharma et al [24] studied the Li-cyclability of the micron-size particles of Sn-hollandites, $K_2(M_x,Sn_{8-x})O_{16}$, $M = Li, Mg, Fe, Mn$ and found initial reversible capacities ranging from 420 to 600 $mAhg^{-1}$ depending on M, when cycled at 60 mAg^{-1} in the

voltage range, 0.005-1.0 V vs. Li. Capacity-fading was noticed in all cases, ranging from 17 % for M = Fe to as high as 47 % for M = Mn, up on cycling to 50 cycles, and it was pointed out that Fe is a good matrix element for Li-cycling of Sn in the hollandite structure. The present work represents the extended studies to explore other tin-hollandites with cobalt (Co) and indium (In) incorporated in to the structure. It is to be noted that In also can form an alloy with Li [22], and hence a higher reversible capacity can be expected. Results are reported here.

V. 2. Experimental

The compounds, $K_2(Co_2Sn_6)O_{16}$ and $K_2(In_2Sn_6)O_{16}$ were prepared by the conventional solid state reaction by using the stoichiometric mixture of K_2CO_3 (99.99%, Merck), Co_3O_4 (99.9%, Merck) or In_2O_3 (99.99%, Cerac) and SnO_2 (99.9%, Merck) to give ~8 g of the product compound. The mixture was ground in a mechanical grinder for 15 min into fine powder. The powder was pressed into a pellet and subjected to a series of heatings in a box furnace (Carbolite, UK) at 500, 950 and 1150 °C for 5 h in air at a heating rate of 4 °C/min with intermediate grinding and pelletising and cooling to room temperature. Finally, the product was ground to fine powder and kept in a desiccator.

The structural and morphological characterizations were carried out as discussed in earlier Chapters- II to IV. The procedure of electrode fabrication, cell fabrication and electrochemical characterization and ex-situ-XRD studies were adopted as mentioned in Chapters- III and IV. For recording the ex-situ XRD patterns of cycled electrode, the cells were disassembled in the glove box, the electrode was removed, washed with DEC, and dried.

V. 3. Results and Discussion

V. 3.1. Structure and Morphology

The compounds $K_2(Co_2Sn_6)O_{16}$ (here after (K-Co)) and $K_2(In_2Sn_6)O_{16}$ (K-In), are grey and white colored crystalline powders, respectively. The XRD patterns of the compounds showed lines characteristic of tetragonal system with $I4/m$ space group (Fig. V.2a). The calculated lattice parameters are: $a=10.480(2)$ Å; $c= 3.17(2)$ Å for (K-Co) and $a = 10.586(2)$ Å; $c= 3.20(2)$ Å for (K-In). The lattice parameters for (K-In) match well with $a = 10.59$ Å and $c = 3.20$ Å reported by Bayer and Hoffman [26]. The (K-Co) is the new composition presently prepared, and the smaller values of lattice parameters in comparison to (K-In) can be understood because of the smaller ionic radius of Co^{3+} (low spin: 0.545 Å) vs. In^{3+} (0.8 Å) for octahedral coordination [27]. The SEM photographs of (K-Co) and (K-In) showed micron- sized particles due to the high- temperature preparation (Fig.V.2 c, d). The measured densities of (K-Co) and (K-In) powders are 5.803 (3) and 6.222(3) g/cm³, respectively. These values compare well with the X- ray densities of 5.557 (3) for (K-Co) and 5.904 (3) g/cm³ for (K-In), respectively.

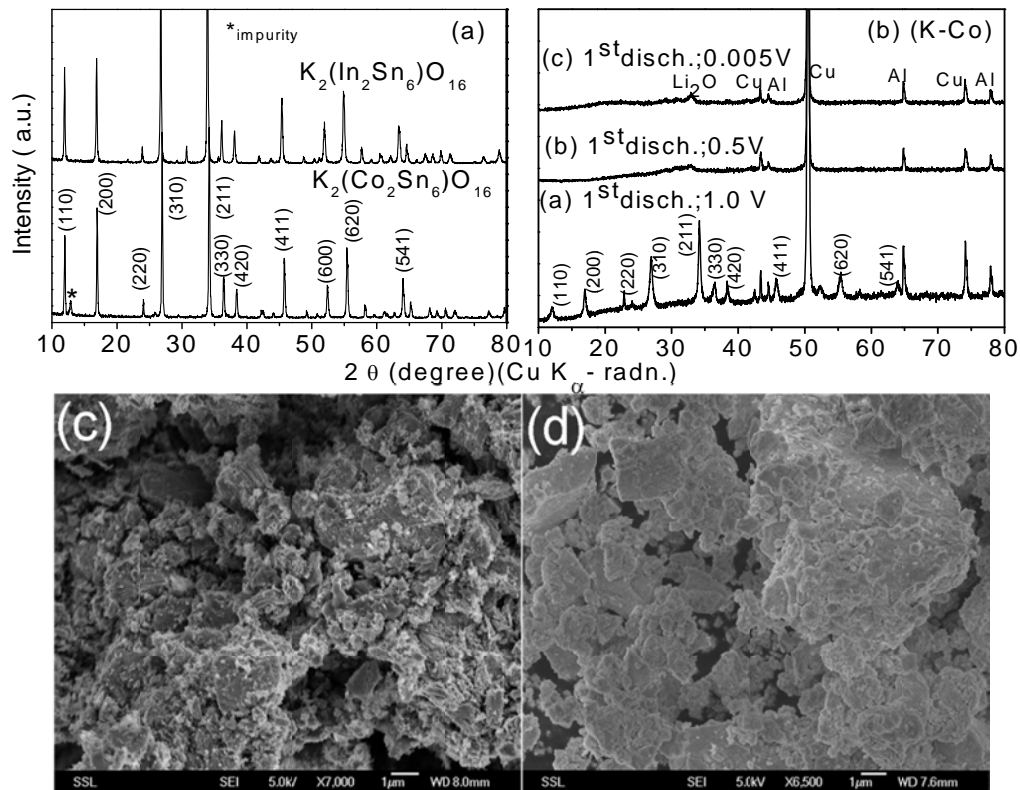


Fig.V.2. Powder X-ray diffraction (XRD) patterns of (a) $K_2(In_2Sn_6)O_{16}$ (K-In) and $K_2(Co_2Sn_6)O_{16}$ (K-Co). Miller indices are indicated. (b) Ex-situ XRD patterns of (K-Co) at 1.0, 0.5 and 0.005 V. Lines due to Cu-metal (substrate) and Al-metal (sample holder) are indicated. Cu $K\alpha$ - radiation. SEM micrograph of (c) $K_2(Co_2Sn_6)O_{16}$ (K-Co) and (d) $K_2(In_2Sn_6)O_{16}$ (K-In). Scale bar is shown.

V. 3.2. Galvanostatic cycling

Fig. V.3 shows the voltage vs. capacity plots of (K-Co) and (K-In) in the voltage window of 0.005-0.8 V vs. Li, at a current density 60 mAhg^{-1} up to 40 cycles. The profiles in both cases show that the 1st discharge starts from the open circuit voltage (OCV~2.6 V). The voltage drops rapidly from OCV to ~0.9 V at which point, a plateau is exhibited indicating a two phase reaction in both the compounds. We note that a similar voltage plateau at ~0.9 V is seen in other Sn- compounds like, SnO_2 [28] and hollandites with $M = Fe, Mg$ and Li [24]. The plateau region extends up to $\sim 480 \text{ mAhg}^{-1}$ (consumption of 20.8 moles of Li per mole of (K-Co)), while for (K-In), the value is 500

mAhg^{-1} (23.8 moles of Li). After the plateau, the voltage - capacity profiles show a continuous decrease up to the deep discharge limit, indicating an essentially a single-phase reaction. At the end of the first discharge, the total capacities for (K-Co) and (K-In) are at $1580 (\pm 10) \text{mAhg}^{-1}$ (68.6 moles of Li) and $1830(\pm 10) \text{mAhg}^{-1}$ (87.1 moles of Li), respectively (Fig. V.3a, c).

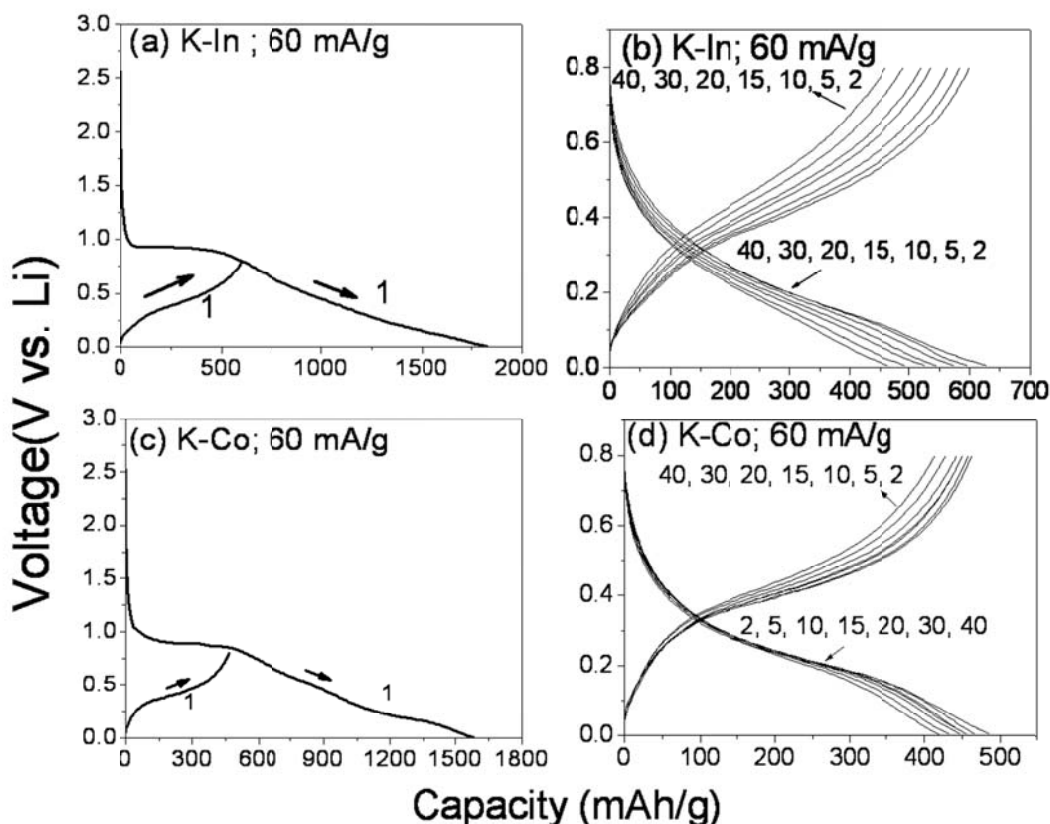
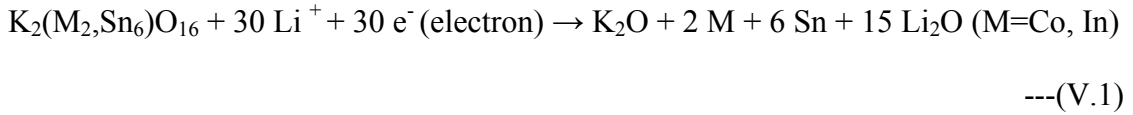


Fig. V.3. Galvanostatic capacity- voltage profiles of (a, b) $\text{K}_2(\text{In}_2\text{Sn}_6)\text{O}_{16}$ (K-In) and (c, d) $\text{K}_2(\text{Co}_2\text{Sn}_6)\text{O}_{16}$ (K-Co). Current density, 60mA/g^{-1} ; voltage range, 0.005-0.8V vs. Li at room temperature. The numbers refer to cycle numbers.

The above experimental values of the first-discharge capacities of (K-Co) and (K-In) may be compared with the theoretical ones, assuming a similar reaction mechanism that was proposed earlier for the other Sn- hollandites [24]. Initially, the electrochemical discharge reaction with Li leads to crystal structure destruction (amorphisation of the

lattice) followed by the reduction of reducible ions like Sn, Co and In to the respective metals, and the formation of K₂O and Li₂O, as per Eqn. (V.1):



The metals, in the form nano-size crystallites, and amorphous to X-rays, will be dispersed in an oxide matrix, (K-Li-O), and exists as a nano-composite. Thus, we expect the voltage plateau region (~0.9V) to consume 30 moles of Li per mole of the hollandite oxide. But, the experimental values are smaller, 20.8 and 23.8 moles of Li in (K-Co) and (K-In), respectively. Further reaction with Li leads to the formation of (Li-Sn) alloy, as per Eqn. (V. 3) consuming an additional 26.4 moles of Li. In the case of (K-In), the alloy (Li-In) also forms, which in the ideal case, consumes an additional 6 moles of Li (Eqn. (V.3)) [22]. The formation of the alloys, (Li-Sn) and (Li-In) may not occur in a single well-defined step, but may involve several intermediate stages, and thus, a continuous decrease in the voltage is noted in the voltage-capacity profiles (Figs.V.3a and c). According to Eqns.(V.1-V.3), we expect the first-discharge capacity to correspond to the consumption of 56.4 and 62.4 moles of Li for (K-Co) and (K-In), respectively. However, the experimental values are much higher, 68.6 and 87.1 moles of Li, respectively. Consumption of excess Li, over and above the theoretical value, during the first-discharge reaction has also been noted in several Sn-oxides, and is usually attributed to the formation of the solid electrolyte interphase (SEI), and the polymer-like layer on the

metal and alloy particles due to the decomposition of the electrolyte effected by Li [10-12, 23, 24, 28, 29].

During oxidation, i.e., in the first- charging process, the Li ions are extracted from (Sn-Li) alloy present in the oxide matrix, due to de-alloying of the (Sn-Li) alloy which is the reverse reaction of Eqn. (V.2) for (K-Co) and Eqns. (V.2 and V.3) for (K-In). The voltage- capacity profiles during the first- charge show a broad plateau, ~0.3- 0.5V for both (K-In) and (K-Co) and the extraction capacities at the cut- off voltage, 0.8 V, correspond to $600(\pm 10) \text{ mAhg}^{-1}$ (~ 28.6 moles of Li) and $465(\pm 10) \text{ mAhg}^{-1}$ (~ 20.2 moles of Li), respectively. These are smaller than the theoretical values of 32.4 and 26.4 moles of Li, respectively for (K-In) and (K-Co) as per Eqns. (V.2 and V.3) and indicate an (first cycle) extraction efficiency of only 88 and 80%, respectively.

Fig. V.3b and d and Fig. V.4 show the voltage- capacity profiles and capacity vs. cycle number plots of (K-In) and (K-Co) compounds, respectively at a current density of $60 \text{ mA} \text{g}^{-1}$, in the voltage window, 0.005- 0.8 V up to 40 cycles. Assuming $1 \text{ C} = 465 \text{ mA} \text{g}^{-1}$ for (K-Co), the current rate of $60 \text{ mA} \text{g}^{-1}$ corresponds 0.13 C. The reversible capacity of (K-Co) decreases from $458(\pm 10) \text{ mA} \text{g}^{-1}$ at the 5th cycle to $415(\pm 10) \text{ mA} \text{g}^{-1}$ at the end of 40th cycle. Thus the 5th cycle capacity retention for (K-Co) at the end of 40th cycle is 91 %.

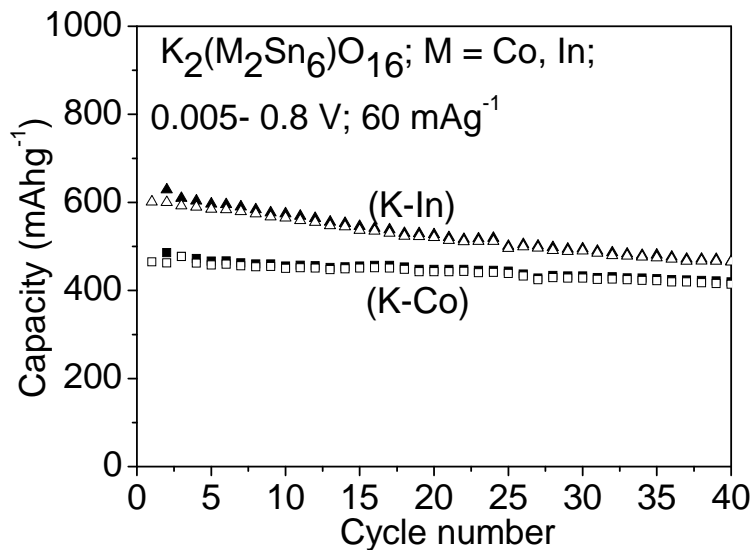


Fig.V.4. Capacity vs. cycle number plot at a current density 60 mA g^{-1} in the voltage window $0.005\text{-}0.8 \text{ V}$. Filled symbols: discharge capacity; open symbols: charge capacity.

The coulombic efficiency (η) can be calculated as the difference between the discharge and charge capacity at a particular cycle and is found to be 96-97% for (K-Co) in the range of 10- 40 cycles. For (K-In), the current rate of 60 mA g^{-1} corresponds to 0.1C ($1\text{C} = 600 \text{ mA g}^{-1}$). The reversible capacity decreases from $584(\pm 10) \text{ mA h g}^{-1}$ at the 5th cycle to $465(\pm 10) \text{ mA h g}^{-1}$ at the end of the 40th cycle, showing capacity retention of 80%. The η is calculated to be 96-97 % (10- 40 cycles). It can be clearly seen from Fig. V.4, that the capacity- fading in the case of (K-In) is more than in (K-Co). The better capacity retention during cycling in (K-Co) is probably due to Co-matrix element. The effect of matrix element on the cycling performance in the case of $\text{K}_2(\text{M},\text{Sn})_8\text{O}_{16}$, $\text{M} = \text{Mg}, \text{Li}, \text{Fe}, \text{Mn}$ has been studied by Sharma et al [24], who found that the hollandites with $\text{M} = \text{Li}$ and Fe showed better performance with capacities of 470 and 400 mA h g^{-1} , respectively at the end of 50th cycle. The (K-Co) and (K-In), in the present study show cycling performance comparable that found in $\text{K}_2(\text{Li}_{2/3}\text{Sn}_{22/3})\text{O}_{16}$ [24].

V. 3.3. Cyclic Voltammetry

The cyclic voltammograms (CV) of (K-Co) are shown in Fig. V.5 a. They were recorded at the slow scan rate of $58 \mu\text{Vs}^{-1}$, in the voltage window 0.005-0.8 V. The counter and reference electrode was Li- metal. The first cathodic scan (reaction with Li) of (K-Co), started from the OCV (~ 2.5 V) and shows a small shoulder peak at ~ 1.0 V, followed by sharp peaks at 0.73 V and 0.11 V. There is also a low- intensity peak at ~ 0.4 V. The peaks indicate a two- phase reaction and accordingly the structure destruction and formation of Sn- nano particles. The cathodic peak at ~ 0.11 V indicates the (Sn- Li) alloy formation (Eqn. (V.2)). The first anodic scan (Li extraction) in (K-Co) shows only one peak at 0.45 V, which is due to the de-alloying reaction. The second cycle cathodic scan starting from 0.8 V, shows only one split peak at ~ 0.11 V similar to the first- cathodic scan. The second cycle anodic scan overlaps very well with that of the first- cycle indicating good reversibility (Fig. V.5a) in accordance with Eqn.(V.2). The CV profiles of (K-In) are similar to those of (K-Co) except for minor changes in the potentials (Fig. V.5b). In the case of In_2O_3 - Li system, Li et al [30] found that alloying -de- alloying reactions occur at potentials, ~ 0.35 and ~ 0.65 V vs. Li respectively. Due to the smaller content of In in comparison to Sn in (K-In), the peaks due to the alloy (Li-In) are not revealed in the CV (Fig. V.5b). From the CVs it is clear that the average discharge potential and average charge potential are ~ 0.2 and ~ 0.47 V, respectively in both (K-In) and (K-Co). These match well with the differential capacity vs. voltage curves (Fig. V.5 c, d) extracted from the galvanostatic discharge- charge profiles of Fig. V.3 a, c.

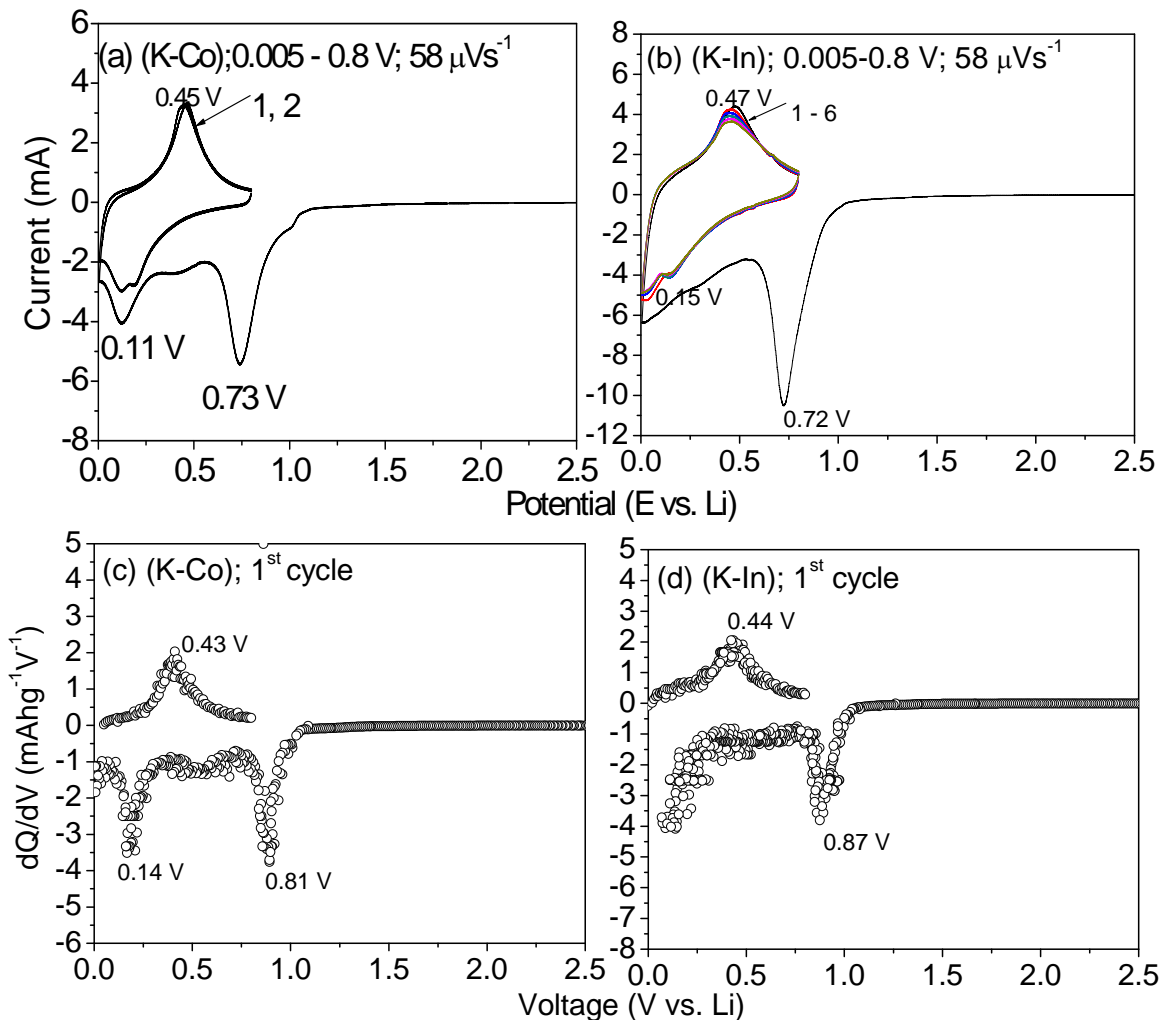


Fig.V.5. Cyclic voltammograms of (a) $\text{K}_2(\text{In}_2\text{Sn}_6)\text{O}_{16}$ (K-In) and (b) $\text{K}_2(\text{Co}_2\text{Sn}_6)\text{O}_{16}$ (K-Co) at the scan rate of $58 \mu\text{Vs}^{-1}$ and voltage range of 0.005-0.8V vs. Li at room temperature. The integer numbers indicate cycle numbers. The differential capacity vs. voltage plots of (c) (K-In) and (d) (K-Co) extracted from the galvanostatic data of the 1st cycle from Fig. V.3 a , c.

V.3.4. Ex- situ XRD

In order to establish the crystal structure destruction and amorphisation of the lattice, ex-situ XRD patterns have been recorded for (K-Co) at different discharge potentials during the 1st cycle. Three identical cells were fabricated and discharged to 1.0, 0.5 and 0.005V vs. Li and equilibrated for 2 h, and the electrodes were recovered and

treated as described in Chapters II-IV. The ex-situ XRD patterns are shown in Fig.V.2b. It is clear that the pattern of the electrode at 1.0V, remains unchanged in comparison to Fig. V.2a, showing no structural destruction. The patterns at 0.5 V and 0.005 V indeed show the amorphisation of (K-Co) due to the complete disappearance of the compound peaks. The low- intensity peak at $2\theta \sim 33^\circ$ corresponds to the Miller index (111) of Li_2O formed as per Eqn.(V.1) [JCPDS card no. 77-2144]. The XRD patterns do not show peaks due to Co and Sn metal or Li_xSn alloy probably due to very small (nano- size) particles, dispersed in the matrix of Li_2O .

V. 4. Conclusions

The tin- based hollandites, $\text{K}_2(\text{M}_2\text{Sn}_6)\text{O}_{16}$, $\text{M} = \text{Co}$ and In were prepared by the solid-state reaction, characterized by XRD and SEM and investigated for their Li-cyclability. Here, both K and M play the role of matrix element and In can also contribute to the reversible capacity in addition to Sn as per Eqns. (V.2) and (V.3). The galvanostatic cycling performance was carried out at a current density of 0.1 or 0.13 C, in the voltage window 0.005- 0.8 V. The first charge capacities of (K-Co) and (K-In) are $465(\pm 10)$ and $600(\pm 10) \text{ mAhg}^{-1}$, respectively. These values corresponds to 20.2 and 28.6 moles of Li per mole of (K-Co) and (K-In), respectively, as compared to the theoretical capacities of 26.4 and 32.4 moles of Li (Eqns. (V.2 and V.3)). For (K-Co) and (K-In), 91 % and 80 % of the 5th cycle capacity is retained at the end of 40 cycles, respectively with a coulombic efficiency of 96- 97%. The better cycling performance in the case of (K-Co) shows that Co acts as a better matrix element in comparison to In. The cyclic voltammograms are complementary to the galvanostatic cycling data and show that for both (K-Co) and (K-In), the average discharge potential is $\sim 0.2\text{V}$, whereas the average

charge potential is ~ 0.47 V vs. Li. The ex-situ XRD patterns of the discharged-electrodes taken at 1.0, 0.5 and 0.005 V show that amorphisation of the crystal lattice of (K-Co) takes place at ≤ 0.5 V, as can be expected from Eqn.(V.1) and the galvanostatic cycling profiles. Optimization of the cycling performance of (K-Co) and (K-In) may be possible, if they can be prepared as nano-size crystallites.

Chapter V

Part II

Nano-phase tin hollandites, $K_2(M_2Sn_6)O_{16}$ (M = Co, In) as anodes for Li- ion batteries

Abstract

The nano-phase tin hollandites, $K_2(M_2Sn_6)O_{16}$ (M = Co, In) of particle size < 10 nm are prepared by high energy ball-milling (HEB) of the pre-synthesized powders and characterized by X-ray diffraction (XRD), scanning electron microscopy (SEM), high-resolution transmission electron microscopy (HR-TEM) and selected area electron diffraction (SAED) techniques. The Li- cycling behavior of M = Co (nano-(K-Co)) and M = In (nano-(K-In)) is evaluated by galvanostatic cycling and cyclic voltammetry (CV) with Li- metal as counter electrode in the voltage range, 0.005-0.8 V (or 1.0 V). When cycled at 60 mA g^{-1} (0.12 C) in the voltage range, 0.005 – 0.8 V, a stable capacity of 500 (± 5) mA $h g^{-1}$ up to 60 cycles is noticed for nano-(K-Co), whereas nano-(K-In) showed an initial capacity of 570 (± 5) mA $h g^{-1}$, which dropped to 485 (± 5) mA $h g^{-1}$ (15 % loss) at the end of 60 cycles. At 1 C-rate, the nano- (K-Co) showed a capacity of 410 (± 5) mA $h g^{-1}$ stable up to at least 100 cycles. Under similar cyclic conditions, the heat- treated- electrode (300 °C; 12 h; Ar) of nano-(K-In), showed a significant improvement and gave a stable capacity of 570 (± 5) mA $h g^{-1}$ in the range of 5-50 cycles. The coulombic efficiencies in both the compounds increased to 96-98% in the range of 10-60 cycles. These results show that nano-phase compounds perform much better than the micron-size particles of the same compounds. For both the nano-phases, the average discharge potential is 0.13 V and average charge potential is 0.5 V vs. Li, as determined by the galvanostatic and CV data. Electrochemical impedance spectroscopy (EIS) data on nano-

(K-Co) as a function of voltage are presented and discussed. The apparent Li- diffusion co-efficient (D_{Li^+}), estimated from EIS data, is $2.0 - 2.6 (\pm 0.1) \times 10^{-14} \text{ cm}^2 \text{ s}^{-1}$ between 0.25 – 0.45 V during the first- cycle. The observed galvanostatic cycling, CV, EIS, ex-situ -XRD and -TEM data have been interpreted in terms of the alloying- de-alloying reaction of Sn in the nano-composite, ‘Sn-K₂O-Co/In- Li₂O’.

V.5. Introduction

The micron-size Sn, Sn-alloys, Sn-based oxides and composite oxides show poor electrochemical Li- cycling performance due to the large volume variation (~300%) during cycling, which leads to the generation of strong internal mechanical stresses and cracking of the particles, resulting in the loss of electrical contact with the current collector. The large particle size causes high agglomeration and retard the rate of Li-ion diffusion, thereby causing the capacity fading [1, 3-5]. As mentioned in Part I, the capacity retention in the case of Sn-based oxides has been improved to some extent by reducing the particle size of the active material to nano- size. The advantages associated with nanomaterials, which make them potentially feasible for use as electrode materials for Li-ion batteries (LIBs) are: (i) They enable the electrode reactions, which may not take place when micron- size particles are employed [31]. (ii) The rate of Li-ion intercalation/de-intercalation is highly increased due to the smaller diffusion length (L). The characteristic time (τ) for intercalation/de-intercalation is decreased due to decrease in diffusion length, since $\tau = L^2/D$, where D is the diffusion co-efficient [4, 8]. (iii) The electron transport is enhanced within the particles due to nanometer- sized particles. (iv) The smaller particle size can modify the chemical potentials for Li-ions and electrons, thereby changing the electrode potential to some extent (~ mV)[4, 5, 9].

It will be of interest to examine the Li-cyclability of the nano-size particles of the $K_2(M_2Sn_6)O_{16}$ and compare their performance with that of the micron-size particles described in Part I. In the present work, nano-size $K_2(M_2,Sn_6)O_{16}$ (M= Co, In) were prepared by high energy ball milling (HEB) of the pre-synthesized compounds and their Li-cyclability were examined. The results show that, indeed, the cycling stability and C-rate capability are greatly improved, in comparison to the performance of the micron-size particles. Complementary cyclic voltammetry and impedance data are reported.

V.6. Experimental

V.6.1. Preparation of nano-phase $K_2(M_2Sn_6)O_{16}$

For the preparation of nano- $K_2(M_2Sn_6)O_{16}$, appropriate amount (~2.5 g) of the pre-synthesized powder (Chapter-V; Part I) was weighed and transferred to stainless steel vial inside in an Ar- filled glove box (MBraun, Germany), sealed and taken out for high-energy ball-milling (HEB) at 1400 rpm using the equipment, Spex, 8000D, USA. Stainless steel balls were used for milling with a ball to active mass ratio, 4:1. Ball milling was carried out for 18 h, in three steps of 6 h each, to avoid significant rise in temperature of the vial. After milling, the vials containing the products were opened in the glove box, collected and kept in a desiccator.

Structural, morphological, electrochemical characterizations and ex-situ-XRD and –TEM studies were carried out as described in Chapters II to IV.

V.7. Results and Discussion

V.7.1. Structure and morphology

The X-ray diffraction (XRD) patterns of nano- $K_2(Co_2Sn_6)O_{16}$ (here after nano-(K-Co)) and nano- $K_2(In_2Sn_6)O_{16}$ (nano-(K-In)) are shown in Fig.V.6. The compounds show lines characteristic of tetragonal hollandite- structure with the $I4/m$ space group

indicating that high energy ball-milling (HEB) did not destroy the crystal structure. However, the diffraction lines are broadened in comparison to the XRD of micron-size (K-Co) and (K-In) (Fig. V.2a). This is due to the reduction of the particle size as a result of HEB. The lattice parameters, calculated by the Rietveld refinement (Topas R 2.1 software) are: $a = 10.510(2)$ Å; $c = 3.172(2)$ Å for nano-(K-Co) and $a = 10.601(2)$ Å; $c = 3.200(2)$ Å for nano-(K-In) in good agreement with those calculated for the compounds before HEB ($a = 10.480(2)$ Å; $c = 3.17(2)$ Å for (K-Co) and $a = 10.586(2)$ Å; $c = 3.20(2)$ Å for (K-In)).

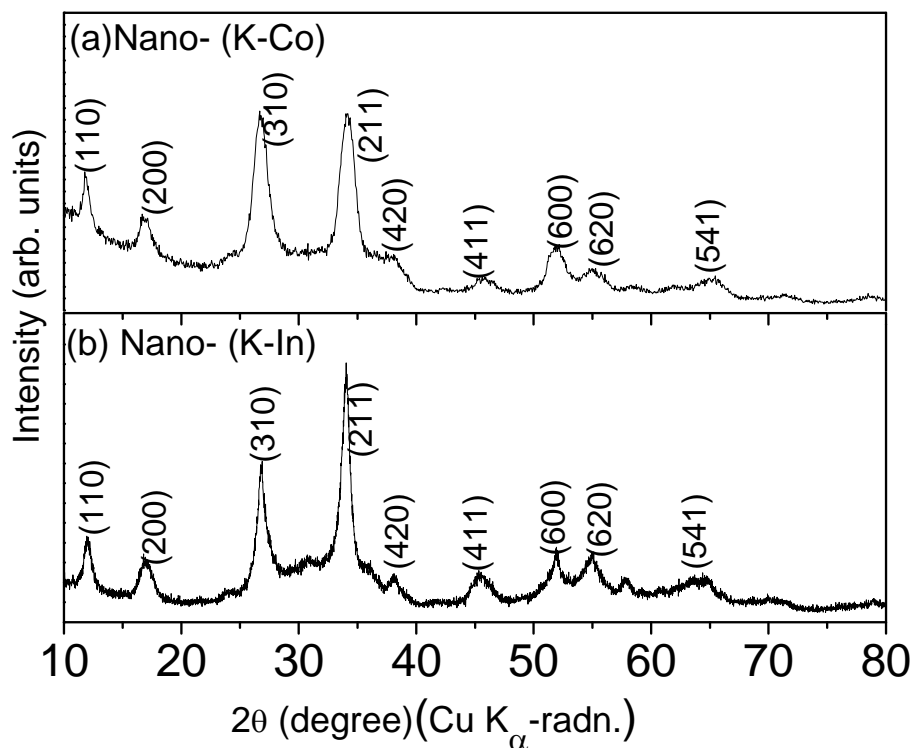


Fig.V.6. Powder X-ray diffraction patterns. (a) Nano- (K-Co); (b) nano- (K-In). Miller indices (hkl) are shown.

The TEM photograph of nano- (K-Co) shows the particle size of ≤ 10 nm with an agglomerated morphology (Fig. V.7a). The HR-TEM lattice image clearly indicates the nano-crystalline regions (5-10 nm) in nano- (K-Co) (Fig. V.7b). Some of the regions in

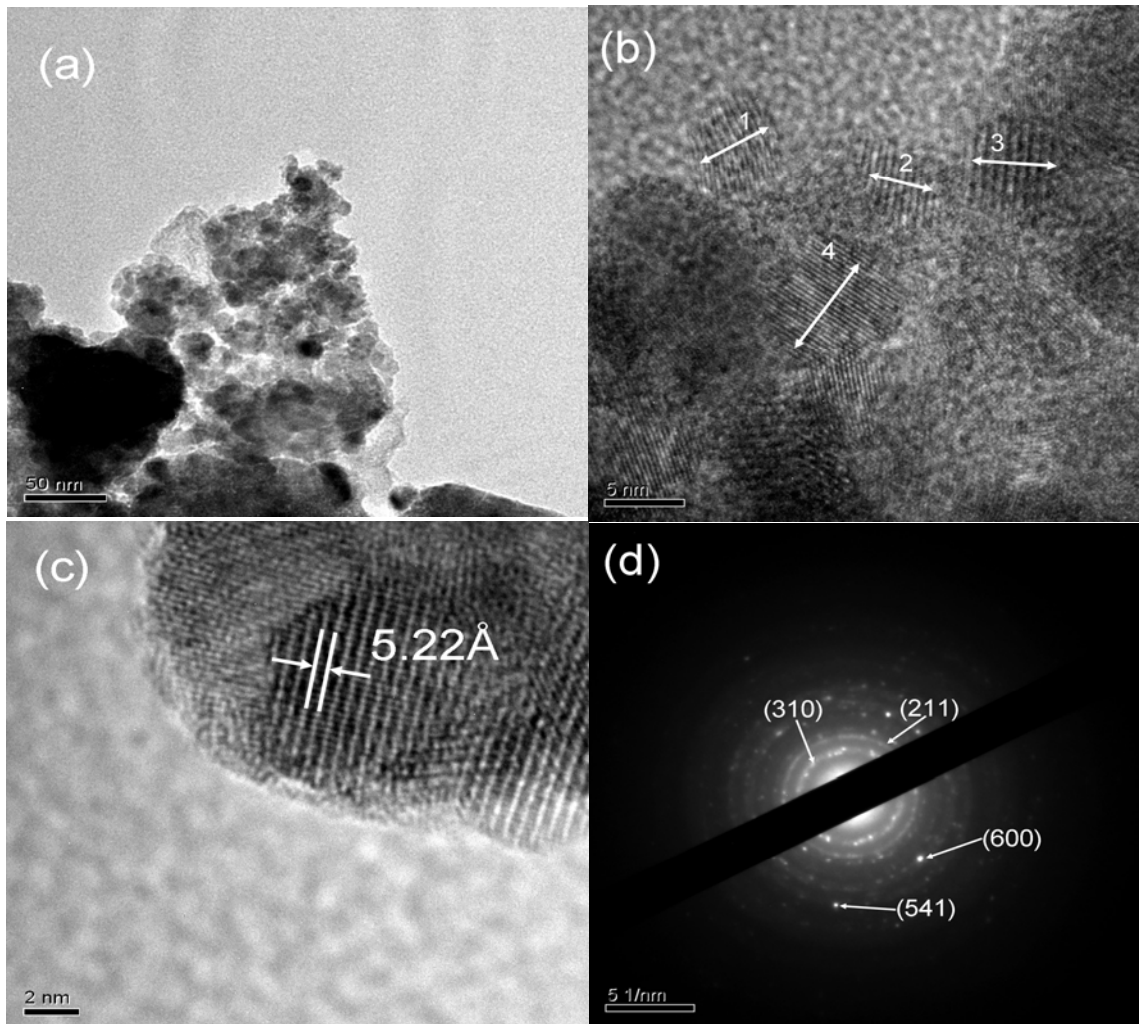


Fig.V.7. Nano- (K-Co): (a) TEM photograph showing agglomerated nano-size particles. (b) HR-TEM lattice image. (c) HR-TEM lattice image at higher magnification. (d) Selected area electron diffraction (SAED) pattern. Scale bars are shown.

Fig. V.7b are marked as 1, 2, 3 and 4 and the interplanar d-spacings corresponding to the regions are measured. The values are ($\pm 0.02\text{\AA}$): 2.65 \AA , 5.21 \AA , 7.40 \AA and 3.29 \AA , respectively for regions 1 to 4. These d- values can be assigned to the Miller indices (211), (200), (110) and (310), respectively. Fig. V.7 c is the HR-TEM lattice image at a higher magnification and the d-spacing of 5.22 (± 0.02) \AA corresponds to the Miller index of (200). The selected area electron diffraction (SAED) pattern of the nano- (K-Co)

shown in Fig.V.7d, indicates diffuse rings with occasional bright spots. The d- values corresponding to these concentric rings were evaluated by measuring the rings from the center and the assigned Miller indices are shown.

The crystallite sizes of nano-(K-Co) and nano-(K-In) were calculated by using the Scherrer's formula, $P = K \lambda / (\beta_{1/2} \cos\theta)$, where P is crystallite size, K is Scherrer constant (0.9), λ is the wavelength of Cu K α - radiation (1.54059 Å), $\beta_{1/2}$ is the full width at half maximum (FWHM) in radians of the XRD peak and θ is the scattering (Bragg) angle [12]. The instrumental broadening was calculated by using the nano-TiO₂ (anatase) (Evonik Degussa; 99.5%) of ~25 nm particle size as standard and was found to be 0.08°. For TiO₂, it is assumed that the crystallite size is of the same order as particle size. The crystallite sizes were calculated by using $\beta_{1/2}$ (FWHM) of two or three high intensity peaks and the corresponding θ values in the XRD patterns. The values are 6 (± 2) nm for nano-(K-Co) and 8 (± 2) nm for nano- (K-In). To summarize, XRD and HR-TEM data confirm that HEB of micron- sized particles has resulted in nano- (K-Co) and nano- (K-In) without destroying the hollandite crystal structure.

V.7.2. Electrochemical characterization

V.7.2.1. Galvanostatic cycling

The capacity vs. voltage profiles of nano- (K-Co) at a current density 60 mA g^{-1} , in the voltage range of 0.005-0.8 V vs. Li are shown in Fig.V.8 a & b. The first-discharge profile shows a voltage plateau at ~0.85 V, which onsets at ~1.25 V, up to a capacity of 420(± 5) mA $h g^{-1}$ (18.3 moles of Li per formula unit of (K-Co)). Thereafter, a sloping profile is noticed till the deep discharge 0.005 V. The total first- discharge capacity is 1910(± 5) mA $h g^{-1}$ (83 moles of Li). The voltage plateau at ~0.85 V

corresponds to the amorphization of crystal lattice and formation of Co and Sn metal particles (Eqn.V.1) and the continuous sloping profile up to 0.005 V is due to the alloying of electrochemically- formed Sn- metal with Li as per the forward reaction of Eqn.V.2. The absence of well-defined voltage plateaus in the range 0.5 – 0.005 V indicates that the Eqn. V.2 may be occurring in stages. The Eqns. (V.1 and V.2) indicate the overall consumption of 56.4 moles of Li per mole of nano- (K-Co) corresponding to a capacity of 1300 mAhg⁻¹ as the theoretical first-discharge capacity. However, the experimental value is 1910(±5) mAhg⁻¹ (83 moles of Li), which is larger than the theoretical capacity. The consumption of extra Li is due to the solid electrolyte interphase (SEI) formation and due to the formation of polymer- like layer on the metal particles under deep discharge conditions, as mentioned in Part I [10-12, 23, 24, 28, 29].

The first- charge profile of nano- (K-Co) (Fig. V.8a) shows a voltage plateau at ~0.5 V. The total first- charge capacity at the end of cut- off voltage, 0.8 V is 500(±5) mAhg⁻¹ (21.7 moles of Li) (reverse reaction of Eqn. V.2). The observed second-discharge capacity is 530(±5) mAhg⁻¹ (23 moles of Li), which is almost same as the first-charge capacity, showing good reversibility of the system. The charge- discharge profiles from 2-60 cycles overlap well showing good stability (Fig. V.8b).

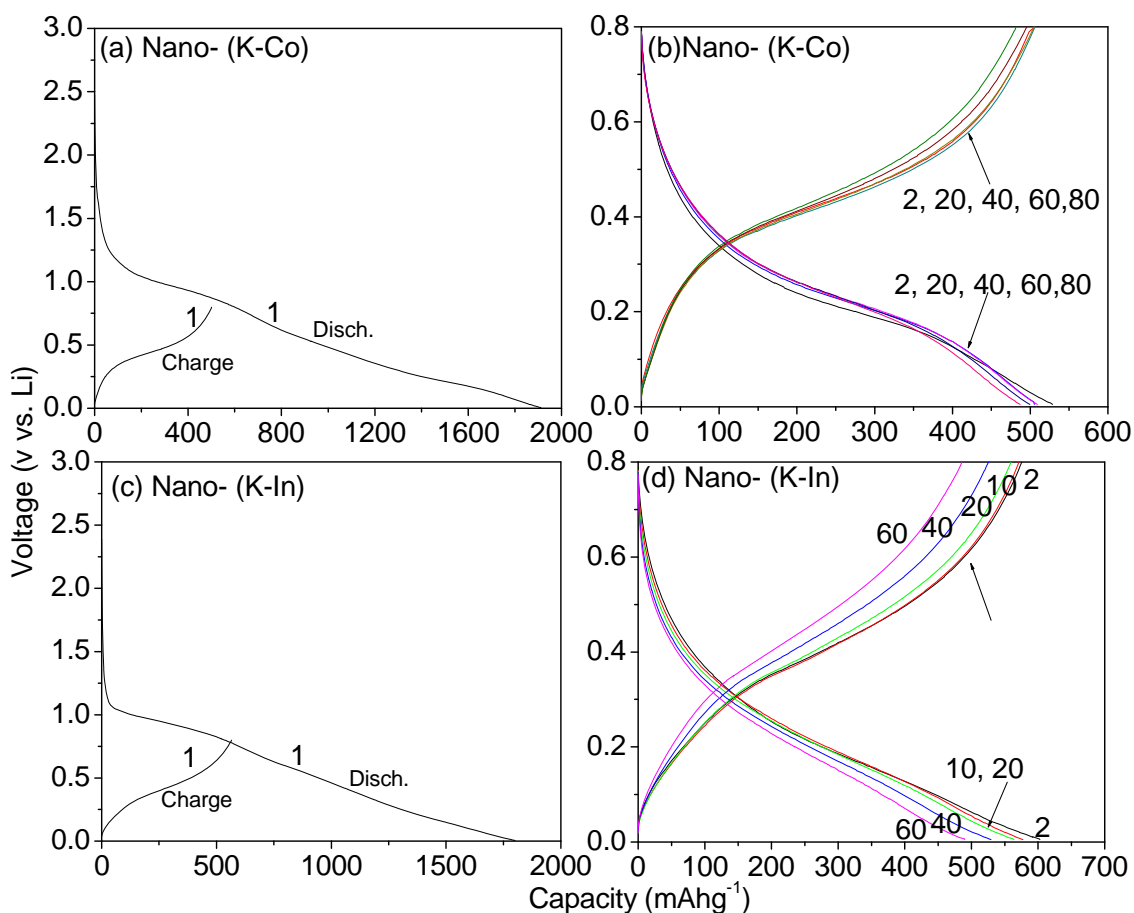


Fig.V.8. Galvanostatic discharge-charge profiles. Nano- (K-Co): (a) 1st cycle and (b) 2-80 cycles. Nano- (K-In): (c) 1st cycle and (d) 2- 60 cycles. The numbers indicate cycle number. Voltage range, 0.005- 0.8 V vs. Li, at a current density of 60 mA g^{-1} (0.12 C).

The capacity vs. cycle number plots of nano- (K-Co) in two voltage windows, 0.005-0.8 V and 0.005 – 1.0 V, at 60 mA g^{-1} are shown in Fig. V.9a and b, respectively. In the voltage range 0.005 – 0.8 V, a stable capacity of 500(\pm 5) mA $h g^{-1}$ is obtained up to 60 cycles, with no noticeable capacity - fading. However, a capacity- fading of 4% is noticed in the range of 60-80 cycles. When cycled in the range 0.005 – 1.0 V, a stable capacity of 525 (\pm 5) mA $h g^{-1}$ is noticed up to 40 cycles, and thereafter, a slow capacity- fading is noticed. The capacity- fading is 11% in the range of 40-60 cycles. The columbic efficiency in both the voltage windows is 96-98%, in the range of 10-60 cycles.

Assuming $1\text{ C} = 500\text{ mAhg}^{-1}$, the current density 60 mAhg^{-1} corresponds to 0.12 C - rate. It has been noted in the literature that the operating voltage window is crucial for better reversibility of Sn-based oxides [12, 13, 28]. The good cycling response of nano- (K-Co) is attributed to the buffering ability of the nano-composite, $\text{K}_2\text{O}/\text{Li}_2\text{O}/\text{Co}$ against the unit cell volume variations occurring during alloying-de-alloying of Sn-metal (Eqns. V.1 and V.2). The Co-metal particles act as an electronically conducting medium for Li-diffusion and thereby enhance the reversible reaction. The literature studies show that the presence of Co- metal as an inactive matrix is highly beneficial both for alloying- de- alloying reactions and conversion reactions [32, 33]. It is pertinent to compare the present results with those obtained on the micron- size particles of (K-Co). Under similar cycling conditions ($0.005\text{-}0.8\text{ V}$ at 60 mAhg^{-1}), a 5th cycle capacity of $460 (\pm 10)\text{ mAhg}^{-1}$ degraded to $415 (\pm 10)\text{ mAhg}^{-1}$ at the end of 40th cycles corresponding to a capacity- fade of 10% (Chapter V; Part I). Thus, a reduction of the particle size is highly beneficial in giving a high and stable capacity in the Sn- hollandite oxides.

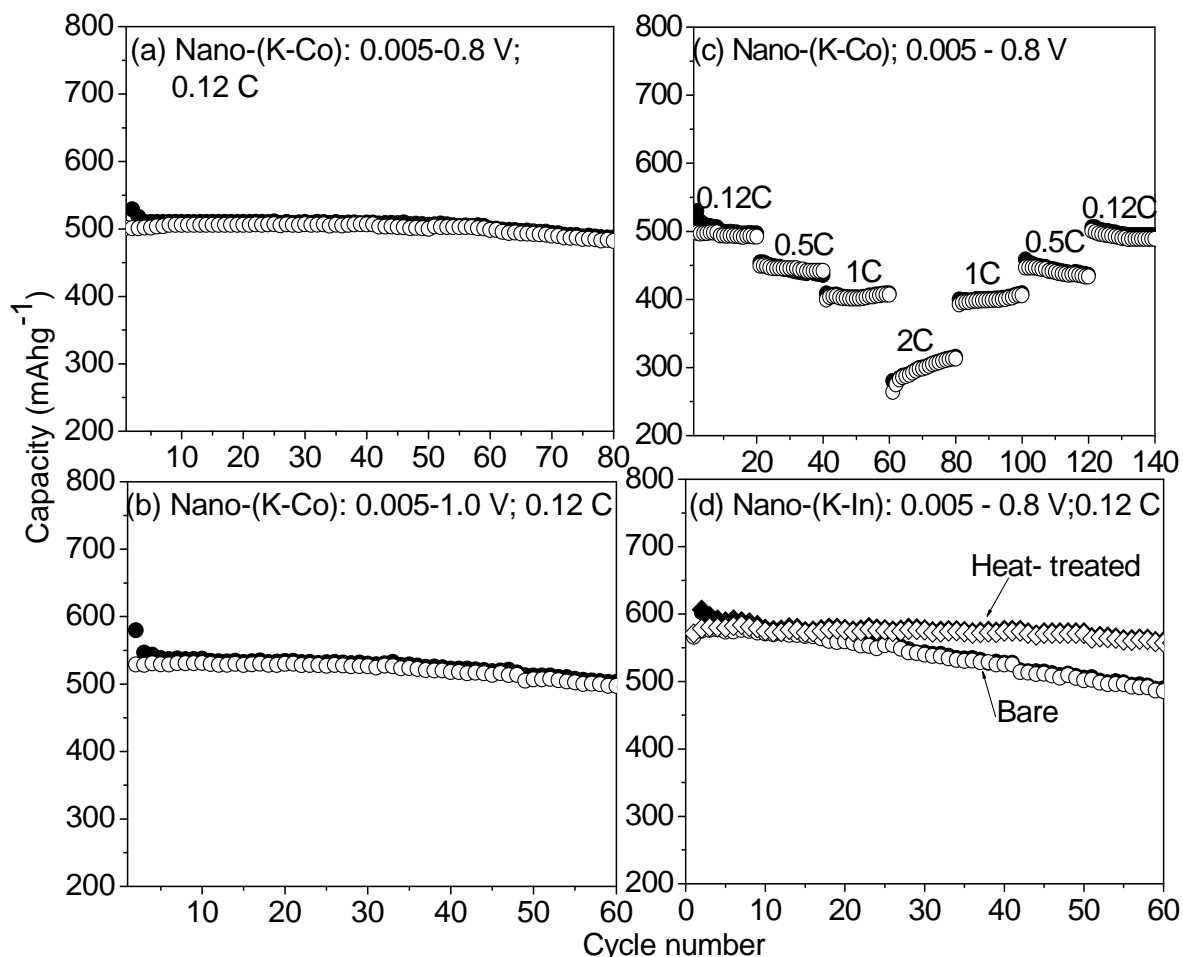


Fig.V.9. Capacity vs. cycle number plots. (a, b) Nano- (K-Co) in different voltage ranges. (c) At various current (C) rates of nano- (K-Co). (d) Nano- (K-In). Voltage range, 0.005-0.8 V vs. Li, at current density of 60 mA_g⁻¹ (0.12 C) assuming 1 C = 500 mA_g⁻¹. Filled symbols: Discharge capacity; Open symbols: Charge capacity.

The C- rate capability test was carried out on a duplicate cell with nano- (K-Co) in the voltage range of 0.005 – 0.8 V, at different current rates. The specific current was increased after 20 cycles in steps from 0.12 to 2 C, and then decreased in steps up to 140 cycles (1C = 500 mA_g⁻¹). The results are shown in Fig. V.9c. The observed capacity, 500(±5) mA_g⁻¹ at 0.12 C decreases to 315(±5) mA_g⁻¹ upon increasing the current almost 16 fold, to 2 C. At each C-rate, the reversible capacity remains stable on cycling.

The recovery of the capacity to almost the original value after the step- decrease of C- rate indicates an excellent rate- capability, which signifies the potential application of nano- (K-Co) as anode material for LIBs.

The voltage vs. capacity profiles of nano- (K-In) at a current density 60 mA g^{-1} in the voltage range, 0.005 – 0.8 V are shown in Fig. V.8 c and d. The discharge- charge profiles are qualitatively similar to those of nano- (K-Co). The observed first- discharge capacity is $1800 (\pm 5) \text{ mA h g}^{-1}$ (85.7 moles of Li per mole of (K-In)) which includes contribution from the formation of alloy, Li_3In (Eqn. (V.3)) in addition to Eqns. (V.1 and V.2) ($M = \text{In}$). Similar to the case of nano-(K-Co), there is an extra consumption of 23.3 moles of Li in nano- (K-In) during the first- discharge. The first- charge profile of nano- (K-In) shows a voltage plateau at $\sim 0.45 \text{ V}$ followed by a continuous sloping profile till 0.8 V (Fig. V.8c). The first- charge capacity is $565 (\pm 5) \text{ mA h g}^{-1}$ (26.9 moles of Li per mole of (K-In)) in comparison to the theoretical capacity of 32.4 moles of Li (reverse reactions of Eqns.(V.2 and V.3)). The second- discharge capacity is $600 (\pm 5) \text{ mA h g}^{-1}$ (28.6 moles of Li), which is slightly larger than the first- charge capacity. The charge- discharge profiles from 2-to- 20 cycles overlap well indicating good reversibility, but the capacity shows a decreasing trend up to 60 cycles (Figs. V.8d and V.9d). A reversible capacity of $565(\pm 5) \text{ mA h g}^{-1}$ remains stable up to 20 cycles and a capacity- fading of 15% is observed in the range, 20-60 cycles. The columbic efficiency is 96-98 % in the range of 10-60 cycles.

Improvement of the Li- cyclability of a heat- treated oxide electrode (Fe_2O_3 ; 300 °C; 12 h; Ar-gas) involving ‘conversion’ reaction was recently reported by Li et al. [34]. This improvement is ascribed to a better binder distribution, caused by melting and

spreading of the binder, followed by adhesion to the active material particles and to the current collector of the electrode. Accordingly, the cycling performance of nano- (K-In) electrode heat treated at 300°C for 12 h in Ar- gas was carried out. The results are shown in Fig. V.9d and as can be seen, there is no increase in the reversible capacity in comparison to the bare electrode of nano- (K-In). However, the cycling stability is greatly improved. A stable reversible capacity of 570 (± 5) mAhg⁻¹ is noticed with nil capacity-fading up to 50 cycles. A 3% capacity- fading occurs in the range 50-60 cycles. Under similar cycling conditions, micron-size (K-In) showed a 5th cycle capacity of 584 (± 10) mAhg⁻¹ which degraded to 465 (± 10) mAhg⁻¹ after 40 cycles corresponding to a capacity-fading of 20% (Chapter V; Part I). Thus bare and heat- treated electrodes of nano-(K-In) perform much better than that of the electrode with micron- size particles of (K-In).

V.7.2.2. Cyclic Voltammetry

The cyclic voltammetry on nano- (K-Co) and nano- (K-In) as cathodes in cells with Li- metal as the counter electrode were carried out at the slow scan rate of 58 μVs^{-1} , in the potential range of 0.005- 0.8 V up to 10 cycles, to complement the galvanostatic cycling data and to ascertain the potentials where the charge/discharge reactions occur. The cyclic voltammograms (CVs) of nano- (K-Co) are shown in Fig. V.10 a.

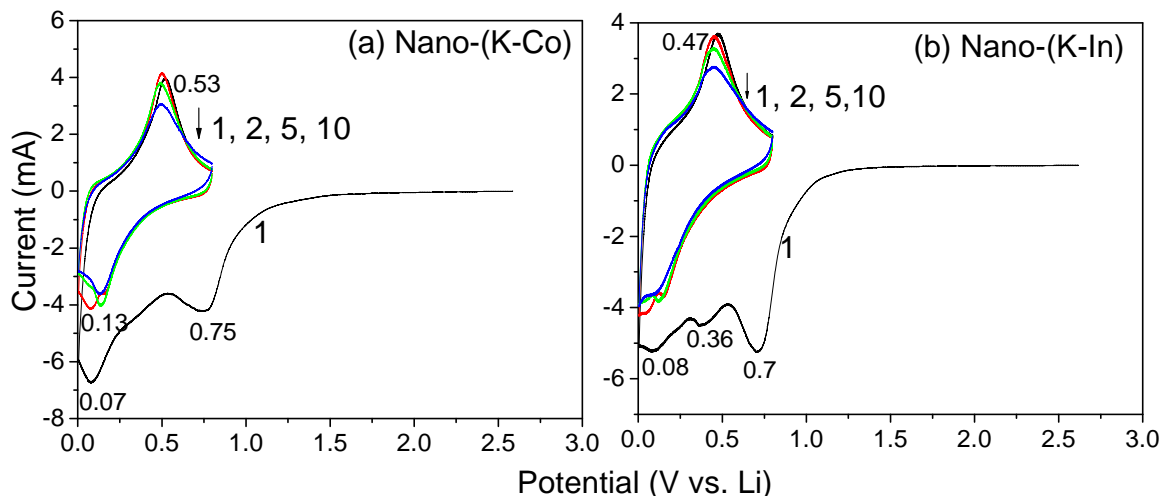


Fig.V.10. Cyclic voltammograms. (a) Nano- (K-Co) and (b) Nano- (K-In). Scan rate, 58 μVs^{-1} . Li- metal anode was the counter and reference electrode. Numbers represent the potentials in Volts. Integer numbers represent cycle numbers.

As can be seen, the first- cathodic scan commenced from the open circuit voltage (OCV) ~ 2.75 V. A broad cathodic peak at 0.75 V is observed followed by another peak at 0.07 V. The former peak can be attributed to the crystal structure destruction to form the Sn-metal (Eqn. V.1) and the latter can be assigned to the formation of $\text{Li}_{4.4}\text{Sn}$ alloy (forward reaction of Eqn. V.2). During the first anodic scan up to an upper cut- off voltage 0.8 V, only a single well- defined peak is noticed at 0.53 V. This peak corresponds to the de-alloying process of the alloy formed during the cathodic scan (reverse reaction of Eqn. V.2). From 2- 10 cycles, both cathodic and anodic scans show well defined peaks at 0.13 V and at 0.53 V, respectively (Fig. V.10a). During the initial few cycles, there is a splitting of the cathodic peak into a doublet, (0.16 V and 0.07 V) during 2-5 cycles indicating that the Li-Sn alloying reaction occurs in two stages instead of a single step. But the doublet cathodic peak gradually merged as one well- defined peak in the 10th cycle, presenting a single stage alloy reaction. The CVs from 2-10 cycles

overlap well, indicating good reversibility. The area under both cathodic and anodic scan remains preserved during the cycling indicating good reversibility, in agreement with the galvanostatic cycling data (Fig.V.8 a, b). From the CVs, the average discharge and charge potentials are 0.13 V and 0.53 V, respectively, which match well with the voltage plateaus noticed during galvanostatic cycling. (Fig. V.8a, b).

Fig. V.10b shows the CV of nano- (K-In) in the potential range 0.005-0.8 V. The CVs from 1-10 cycles are analogous to that of nano- (K-Co) (Fig. V.10a), except for an additional low- intensity peak at 0.36 V noticed during the first-cathodic scan. This peak can be attributed to the Li_3In formation. The crystal structure destruction of nano- (K-In) occurs at 0.7 V (Eqn. V.1; $\text{M} = \text{In}$). During the first anodic scan, a single peak is noticed at 0.47 V, which is due to the de-alloying reaction of both Li_3In and $\text{Li}_{4,4}\text{Sn}$. The de-alloying reaction in the case of nano- (K-In) occurs at a slightly lower potential as compared to that of nano- (K-Co), possibly due to the synergetic effect of the presence of In. From the studies on In and its oxides, the de-alloying reaction is known to occur at $\sim 0.4 \text{ V} - 0.6 \text{ V}$ [30, 35, 36]. The CVs of 2-10 cycles overlap well indicating good reversibility of the system. The average discharge and charge potentials are 0.12 V and 0.47 V, respectively. Thus, it can be concluded that the CV results corroborate the galvanostatic cycling data.

V.7.3. Ex-situ XRD and TEM

In order to complement the observed galvanostatic and cyclic voltammetry data and to ascertain the reaction mechanism during charge and discharge cycling, ex-situ XRD and -TEM on nano- (K-Co) were performed. For ex-situ XRD, three cells were discharged/charged to different voltages and then equilibrated for 2-3 h before

dismantling the cells for XRD measurement. Results are shown in Fig. V.11. The y-axis values have been normalized for better comparison. The pattern at 0.5 V during the 1st discharge (Fig. V.11a) shows the lines characteristics of both Li-Sn alloy and Sn-metal (Eqn. V.1 and forward reaction of Eqn. V.2). This is expected since the crystal structure is destroyed at a voltage of ~ 0.7 V and (Li-Sn) alloy formation is initiated. But at the voltage of 0.005 V, there are no characteristic lines of Sn and Li-Sn alloy (Fig. V.11b). This could be due to very small particle size. At 0.8 V during first-charge, the XRD pattern shows absence of lines due to Sn-metal which can be due to the nano-nature of Sn (Fig. V.11c).

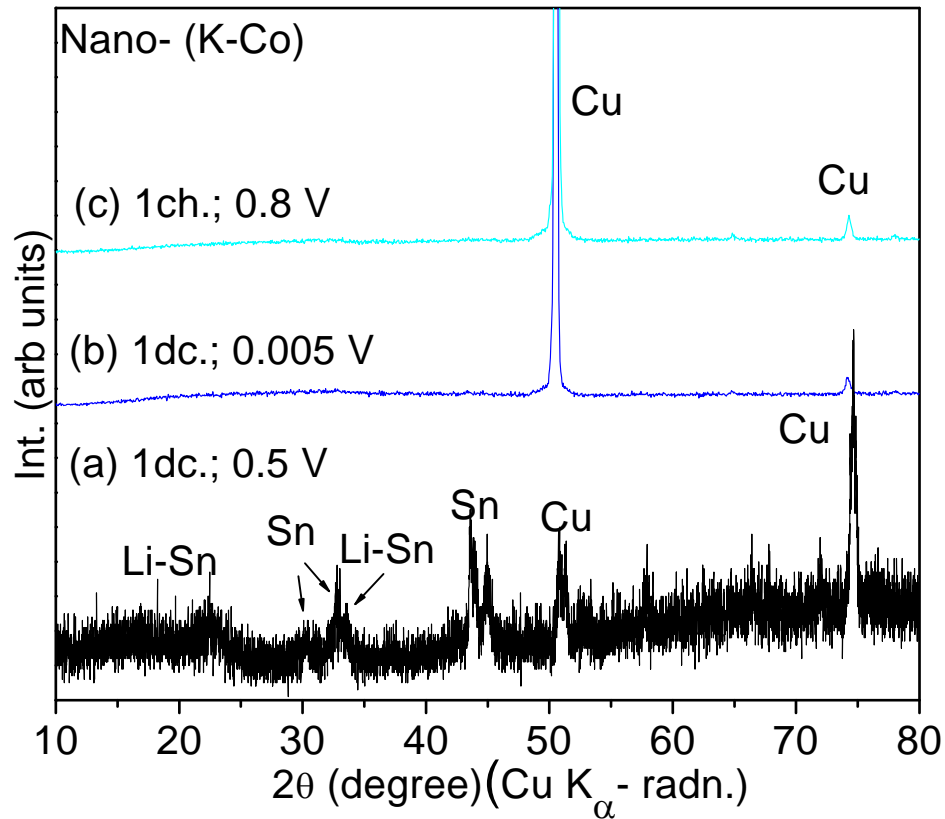


Fig.V.11. Ex-situ XRD patterns of nano- (K-Co). (a) During first- discharge at 0.5 V; (b) during first- discharge at 0.005 V, and (c) during first- charge at 0.8 V vs. Li. Substrate (Cu) lines are indicated.

The ex-situ TEM data of nano- (K-Co) at 0.8 V at the end of the 15th charge are shown in Fig.V.12. The lattice image indicates the existence of nano-crystalline regions, size of 6-8 nm embedded in amorphous regions of mainly K₂O and Li₂O (Fig.V.12a). The crystalline region can be assigned to the nano-Sn-metal with inter-planar distance (d-value) of 2.93(±0.02) Å. This value corresponds to the Miller index of (200) plane of tetragonal Sn-metal (JCPDS # 04-0673). The SAED pattern, shown in Fig.V.12b, consists of diffuse spots superimposed on the diffuse rings indicating the nano-phase crystalline regions coexisting with the amorphous regions. The d-values corresponding to these rings and spots were derived by measuring the diameters of the rings. The d-values of 2.94(±0.02) Å, 2.81(±0.02) Å and 2.04 (±0.02) Å can be assigned to the (200), (101) and (211) planes of Sn-metal, respectively. Thus, both ex-situ XRD and –TEM confirm the formation of (Li_xSn alloy) during discharge process at 0.005 V and formation of nano crystals of Sn- metal during charge process at 0.8 V, respectively and confirm the proposed reaction mechanism of Eqns. V.1 and V.2.

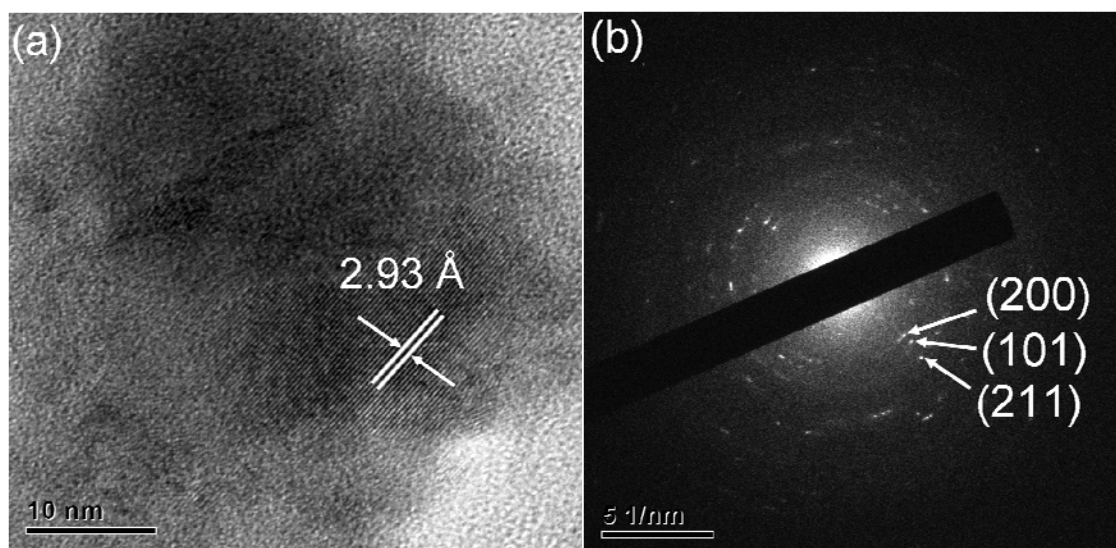


Fig.V.12. Ex-situ TEM pattern of nano- (K-Co) at the 15th charge cycle at 0.8 V: (a) HR-TEM lattice image and (b) SAED pattern. Scale bars are shown.

V.7.4. Electrochemical Impedance Spectroscopy

Electrochemical impedance spectroscopy (EIS) measurements on electrode materials at different discharge and charge voltages will give information on the factors responsible for the overall impedance during the Li-cycling. The impedance measurements were reported on some of the Sn-oxide anodes like, SnO [29], hollandite $K_2(Li_{2/3}Sn_{22/3})O_{16}$ [24] and nano-composite, CaO. SnO₂ [12]. Studies on transition metal oxides like, Co₃O₄ [37], TiOF₂ [38] and Li₄Ti₅O₁₂ [39] are also reported in the literature and interpreted to understand the electrode reaction kinetics. Presently, impedance studies were carried out on the cell comprising of nano- (K-Co) as the working electrode vs. Li during the first discharge- and charge- cycle and during the 11th discharge, at selected voltages after relaxing the cells for 3 h. The results are presented as Nyquist plots (Z' vs. $-Z''$), where Z' and Z'' refer to the real and imaginary parts of cell impedance, respectively (Figs. V.13 a-c). The impedance spectra have a qualitative resemblance to those observed with $K_2(Li_{2/3}Sn_{22/3})O_{16}$ [24]. The spectra were fitted with an equivalent electrical circuit using series and parallel combinations of resistances (R), CPEs (constant phase element), W_s (Warburg impedance) and intercalation capacitance (C_i). The experimental data are represented as symbols, whereas the fitted data are represented as continuous lines in Figs. V.13a-c. The equivalent circuit is shown in Fig. V.13d [12, 24, 38].

The observed total impedance is made up of contributions from different factors such as electrolyte resistances (R_e), impedance due to surface film and charge transfer resistance ($R_{(sf+ct)}$) and the associated surface film and double layer capacitance (CPE_(sf+dl)), bulk (b) impedance (R_b) and capacitance (CPE_b) and W_s . The CPEs are used instead of pure capacitor, since the Nyquist plots show depressed semicircles, which

indicate the deviation from the ideal behavior. The impedance due to constant phase element, $Z_{CPE} = 1/[C(j\omega)^\alpha]$ where $j = \sqrt{-1}$, ω is the angular frequency, C is the capacitance and α is a constant. The value of α varies as $0 < \alpha < 1$, which gives the degree of distortion from the pure capacitor behavior ($\alpha = 1$ for pure capacitor). The extracted impedance parameters are given in Table V.1.

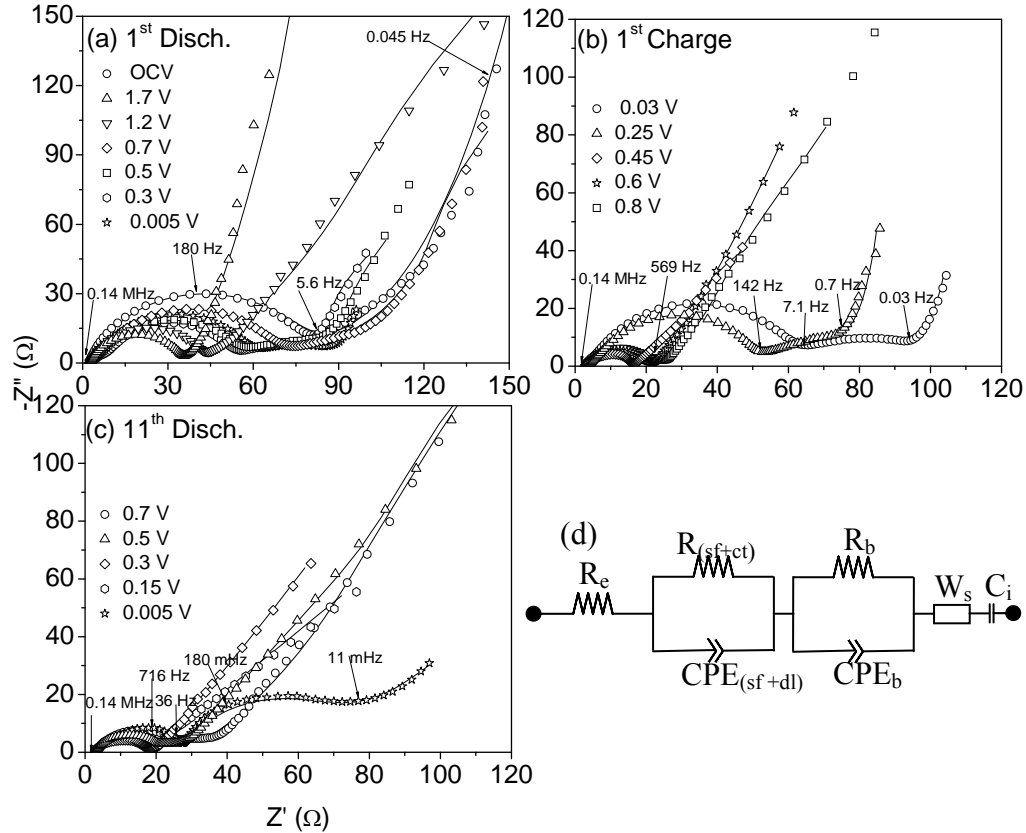


Fig.V.13. Impedance spectra (Nyquist plots: Z'' vs. $-Z''$) for the cell with nano- (K-Co) as cathode vs. Li- metal at different voltages. (a) During the first-discharge. (b) During the first-charge. (c) During the 11th discharge. Stabilized cell voltages, after 3-h stand, are shown. Selected frequencies are shown. (d) Equivalent circuit used for fitting the impedance spectra. Different resistances, R_i and/or $R_i \parallel CPE_i$ components, Warburg element (W_s) and intercalation capacitance (C_i) are shown.

From the fitting of all impedance spectra (Nyquist plots), the electrolyte resistance (R_e) was found to be 4-6 (± 0.5) Ω irrespective of the state of discharge/charge of the cell which indicates that the cells were properly fabricated. At open circuit voltage (OCV, ~ 2.6 V), the Nyquist plot showed a single semicircle at high to medium frequency range of 2.8 kHz to 5.6 Hz. In the low frequency regions (< 5 Hz) a straight line making an angle of $\sim 45^\circ$ with real-axis is observed and ascribed to Warburg region (W_s). The spectrum was fitted using the parallel combination of resistance (R) and constant phase element (CPE) with an overall impedance of 70 (± 5) Ω , which is due to the surface film resistance (R_{sf}) and associated capacitance, (CPE_{sf}) (Table V.1). From the Nyquist plots of first- discharge at different voltages, it is clear that the overall impedance is due to both the surface film and charge transfer resistances (R_{sf+ct}), even though a single semicircle is observed in the impedance spectra at voltages, $V = 1.7$ V and 1.2 V. At $V = 0.7$ V, there is an indication of the development of a second semicircle, which is clearly de-lineated at $V < 0.7$ V (Fig. V.13a). Accordingly, the spectra were fitted with a single semicircle for $V \geq 0.7$ V and two semicircles for $V < 0.7$ V, the latter taking into account the contribution from the bulk resistance (R_b). As can be seen from Table V.1, the $R_{(sf+ct)} = 32$ (± 5) Ω at 1.7 V and shows a gradual increasing tendency upto the deep discharge voltage of 0.005 V. The capacitance ($CPE_{(sf+dl)}$) values vary from 37 to 76 (± 5) μF . The R_b values range from 23 to 33 (± 5) Ω at $V \leq 0.5$ V.

In the range of 0.5-0.005 V, the significant changes in the spectra is due to the amorphisation of the lattice of nano- (K-Co) and formation of Sn and Li_xSn as per Eqns. V.1 and V.2. The degree of distortion (α) remains almost constant 0.82 (± 0.02) in the

voltage range of 1.7 V to 0.7 V and shows a decreasing trend with a decrease in the voltage and reaches a value of 0.75 at 0.005 V.

Table V.1. Impedance parameters obtained by fitting the impedance spectra of the nano-(K-Co) (vs. Li) to the equivalent circuit elements during the first- cycle and 11th discharge. The apparent diffusion coefficients (D_{Li^+}) are calculated using Eqn. V.4.

Voltage (V)	$R_{(sf+ct)}$ (± 5) Ω	$CPE_{(sf+dl)}$ (± 5) μF	R_b (± 5) Ω	CPE_b (± 5) (mF)	α (± 0.02)	Frequency f_L (± 3), mHz	App.diff. coeff. (D_{Li^+} ; (± 0.1) $\times 10^{-14}$) $cm^2 s^{-1}$
First- discharge							
OCV	70	37	---	---	0.84	----	---
1.7	32	37	---	---	0.82	51	5.6
1.2	38	33	---	---	0.84	---	---
0.7	58	44	---	---	0.80	18	2.0
0.5	53	63	28	16	0.75; 0.64	22	2.5
0.3	51	76	23	21	0.79; 0.68	23	2.6
0.005	55	47	33	19	0.80; 0.55	28	3.2
First- charge							
0.03	58	50	36	17	0.78; 0.58	11	1.2
0.25	47	58	30	34	0.79; 55	18	2.0
0.45	13	156	---	---	0.70	23	2.6
0.6	18	186	---	---	0.68	---	---
0.8	20	177	---	---	0.67	----	---
11 th -discharge							
0.7	27	221	---	---	0.75	---	---
0.5	21	269	---	---	0.65	---	---
0.3	16	347	---	---	0.65	---	---
0.15	15	145	---	---	0.68	---	---
0.005	24	117	40	22	0.73	---	---

The impedance spectra at various voltages during the first- charge reaction are shown in Fig. V.13b. At $V = 0.03$ V and 0.25 V, a depressed semicircle almost parallel to X-axis is noticed in the frequency range $140 - 0.03$ Hz and this is followed by Warburg and intercalation capacitance regions. For $V \geq 0.45$ V, only a single semicircle is seen, indicating the absence of contribution from the bulk resistance. The fitted impedance parameters, in Table V.1, show that $R_{(sf+ct)}$ decreases from $58 (\pm 5)$ Ω to $13 (\pm 5)$ Ω in the voltage range of $0.03 - 0.45$ V and stabilizes at about $18 (\pm 5)$ Ω for $V = 0.6$ and 0.8 V. The R_b decreases slightly from $36 (\pm 5)$ Ω at 0.03 V to $30 (\pm 5)$ Ω at 0.25 V and not seen for $V > 0.25$ V.

The first- discharge and first- charge cycle is known as the formatting cycle which involves both Eqns.V.1 and V.2, whereas the successive cycles only involve reversible reactions of the Eqn. V.2. The impedance spectra during the 11th discharge process at 0.7 , 0.5 and 0.3 V are qualitatively similar to those during the first-charge cycle at 0.45 , 0.6 and 0.8 V and show only a single semicircle (Figs.V.13b and c). This reflects the reversibility of the electrochemical processes in nano-(K-Co). The $R_{(sf+ct)}$ decreases from $27 (\pm 5)$ Ω at 0.7 V to $15 (\pm 5)$ Ω at both 0.3 V and 0.15 V, and then increases to $24 (\pm 5)$ Ω at 0.005 V. The $CPE_{(sf+dl)}$ decreases from 269 to $117 (\pm 5)$ μF . The spectrum at 0.005 V shows an increase in the spread of the first- semicircle and the development of a second semicircle at low frequency region (< 1 Hz). The latter semicircle, attributed to the R_b has the value, $40 (\pm 5)$ Ω . The α value gradually decreases from 0.75 to a value of 0.65 in the voltage range of 0.7 -to- 0.3 V and increases to 0.73 at 0.005 V (Table V.1). From the impedance data of nano-(K-Co), it can be concluded that $R_{(sf+ct)}$ value decreases by a factor two after the first- discharge reaction and stabilizes at 15 - 25 Ω during the first-

charge and 11th discharge cycle. The R_b contribution is seen only for $V \leq 0.5$ V during the first cycle and the 11th discharge cycle and the values range from 23 to 40 Ω (Table V.1). A similar behavior has been noted by Sharma et al. [24] in their impedance spectral studies on Sn- hollandite, $K_2(Li_{2/3}Sn_{22/3})O_{16}$.

V.7.4.1. Li-ion diffusion coefficient

An estimate of the ‘apparent’ Li-ion diffusion coefficient (D_{Li+}) can be obtained from the impedance data. The D_{Li+} has been determined for both thin films and polycrystalline cathode and anode materials and reported in the literature and a clear picture of its variation with different discharge/ charge voltages is presented. Xie et al. [40] calculated the D_{Li+} by a variety of techniques including EIS for $LiCoO_2$ thin films of different thickness. The calculation of D_{Li+} for polycrystalline $LiCoO_2$ was reported by Garcia et al [41] and Cho et al [42]. Recently, Sharma et al [12] estimated the D_{Li+} in the nano-composite anode, $CaO. SnO_2$ from the EIS data and found that the value is in the range, $0.8 - 1.5 \times 10^{-14} \text{ cm}^2\text{s}^{-1}$ at $V \leq 1.0$ V during the first cycle and the 11th discharge cycle. The D_{Li+} can be calculated by using the formula [12]:

$$D_{Li+} = \pi f_L L^2 \quad \text{--- (V.4)}$$

where f_L is the limiting frequency in the Nyquist plots where the Warburg region gives way to the intercalation capacitance region. That is, the transition from straight line (semi-infinite diffusion) of angle $\sim 45^\circ$ with the real (Z') axis in the spectrum to almost a vertical line (finite diffusion) making angle $\sim 80^\circ$ with the real axis. Generally, the f_L is seen at lower frequency region (< 0.1 Hz). The L refers to the finite diffusion length in the electrode, which is generally considered as the diameter of the grain of the active material

in the case of polycrystalline compounds or the thickness of the electrode in the case of thin films.

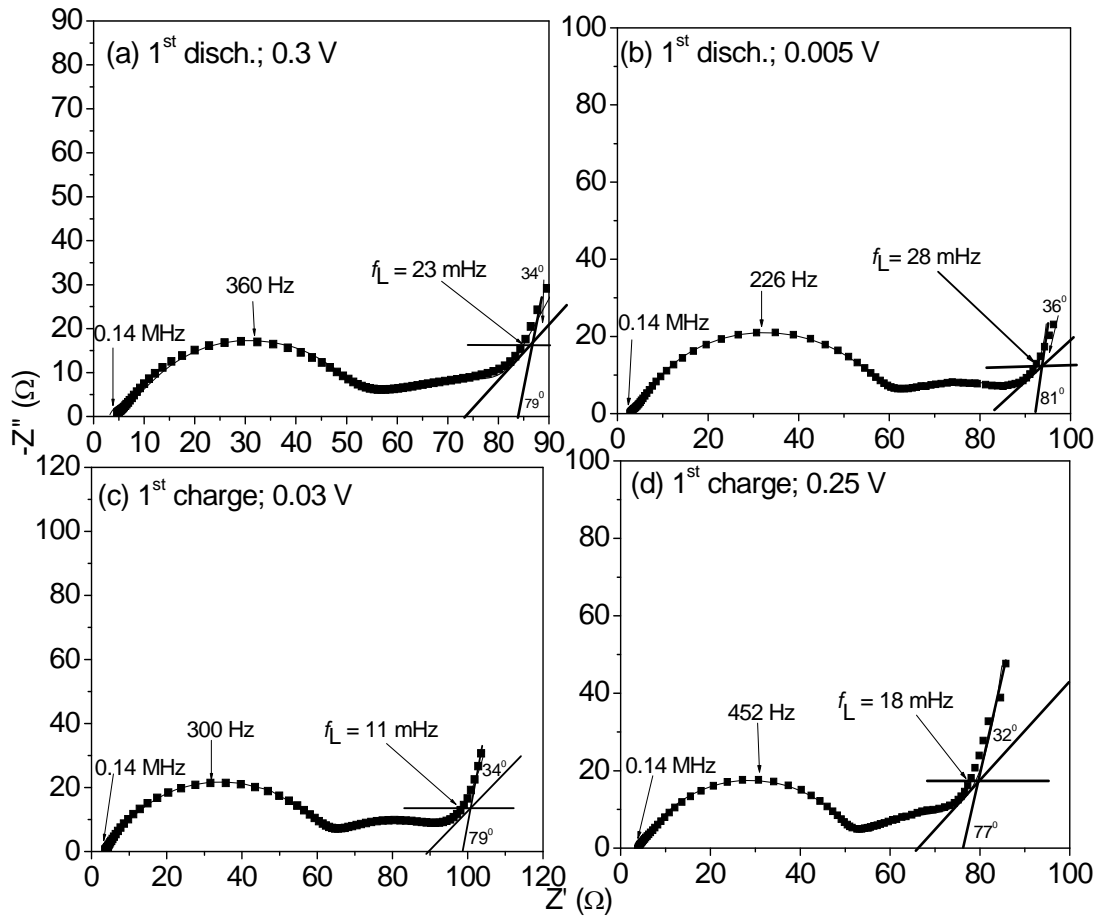


Fig.V.14. Selected impedance spectra of nano- (K-Co) redrawn from Fig. V.13 a, b in an expanded scale, for the determination of the limiting frequency (f_L). First- discharge: (a) At 0.3 V and (b) at 0.005 V. First- charge: (c) At 0.03 V and (d) at 0.25 V. The f_L values and selected frequencies are shown.

Presently, the D_{Li^+} at different discharge/charge voltages during the first cycle and the 11th discharge cycle are calculated by extracting the f_L values from the impedance spectra of Fig. V.13, in those cases where the Warburg and intercalation capacitance regions could be de-lineated. Representative spectra, redrawn from Fig.V.13 are shown in Fig. V.14. The Warburg slope ranges from 32^0 to 36^0 , indicating the non-ideal nature of

the electrode. The values of f_L are listed in Table V.1. The L value for nano- (K-Co) is 6 (± 2) nm as estimated from the XRD and TEM data (Figs. V.6 and V.7) and the D_{Li^+} values are given in Table V.1. The order of magnitude of D_{Li^+} is same as that reported by Sharma et al. [12] on nano-CaO.SnO₂ system. During the first- discharge, at V = 1.7 V, D_{Li^+} is as high as $5.6 (\pm 0.1) \times 10^{-14} \text{ cm}^2 \text{ s}^{-1}$. However, in the voltage range, 0.7 – 0.3 V in which the formation of Sn and (Li-Sn) are involved simultaneously, D_{Li^+} varies from 2.0 to $2.6 (\pm 0.1) \times 10^{-14} \text{ cm}^2 \text{ s}^{-1}$. At 0.005 V, at which the (Li- Sn) alloy formation is complete, D_{Li^+} increases slightly to $3.2 (\pm 0.1) \times 10^{-14} \text{ cm}^2 \text{ s}^{-1}$. During the first- charge, the D_{Li^+} is $1.2 (\pm 0.1) \times 10^{-14} \text{ cm}^2 \text{ s}^{-1}$ at 0.03 V. The reason for such a low value is not clear at present. The value increases two- fold when the charging voltage is increased to 0.25 V and 0.45 V, which correspond to the onset of the de-alloying reaction (Table.V.1).

From impedance data of nano-(K-Co), it can be concluded that the $R_{(sf+ct)}$ and $CPE_{(sf+dl)}$ dominate at high voltage range (0.7-1.7 V) and R_b significantly contributes to the overall impedance in the low voltage range, 0.005-0.5 V. The apparent D_{Li^+} obtained from EIS is in the range, 2.0 - 2.6 (± 0.1) $\times 10^{-14} \text{ cm}^2 \text{ s}^{-1}$ at V = 0.25 – 0.45 V during the first- cycle.

V. 8. Summary and Conclusions

The nano- (K-Co) and nano- (K-In) are prepared by HEB of pre-synthesized compounds and characterized by XRD, SEM, and HR-TEM techniques. The SEM and HR-TEM data revealed the particle sizes of both are <10 nm whereas the crystallite sizes, estimated from the XRD data are 6 – 8 nm. When cycled at 60 mA g^{-1} (0.12 C) in the voltage range of 0.005-0.8 V vs. Li, nano- (K-Co) showed a stable capacity of 500 (± 5) mAh g^{-1} upto 60 cycles after which a capacity- fade of 4 % occurs in the range of 60-80

cycles. At 1 C-rate, the nano- (K-Co) showed a capacity of 410 (± 5) mAhg⁻¹ stable up to at least 100 cycles. Under similar cycling conditions (0.12 C) nano- (K-In) showed an initial capacity of 570 (± 5) mAhg⁻¹, which dropped to 485 (± 5) mAhg⁻¹ (15 % loss). Significant improvement has been noted in the heat- treated (300 °C; 12 h; Ar) electrode of nano-(K-In) which showed a stable capacity of 570 (± 5) mAhg⁻¹ in the range of 5-50 cycles. Small capacity- fading (3%) is noted between 50 to 60 cycles. When cycled to upper cut- off voltage 1.0 V, the nano- (K-Co) showed slightly higher capacity which is stable up to 30 cycles, after which capacity- fading of 6% occurs in the range of 30-60 cycles. The coulombic efficiencies in both the compounds increased to 96-98% in the range of 10-60 cycles. For all the nano-phases presently studied, the average discharge potential is 0.13 V and average charge potential is 0.5 V vs. Li, as determined by the galvanostatic and CV data in good agreement with literature. The cycling performance of nano-(K-Co) and nano-(K-In) is much better in terms of the obtainable capacity and its stability up to 80 cycles when compared to the performance of micron- size (K-Co) and (K-In) described in Part I.

Impedance spectra were measured on nano-(K-Co) during the first- cycle and 11th discharge cycle. The relevant impedance parameters and the apparent Li- diffusion coefficient (D_{Li+}) have been evaluated and interpreted in order to support the galvanostatic and cyclic voltammetry results. The impedance due to surface film and charge transfer ($R_{(sf+ct)}$) and Warburg impedance (W_s) dominate at higher voltages (> 0.5 V), whereas bulk impedance (R_b) also contributes at lower voltages (< 0.5 V). The observed value of D_{Li+} is found to be in the range of $2.0 - 2.6 \times 10^{-14}$ cm² s⁻¹ between 0.25 - 0.45 V during the first- cycle. The observed galvanostatic cycling, CV, ex- situ -XRD and -TEM data

have been interpreted in terms of the alloying- de-alloying reaction of Sn in the nano-composite, 'Sn-K₂O-Co/In- Li₂O'. The C- rate performance of nano- (K-Co) is very satisfactory and it is concluded that optimized nano-(K-Co) and nano-(K-In) can be good alternative anode materials for LIBs.

References

- [1] G.-A. Nazri, G. Pistoia (Eds.), *Lithium Batteries: Science and Technology*, Kluwer Academic Publ., New York, 2003.
- [2] A. S. Arico, P. Bruce, B. Scrosati, J.-M. Tarascon, W. V. Schalkwijk, *Nature Mater.* 4 (2005) 366.
- [3] H. Li, Z. Wang, L. Chen, X. Huang, *Adv. Mater.* 21 (2009) 4593.
- [4] P.G. Bruce, B. Scrosati, J.-M. Tarascon, *Angew. Chem. Int. Ed.* 47 (2008) 2930.
- [5] M. Winter, J. O. Besenhard, *Electrochim. Acta* 45 (1999) 31.
- [6] J. Graetz, C. C. Ahn, R. Yazami, B. Fultz, *Electrochem. Solid State Lett.* 6 (2003) A194.
- [7] M.-S. Park, Y.-M. Kang, G.-X. Wang, S.-X. Dou, H.-K. Liu, *Adv. Funct. Mater.* 18 (2008) 455.
- [8] G. Derrien, J. Hassoun, S. Panero, B. Scrosati, *Adv. Mater.* 19 (2007) 2336.
- [9] J. Hassoun, G. Mulas, S. Panero, B. Scrosati, *Electrochem. Commun.* 9 (2007) 2075.
- [10] N. Sharma, K. M. Shaju, G. V. Subba Rao, B. V. R. Chowdari, *Electrochem. Commun.* 4 (2002) 947.
- [11] N. Sharma, K. M. Shaju, G. V. Subba Rao, B. V. R. Chowdari, *J. Power Sources* 139 (2005) 250.
- [12] Y. Sharma, N. Sharma, G. V. Subba Rao, B. V. R. Chowdari, *Chem. Mater.* 20 (2008) 6829.
- [13] Y. Sharma, N. Sharma, G. V. Subba Rao, B. V. R. Chowdari, *J. Power Sources* 192 (2009) 627.
- [14] P. A. Connor, J. T. S. Irvine, *J. Power Sources* 97-98 (2001) 223.

- [15] R. Alcantara, G. F. Ortiz, P. Lavela, J. L. Tirado, *Electrochem. Commun.* 8 (2006) 731.
- [16] X. J. Zhu, L. M. Geng, F. Q. Zhang, Y. X. Liu, L. B. Cheng, *J. Power Sources* 189 (2009) 828.
- [17] S. Lei, K. Tang, C. Chen, Y. Jin, L. Zhou, *Mater. Res. Bull.* 44 (2009) 393.
- [18] T. Xiao, Y. Tang, Z. Jia, S. Feng, *Electrochim. Acta* 54 (2009) 2396.
- [19] G. Wang, X. P. Gao, P. W. Shen, *J. Power Sources* 192 (2009) 719.
- [20] N. Sharma, G. V. Subba Rao, B. V. R. Chowdari, *J. Power Sources* 159 (2006) 340.
- [21] N. Sharma, K. M. Shaju, G. V. Subba Rao, B. V. R. Chowdari, *J. Power Sources* 124 (2003) 204.
- [22] M. V. V. M. Satya Kishore, U. V. Varadaraju, B. Raveau, *J. Solid State Chem.* 177 (2004) 3981.
- [23] M. Behm, J. T. S. Irvine, *Electrochim. Acta* 47 (2002) 1727.
- [24] N. Sharma, J. Plevert, G. V. Subba Rao, B. V. R. Chowdari, T. J. White, *Chem. Mater.* 17 (2005) 4700.
- [25] Y. Michiue, A. Sato, *Solid State Ionics* 181 (2010) 257.
- [26] G. Bayer, W. Hoffmann, *Naturwissen.* 58 (1966) 381.
- [27] R. D. Shannon, *Acta Cryst.* A32 (1976) 751.
- [28] I. A. Courtney, J. R. Dahn, *J. Electrochem. Soc.* 144 (1997) 2045.
- [29] D. Aurbach, A. Nimberger, B. Markovsky, E. Levi, E. Sominski, A. Gedanken, *Chem. Mater.* 14 (2002) 4155.
- [30] H. Li, X. Huang, L. Chen, *Solid State Ionics*, 123 (1999) 189.
- [31] D. Larcher, C. Masquelier, D. Bonnin, Y. Chabre, V. Masson, J.-B. Leriche, J.-M. Tarascon, *J. Electrochem. Soc.* 150 (2003) A133.

- [32] S.-I. Lee, S. Yoon, C.-M. Park, J.-M. Lee, H. Kim, D. Im, S.-G. Doo, H.-J. Sohn, *Electrochim. Acta* 54 (2008) 364.
- [33] Y. Sharma, N. Sharma, G. V. Subba Rao, B. V. R. Chowdari, *Adv. Funct. Mater.* 17 (2007) 2855.
- [34] J. Li, H. M. Dahn, L. J. Krause, D.-B. Le, J. R. Dahn, *J. Electrochem. Soc.* 155 (2008) A812.
- [35] Y. S. Jung, K. T. Lee, J. H. Kim, J. Y. Kwon, S. M. Oh, *Adv. Funct. Mater.* 18 (2008) 3010.
- [36] R. Yang, J. Zheng, J. Huang, X. Z. Zhang, J. L. Qu, X. G. Li, *Electrochem. Commun.* 12 (2010) 784.
- [37] Y.-M. Kang, M.-S. Song, J.-H. Kim, H.-S. Kim, M.-S. Park, J.-Y. Lee, H. K. Liu, S. X. Dou, *Electrochim. Acta* 50 (2005) 3667.
- [38] M. V. Reddy, S. Madhavi, G. V. Subba Rao, B. V. R. Chowdari, *J. Power Sources* 162 (2006) 1312.
- [39] G. X. Wang, D. H. Bradhurst, S. X. Dou, H. K. Liu, *J. Power Sources* 83 (1999) 156.
- [40] J. Xie, N. Imanishi, T. Matsumura, A. Hirano, Y. Takeda, O. Yamamoto, *Solid State Ionics* 179 (2008) 362.
- [41] B. Garcia, J. Farcy, J. P. Pereira-Ramos, N. J. Baffier, *J. Electrochem. Soc.* 144 (1997) 1179.
- [42] P.-J. Cho, E.-D. Jeong, Y.-B. Shim, *Bull. Korean Chem. Soc.* 19 (1998) 39.

Chapter VI

Nano- composites, SnO(VO_x) as anodes for lithium ion batteries*

Abstract

Nano-composites of SnO(V₂O₃)_x (x = 0, 0.25 and 0.5) and SnO(VO)_{0.5} are prepared from SnO and V₂O₃/VO by high energy ball-milling (HEB) and are characterized by X-ray diffraction (XRD), scanning electron microscopy (SEM) and high resolution transmission electron microscopy (HR-TEM) techniques. Interestingly, SnO and SnO(VO)_{0.5} are unstable to HEB and disproportionate to Sn and SnO₂, whereas HEB of SnO(V₂O₃)_x gives rise to SnO₂.VO_x. Galvanostatic cycling of the phases are carried out at 60 mA g⁻¹ (0.12 C) in the voltage range, 0.005-0.8 V vs. Li. The nano-SnO(V₂O₃)_{0.5} showed a first- charge capacity of 435(±5) mAhg⁻¹ which stabilized to 380(±5) mAhg⁻¹ with no noticeable fading in the range of 10- 60 cycles. Under similar cycling conditions, nano-SnO (x = 0), nano-SnO(V₂O₃)_{0.25} and nano-SnO(VO)_{0.5} showed initial reversible capacities between 630 and 390 (±5) mAhg⁻¹. Between 10-50 cycles, nano-SnO showed a capacity- fade as high as 59%, whereas the above two VO_x- containing composites showed capacity- fade ranging from 10 to 28%. In all the nano- composites, the average discharge potential is 0.2-0.3 V and average charge potential is 0.5-0.6 V vs. Li, and the coulombic efficiency is 96-98% after 10 cycles. The observed galvanostatic cycling, cyclic voltammetry and ex- situ XRD data are interpreted in terms of the alloying- de-

* One paper has been published and one paper was presented at an Intl. Conference based on the work described in this Chapter.

alloying reaction of Sn in the nano-composite, 'Sn-VO_x- Li₂O' with VO_x acting as an electronically- conducting matrix.

VI.1. Introduction

Lithium ion rechargeable batteries (LIBs) are the promising dc- energy source for portable electronic devices. To satisfy the ever-increasing demand for high energy density LIBs for applications in electric and hybrid electric vehicles (EV/HEVs) and off-peak energy storage, lot of research effort is expended to find electrode materials, especially the anodes (negative electrodes) which possess high capacity and excellent cyclability [1-4]. Li- alloy forming elements M (M = Sn, Si, Sb) [1-8] have received much attention due to their ability of reversibly reacting with large amount of Li per formula unit. Among these, Si and Sn are considered as most promising elements, as they form alloys, Li_{4.4}M. Sn-based intermetallics, oxides and composites are well studied as possible alternatives to graphite anode presently employed in the LIBs. However, almost all of them suffer from poor cycling performance due to the large unit cell volume variation (~300%), which causes disintegration of the electrode material during long-term charge/discharge process. The capacity fading can be suppressed to some extent by (i) incorporating suitable 'matrix' elements, (ii) reducing the particle size to nano-meter scale, and (iii) choosing a suitable voltage range of cycling. Accordingly, nano-structured materials are explored as potential candidate anodes for LIBs, because they can show large reversible capacities due to high surface area, high current- rate capability due to short Li- ion diffusion path length and minimization of the strain caused due to large volume variations during charge/discharge process [5].

Sn- based binary and ternary oxides in nano- form such as, SnO [9], SnO₂ [10, 11], CaO.SnO₂ [12], CoSnO₃ [13] have been studied as anode materials. The advantage of using oxides is that they can be synthesized with varying morphology, and particle and crystallite size can be manipulated, in comparison to Sn- metal. However, an obvious disadvantage is that the binary/ ternary oxide is first reduced to Sn- metal by Li, and only then the Li- Sn alloy formation can take place. Hence, a large irreversible capacity loss (ICL) occurs during the first discharge- charge process. Among all Sn-based oxides, SnO is attractive because it has a theoretical capacity as high as 875 mAhg⁻¹ and will have a lower ICL compared to other Sn- oxides. There are a few reports on the Li- cyclability of bulk (micron- size) and nano- SnO in the literature. Courtney and Dahn [14] found that bulk SnO can give an initial reversible capacity of 825 mAhg⁻¹, but the capacity fades drastically on long-term cycling in the voltage range, 0.0-1.3 V vs Li. But, when the voltage range is restricted to 0.4-1.3 V, somewhat stable capacity is obtained up to 10 cycles. Li et al [15] reported that the Li-cycling properties of SnO were influenced by the particle size, as was clear from studies on ball-milled SnO. Un-milled SnO gave a first-charge capacity as high as 760 mAhg⁻¹, but capacity-fading occurred giving only 420 mAhg⁻¹ at the end of 11th cycle. Similar was the case with ball-milled SnO. Uchiyama et al. [16] reported a comparative Li-cyclability study of SnO of different morphologies with that of commercial SnO. They found that both meshed and flat plate SnO showed initial capacities of 760 and 880 mAhg⁻¹, respectively as compared to 525 mAhg⁻¹ for commercial SnO in the voltage range 0.1- 1.0 V at 100 mA g⁻¹. However, drastic capacity-fading was noticed in all cases after 20 cycles. Wang et al. [17] studied Li- cycling of SnO and Sn.Li₂O composite prepared by ball milling of SnO and Li- metal. They noticed

lesser ICL in the case of composite and better capacity- retention when cycled in the voltage range, 0.02- 1.5 V at 0.1 mA cm^{-2} . The composite electrode showed 170 mAhg^{-1} at the 100th cycle whereas ball- milled SnO showed only 20 mAhg^{-1} . Yang et al. [18] studied the Li- cycling of SnO particles of different sizes in the voltage window, 0.1- 1.3 V and found an initial capacity of 530 mAhg^{-1} at 0.4 mAcm^{-2} . Fairly high ICL was noted for fine- particle SnO and a comparatively better capacity- retention till 50 cycles ($\sim 350 \text{ mAhg}^{-1}$). Ning et al. [19] studied the Li- cycling of nanoflower SnO in the voltage range of 0.01- 2.0 V at 0.1 C rate. A 4th cycle charge- capacity of $\sim 750 \text{ mAhg}^{-1}$ was noticed, but the capacity faded to 450 mAhg^{-1} within 20 cycles. Chen et al. [20] reported the cycling behavior of SnO- carbon nanotube (CNT) nanocomposite and observed a first charge capacity of $\sim 780 \text{ mAhg}^{-1}$ in the voltage range 0 - 2.0 V at 40 mA^{-1} . However, capacity- fading was noticed within ten cycles, giving $\sim 450 \text{ mAhg}^{-1}$. From the above discussion, it is clear that pure SnO in micron/ nano- size and with various morphologies is prone to significant capacity- fading on cycling. Composites with SnO appear to show some promise, even though not many studies are reported.

Recently, Reddy et al. [21,22] studied the Li- cycling properties of VSbO_4 and $(\text{V}_{1/2}\text{Sb}_{1/2}\text{Sn})\text{O}_4$ and found that the presence of vanadium oxide (VO_x) in the composite can act as a good matrix and helps in suppressing the capacity- fading of Sb and Sn- oxide upon long term cycling. It appears that the strain due to large volume variations caused by alloying- de- alloying reactions of Li_3Sb and $\text{Li}_{4.4}\text{Sn}$ is highly buffered due to the presence of VO_x . Recently, Park et al [23] prepared the composite, SnO.Ti.C by ball milling to yield nano-Sn.TiO₂.C and examined its Li- cyclability. When cycled in the voltage range, 0- 2.5 V vs. Li at 100 mA^{-1} , an initial reversible capacity of $\sim 750 \text{ mAhg}^{-1}$

¹ was observed which slowly degraded to $\sim 610 \text{ mAhg}^{-1}$ over 100 cycles ($\sim 18\%$ capacity-fading).

In the present study, the Li- cycling behavior of the nanocomposites, SnO, $(\text{SnO}(\text{V}_2\text{O}_3)_x; x = 0.25, 0.5)$ and $(\text{SnO}(\text{VO})_{0.5})$ prepared by high energy ball- milling (HEB), has been examined. It is known that V_2O_3 and VO exhibit metallic- type electronic conductivity at ambient temperature [24- 26]. Studies by Reddy et al. [21, 22] and unpublished results (from the author's laboratory) have shown that pure V_2O_3 and VO_x ($x \leq 1$) do not show any significant Li- cycling behavior in the voltage range, 0.005- 1.0 V vs. Li. Thus, it can be concluded that the nanocomposites, $\text{SnO}(\text{VO}_x)$ are comprised of only one electrochemically- active element (Sn) towards Li. Accordingly, the present results show that the nanocomposite $\text{SnO}(\text{V}_2\text{O}_3)_{0.5}$ exhibits a reversible capacity of $380 (\pm 5) \text{ mAhg}^{-1}$ with no noticeable capacity- fading in the range, 10- 60 cycles when cycled at 0.12 C in the voltage range, 0.005- 0.8 V vs. Li.

VI.2. Experimental

Commercial SnO (Acros Organics, 98%), V_2O_3 (Acros Organics, 99%) and VO (Alfa Aesar, 99%) were employed to prepare the nano-composites by high energy ball milling (HEB). The same procedure as described in Part II of Chapter V for the preparation of nano-phase $\text{K}_2(\text{M}_2\text{Sn}_6)\text{O}_{16}$, is followed. For the sake of convenience, the nano-composites prepared by HEB are referred as nano-SnO ($x = 0$), $\text{nano-SnO}(\text{V}_2\text{O}_3)_x$ ($x = 0.25, 0.50$) and $\text{nano-SnO}(\text{VO})_{0.5}$.

Structural and morphological characterizations were carried out as described in earlier Chapters. Chemical analysis for Fe and Cr of selected nano-composites was performed by inductively coupled plasma optical emission spectrometer (ICP-OES)

system (Perkin Elmer Dual-View Optima 5300 DV). The composites were dissolved in an acid mixture using Milestone microwave laboratory system for the analysis. The electrode fabrication, electrochemical characterization and ex-situ- XRD studies were carried out as described in earlier Chapters.

VI.3. Results and discussion

VI.3.1. Structure and morphology

The powder X-ray diffraction (XRD) pattern of SnO-C (commercial) is shown in Fig.VI.1a. It is indexed as per the tetragonal structure (space group, P4/nmm). The lattice parameters, calculated by the Rietveld refinement (Topas R 2.1 software) are: $a = 3.801$ (2) Å and $c = 4.835$ (2) Å. These agree with those reported in the JCPDS card no 85-0712. Fig.VI.1b shows the XRD pattern of nano-SnO. Surprisingly, the XRD pattern shows the characteristic lines of SnO₂ [JCPDS card no. 77-0452] and Sn- metal [JCPDS card no. 04-0673] and the lines due to SnO are completely absent. This can be ascribed to the disproportionation of SnO by self oxidation-reduction during the HEB in Ar- atmosphere as per Eqn. VI.1.



The forward reaction of Eqn. (VI.1) is energetically favorable due to negative Gibbs free energy change ($\Delta G_{298}^0 = -5.9 \text{ kJ mol}^{-1}$) and is aided by moderately mild temperatures [27]. It is well known that HEB gives rise to local heating of the material particles, to temperatures as high as 500-600 °C, and this can enhance the rate of reaction of Eqn. (VI.1). Thus, it is concluded that SnO is unstable to HEB in an inert atmosphere.

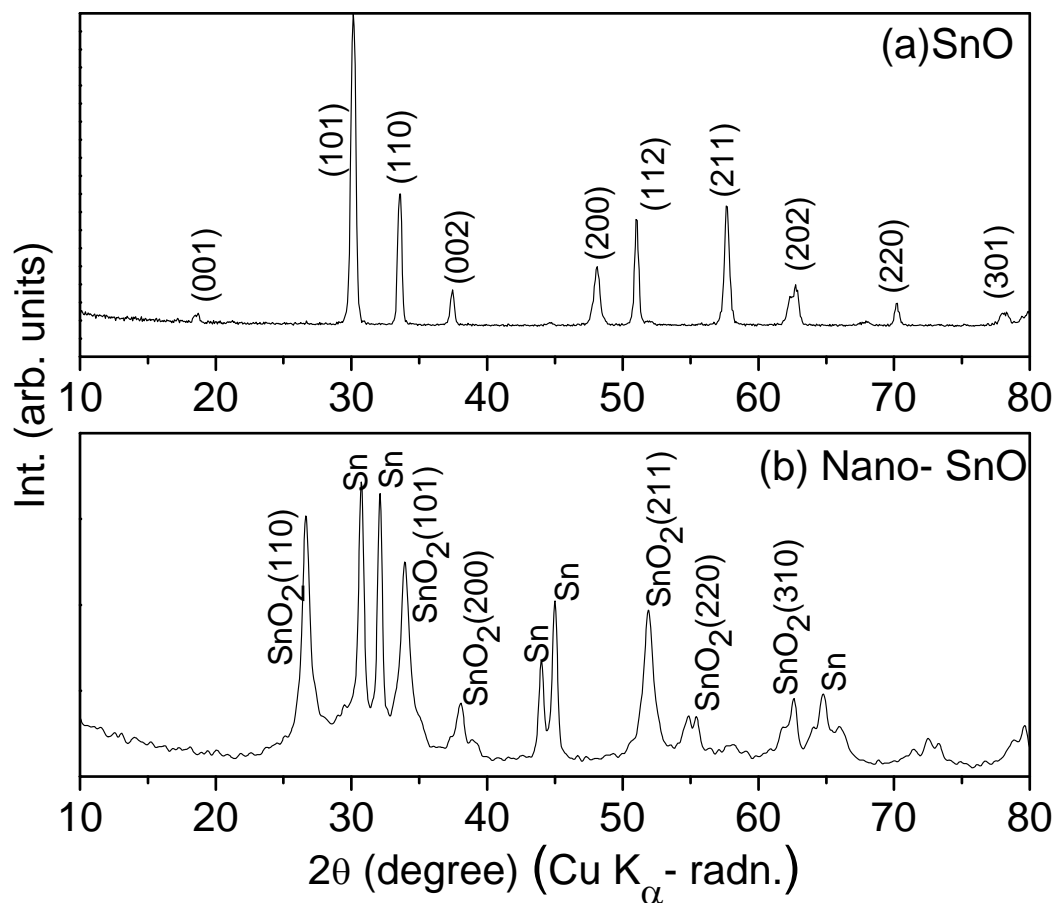


Fig.VI.1. Powder X-ray diffraction patterns. (a) SnO (commercial), and (b) nano-SnO (after high energy ball milling). Miller indices (h k l) are shown.

Fig. VI.2a shows the XRD pattern of nano-SnO(V₂O₃)_{0.25}. It shows only lines due to tetragonal SnO₂ [JCPDS card no. 77-0452] except for a very small amount of SnO (peak at $2\theta = 30.2^\circ$). As SnO is a good reducing agent, it forms SnO₂ by reducing V₂O₃ to its lower valency state (VO_x, x ~1.0). No lines due to Sn- metal are seen. Thus, the composite consists of SnO₂.VO_x. Fig. VI.2b shows the XRD pattern of nano-SnO(VO)_{0.5} and as can be seen, lines due to both SnO₂ and Sn- metal are present, as can be expected because VO can not be reduced to V- metal by SnO. Thus, the composite consists of

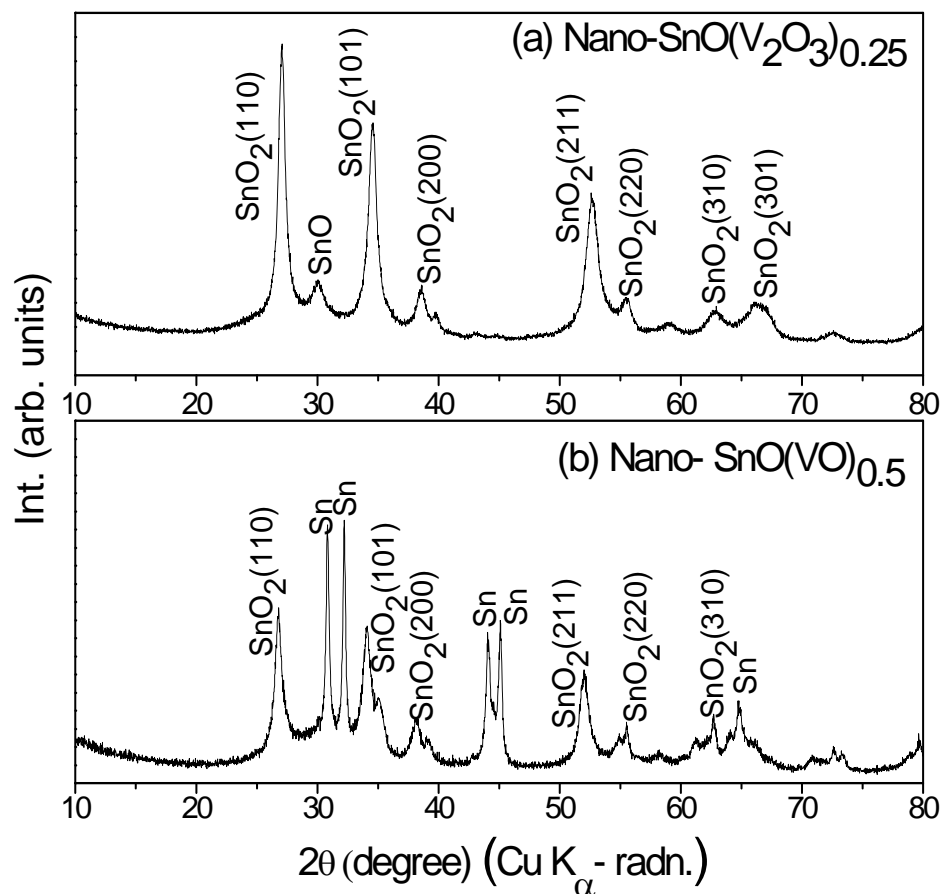


Fig.VI.2. Powder X-ray diffraction patterns. (a) Nano-SnO(V₂O₃)_{0.25}, and (b) nano-SnO(VO)_{0.5}. Miller indices (h k l) are shown.

SnO₂.Sn.VO_x (x~1) and Figs. VI.1b and VI.2b bear good resemblance. In the XRD patterns of nano-SnO(V₂O₃)_{0.25} and nano-SnO(VO)_{0.5}, lines due to VO_x are not seen, possibly due to their amorphous nature, as a result of HEB. It may be pointed out that Park et al. [23] did not notice lines due to TiO₂ in their composite, Sn.TiO₂.C prepared by the ball-milling of SnO.Ti.C.

It is known that HEB of reactants employing stainless steel balls and vials gives rise to iron (Fe) and chromium (Cr) metal impurities as a result of non-negligible deterioration of the components. Lee et al [28] during their studies on the synthesis of Ti-

Si and Ti-Si-Al alloys by HEB noticed ~5 and ~1 at. % of Fe and Cr respectively, as impurities after 20 h of HEB. In the present study, chemical analysis of nano-SnO(V₂O₃)_x (x = 0.25 and 0.5) and SnO(VO)_{0.5} by ICP-OES yielded ~0.9- 3.3 wt. % and ~ 0.1- 0.2 wt. % of Fe and Cr, respectively depending on the value of x. The XRD patterns did not reveal any lines due to the Fe and Cr metals in the above composites, due to their small content and amorphous nature.

Fig. VI.3a shows the SEM photograph of nano-SnO(VO)_{0.5} with a flake- type morphology containing agglomerated particles. The TEM photograph of nano-SnO(V₂O₃)_{0.25}, shown in Fig. VI.3b also indicates the agglomeration of nano-particles of size, 20- 30 nm. The crystallite sizes of nano-SnO and nano-SnO(V₂O₃)_{0.25} were calculated by using the Scherrer's formula, $P = K \lambda / (\beta_{1/2} \cos\theta)$, where P is crystallite size, K is Scherrer constant (0.9), λ is the wavelength of Cu K α - radiation (1.54059 Å), $\beta_{1/2}$ is the full width at half maximum (FWHM) in radians of the XRD peak and θ is the scattering (Bragg) angle [12]. The XRD- instrumental broadening was calculated by using the nano-TiO₂ (anatase) (Evonik Degussa; 99.5%) of ~25 nm particle size as the standard and was found to be 0.08°. For TiO₂, we assume the crystallite size is of the same order as particle size. The crystallite sizes of the composites were calculated by using $\beta_{1/2}$ (FWHM) values of two or three high intensity peaks and the corresponding θ values in the XRD patterns (Fig. VI.1b and VI.2a). The average crystallite sizes (P) obtained are, nano-SnO: 12 (\pm 3 nm); and nano-SnO(V₂O₃)_{0.25}: 13 (\pm 3 nm), thereby confirming the nano-nature of the composites prepared by HEB.

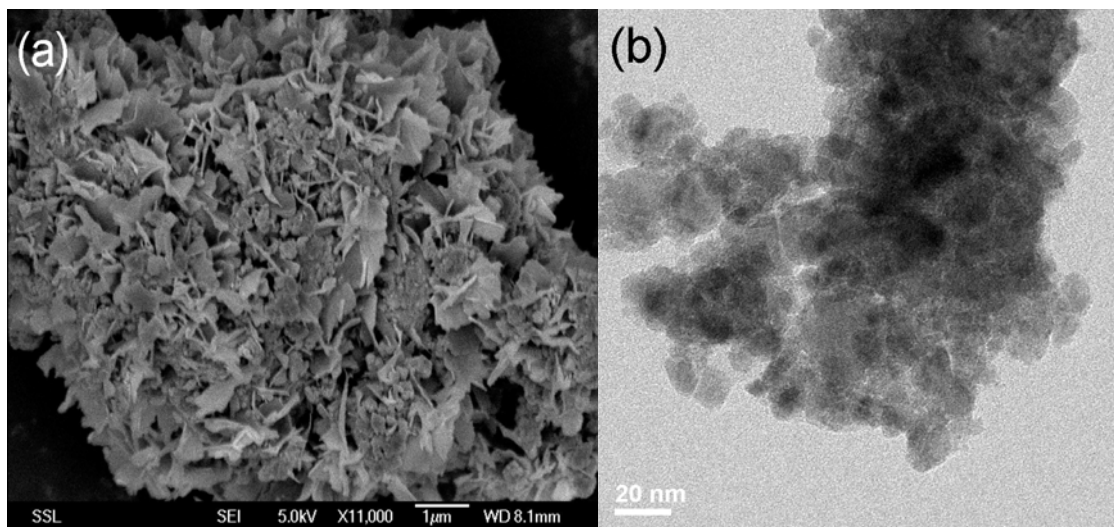


Fig.VI.3. (a) SEM photograph of nano-SnO(VO)_{0.5}. (b) HR- TEM photograph of nano-SnO(V₂O₃)_{0.25}. Scale bars are shown.

VI.3.2. Electrochemical Studies

VI.3.2.1. Galvanostatic cycling of nano- SnO

The capacity- voltage profiles of discharge and charge cycles of nano-SnO, at a current density 60 mA g^{-1} (0.12 C) in the voltage range of 0.005- 0.8 V vs. Li, up to 50 cycles are shown in Fig. VI.4 a and b. Only selected cycles are shown for clarity. The first discharge profile (Fig. VI.4a) commenced from the open circuit voltage (OCV \sim 2.0 V) to the lower cut off voltage, 0.005 V. The voltage drops continuously and a broad plateau at \sim 0.9 V followed by a continuous sloping region is noticed up to the voltage of 0.005 V. This is expected, since the nano-SnO consists of the composite, Sn.SnO₂. Amorphisation/crystal structure destruction of SnO₂ will occur according to Eqn. (VI.2). At the same time, alloying reaction of Sn will also occur as per Eqn. (VI.3), thus giving rise to a small voltage plateau at \sim 0.4 V and a continuously sloping profile is noticed till the end of discharge. The total first- discharge capacity is 1500(\pm 5) mA $h g^{-1}$ (7.5 moles of Li per mole of nano-SnO). The expected first- discharge capacity according to Eqns. VI.2

and VI.3 is only 6.4 moles of Li. The extra consumption of 1.1 moles of Li can be ascribed to the solid-electrolyte interphase (SEI) formation [9, 12, 14, 15, 29].

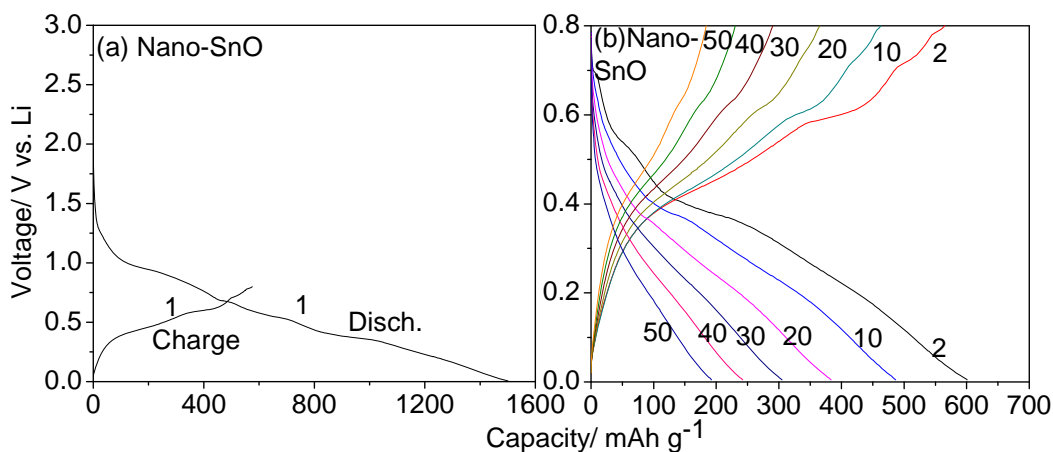
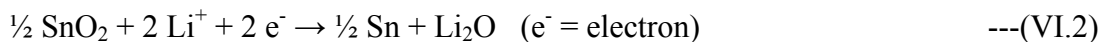


Fig.VI.4. Galvanostatic discharge-charge profiles of nano-SnO: (a) 1st cycle; (b) 2- 50 cycles. The numbers indicate cycle number. Voltage range, 0.005- 0.8 V vs. Li, at a current density of 60 mA_g⁻¹ (0.12 C).

During the first- charge, a broad voltage plateau is noticed at ~0.6 V corresponding to the de-alloying reaction (Eqn. (VI.3); Fig. VI.4a). The total first charge capacity is 575(±5) mA_hg⁻¹ (2.9 moles of Li), with a net ICL value 925(±5) mA_hg⁻¹ (4.6 moles of Li). The discharge- charge profiles between 2- 50 cycles are analogous to that of the first-charge profile. It is clear from Figs. VI.4 b and VI.5a (capacity vs. cycle number plot) and the data presented in Table VI.1, large capacity- fading occurs in nano-SnO and between 10-50 cycles, the total capacity loss is 59%. These results are in agreement with those reported on micron-SnO and nano-SnO in the literature [9, 15, 17].

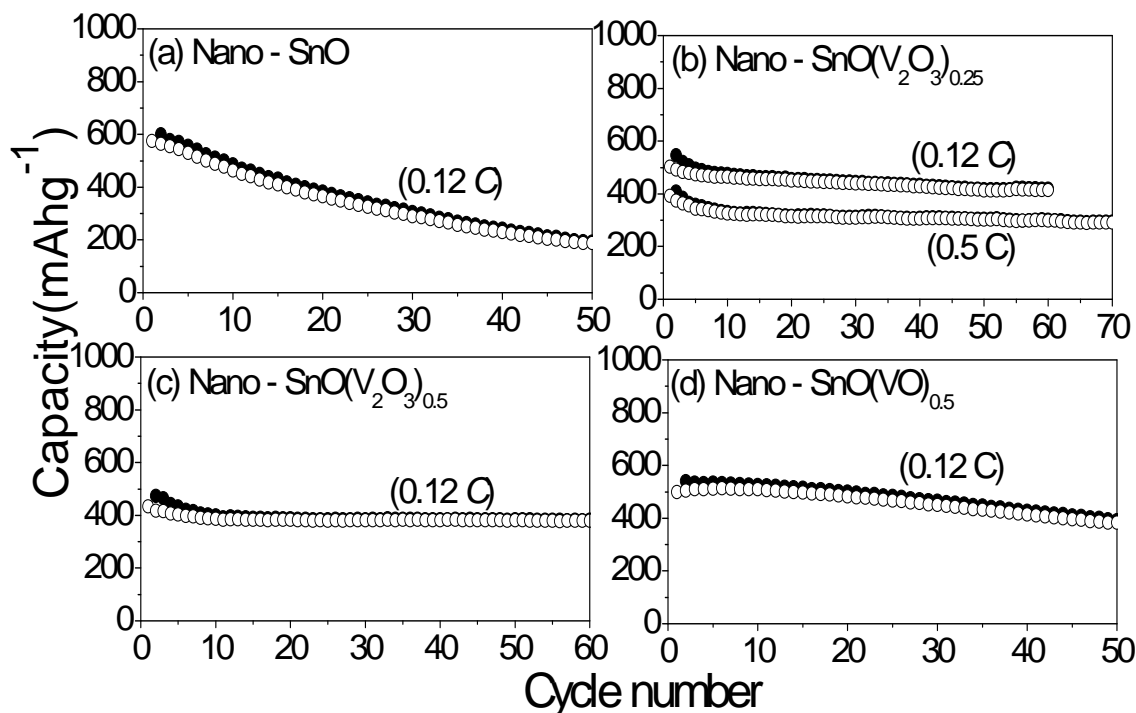


Fig.VI.5. Capacity vs. cycle number plots. (a) Nano-SnO; (b) Nano-SnO(V₂O₃)_{0.25} at 0.12 C and 0.5 C (1 C = 500 mA g⁻¹); (c) Nano-SnO(V₂O₃)_{0.5} and (d) Nano-SnO(VO)_{0.5}. Voltage range, 0.005-0.8 V vs. Li, at current density of 60 mA g⁻¹ (0.12 C). Filled symbols: Discharge capacity; Open symbols: Charge capacity.

VI.3.2.2. Galvanostatic cycling of composites, nano-SnO(VO_x)

The capacity- voltage profiles of nano-SnO(V₂O₃)_{0.25} at 60 mA g⁻¹ (0.12 C), in the voltage range, 0.005- 0.8 V are shown in Fig.VI.6a and b. As discussed earlier, the nano-composite consists of SnO₂.VO_x. The first- discharge starts from the OCV (~2.5 V) and broad voltage plateaus at ~1.0 V and ~0.7 V are noticed until a capacity of 900(±5) mA h g⁻¹ (consumption of 5.8 moles of Li per mole of composite) is reached. This is followed by a minor plateau at ~0.2 V, at the end of which a total capacity of 1915(±5) mA h g⁻¹ (12.3 moles of Li) is obtained (Fig.VI.6a and Table VI.1). The voltage plateaus at ~1.0 V and ~0.7 V may correspond to the structure destruction of SnO₂ and formation of

Sn- metal and the plateau at ~0.2 V corresponds to the alloy formation, $\text{Li}_{4.4}\text{Sn}$ (Eqn. VI.3). The theoretical first- discharge capacity, as per Eqns. (VI.3 and VI.4) is 1075 mAhg^{-1} (6.9 moles of Li) (Table VI.1).

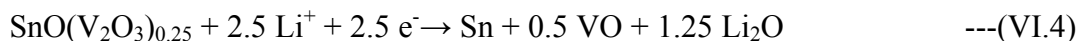


Table.VI.1 Theoretical and observed capacities (corresponding number of moles of Li per formula unit) of nano-SnO and nano-SnO(VO_x) composites. Voltage range, 0.005-0.8 V vs. Li at a current density 60 mA g^{-1} (0.12 C) ($1 \text{ C} = 500 \text{ mA g}^{-1}$).

Composite (Formula weight)	Theor. Capacity, mAhg^{-1} (moles of Li)		Observed capacity, (± 5) mAhg^{-1}				Capacity - fading (%) (10- 50 cycles)
	1 st Discharge	Reversible capacity (4.4 Li)	1 st Discharge	1 st Charge	50 th Discharge	50 th Charge	
Nano- SnO (134.7 g)	1275 (6.4 Li)	875	1500 (7.5 Li)	575 (2.9 Li)	195 (0.98 Li)	190 (0.95 Li)	59
Nano- $\text{SnO}(\text{V}_2\text{O}_3)_{0.25}$ (172.2 g)	1075 (6.9 Li)	685	1915 (12.3 Li)	500 (3.2 Li)	415 (2.7 Li)	410 (2.6 Li)	11
Nano- $\text{SnO}(\text{V}_2\text{O}_3)_{0.25}$ Current rate, 0.5 C	1075 (6.9 Li)	685	1760 (11.3 Li)	390 (2.5 Li)	295 (1.9 Li) (70 th cyc)	290 (1.86 Li) (70 th cyc)	10 (10-70 cyc)
Nano- $\text{SnO}(\text{V}_2\text{O}_3)_{0.25}$ Voltage range, 0.005-1.0 V	1075 (6.9 Li)	685	1810 (11.6 Li)	565 (3.6 Li)	450 (2.9 Li) (40 th cyc)	445 (2.8 Li) (40 th cyc)	14 (5-40 cyc)
Nano- $\text{SnO}(\text{V}_2\text{O}_3)_{0.5}$ (209.6 g)	940 (7.4 Li)	562	1850 (14.5 Li)	435 (3.4 Li)	385 (3.1 Li)	380 (3.0 Li)	Nil
Nano- $\text{SnO}(\text{VO})_{0.5}$ (168.2 g)	1020 (6.4 Li)	700	1375 (8.6 Li)	500 (3.1 Li)	390 (2.45 Li)	380 (2.4 Li)	25
Nano- $\text{SnO}(\text{VO})_{0.5}$ Voltage range, 0.005-1.0 V	1020 (6.4 Li)	700	1600 (10 Li)	630 (4 Li)	480 (3 Li) (40 th cyc)	460 (2.9 Li) (40 th cyc)	28 (5-40 cyc)

During the first- charge cycle, a broad voltage plateau, which is due to the de-alloying reaction of $\text{Li}_{4.4}\text{Sn}$, onsets at ~ 0.6 V (Fig. VI.6a). The total first- charge capacity is $500(\pm 5)$ mAhg^{-1} (3.2 moles of Li per mole of composite), whereas 685 mAhg^{-1} (4.4 moles of Li) is expected theoretically. The second- discharge profile is different from the first- discharge profile, where only a sloping region is noticed from ~ 0.7 V to ~ 0.2 V and another sloping region till 0.005 V (Fig.VI.6b). The total second- discharge capacity is $545(\pm 5)$ mAhg^{-1} (3.5 moles of Li). The charge profiles in the range, 2-60 cycles are analogous to the first charge- profile establishing the same reaction mechanism, i.e., de-alloying of $\text{Li}_{4.4}\text{Sn}$ formed during the discharge reaction. The capacity vs. cycle number plot, shown in Fig.VI.5b, indicates small capacity- fading between 10-50 cycles corresponding to the loss of 11%, and the coulombic efficiency reaches 96-98% (Table VI.1). The capacity contribution due to the VO_x present in the nano-composite can be neglected, because unpublished results from the author's laboratory indicated that ball-milled V_2O_3 shows only $75 (\pm 5)$ mAhg^{-1} at 60 mA g^{-1} when cycled in the voltage range 0.005 - 0.8 V and this includes the conducting carbon contribution.

Galvanostatic cycling was also carried out with an upper cut- off voltage of 1.0 V at 60 mA g^{-1} . The voltage- capacity profiles, shown in Fig. VI.7a, b, are analogous to the profiles of nano- $\text{SnO}(\text{V}_2\text{O}_3)_{0.25}$ in the range, 0.005 - 0.8 V (Fig.VI.6a, b). The observed first- discharge capacity is $1810(\pm 5)$ mAhg^{-1} (11.6 moles of Li), whereas the first- charge capacity is $565(\pm 5)$ mAhg^{-1} (3.6 moles of Li) with the observed ICL being $1245(\pm 5)$ mAhg^{-1} (8 moles of Li). The reversible capacity at the end of 40th cycle is $450(\pm 5)$ mAhg^{-1} (2.9 moles of Li) (Table VI.1). Capacity- fading occurs similar to the cycling behavior

with the upper cut-off voltage of 0.8 V, and the capacity-fade is 14% between 5-40 cycles (Table VI.1).

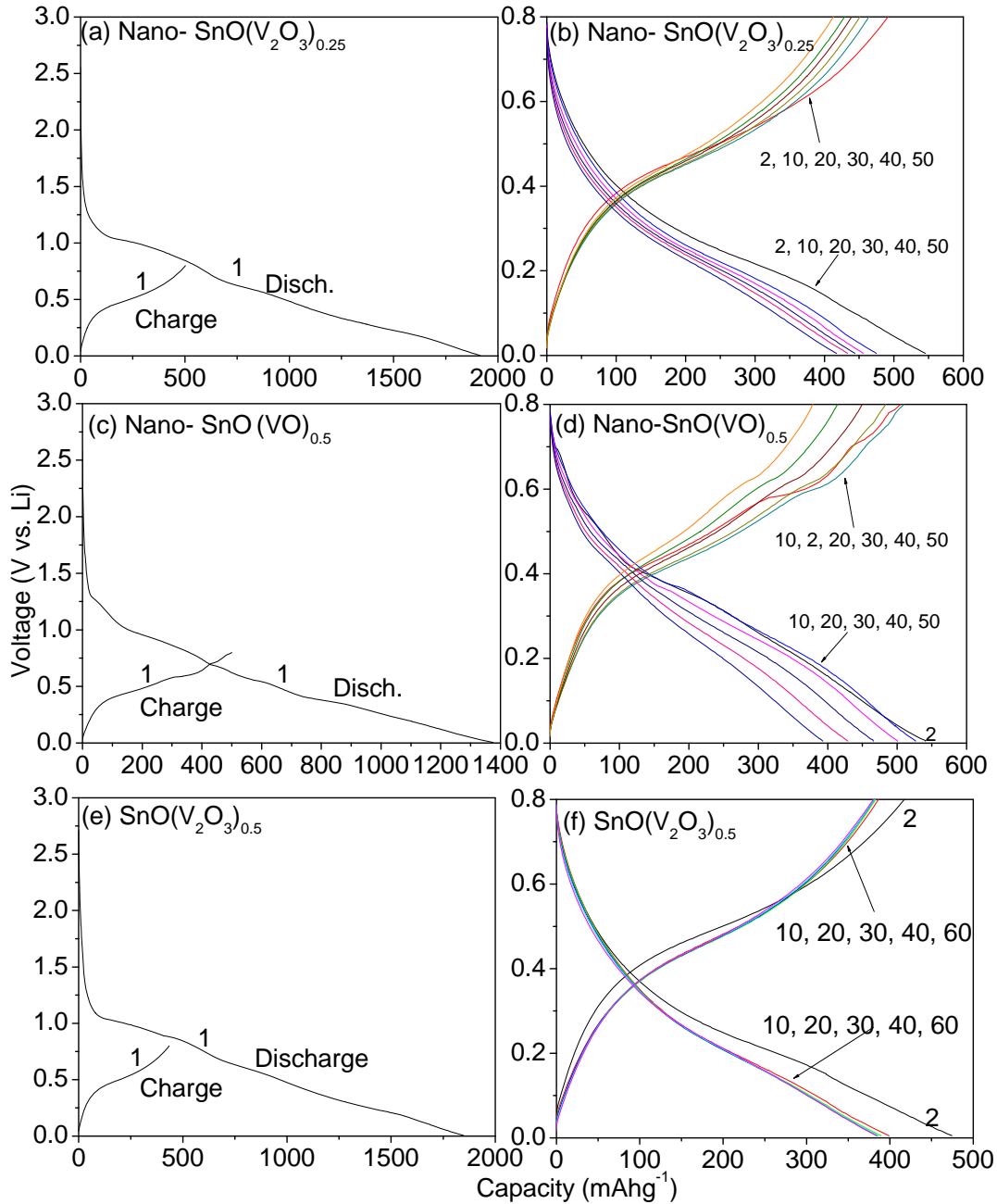


Fig.VI.6. Galvanostatic discharge-charge profiles. Nano-SnO(V₂O₃)_{0.25}: (a) 1st cycle and (b) 2- 50 cycles. Nano-SnO(VO)_{0.5}: (c) 1st cycle and (d) 2- 50 cycles. Nano-SnO(V₂O₃)_{0.5}: (e) 1st cycle and (f) 2- 60 cycles. The numbers indicate cycle number. Voltage range, 0.005- 0.8 V vs. Li, at a current density of 60 mA_g⁻¹ (0.12 C).

The rate capability of nano-SnO(V₂O₃)_{0.25} was tested on a duplicate cell at the current rate of 0.5 C (250 mA_g⁻¹), in the voltage range of 0.005- 0.8 V up to 70 cycles (Fig. VI.5b). The initial capacities during 1st discharge and charge cycle are 1760(±5) mA_h_g⁻¹ (11.3 moles of Li) and 390(±5) mA_h_g⁻¹ (2.5 moles of Li), respectively. A capacity of 330- 300(±5) mA_h_g⁻¹ (1.9 moles of Li) is observed in the range, 10-70 cycles with a capacity- fade of only 10% (Table VI.1 and Fig. VI.5b).

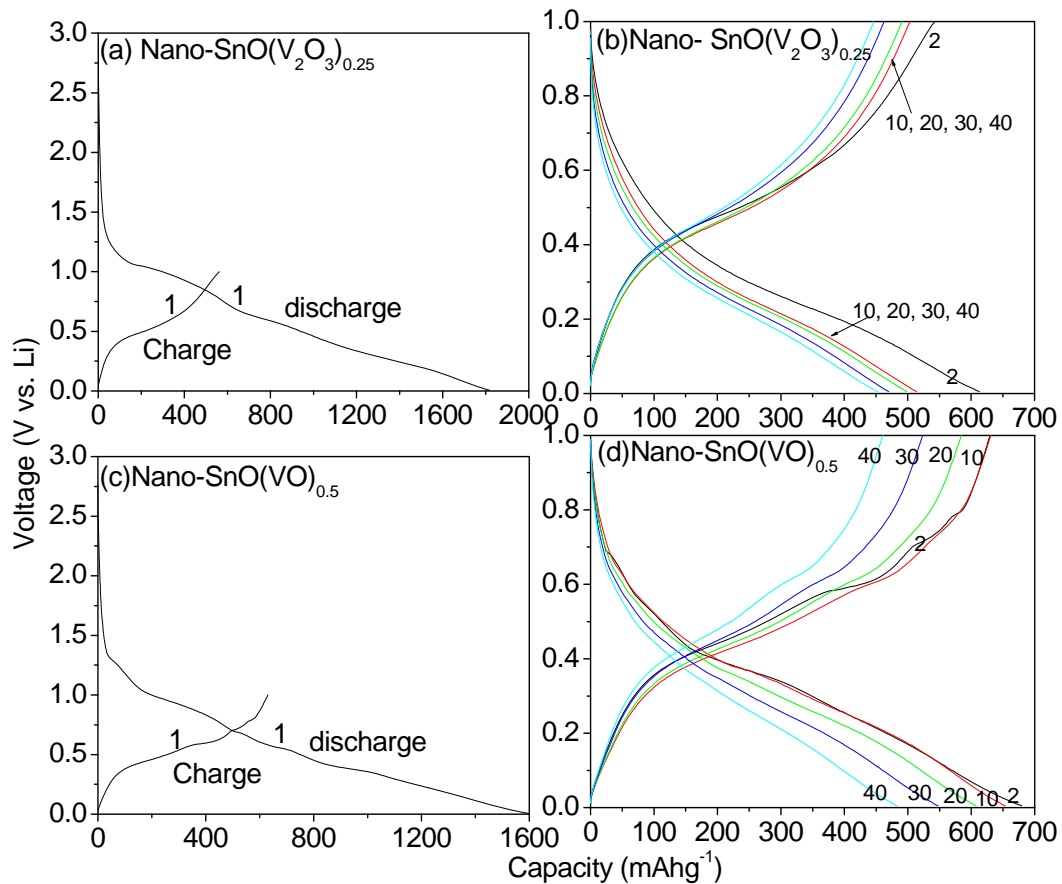


Fig. VI.7. Galvanostatic discharge-charge profiles. Nano-SnO(V₂O₃)_{0.25}: (a) 1st cycle and (b) 2- 40 cycles. Nano-SnO(VO)_{0.5}: (c) 1st cycle and (d) 2- 40 cycles. The numbers indicate cycle number. Voltage range, 0.005- 1.0 V vs. Li, at a current density of 60 mA_g⁻¹ (0.12 C).

The capacity- voltage profiles of nano-SnO(V₂O₃)_{0.5} at 60 mA_g⁻¹ (0.12 C), in the voltage range, 0.005- 0.8 V are shown in (Fig. VI.6e, f). They are similar to those

observed for nano-SnO(V₂O₃)_{0.25}. The first- discharge capacity is 1850(±5) mAhg⁻¹ (14.5 moles of Li) and the first- charge capacity is 435(±5) mAhg⁻¹ (3.4 moles of Li). The observed ICL (1415 mAhg⁻¹; 11.2 moles of Li) is larger in comparison to that found in nano-SnO(V₂O₃)_{0.25}, as can be expected due to the increased content of V-oxide. The reversible capacity showed a slight decrease up to 10 cycles, and stabilized to 380(±5) mAhg⁻¹ (3 moles of Li) up to 60 cycles, with no noticeable capacity- fading (Fig. VI.5c and Table VI.1).

Fig. VI.6 c,d show the capacity- voltage profiles of nano-SnO(VO)_{0.5} at 60 mA g⁻¹ (0.12 C) in the voltage range, 0.005- 0.8 V up to 50 cycles. The profiles are analogous to those measured on nano-SnO and contain Sn, SnO₂, and VO_x as a result of ball milling. The total first- discharge capacity is 1375(±5) mAhg⁻¹ (8.6 moles of Li) which is larger than the expected value 1020 mAhg⁻¹ (6.4 moles of Li). During the first- charge, a broad voltage plateau at ~0.45 V followed by two more small plateau regions at ~0.6 and ~0.7 V are seen. These plateaus are due to the de- alloying reaction to form Sn metal particles. These plateau regions persist in subsequent cycles (up to 20) as is clear in Fig. VI.6d, and are almost similar to the profiles shown by nano-SnO (Fig. VI.4b). The total first- charge capacity is 500(±5) mAhg⁻¹ (3.1 moles of Li). Thus, the ICL during the first cycle is 875(±5) mAhg⁻¹ (5.5 moles of Li). The second- discharge and -charge profiles are analogous to the first- discharge and -charge profiles, and showed total capacities of 540(±5) mAhg⁻¹ (3.4 moles of Li) and 505(±5) mAhg⁻¹ (3.2 moles of Li), respectively. The reversible capacity remains stable up to 10 cycles but decreases thereafter. At the end of 50th cycle, the capacity is 380(±5) mAhg⁻¹ (2.4 moles of Li) which corresponds to a capacity-fade of 25% between 5-50 cycles (Fig. VI.5d and Table VI.1). The capacity-

voltage profiles of nano-SnO(VO)_{0.5} in the voltage range, 0.005 – 1.0 V, at 60 mA g⁻¹ are similar to the profiles in the voltage range, 0.005- 0.8 V (Fig. VI. 6 c, d and VI.7 c, d). The total first- discharge capacity is 1600(±5) mA h g⁻¹ (10 moles of Li), whereas the first-charge capacity is 630(±5) mA h g⁻¹ (4 moles of Li). The reversible capacity at the end of 40th cycle is 460(±5) mA h g⁻¹ (2.9 moles of Li), showing a capacity fade of 28% between 5-40 cycles (Table VI.1). Thus, cycling of nano-SnO(VO)_{0.5} to an upper cut- off voltage of 1.0 V gave only a small increase in capacity, but the capacity- fading behavior is similar to that encountered when cycled to 0.8 V cut- off.

From Fig. VI.5 and Table VI.1, the following conclusions can be drawn: 1. Nano-SnO shows capacity-fading on cycling up to 50 cycles at 0.12 C-rate in the voltage range, 0.005-0.8 V vs. Li. It shows a large capacity-fading (59% between 10-50 cycles), possibly due to the presence of nano-Sn-metal and nano-SnO₂ as a result of HEB of SnO. Hence, nano-SnO or (Sn.SnO₂), without any matrix element shows capacity-fading, and this result is in agreement with several reports on the Li- cycling of micro- and nano-SnO in the literature [9,14,15,16,17,19]. 2. Nano-SnO(V₂O₃)_{0.25} shows smaller reversible capacity in comparison to nano- SnO, as can be expected due to the presence of matrix of VO_x. This nano-composite consisting of SnO₂.VO_x shows capacity-fading under the above cycling conditions, with a loss of only 11% between 10-50 cycles. The nano-composite with a higher content of V₂O₃, namely, nano-SnO(V₂O₃)_{0.5} shows no noticeable capacity-fading up to at least 60 cycles. Thus, increasing the VO_x content with respect to Sn- content has a profound effect on the Li- cyclability of the nano- composite. 3. The nano-composite with VO as the matrix, namely, nano-SnO(VO)_{0.5} shows capacity-

fading of 25%, in comparison to the value of 11% encountered in nano-SnO(V₂O₃)_{0.25}, even though the nominal VO_x- content in both the composites is the same. This is understandable because the latter phase is composed of (SnO₂.VO_x) whereas the former phase is composed of (Sn.SnO₂.VO_x). Here, we may mention that the effect of Fe/Cr impurities, noticed as a result of HEB, on the electrochemical behavior of the nanocomposites is negligible, since they do not form alloys with Li- metal. Further, because the upper cut-off voltage for cycling is 0.8 V, no oxidation of Fe/Cr can occur at this voltage by the ‘conversion reaction’ (Fe + Li₂O ⇌ FeO + 2 Li). Thus, it is concluded that both nano- size SnO₂ and inactive matrix (VO_x) mutually help each other to buffer the large unit cell volume variations and help in better Li- cycling via Eqn.VI.3, and the Sn- V ratio of 1:1, as in nano-SnO(V₂O₃)_{0.5}, is found to be the optimum.

VI.3.2.3. Cyclic voltammetry

Cyclic voltammetry, a complementary tool to galvanostatic cycling performance, is commonly employed to establish the reversibility of electrode materials vs. Li and to evaluate the potentials at which the discharge- charge reactions take place. Cyclic voltammograms (CV) of nano-SnO(V₂O₃)_{0.5} and nano-SnO(VO)_{0.5} at the slow scan rate of 58 μV s⁻¹, in the potential range of 0.005- 0.8 V, were recorded up to 40 cycles and up to 6 cycles, respectively and are shown in Fig. VI.8. The Li- metal acts as the counter and reference electrode.

The first- cathodic scan of nano-SnO(V₂O₃)_{0.5} started from an OCV (~3.0 V), with a broad peak at ~ 0.8 V, which corresponds to the crystal structure destruction and formation of Sn nanoparticles embedded in VO and Li₂O amorphous matrix (Eqn. VI.4)(Fig. VI.8a). This is followed by a shoulder peak at 0.4 V and a broad peak centered

at 0.14 V. These two peaks correspond to the alloying of Sn in stages to reach the composition, $\text{Li}_{4.4}\text{Sn}$ (forward reaction of Eqn. VI.3). During the first- anodic scan, a broad peak at 0.56 V is seen, which corresponds to de- alloying reaction to form Sn metal nanoparticles. The second- cathodic scan is similar to the first- cathodic scan except for the absence of the shoulder peak at ~ 0.4 V. Between 2 - 40 cycles the anodic peak shifted to a slightly lower potential value (~ 0.5 V), which indicates that the de-alloying reaction occurs at lower potential due to nano-size effect and ‘conditioning’ of the electrode. The average charge and discharge potentials noticed from CV are ~ 0.5 and ~ 0.2 V, respectively which match well with the voltage plateaus seen in the galvanostatic charge-discharge profiles. The areas under the peaks in the CVs decrease slowly from 2 to 10 cycles showing slow capacity- fading. On the other hand, the areas under the peaks from 11-to-40 cycles are almost same which indicate almost nil capacity- fading and this is corroborated by the galvanostatic data (Fig.VI.5c).

The CVs of nano- $\text{SnO}(\text{VO})_{0.5}$ are shown in Fig. VI.8b. The first- cathodic scan started from the OCV (~ 2.3 V) and shows several low- intensity peaks in the potential range, 0.4- 1.2 V. The crystal structure destruction (amorphization of lattice) to form Sn nanoparticles embedded in VO and Li_2O occurs in this potential region and, as mentioned earlier, XRD shows that the nano-composite consists of $\text{Sn.SnO}_2.\text{VO}$. The first- cathodic scan also shows a broad split peak centered at 0.24 V, which corresponds to the alloy ($\text{Li}_{4.4}\text{Sn}$) formation. The first- anodic scan shows medium- intensity peaks at 0.47 V and 0.62 V and a low- intensity peak at 0.73 V. These peaks correspond to the de- alloying reaction to form Sn metal nanoparticles and seem to occur in stages. The second- cathodic scan differs from the first- cathodic scan, in that the low- intensity peaks are

seen at 0.68 V and ~ 0.5 V and the split peak is now centered at 0.31 V. This shows that alloying reaction is occurring in stages. The CVs of 2- 6 cycles overlap well showing good reversibility, but also indicate capacity- fading due to the decrease in the areas under the peaks from 2-to-6 cycles. The CV peaks are reflected as voltage plateaus in the galvanostatic profiles in Figs. VI.6c and d. The CVs of nano-SnO are analogous to those observed in nano-SnO(VO)_{0.5}, thereby indicating that VO_x is not participating in the Li-

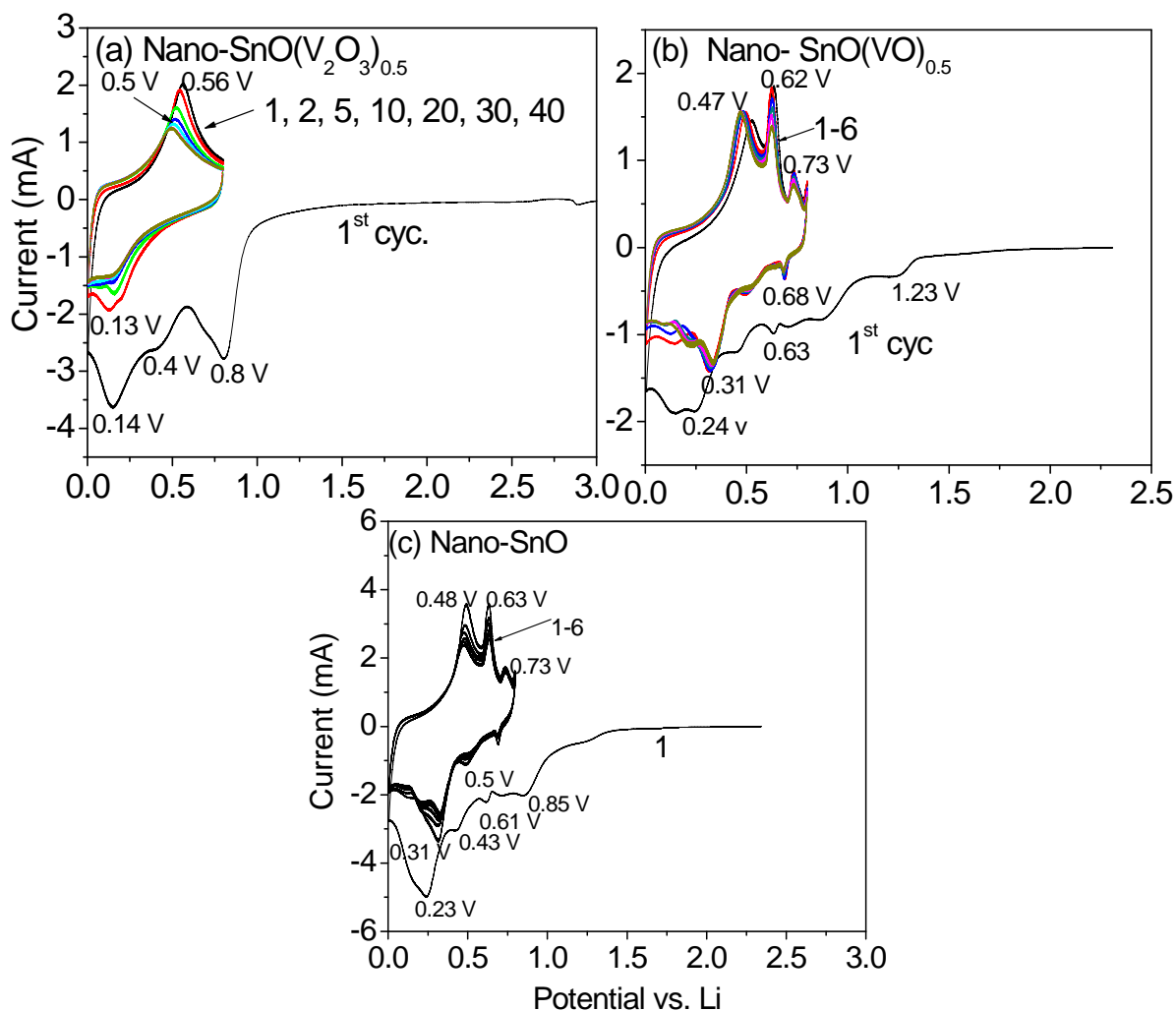


Fig.VI.8. Cyclic voltammograms of (a) Nano-SnO(V₂O₃)_{0.5}, 1-40 cycles, (b) Nano-SnO(VO)_{0.5}, 1- 6 cycles and (c) Nano-SnO, 1-6 cycles. Scan rate, 58 $\mu\text{V s}^{-1}$. Li- metal anode was the counter and reference electrode. Numbers represent the potentials in volts. Integer numbers represent cycle numbers.

cycling behavior in the composites in the potential range, 0.005-0.8 V and acts only as an electrochemically-inactive, but electronically-conducting matrix (Fig. VI.8c).

A comparison of CVs of Fig. VI.8a and b clearly reveal the difference in cycling behavior of electrochemically-formed nano-particles of Sn (via Eqn.VI.2) and that of nano-Sn obtained by the HEB process. Fig.VI.8a shows only one well-defined cathodic and anodic peak indicating that the alloying-de-alloying reaction (Eqn.VI.3) takes place in a continuous fashion. The fine structure, by way of additional cathodic and anodic peaks noticed in Fig.VI.8b for the nano-SnO(VO)_{0.5} are due to the alloying –de-alloying reaction of nano-Sn (along with SnO₂) formed during the ball-milling process. Studies by Courtney et al [30] on the Li-Sn system, by Park and Sohn [31] and Hassoun et al [32] on the nano-composite, Sn-C have shown that whenever Sn- metal is used as the active material, the alloying –de-alloying reaction always goes through several stages, depending on the value of y from 0 to 4.4 in Li_ySn at various fixed potentials ranging from 0.2 to 0.8 V vs Li. Indeed, the observed anodic peaks at 0.62 V and 0.73 V in Fig.VI.8b correspond to y = 1.75-2.5 and 1.0, respectively [30]. The matrix (VO_x, x~1) is not able to buffer the volume changes occurring, in stages, during the reactions of Eqn.VI.3 in nano-SnO(VO)_{0.5}, and hence the observed capacity-fading on cycling (Fig. VI.5d). On the other hand, VO_x is able to buffer the volume changes occurring during cycling of nano-SnO(V₂O₃)_{0.5}, since no stages were observed in the alloying-de-alloying reactions of Eqn.VI.3 (Fig. VI.5c). To summarize, the CV studies corroborate the galvanostatic cycling data and clearly distinguish between the cycling behavior of

electrochemically-generated Sn and that produced in the nano-composite as a result of HEB.

VI.3.3. Ex-situ XRD of nano-SnO(V₂O₃)_{0.25}

To establish the reaction mechanism and to supplement the galvanostatic and CV data, ex-situ XRD studies were performed on the multiple cells of nano-SnO(V₂O₃)_{0.25} at selected discharge/ charge voltages during the 1st cycle. The ex-situ XRD patterns are shown in Fig. VI.9. The y- axis values have been normalized for better comparison.

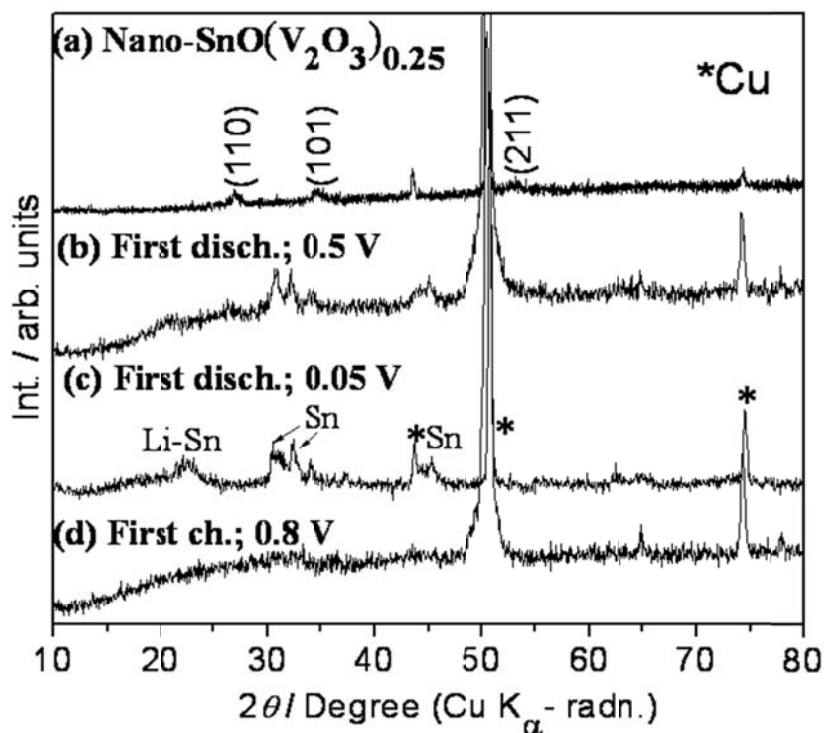


Fig.VI.9. Ex-situ XRD patterns of nano-SnO(V₂O₃)_{0.25}. (a) Bare electrode (Miller indices are indicated); (b) During first- discharge at 0.5 V; (c) During first- discharge at 0.05 V, and (d) During first- charge at 0.8 V vs. Li.

The pattern of bare electrode (Fig. VI.9a) shows the characteristic lines of SnO₂, similar to that of Fig. VI.2a, along with the Cu- metal lines due to the substrate. The pattern at 0.5 V during the first- discharge shows the characteristic lines of Sn- metal due to the

reaction of SnO_2/SnO with Li-metal as per Eqn.VI.4 (Fig. VI.9b). This is in accord with galvanostatic and CV data. The pattern at 0.05 V (Fig.VI.9c) shows the characteristic lines of both Li-Sn alloy ($2\theta = 20 - 25^\circ$) and Sn- metal ($2\theta = 30 - 35^\circ$) as per the forward reaction of Eqn.VI.3, which is expected to be completed upon deep discharge to 0.005 V. The XRD pattern at 0.8 V at the end of first- charge, shown in Fig. VI.9d, does not show the lines of Sn-metal (reverse reaction of Eqn.VI.3), possibly due to the nano- size nature of the particles. Thus, the ex-situ XRD measurements corroborate the galvanostatic and CV data and lend support to the Li- cycling mechanism.

VI.4.Conclusions

The nano-composites, $\text{SnO}(\text{V}_2\text{O}_3)_x$ ($x = 0, 0.25$ and 0.5) and $\text{SnO}(\text{VO})_{0.5}$ are prepared from SnO and $\text{V}_2\text{O}_3/\text{VO}$ by high energy ball-milling (HEB) and are characterized by XRD, SEM, and HR-TEM techniques. Interestingly, SnO and $\text{SnO}(\text{VO})_{0.5}$ are not stable to HEB and undergo self oxidation- reduction to give Sn and SnO_2 . Ball-milling of $\text{SnO}(\text{V}_2\text{O}_3)_x$ gives rise to a nano-composite of SnO_2 and VO_x . The Li- cycling properties are evaluated by galvanostatic discharge- charge cycling and cyclic voltammetry with Li as the counter electrode at room temperature. The nano- $\text{SnO}(\text{V}_2\text{O}_3)_{0.5}$ showed a first- charge capacity of $435(\pm 5) \text{ mAhg}^{-1}$ which stabilized to $380(\pm 5) \text{ mAhg}^{-1}$ with no noticeable fading in the range of 10- 60 cycles when cycled at 60 mA g^{-1} (0.12 C), in the voltage range 0.005- 0.8 V. Under similar cycling conditions, nano-SnO, nano- $\text{SnO}(\text{V}_2\text{O}_3)_{0.25}$ and nano- $\text{SnO}(\text{VO})_{0.5}$ showed initial reversible capacities between 630 and $390 (\pm 5) \text{ mAhg}^{-1}$. Between 10-50 cycles, nano-SnO showed a capacity-fade as high as 59% in good agreement with literature reports, whereas the above two VO_x - containing composites showed capacity- fade ranging from 10 to 28%. Cycling to

an upper cut-off voltage, 1.0 V gives rise to a slight increase in the reversible capacity in the case of nano-SnO(V₂O₃)_{0.25} and nano-SnO(VO)_{0.5}. However, capacity-fading also increased in them in comparison to the performance with 0.8 V cut-off (Table VI.1). The coulombic efficiency increased in all the nano-composites to 96 - 98% after 10 cycles. The presence of matrix (VO_x) enhances the Li-cycling behaviour by buffering the unit cell volume variations and providing an electronically conducting network to Li-diffusion in the nano-composites. The observed galvanostatic cycling, CV and ex-situ XRD data have been interpreted in terms of the alloying-de-alloying reaction of Sn in the nano-composite, 'Sn-VO_x-Li₂O'. In all the nano-composites presently studied, the average discharge (alloying) potential is 0.2-0.3 V and average charge (de-alloying) potential is 0.5-0.6 V vs. Li, in good agreement with literature reports on the Sn-oxides. It is concluded that upon further optimization, the nano-SnO(VO_x) can be a prospective anode material for future generation LIBs.

References

- [1] G.-A. Nazri, G. Pistoia (eds) (2003) *Lithium Batteries: Science and Technology*, Kluwer Academic Publ., New York, USA.
- [2] A. S. Arico, P. Bruce, B. Scrosati, J.-M. Tarascon, W. V. Schalkwijk, *Nature Mater.* 4(2005) 366.
- [3] A. K. Shukla, T. P. Kumar, *Curr. Sci. (India)* 94 (2008) 314.
- [4] H. Ma, F. Cheng, J. Chen, J. Zhao, C. Li, Z. Tao, J. Liang, *Adv. Mater.* 19(2007) 4067.
- [5] P. G. Bruce, B. Scrosati, J.-M. Tarascon, *Angew. Chem. Int. Ed.* 47 (2008) 2930.
- [6] M. G. Kim, J. Cho, *J. Electrochem. Soc.* 156 (2009) A277.
- [7] H. Kim, B. Han, J. Choo, J. Cho, *Angew. Chem. Int. Ed.* 47 (2008)10151.
- [8] D. Larcher, S. Beattie, M. Morcrette, K. Edström, J. -C. Jumas, J.-M. Tarascon, *J. Mater. Chem.* 17(2007) 3759.
- [9] D. Aurbach, A. Nimberger, B. Markovsky, E. Levi, E. Sominski, A. Gedanken, *Chem. Mater.* 14 (2002) 4155.
- [10] C. Kim, M. Noh, M. Choi, J. Cho, B. Park, *Chem. Mater.* 17 (2005)3297.
- [11] M.-S. Park, Y.-M. Kang, G.-X. Wang, S.-X. Dou, H.-K. Liu, *Adv. Funct. Mater.* 18 (2008) 455.
- [12] Y. Sharma, N. Sharma, G. V. Subba Rao, B. V. R. Chowdari, *Chem. Mater.* 20 (2008) 6829.
- [13] F. Huang, Z. Yuan, H. Zhan, Y. Zhou, J. Sun, *Mater. Lett.* 57 (2003)3341.
- [14] I. A. Courtney, J. R. Dahn, *J. Electrochem. Soc.* 144 (1997) 2045.
- [15] H. Li, X. Huang, L. Chen, *Solid State Ionics* 123 (1999) 189.

- [16] H. Uchiyama, E. Hosono, I. Honma, H. Zhou, H. Imai, *Electrochem. Commun.* 10 (2008) 52.
- [17] X. Wang, Z. Wen, X. Yang, B. Lin, *Solid State Ionics* 179 (2008)1238.
- [18] J. Yang, Y. Takeda, N. Imanishi, J. Y. Xie, O. Yamamoto, *J. Power Sources* 97-98 (2001) 216.
- [19] J. Ning, Q. Dai, T. Jiang, K. Men, D. Liu, N. Xiao, C. Li, D. Li, B. Liu, B. Zou, G. Zou, W. W. Yu, *Langmuir* 25 (2009)1818.
- [20] M. H. Chen, Z. C. Huang, G. T. Wu, G. M. Zhu, J. K. You, Z. G. Lin, *Mater. Res. Bull.* 38 (2003) 831.
- [21] M. V. Reddy, G. V. Subba Rao, B. V. R. Chowdari (2008) in ‘Solid state ionics: New materials for pollution free energy devices’ [Proceedings of the 11th Asian conf. on solid state ionics], (eds) B V R Chowdari et al, MacMillan, India Ltd, New Delhi, pp.187-193.
- [22] M. V. Reddy, G. V. Subba Rao, B. V. R. Chowdari (to be published).
- [23] C.-M. Park, W.-S. Chang, H. Jung, J.-H. Kim, H.-J. Sohn, *Electrochem. Commun.* 11 (2009) 2165.
- [24] B. S. Allimi, S. P. Alpay, C. K. Xie, B. O. Wells, J. I. Budnick, D. M. Pease, *Appl. Phys. Lett.* 92 (2008) 202105.
- [25] C. Grygiel, A. Pautrat, P. Rodière, *Phys. Rev. B* 79 (2009) 235111.
- [26] F. Rivadulla, J. F. Rossier, M. G. Hernández, M. A. L. Quintela, J. Rivas, J. B. Goodenough, *Phys. Rev. B* 76 (2007) 205110.
- [27] M. S. Moreno, G. Punte, G. Rigotti, R. C. Mercader, A. D. Weisz, M. A. Blesa, *Solid State Ionics* 144 (2001) 81.

- [28] K.-M. Lee, Y.-S. Lee, Y.-W. Kim, Y.-K. Sun, S.-M. Lee, *J. Alloys Compds.* 472 (2009) 461.
- [29] M. Wachtler, J. O. Besenhard, M. Winter, *J. Power Sources* 94 (2001) 189.
- [30] I. A. Courtney, J. S. Tse, O. Mao, J. Hafner, J. R. Dahn, *Phys. Rev. B* 58 (1998) 15583.
- [31] C.-M. Park, H.-J. Sohn, *Electrochim. Acta* 54 (2009) 6367.
- [32] J. Hassoun, G. Derrien, S. Panero, B. Scrosati, *Adv. Mater.* 20 (2008) 3169.

Conclusions and Suggestions for Future Work

The results of the present studies deal with the investigations on Li- storage and cyclability of mixed metal oxides and cobalt nitride. The mixed oxides studied are: Mo₃- cluster compounds, Li(Y/Ho)Mo₃O₈, A₂Mo₃O₈ (A = Mn, Co, Zn), Sn- hollandites, K₂(M₂Sn₆)O₁₆ (M = Co, In) and nanocomposites, SnO(V₂O₃)_x (x = 0, 0.25, 0.5) and SnO(VO)_{0.25}. The reaction mechanism involved during Li- cycling is ‘conversion’ (for Mo- compounds and CoN) and/or ‘alloying-de-alloying’ (for Sn- oxides) reactions. The presence of different counter metal ions, the starting crystal structure, particle size, morphology, nature and quantity of matrix (counter) elements and the upper cut- off voltage range influence the Li- cycling behavior.

The following conclusions can be drawn from the present studies:

1. Li- cycling behavior of the Mo₃- cluster compounds depends on the counter metal ions (Li, Y/Ho, Mn, Co, Zn). The heat- treated electrode with A = Co, Zn showed improved Li- cycling performance compared to the bare electrodes. This is ascribed to a more homogeneous distribution of the active material in the composite electrode (containing carbon and binder) and good adherence to the current collector.
2. Nanoflake CoN showed an increasing trend in the reversible capacity with the increase in the cycle number, and with excellent rate capability.
3. The nano-phase tin hollandites, K₂(M₂Sn₆)O₁₆ (M = Co, In) showed better capacity retention on cycling as compared to the corresponding micron- size particles. Excellent rate capability was shown by nano-phase with M = Co. The

heat treated electrode of nano-phase with $M = \text{In}$, showed a stable capacity as compared to the bare electrode.

4. The presence of V_2O_3 and VO (electrochemically- inactive matrix) and reduction of particle size improved the Li- cycling performance of $\text{SnO}(\text{VO}_x)$ composites, but at the cost of lowering the capacity values.

On the basis of the conclusions drawn from the present work, following suggestions are made for further study:

1. Other isostructural compounds, $\text{A}_2\text{Mo}_3\text{O}_8$ with $A = \text{Fe}, \text{Ni}, \text{Cd}, (\text{LiGa})$ and (LiIn) which are already known in the literature, can be prepared by carbothermal/ other methods and their Li- cyclability must be examined, so that the proposed Li- cycling mechanism is substantiated. Also, In can form an alloy with Li , so that the reversible capacity can be increased. It has not been possible to prepare nano- $\text{A}_2\text{Mo}_3\text{O}_8$ compounds by the carbothermal method. It is worthwhile exploring other/ hydrothermal methods to obtain the above nano-phase.
2. Till now, bulk powders/nano- particles of metal nitrides of MN , $M = \text{Co}, \text{Fe}, \text{Ni}$ have not been examined for their Li- cyclability. In view of the excellent Li- cycling performance of nano-flake CoN , it is worthwhile to explore the above.
3. Studies should be continued on tin- oxides with different crystal structures and to optimize the content of electrochemically inactive- or -active 'matrix element' to achieve a high and stable reversible capacity. Some examples are: ZnSnCoO_4 and ZnSnNiO_4 (spinel structure), Sn_2TiO_4 , SnWO_4 , Sn_2WO_5 and Sn_3WO_6 .

4. To reduce the high irreversible capacity loss (ICL) during first- discharge and charge cycle observed in almost all the oxide systems, composite with metal particles may be prepared and studied.